Abstract

The aims of this research project were to manufacture and characterise PDPA-based pH-sensitive functionalised polymersomes using a medium-high content screening method, suitable for CNS drug delivery. Angiopep-2 functionalised polymersome formulations have been found that are able to penetrate the blood-brain barrier (BBB) effectively in both *in vitro* models and *in vivo.*

Using Transmission Electron Microscopy, Dynamic Light Scattering, FACS analysis, and 2D *in vitro* screening gave information on the physical and biological features of polymersomes based on their different chemistries, including size distribution, architecture, topology, cellular localisation, cellular uptake kinetic and immune response. The studies showed the possibility of controlling cellular internalization and cargo destinations by manipulating polymersome surface chemistry and specific ligand(s). The subsequent *in vitro* and *in vivo* studies built on these screening results.

Using extensive Confocal Laser Microscopy and image analysis, Ang-POEGMA-PDPA polymersomes showed effective receptor-mediated transcytosis (RMT) in the 3D *in vitro* BBB model established, while the RVG-functionalised formulation did not. Further *in vivo* studies showed that the Ang-functionalised polymersomes were able to penetrate the mouse BBB via effective RMT. Moreover, primary cargo delivery studies showed successful IgG transport into brain by Angiopep-2-functionalised POEGMA-PDPA polymersomes.

The results in this thesis can provide a useful platform for further examination of CNS delivery of polymersomes and their cargos.

Chapter 1

Introduction to CNS delivery

1.1 Introduction to the Central Nervous System

1.1.1 What is the central nervous system?

The mammalian nervous system is divided into two parts: the peripheral nervous system (PNS) and the central nervous system (CNS). The PNS is made of ganglia and nerves; it is located outside the brain and spinal cord. The CNS consists of the brain (Figure 1.1) and the spinal cord, and plays a fundamental role as a ‘processing centre’ in the control of behaviours.

The CNS contains the majority of the nervous system. Compared to the PNS, the CNS is composed of numerous arrays of neuronal cells, each with a complex pattern of connections, which cooperate in generating perceptions and higher CNS functions. Unlike the PNS which is more exposed to possible physical injury and toxins, the CNS is highly protected by the bones of the spine and skull, associated with the BBB (blood-brain barrier), and the BCSFB (blood-cerebrospinal fluid barrier) [1], which together anatomically and metabolically secure its function. As a result of these

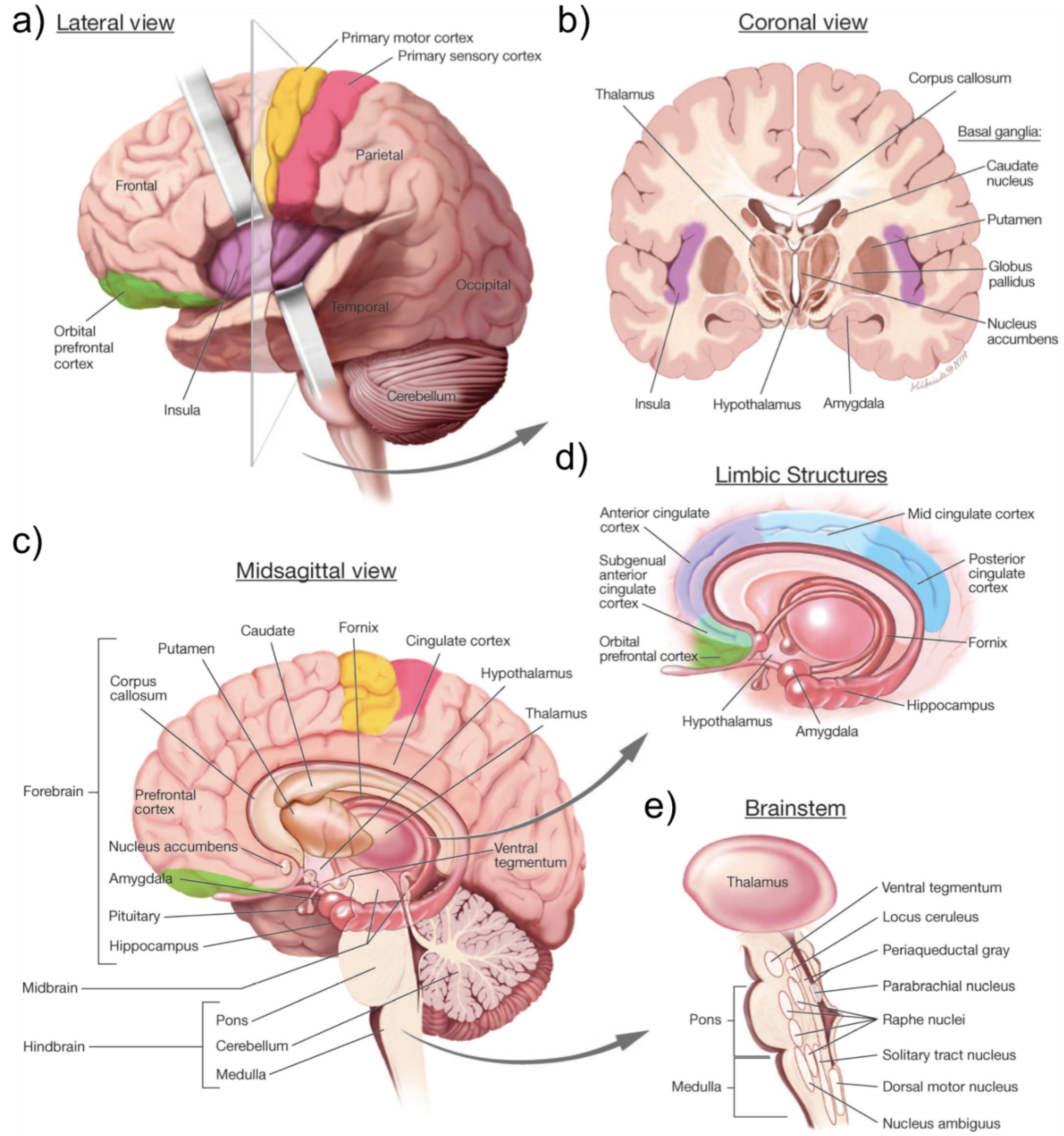

Figure 1.1 Anatomy of the human brain [2]. a) Lateral view. b) Coronal view, depicts the brain viewed from the front after being divided along the plane shown in the lateral view. c) Midsagittal view from dividing the brain in the midline; depicts the medial surface of the right half of the brain. d) Detail of Limbic structures, from midsagittal view, same orientation). e) Detail of Brainstem, from midsagittal view. Color-coding designates the same structure in one or more views. Gold = primary motor cortex; Red = primary sensory cortex; Green = orbital prefrontal cortex; Purple = insula; Different shades of blue = different sub regions of the cingulate cortex.

multiple barriers, the cells of the CNS are bathed in a fluid that serves as brain interstitial fluid (ISF), which differs from that bathing the cells in the rest of the body. Because of the existence of the BBB, the ISF generated across the brain capillary wall contains far less protein including albumin and immunoglobulin G (IgG) than the ISF of tissues such as muscle, and also has a subtly different ionic composition more optimal for neuronal function. However, these barriers create problems for medicines as they stop many therapeutic drugs from reaching the brain, critical in treating CNS disorders.

1.1.2 Barriers to the central nervous system

Normal functioning of the CNS relies on a constant supply of essential molecules from the blood such as nutrients (e.g. glucose, amino acids), exchange of electrolytes between blood and brain extracellular fluids, and efficient removal of metabolic waste products and excess neurotransmitters. Therefore, a number of specific transport proteins and other transport systems are expressed in BBB capillary endothelial cells and BCSFB epithelial cells that regulate the transport of nutrients and ions into the CNS and removal of waste products from the ISF and CSF.

1.1.2.1 Blood-brain barrier (BBB)

Over a century ago, Paul Ehrlich and Edwin Goldmann (one of Ehrlich's students) demonstrated for the first time the existence of some sort of compartmentalisation between the brain and the body, by a series of dye staining experiments [3, 4]. In 1900, a Berlin physician, Lewandowsky, proposed the concept of a blood-brain barrier (originally named the hematoencephalic barrier). However, it was not until 1921 with the work of Lina Stern that the terminology of blood-brain barrier was first used [5]. With the introduction of transmission electron microscopy (TEM) to medical research in the 1960s, the actual membranes at the BBB endothelium with surrounding perivascular endfeet could be visualized. Electron-dense tracers were used to confirm the presence of the blood-brain barrier at the level of the endothelium, with the tight junctions severely restricting paracellular permeation via the intercellular cleft.

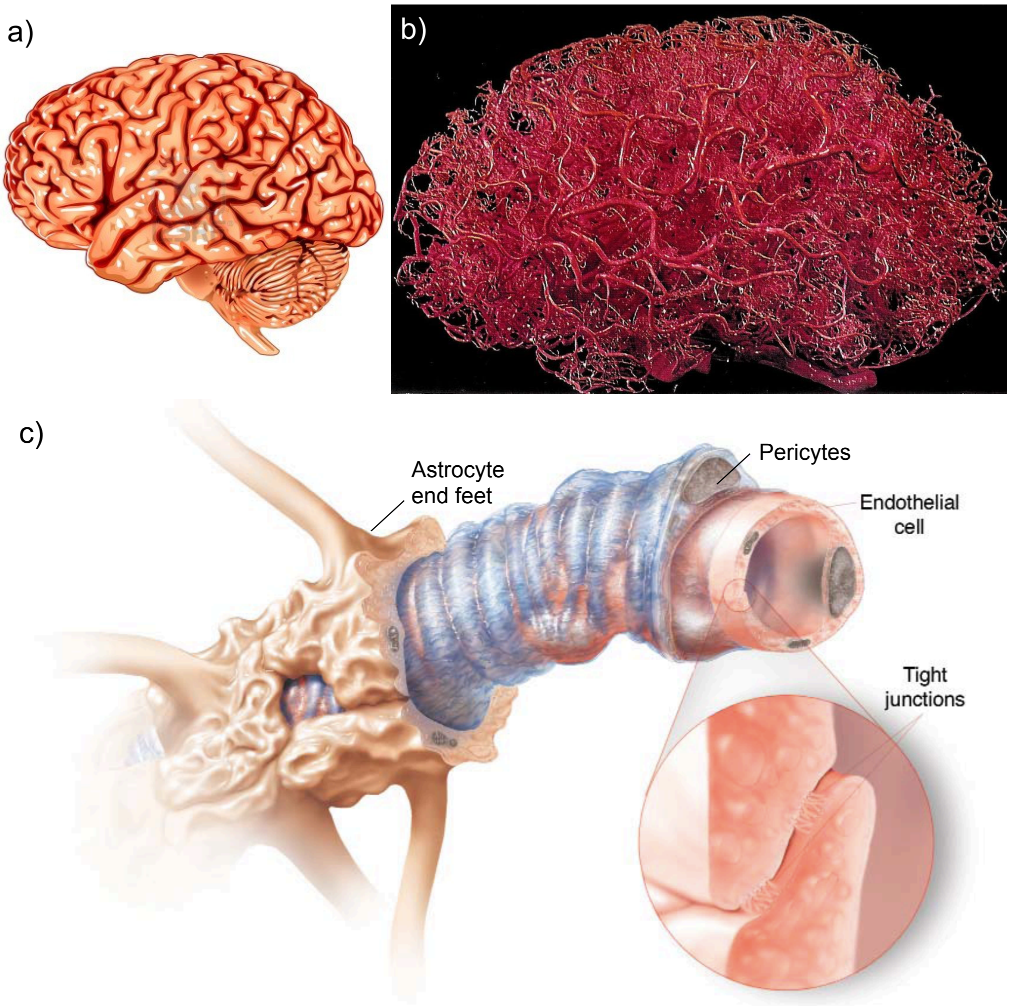

Figure 1.2 The brain vasculature, blood-brain barrier and its associated cells. a) Lateral view of human brain. b) Vasculature of the human brain, injected cast [6]. c) 3-D layered view of a brain capillary and its associated cells, showing endothelial cells and their tight junctions, pericytes and astrocyte end feet [7].

Nowadays, the BBB is recognized as not only an anatomical barrier, but also a metabolic barrier, able to regulate the exchange of nutrients and metabolic waste products, signalling molecules and ions between the blood and ISF. The BBB mainly consists of polarised brain capillary endothelial cells (Figure 1.2) linked by tight junctions (TJ), with a significantly large interface between the vasculature and nervous system (average 12-20m^2 in the human brain); the endothelium is surrounded by a layer of pericytes and astrocyte endfeet. The brain capillaries form the BBB, and are structurally different from the capillaries in other organs, lacking micropores and having a paucity of pinocytotic vesicles, such that the BBB acts almost like a continuous cell layer [8], hence minimising the diffusion of substances into the brain. Brain vessels are also found to have thinner walls (0.2-0.5μm) and smaller diameters than the vessels in other organs [9]; furthermore they contain many more mitochondria than other vascular endothelia [10], suggesting that rapid and ATP-dependent transport mechanisms are very active within the BBB endothelium. Previous studies have also shown that both astrocytes and pericytes are closely associated with the brain endothelium (Figure 1.2 [7]), playing an important role in induction, maintenance and regulation of BBB properties and transport.

Tight junctions: Tight junctions (TJ) are formed by a series of trans-membrane proteins that can also be found in epithelia such as those of the gut, the bladder and the lung. The BBB TJs differ from those of non-brain endothelia and of epithelia both in distinct morphology and molecular properties. So far many tight junction components such as occludin, claudins, ZO-1, ZO-2, ZO-3 and JAM-A/B/C have been identified and characterised (Figure 1.3). Claudins are small trans-membrane proteins that regulate substance diffusion via the intercellular cleft and ionic selectivity. Occludin is a 65kDa protein that is capable of linking with *zonula occludens* proteins (ZO-1, ZO-2, ZO-3), and together they contribute to the higher TEER (trans-endothelial electrical resistance) of the BBB [12]. The value of TEER can be over 1500 Ω.cm^2 compared to TEER of 3-33 Ω.cm^2 in endothelia of other tissues [13]. JAM family proteins are also present in the brain endothelium as junction adhesion molecules. TJ morphology and function is closely associated with that of Adherens Junctions (AJ, Figure 1.3) involved in the formation and maintenance of the tight junctions.

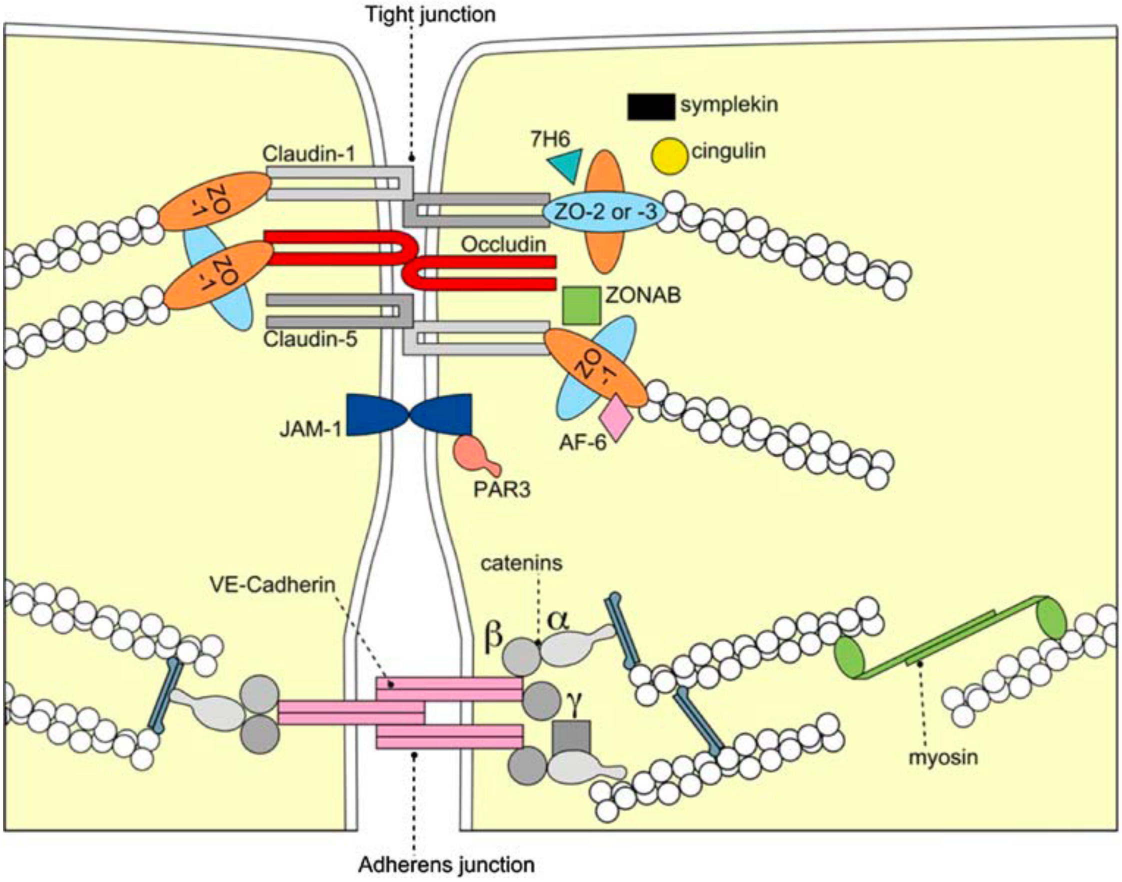

Figure 1.3 Molecular composition of tight and adherens junctions [11].

Astrocyte function: In previous *in vitro* cell co-culture models and conditioned media studies, astrocytes have been demonstrated to play important roles in induction and maintenance of the BBB. In an endothelium-astrocyte co-culture experiment, Trans and co-workers [14] showed that astrocytes produce TGF-β (transforming growth factor-β), which is responsible for the down-regulation of tissue PA (plasminogen activator, tPA) and anticoagulant thrombomodulin (TM) expression in cerebral endothelium.

It was also suggested that TGF-β might induce endothelial cells into a capillary-like structure [15] *in vitro*. However, it is still not clear whether this process occurs *in vivo*. *In vitro* cell culture work showed that astrocytes can regulate several BBB properties, leading to tighter tight junction formation and higher TEER value [16], as well as increased expression of GLUT1 glucose transporter [17] and a specialised enzyme system [18]. *In vivo*, astrocytes show several different morphologies while associating with other cell types [19]. 11 distinct phenotypes have been distinguished and eight of them involve specific interactions with BBB blood vessels [19].

Pericyte (PC) function: Pericytes are cells wrapped around the endothelium that provide primary structural support and vaso-dynamic capability to the microvasculature. Recent studies have also provided evidence that pericytes play a substantial role in regulating BBB functions. Barres and co-workers studied the *in vivo* roles of pericytes during brain development [20, 21]. Brain slices from embryonic mice showed the presence of vascular endothelium from an embryonic age of 11 days (E11), followed by the presence of pericytes at E12. At this time the brain endothelium showed extensive expression of occludin, suggesting that BBB tight junction formation is upregulated by pericytes during embryonic development. By contrast, astrocytes were not fully observed until P5 (postnatal day 5). Pericytes express PDGF receptor β, and Pdgfr-β [22] deficient mutant mice were employed to demonstrate the role of pericytes in BBB regulation. The BBB of pdgfb$^{ret/ret}$ (Ret: retention motif-deficient) mouse was relatively leaky as shown by leakage of intravascularly injected Evans blue (complexing with albumin). Vascular leak was also shown for HRP (horseradish peroxidase, 44kDa), examined in brain slices from pdgfb$^{ret/ret}$ mice by TEM (transmission electron microscopy), with vesicular transfer implicated. The increased trans-endothelial transcytosis that occurs as a result of brain pericyte deficiency in the pdgfb$^{ret/ret}$ mutant mice suggests that pericytes play a role in controlling BBB permeability and macromolecular transport. A role for pericytes in regulating capillary diameter/blood flow [23] and clearance of toxic cellular by-products [24] has also been demonstrated. More discussion based on the experimental study is given in Chapter 5.

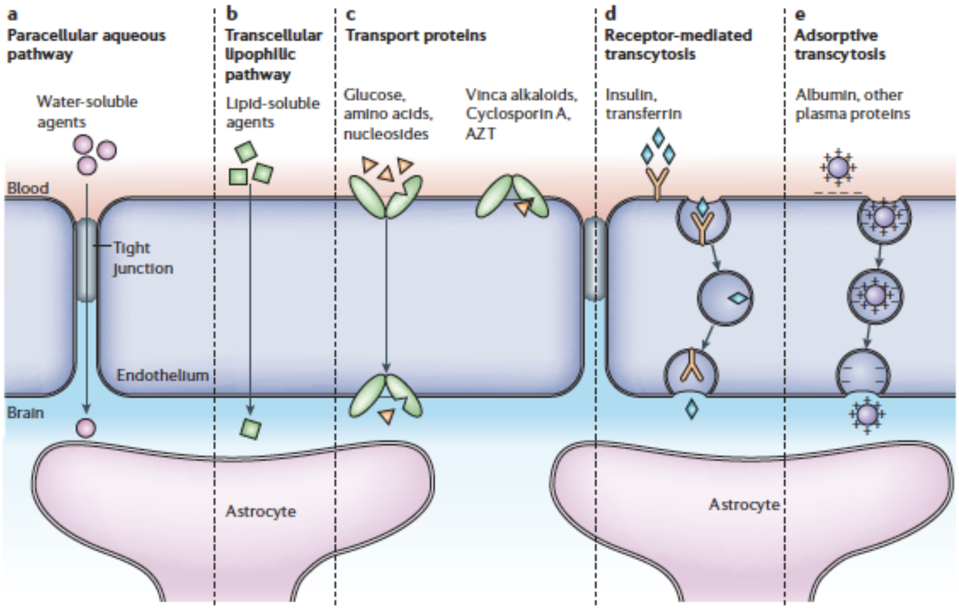

Figure 1.4 Pathways across the blood-brain barrier [25].

As a consequence of the 'tight' characteristics of the BBB, only gases (CO_2, O_2) and low molecular weight lipophilic molecules (normally <600 Da e.g. ethanol) can pass freely across the brain endothelium. Water can move across by several routes, via 'kinks' in the lipid bilayer, tight junctions and transcytosis vesicles, and probably via solute carriers. Diffusion of ions such as Na^+ and Ca^{2+} and polar hydrophilic substances is severely restricted by the membrane and tight junction properties. However, the endothelial lipid membranes also contain several transport carriers supplying the necessary nutrients to the brain, including amino acids (LAT1 carrier), glucose (GLUT1 carrier) and nucleosides. In addition, some specific proteins such as insulin and transferrin are taken up by specific receptor-mediated transcytosis (RMT); permeation of some poorly transported plasma proteins such as albumin can be increased artificially by cationisation, giving access to adsorptive-mediated transcytosis (AMT) (Figure 1.4). In the current CNS therapeutic market, most CNS drugs used enter via the transcellular lipophilic route [25].

1.1.2.1 Blood-cerebrospinal fluid barrier (BCSFB)

The blood-cerebrospinal fluid barrier (BCSFB) at the choroid plexuses (specialised ependyma formed by outpouchings of vascularised pia into the ventricles) is responsible for CSF production, and regulates blood:CSF transport of a range of ions and solutes including vitamins. It also synthesises important growth factors and regulatory molecules such as transthyretin. CSF flows out through cisterns into the subarachnoid space, and from there is drained back via several routes including arachnoid granulations and nasal lymphatics into the venous blood. The arachnoid membrane covers the surface of the brain under the dura, and also forms a blood-CSF barrier, but transport across the arachnoid is not an important route for entry of solutes into the brain [26].

Although both the BBB and CP regulate diffusion/transport of molecules by complex morphological features, the CP displays different properties compared to the BBB, with highly permeable fenestrated capillaries. The barrier layer is formed by the specialised CP ependymal epithelium, coupled by tight junctions, but less tight than those of the BBB. The CP provides the CNS with a high turnover rate of fluid (approx. 400ml/day, human) containing micronutrients, peptides and hormones for the neuronal network. The total CSF volume is approximately 150 ml in a normal human adult, and is replaced rapidly, three or four times every day. The CP is made up of villous structures floating in the CSF, with a brush border of microvilli which increases the fluid contact surface area significantly. A TEM micrograph of mouse brain CP microvilli can be found in ANNEX Figure S11. The CP is attached to the ventricular ependyma by a stalk.

The ependyma is continuous with the epithelial layer of the CP that is composed of a single layer of cells filled with mitochondria and joined together by TJ [27] and adherens junctions. The *in vitro* TEER across these epithelial TJs is lower than across the BBB [28]; it is classed as a leaky epithelium. Such leaky epithelia are found in some segments of the kidney and gut, which form an isotonic fluid and do not generate steep trans-epithelial concentration gradients.

One of the most important roles of the BCSFB is the protection of the brain against toxins and xenobiotics. CP epithelium expresses a number of transport proteins that are involved in regulating CSF-blood substance exchange. MDR 1 Pgp (P-glycoprotein) produced by a multidrug resistance (MDR) gene [29] has been reported in the choroid epithelial cells, but its

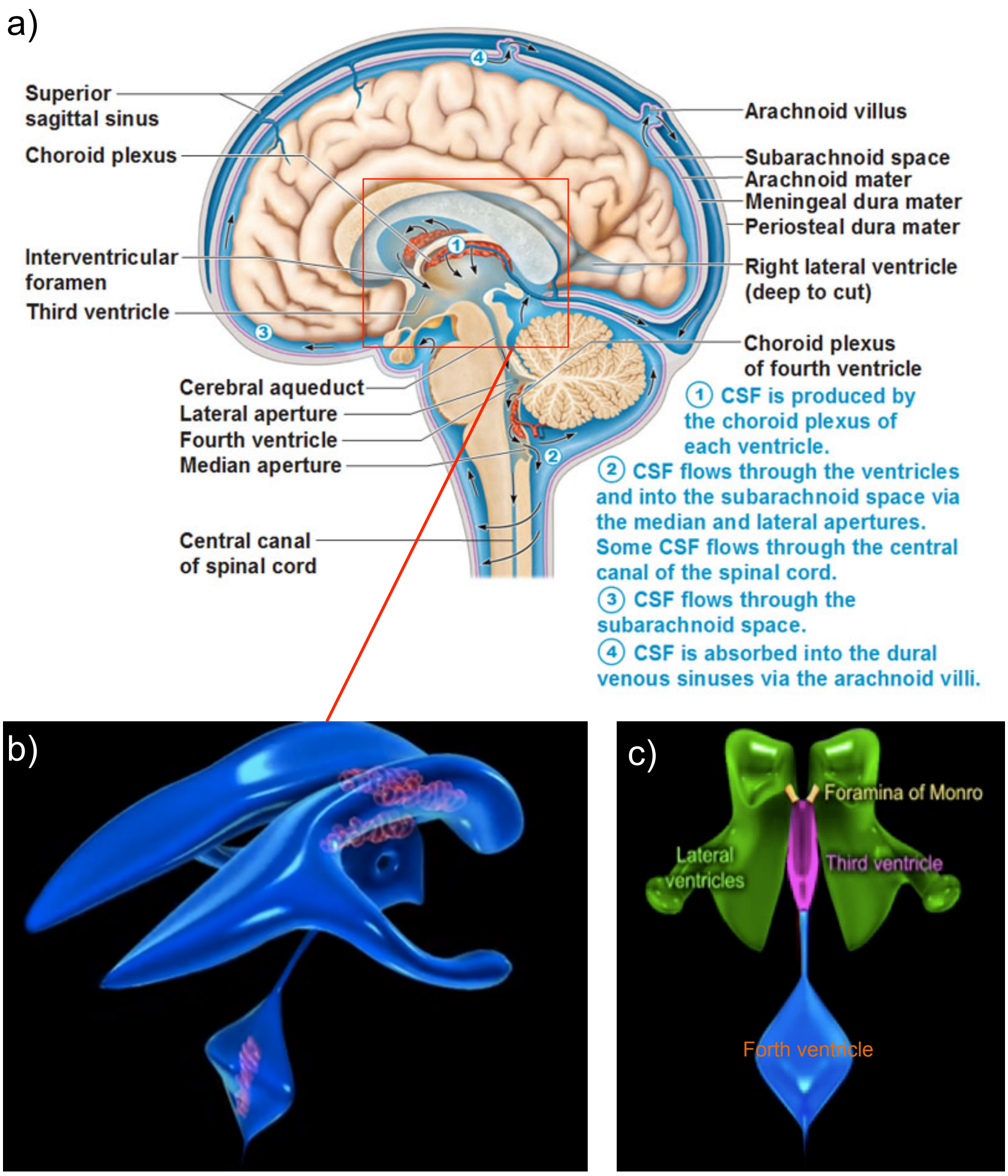

Figure 1.5 Human CSF compartments, CSF circulation and ventricular system. a) Circulation of cerebrospinal fluid in human brain [36]. b) and c) 3-dimensional views of the human ventricular system showing choroid plexus locations (red in b) [37].

localization and physiological role are uncertain. The chief ABC efflux transporter, present on the basolateral (blood-facing) CP membrane is multidrug resistance associated protein 1 (MRP 1), which helps to protect normal and tumour cells against the influx of certain xenobiotics, and confers multidrug resistance to anticancer drugs such as doxorubicin, vinblastine and etoposide [30, 31]. MRP 1 was also found in CP epithelium by immunohistochemical studies [32]. Mutant mice lacking MRP 1 in the CP epithelium showed an approximately 10-fold increase in CSF etoposide (a model cytotoxic agent) after intravenous administration. The CP also controls ion transport, as well as regulating the transport of glucose [33] and amino acids [34] across the apical membrane of CP epithelial cells.

The flow of CSF is shown in Figure 1.5; it travels through the ventricles and into the subarachnoid space via the median and lateral apertures, and some CSF flows along the spinal canal in the centre of the spinal cord. The CSF then flows through the subarachnoid space, and is eventually absorbed into the dual venous sinuses via the arachnoid villi (Figure 1.5); additional CSF clearance routes along blood vessels and nerves into nasal lymphatics and lymph nodes in the neck have been reported. The CSF is described as having a ‘sink’ function, removing metabolic waste from the CNS. A large number of substances formed in the nervous tissue during its very active metabolism need to be cleared; some are effluxed across the CNS barriers, some enter the ISF/CSF and are consequently removed to the bloodstream along ISF and CSF clearance pathways [35].

The BBB and BCSFB together play the role of defence of the CNS; the relationship and major transport interfaces in the CNS are described in Figure 1.6. While all of the BCSFB regions concurrently engage in influx/efflux of solutes and water, the arachnoid is predominantly involved in fluid re-absorption, whereas the CP is specialised for high-capacity secretion using a range of transporters, many of them different from those of the BBB.

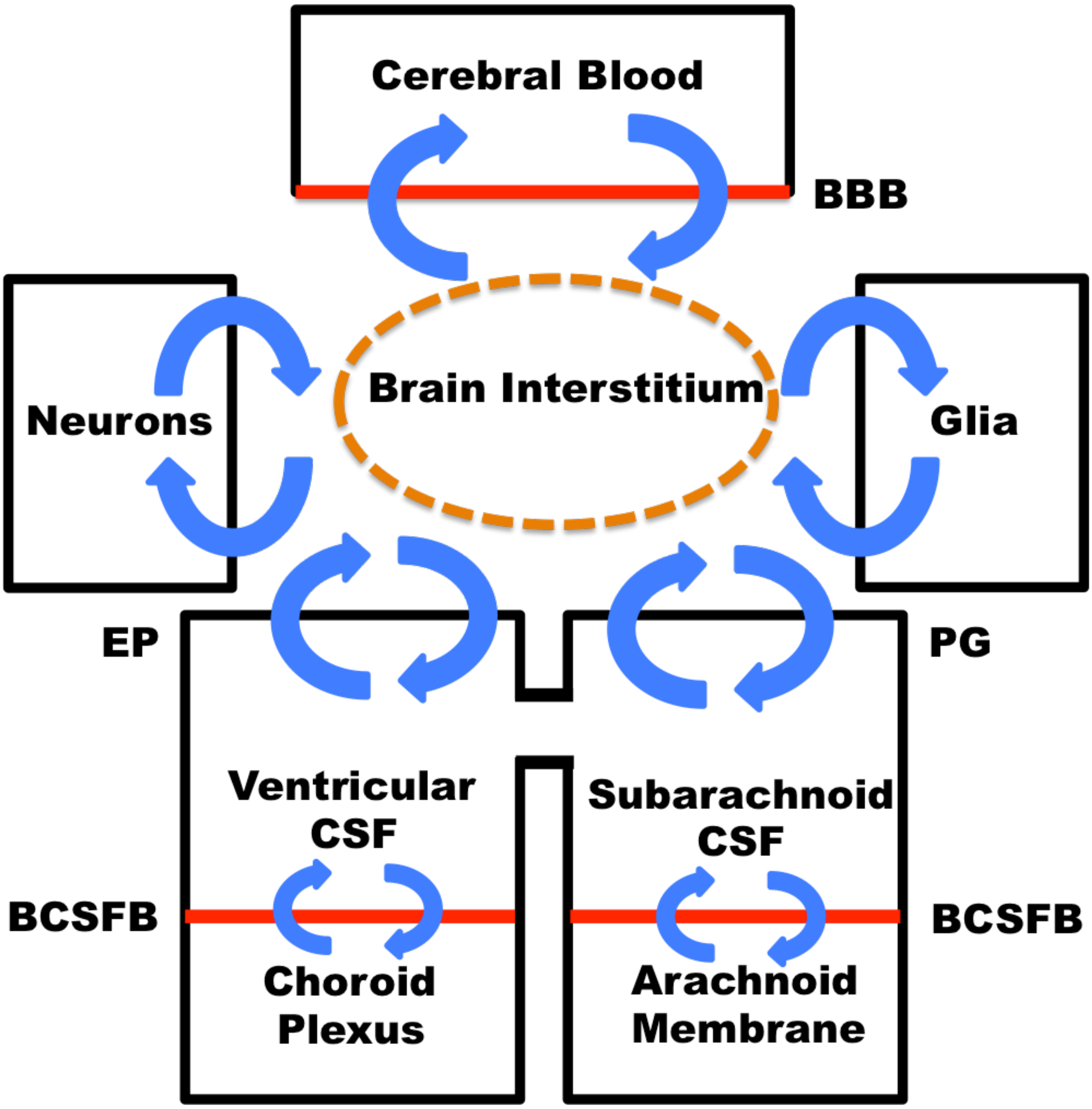

Figure 1.6 The major exchange and transport interfaces in the central nervous system (CNS). The blue arrows indicate substance exchange; the red lines indicate BBB and BCSFB. EP: ependyma. PG: pial cells of the leptomeninges and underlying glia limitans at surface of brain

1.1.3 CNS barriers and therapeutics

Two crucial questions arise from this survey of CNS barriers. Could therapeutics be delivered effectively in sufficient quantity to the CNS across CNS barriers without potential side effects? Could therapeutics be designed to target a site in the CNS specifically to maximise their utility? Until now, many drug compounds have been tested and several methods/models have been developed for assessing and for prediction of their BBB permeability. It is much more difficult to enhance BBB permeability for macromolecules or larger insoluble therapeutics compared to small drugs. Attempts have been made to use the endogenous uptake mechanisms at the BBB endothelium such as GLUT-1 and LAT-1 solute transporters and LRP-1- or transferrin receptor-mediated RMT. There appear to be multiple substrate-binding sites on some of the small solute carriers (SLCs); LAT-1 for example has broader specificity than most of the other solute carriers and may be suitable for transport of some polar pro-drugs.. Nevertheless many potential drugs, particularly macromolecular therapeutics, have failed and been discarded due to failure to respond to these two questions. In this case, hijacking BBB interface transporters for novel CNS disease therapy has become an extensive research topic.

1.1.4 Transcytosis: A gate to the CNS through the BBB

Transcytosis is defined as the transportation of a macromolecular substance from one side of a cell to the other within membrane-bounded vesicles [38] (Figure 1.7) [39], while the cargo maintains stability and is unchanged during the process. The most extensive transcytosis observed *in vivo* is that of plasma proteins across the endothelium that lines the inner surface of most of the non-brain vasculature. However, such transcytosis is severely down-regulated at the BBB, in part *via* influence of pericytes during development.

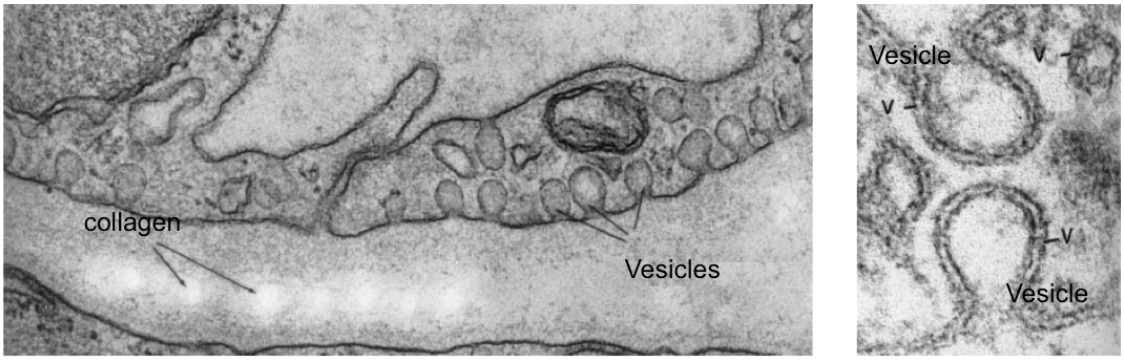

Figure 1.7 Left: Ultrastructure of an endothelial cell forming part of a muscle capillary (transverse section) showing junctional region, membrane vesicles and collagen in basement membrane/perivascular space. **Right: Higher magnification view of caveolae** opening to luminal (above), and abluminal (below) side. [39]. Note that in brain capillary endothelia, there are many fewer vesicles and caveolar openings, endocytosis and transcytosis being strictly regulated.

The limited BBB transcytosis that does occur, observed in the endothelium of brain blood capillaries, transports a limited range of substances required by the brain. However, transcytosis is not a unique BBB property and also occurs across the epithelial cells of the choroid plexus into the cerebrospinal fluid (BCSFB); recently Grapp et al. showed successful delivery of folate into the brain parenchyma via choroid plexus transcytosis [40]. This opens new avenues for cerebral drug targeting.

Transcytosis controls selective macromolecular exchange between the blood and brain, preventing the entry of undesired molecules or pathogens in order to maintain CNS homeostasis. As one of the body’s own transport mechanisms, transcytosis can help to overcome the highly selective BBB that normally stops the uptake of most therapeutics. To date, several macromolecular cargos have been shown to cross the capillary endothelial cells by transcytosis. These include iron-transferrin [41], insulin [42] and low-density lipoprotein (LDL) [43]; these carrier cargos are highly biocompatible and non-immunogenic as they are endogenous. Attempts to use drugs/therapeutics directly conjugated with these proteins have demonstrated the possibility of crossing the BBB by compounds given via intravenous administration.

1.2 CNS diseases and clinical motivation

1.2.1 CNS diseases

The CNS is a sophisticated, complex system that regulates and coordinates the body's basic functions and activities quickly and automatically. When CNS diseases occur, the result can be devastating and problematic. CNS disease has many causes including infection, pathology and hereditary, affecting the brain and/or the spinal cord. Some of the major types of disorder include Alzheimer's disease (AD) [44], Parkinson's disease (PD) [45], Huntington's disease (HD) [46] and brain tumours. Their causes, symptoms and current management are listed in Table 1.1.

Alzheimer's disease (AD) was first described in 1906 by Alois Alzheimer, a German psychiatrist and neuropathologist [44]; its incidence is increasing considerably in ageing populations in Europe and North America. AD is mostly diagnosed in people over 65 years old [47]. There were 26.6 million patients in 2006 globally, and this number was predicted to increase to 1.1% of the global population at 2020 [48]. There is currently no cure for AD. Biochemical evidence points to a loss of choline acetyltransferase and acetylcholine (ACh) in the cerebral cortex of patients with AD, and is associated with the formation of plaques and tangles in the brain [49]. This theory has been widely accepted and translated into several therapies based on reducing the loss of acetylcholine [50, 51]. However, such treatments only mitigate AD symptoms and fail to stop disease progression, which usually occurs over 5-7 years. Another theory driving therapeutic strategy focuses on the accumulation of neurotoxic amyloid-β (Aβ), a significant trademark of AD [52]. The formation of Aβ is catalysed by a protease with numerous substrates called γ-secretase [53, 54]. As a consequence, the development of therapeutically efficient γ-secretase inhibitors might reduce Aβ formation and accumulation [54, 55]. In addition, a novel γ-secretase activating protein (GSAP) has been found which can serve as an Aβ-lowering clinical target without affecting any other key functions of γ-secretase [56]. However, none of the therapies targeting amyloid-β has yet been successfully translated into the clinic.

Parkinson's disease (PD): PD is a degenerative disorder of the CNS. In the early stages of PD, the most obvious symptoms are movement-related such as slowness and shaking, with dementia normally happening in the advanced stages. It is also a common disease among the aged population, mostly occurring after the age of 50, and significantly affects quality of life [57]. Compared to the general population, PD patients experience significantly more pain as measured by the SF-36 Bodily Pain Scale [58]. PD is traditionally considered a non-genetic disorder, however a proportion of PD disease is known to be caused by genetic factors. Mutations in the PARK2 gene encoding for the protein parkin have been identified in some rare familial forms of PD; additional genes with mutations linked with PD include PINK1 and DJ1 [59]. There is no cure for PD so far, however, surgery [60], medication and multidisciplinary management can provide relief from the symptoms; therapeutics include levodopa, dopamine agonists and MAO-B inhibitors [61]. Recent efforts have also generated a novel AVV2-GAD (glutamic acid decarboxylase) gene therapy for advanced PD [62].

Huntington's disease (HD): HD is a neurodegenerative genetic disorder that leads to cognitive decline and psychiatric problems caused by the failure of muscle coordination. Unlike AD and PD, HD patients usually present between the ages of 20 and 50 years old, with about 15 years' disease progression to death. Its may present with choreiform movement, character change or psychotic behaviour. The abnormal gene (HD gene), localised to chromosome 4, encodes the Huntingtin protein [63]. The HD gene contains increased tri-nucleotide CAG repeat sequences, over 99% of HD patients having more than 40 CAG repeats, compared to 26 repeats or less in normal individuals. A consequence of such a mutation is severe loss of small spiny neurons in the caudate and putamen with subsequent astrocytosis [64]. There is currently no cure for HD; treatment is only available to reduce the severity of some of the symptoms [65].

These CNS diseases, resulting in neurological or psychiatric disorder, can affect either the brain or the spinal cord. Effective delivery of therapeutic drugs to the CNS and to treat CNS disease is a huge challenge due to the presence of the BBB and BCSFB. On the other hand, failure of the BBB is an important event in the development and progression of several diseases that affect the CNS. BBB permeability may relate to pathology in some cases such as traumatic brain injury [66]. Moreover, study of the contribution of specific BBB tight junction protein alterations is also a rapidly developing area of inquiry.

Type of CNS Disease	Cause	Symptoms	Pathology	Prevention and Management
Alzheimer's Disease (AD)	1-5% Genetics, mostly unknown	Memory loss, body function loss, leading to death	Loss of neurons and synapses, protein misfolding of β amyloid	Medication, Life style (intellectual activities), Diet
Parkinson's Disease (PD)	Environmental factors (pesticide exposure etc.), 5-15% Genetic disorder	**Motor**: tremor, rigidity, slowness of movement, and postural instability **Non-motor:** autonomic dysfunction, neuropsychiatric problems	Cell death in the substantia nigra and ventral part of the pars compacta.	Caffeine consumption, antioxidants
Huntington's Disease (HD)	Mutation of Htt (Huntingtin) gene, autosomal dominant inheritance	**Early**: Changes in personality, cognition and physical skills **Late**: Difficulty with voluntary movements, rigidity, dystonia and bradykinesia	Neuronal changes due to mHtt, may also cause cell death; brain macroscopic changes due to the mHtt.	Tetrabenazine, benzodiazepines, remacemide (under investigation), physical therapy, nutritional care
Spinal muscular atrophy (SMA)	Mutation of SMN1 (Survival motor neuron protein) gene	Muscle weakness, bell-shaped torso, poor feeding, arthrogryposis, weight lower than normal	Mutation of SMN1 leads to gradual death of motoneurons in anterior horn of spinal cord and in brain. Muscles undergo progressive atrophy.	Palliative care: orthopaedics, respiratory care

Other CNS diseases and disorders include epilepsy, meningitis, migraine, locked-in syndrome, multiple sclerosis, traumatic brain injury (TBI) and stroke.

Table 1.1 Main features of some common CNS diseases and their causes, symptoms and current management.

1.2.2 Clinical motivation: market and research

As described above, CNS diseases such as PD, AD and HD can be devastating and have diverse causes. Therefore, identifying methods to improve CNS therapeutics and their delivery represent an enormous drug discovery effort. In recent decades, influenced by the economic crisis, the unemployment rate has risen significantly. As a result of people's mental pressure, the incidence of anxiety disorder and other CNS diseases is rapidly increasing. Furthermore, due to global ageing, the drive for sales of CNS therapeutics has grown sharply. The global sale of CNS drugs was 90 trillion US dollars at 2010, and this number has increased to 104 trillion US dollars –

approximately 1/7 (14%) of global sales in the therapeutic industry [67]. Interestingly, early in 2002, the World Health Organisation (WHO) predicted this number (14%) would be reached in 2020. They believe increasing anxiety disorder and global ageing are the two main reasons why this has been brought forward 12 years.

The requirement for CNS drugs gives scientists considerable motivation and there is a large amount of funding towards related research. For instance, the National Cancer Institute's (NCI, USA) investment in brain and CNS research increased from 148.2 million US dollars in 2007 to 172.6 million US dollars in 2011. In addition to this funding, NCI supported brain and CNS cancer research in 2009 and 2010 using 53.8 million US dollars in funding from the American Recovery and Reinvestment Act (ARRA) [68]. Particularly in recent decades, as state-of-the-art nanotechnology has grown and more and more investment has been put into developing novel CNS therapeutics, it is clear that the industry has a promising future.

References:

1. Abbott, N.J., et al., *Structure and function of the blood-brain barrier.* Neurobiology of Disease, 2010. **37**(1): 13-25.
2. Lane, R.D., et al., *The Rebirth of Neuroscience in Psychosomatic Medicine, Part I: Historical Context, Methods, and Relevant Basic Science.* Psychosomatic Medicine, 2009. **71**(2): 117-134.
3. Elrich, P., *Das sauerstoff-bedürfnis des organismus.* Eine Farbenanalytiche Studie, 1885: 1-167.
4. Goldmann, *Vitalfärbung am Zentralnervensystem.* Abh. Preuss Akad. Wiss.Phys. Math. , 1913. **1**: 1-60.
5. Stern, L., *Le liquide céphalo rachidien au point de vue de ses rapports avec la circulation sanguine et avec les éléments de l'axe cérébrospinal.* Schweiz. Arch. Neurol. Psychiatr, 1921. **8**: 215-232.

6. Ponkshe, S., *Computer Modeling of Physiological Conditions for Better Understanding of Intracranial Blood Pressure and Brain Vasculature.* Journal of Young Investigators, 2008 (web journal).

7. Miller, G., *Drug targteting - Breaking down barriers.* Science, 2002. **297**(5584): 1116-1118.

8. Reese, T.S. and M.J. Karnovsky, *Fine structural localization of a blood-brain barrier to exogenous peroxidase.* The Journal of cell biology, 1967. **34**(1): 207-217.

9. Roggendorf, W. and J. Cervosnavarro, *Ultrastructure of Arterioles in Cat Brain.* Cell and Tissue Research, 1977. **178**(4): 495-515.

10. Ramsey, H.J., *Fine Structure of Surface of Cerebral Cortex of Human Brain.* Journal of Cell Biology, 1965. **26**(2): 323-329.

11. Forster, C., *Tight junctions and the modulation of barrier function in disease.* Histochemistry and cell biology, 2008. **130**(1): 55-70.

12. Wolburg, H. and A. Lippoldt, *Tight junctions of the blood-brain barrier: Development, composition and regulation.* Vascular Pharmacology, 2002. **38**(6): 323-337.

13. Crone, C. and O. Christensen, *Electrical-Resistance of a Capillary Endothelium.* Journal of General Physiology, 1981. **77**(4): 349-371.

14. Tran, N.D., et al., *Transforming growth factor-beta mediates astrocyte-specific regulation of brain endothelial anticoagulant factors.* Stroke, 1999. **30**(8): 1671-1677.

15. Ramsauer, M., D. Krause, and R. Dermietzel, *Angiogenesis of the blood-brain barrier in vitro and the function of cerebral pericytes.* The FASEB Journal, 2002. **16**(8): 1274-1276.

16. Rubin, L.L., et al., *A cell culture model of the blood-brain barrier.* The Journal of cell biology, 1991. **115**(6): 1725-1735.

17. McAllister, M.S., et al., *Mechanisms of glucose transport at the blood–brain barrier: an in vitro study.* Brain research, 2001. **904**(1): 20-30.

18. Hayashi, Y., et al., *Induction of various blood-brain barrier properties in non-neural endothelial cells by close apposition to co-cultured astrocytes.* Glia, 1997. **19**(1): 13-26.

19. Abbott, N.J., L. Rönnbäck, and E. Hansson, *Astrocyte–endothelial interactions at the blood–brain barrier.* Nature Reviews Neuroscience, 2006. **7**(1): 41-53.

20. Daneman, R., et al., *Pericytes are required for blood-brain barrier integrity during embryogenesis.* Nature, 2010. **468**(7323): 562.

21. Armulik, A., et al., *Pericytes regulate the blood-brain barrier.* Nature, 2010. **468**(7323): 557.

22. Bjarnegard, M., et al., *Endothelium-specific ablation of PDGFB leads to pericyte loss and glomerular, cardiac and placental abnormalities.* Development, 2004. **131**(8): 1847-1857.

23. Bell, R.D., et al., *Pericytes control key neurovascular functions and neuronal phenotype in the adult brain and during brain aging.* Neuron, 2010. **68**(3): 409-427.

24. Diaz-Flores, L., et al., *Pericytes. Morphofunction, interactions and pathology in a quiescent and activated mesenchymal cell niche.* Histology and Histopathology, 2009. **24**(7): 909-969.

25. Abbott, N.J., L. Ronnback, and E. Hansson, *Astrocyte-endothelial interactions at the blood-brain barrier.* Nature Reviews Neuroscience, 2006. **7**(1): 41-53.

26. Abbott, N.J., *Blood-brain barrier structure and function and the challenges for CNS drug delivery.* Journal of Inherited Metabolic Disease, 2013. **36**(3): 437-449.

27. Delbigio, M.R., *The Ependyma - a Protective Barrier between Brain and Cerebrospinal-Fluid.* Glia, 1995. **14**(1): 1-13.

28. Saito, Y. and E.M. Wright, *Regulation of Bicarbonate Transport across the Brush-Border Membrane of the Bull-Frog Choroid-Plexus.* Journal of Physiology-London, 1984. **350**(05): 327-342.

29. Rao, V.V., et al., *Choroid plexus epithelial expression of MDR1 P glycoprotein and multidrug resistance-associated protein contribute to the blood-cerebrospinal-fluid drug-permeability barrier.* Proceedings of the National Academy of Sciences of the United States of America, 1999. **96**(7): 3900-3905.

30. Lee, D.W., R.G. Deeley, and S.P.C. Cole, *Biology of the multidrug resistance-associated protein, MRP.* European Journal of Cancer, 1996. **32A**(6): 945-957.

31. Hipfner, D.R., R.G. Deeley, and S.P.C. Cole, *Structural, mechanistic and clinical aspects of MRP1.* Biochimica Et Biophysica Acta-Biomembranes, 1999. **1461**(2): 359-376.

32. Wijnholds, J., et al., *Multidrug resistance protein 1 protects the choroid plexus epithelium and contributes to the blood-cerebrospinal fluid barrier.* Journal of Clinical Investigation, 2000. **105**(3): 279-285.

33. Kumagai, A.K., K.J. Dwyer, and W.M. Pardridge, *Differential glycosylation of the Glut1 glucose-transporter in brain capillaries and choroid-plexus.* Biochimica Et Biophysica Acta-Biomembranes, 1994. **1193**(1): 24-30.

34. Davson, H., et al., *Ventriculo-cisternal perfusion of 12 amino-acids in the rabbit.* Journal of Neurobiology, 1982. **13**(4): 293-318.

35. Allan H. Ropper, R.H., *Brown Adams and Victor's principles of neurology McGraw-Hill Professional*. 8 edition ed. 2005.

36. Antranik. *Protection for the Brain: Meninges, CSF, Blood-Brain Barrier*. 2011; Available from: http://antranik.org/protection-for-the-brain-meninges-csf-blood-brain barrier/.

37. Calle, D.d.l. *Anatomy of the brain: The Cerebrospinal Fluid CSF*. 2011; Available from: http://www.youtube.com/watch?v=K9BYEO9725k.

38. Tuma, P.L. and A.L. Hubbard, *Transcytosis: Crossing cellular barriers.* Physiological Reviews, 2003. **83**(3): 871-932.

39. Bruns, R.R. and G.E. Palade, *Studies on Blood Capillaries .I. General Organization of Blood Capillaries in Muscle.* Journal of Cell Biology, 1968. **37**(2): 24.

40. Grapp, M., et al., *Choroid plexus transcytosis and exosome shuttling deliver folate into brain parenchyma.* Nature communications, 2013. **4**.

41. Chang, J., et al., *Characterization of endocytosis of transferrin-coated PLGA nanoparticles by the blood-brain barrier.* International Journal of Pharmaceutics, 2009. **379**(2): 285-292.

42. Skjorringe, T., T. Gjetting, and T.G. Jensen, *A modified protocol for efficient DNA encapsulation into pegylated immunoliposomes (PILs).* Journal of Controlled Release, 2009. **139**(2):140-145.

43. Dehouck, B., et al., *A new function for the LDL receptor: Transcytosis of LDL across the blood-brain barrier.* Journal of Cell Biology, 1997. **138**(4): 877-889.

44. Berchtold, N.C. and C.W. Cotman, *Evolution in the conceptualization of dementia and Alzheimer's disease: Greco-Roman period to the 1960s.* Neurobiology of Aging, 1998. **19**(3): 173-189.

45. Jankovic, J., *Parkinson's disease: clinical features and diagnosis.* Journal of Neurology Neurosurgery and Psychiatry, 2008. **79**(4): 368-376.

46. Walker, F.O., *Huntington's disease.* Seminars in Neurology, 2007. **27**(2): pp:143-150.

47. Brookmeyer, R., S. Gray, and C. Kawas, *Projections of Alzheimer's disease in the United States and the public health impact of delaying disease onset.* American Journal of Public Health, 1998. **88**(9): 1337-1342.

48. Brookmeyer, R., et al., *Forecasting the global burden of Alzheimer's disease.* Alzheimers & Dementia, 2007. **3**(3):186-191.

49. Tiraboschi, P., et al., *The importance of neuritic plaques and tangles to the development and evolution of AD.* Neurology, 2004. **62**(11): 1984-1989.

50. Greig, N.H., et al., *A new therapeutic target in Alzheimer's disease treatment: Attention to butyrylcholinesterase.* Current Medical Research and Opinion, 2001. **17**(3): 159-165.

51. Levy, M.L., J.L. Cummings, and R. Kahn-Rose, *Neuropsychiatric symptoms and cholinergic therapy for Alzheimer's disease.* Gerontology, 1999. **45**: 15-22.

52. Selkoe, D.J., *Alzheimer's disease: Genes, proteins, and therapy.* Physiological Reviews, 2001. **81**(2): 741-766.

53. Steiner, H., R. Fluhrer, and C. Haass, *Intramembrane proteolysis by gamma-secretase.* Journal of Biological Chemistry, 2008. **283**(44): 29627-29631.

54. Lathia, J.D., M.P. Mattson, and A. Cheng, *Notch: from neural development to neurological disorders.* Journal of Neurochemistry, 2008. **107**(6): p. 1471-1481.

55. Wong, G.T., et al., *Chronic treatment with the gamma-secretase inhibitor LY-411,575 inhibits beta-amyloid peptide production and alters lymphopoiesis and intestinal cell differentiation.* Journal of Biological Chemistry, 2004. **279**(13): 12876-12882.

56. He, G., et al., *Gamma-secretase activating protein is a therapeutic target for Alzheimer's disease.* Nature, 2010. **467**(7311): 95-101.

57. Schrag, A., M. Jahanshahi, and N. Quinn, *How does Parkinson's disease affect quality of life? A comparison with quality of life in the general population.* Movement Disorders, 2000. **15**(6): 1112-1118.

58. Beiske, A.G., et al., *Pain in Parkinson's disease: Prevalence and characteristics.* Pain, 2009. **141**(1-2): 173-177.

59. Eriksen, J.L., Z. Wszolek, and L. Petrucelli, *Molecular pathogenesis of Parkinson disease.* Archives of Neurology, 2005. **62**(3): 353-357.

60. Thobois, S., et al., *Non-motor dopamine withdrawal syndrome after surgery for Parkinson's disease: predictors and underlying mesolimbic denervation.* Brain, 2010. **133**(4): 1111-1127.

61. Grosset, D.G., et al., *Guidelines Diagnosis and pharmacological management of Parkinson's disease: summary of SIGN guidelines.* British Medical Journal, 2010. **340**.

62. LeWitt, P.A., et al., *AAV2-< i> GAD</i> gene therapy for advanced Parkinson's disease: a double-blind, sham-surgery controlled, randomised trial.* The Lancet Neurology, 2011. **10**(4): 309-319.

63. Levin, B.C., K.L. Ritchie, and J.P. Jakupciak, *Advances in Huntington's disease diagnostics: development of a standard reference material.* Expert Review of Molecular Diagnostics, 2006. **6**(4): 587-596.

64. Purdon, S.E., et al., *Huntingtons-Disease - Pathogenesis, Diagnosis and Treatment.* Journal of Psychiatry & Neuroscience, 1994. **19**(5): 359-367.

65. Frank, S. and J. Jankovic, *Advances in the Pharmacological Management of Huntington's Disease.* Drugs, 2010. **70**(5): 561-571.

66. Morganti-Kossmann, M.C., et al., *Inflammatory response in acute traumatic brain injury: a double-edged sword.* Current opinion in critical care, 2002. **8**(2): 101-105.

67. Sullivan, R.F. *Drug Discovery Technology Alert. Therapies for CNS-Related Diseases; Therapies for Cardiovascular Diseases; Innovative Drugs for Pain and CNS-Related Diseases,* http://www.frost.com/sublib. [Website] 2008.

68. NCI. *A Snapshot ofBrain and Central Nervous System Cancers,* http://www.cancer.gov/researchandfunding. 2008.

Chapter 2

Drug Delivery to the CNS

2.1 CNS delivery and challenges

CNS drug delivery aims to enhance the penetration of the barriers that surround and protect the CNS so as to reach a sufficient concentration of drugs and other active molecules. Infusion of liquid therapeutic substances directly into a vein (so-called intravenous or IV therapy) is known to be the fastest way to deliver medication throughout the body. However, alternative routes that do not rely on the cardiovascular system have been previously studied. Intra-lumbar injection and intra-ventricular infusion aim to inject drugs directly from the lumbar spinal cord/ventricles into the CSF; such approaches offer several benefits compared to vascular drug delivery systems, such as quicker administration, higher drug concentration and longer drug half-life time in CNS [1]. However, this administration route suffers from lack of drug diffusion through the brain, particularly for some high-molecular-weight drugs and biomolecules [2]. This results in very high local concentration at the site of administration and almost zero concentration farther from the injection site. By contrast, targeting the brain vasculature should in principle allow distribution to any area of the CNS. Therapeutics can also be delivered into the brain interstitium directly by injections, pumps and catheters [3-5].

Blood-brain barrier disruption is another method to enhance CNS penetration. Numerous techniques have been investigated for such a method: intra-carotid injection of mannitol or arabinose can cause osmotically--induced endothelial cell shrinkage and opening of tight junctions for a few hours. This osmotic BBB disruption gives a short window for CNS agent entry, and has been used for delivery of chemotherapy [6] and genes [7].

CNS drug delivery based on receptor- or adsorptive-mediated transport (RMT, AMT) mechanisms has also been extensively studied in both laboratories and clinics. The brain requires a continuous supply of nutrients and macromolecules. Combining RMT ligands with non-transportable drugs by engineering carriers can achieve transport to CNS across the BBB. Ligand-drug/carrier conjugation can be achieved by chemical (covalent) bonds, polyethylene glycol and biotin-streptavidin systems [8]. Several efforts have demonstrated successful CNS targeting and primary clinical results by intravenous (IV) drug delivery. AAV9 achieved gene delivery to the brain and spinal cord in both neonatal and adult mice [9], and furthermore revealed a positive result in an SMA (spinal muscular atrophy) mouse model [10]. J. Chen’s group applied Angiopep-2-functionalised dendrimers and polymer micelles, showing that both genes and insoluble molecules can be delivered to the brain [11, 12]. RVG (rabies virus glycoprotein), a specific molecule that reacts with the nicotinic acetylcholine receptor (AchR) on neuronal cells, was also used to deliver small interfering RNA (siRNA), enabling specific gene knockdown therapy [13].

Most recently, polymeric nano-sized vesicles (also named polymersomes) have been shown to penetrate the BBB and deliver protein into the CNS [14, 15]. Polymeric or lipid-based nanocarriers now attract more attention due to their biocapability, low toxicity and stealth characteristics [16].

These various strategies of CNS delivery systems are promising for potential clinical application, yet some of this work remains problematic: although some results show positive CNS targeting, most of the vectors/conjugates do not reach the CNS, leading to retention in other organs, particularly the reticuloendothelial system (RES). This, in turn, can lead to overdosing and potentially adverse immune responses. The site of targeting in the CNS requires more precise identification and investigation, as the CNS is a complex system that contains numerous structures, chemical compositions and cell-cell associations, which vary in function and mechanisms. It is important to emphasise the difference between ‘brain endothelial uptake’ and ‘brain tissue uptake’. How ‘smart’ these delivery systems are and how well they can release cargo within the CNS to a specific site are critical questions yet to be answered. This motivates the search for more effective tools that can be adapted to ‘deliver’ and ‘release’ to the Central Nervous System.

2.2 Amphiphilic diblock copolymers

Amphiphilic (from the Greek αμφις (‘amphis’ or ‘both’) and φιλία (‘philia’ or ‘love, friendship’)) diblock polymers comprise both hydrophilic (water-loving, polar) and hydrophobic (lipid-loving) chains. The capability of amphiphilic copolymers to self-assemble above a certain CAC (critical assembly concentration) into organised membrane-enclosed structures has been the subject of several studies [17].

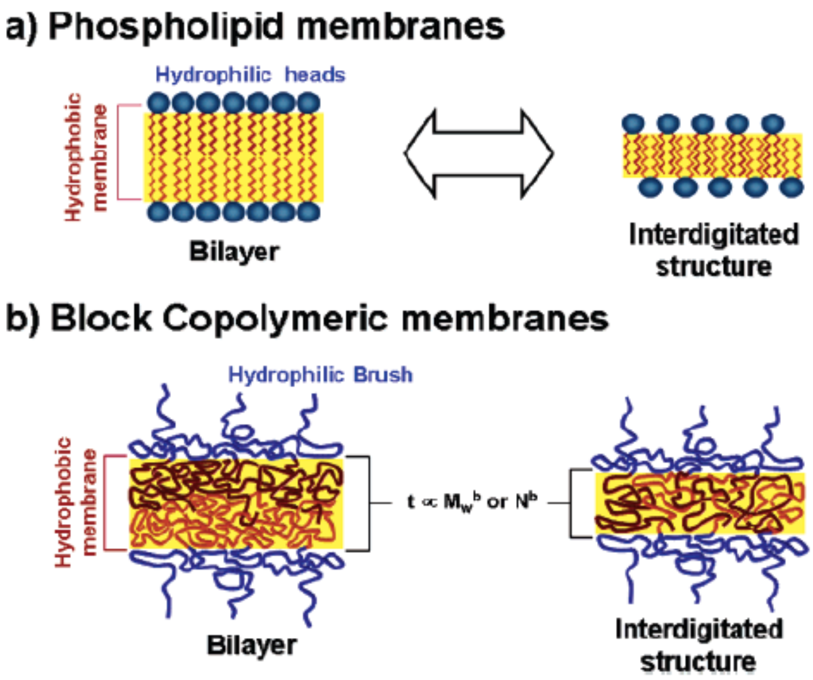

Figure 2.1 *Amphiphilic copolymers mimicking natural phospholipids.*

Amphiphilic copolymers (Figure 2.1) mimic the ability of natural phospholipids to form membrane and membrane-enclosed compartments [18]. However, they have much higher molecular weight than phospholipids, and thus form entangled membranes. The final properties of the membrane, including mechanical properties, permeability, responsiveness and protein interaction, can be finely controlled by the choice of polymer blocks [19]. Moreover, the final architectures of self-assembly can be manipulated by the volume ratio between insoluble and soluble blocks (the insoluble:soluble ratio, ISR). As shown in Figure 2.2, depending on the ISR, copolymers can assemble into a membrane, cylindrical micelle or spherical micelle. It is important to know that spherical micelles are self-contained assemblies and their diameter solely depends on the molecular mass of the block copolymer. By contrast, for both cylindrical micelles and membranes, the molecular mass of the block copolymer only controls the cylinder diameter and the membrane thickness,

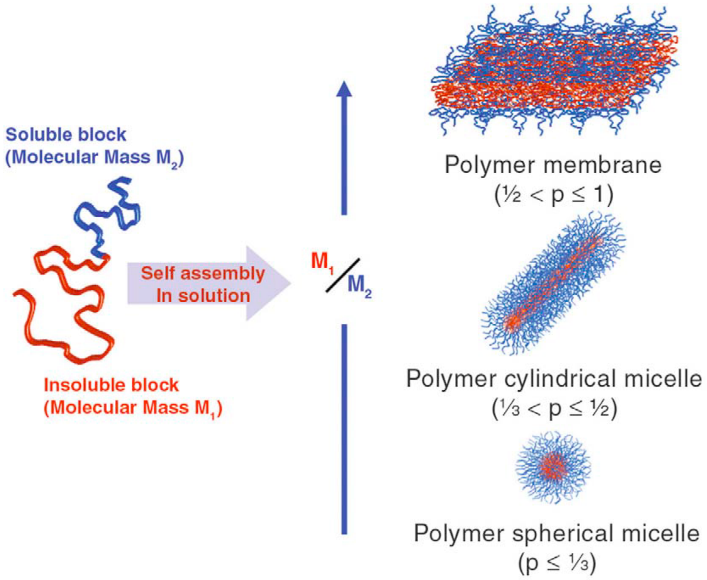

Figure 2.2 | *Different geometries self-assembled by block copolymers in selective solvent conditions [20].*

respectively [20]. Cylinder and large membranes are considered the most stable conditions from a theoretical point of view. However, curvature of these aggregates is necessary in order to avoid contact between the solvent and insoluble domains. As a result, “the cylinders bend, forming toroidal micelles, while membranes close up, forming core-shell spherical structures known as vesicles” [20] or ‘polymersomes’.

As these synthetic macromolecular amphiphiles form assemblies and the final architecture is well manipulated and significantly similar to biological analogues’ tissue-like structure, polymersomes are very attractive from several technological points of view. The choice of synthetic polymers, such as chemistry, hydrophilic/hydrophobic ratio and molecular weight (MW), is crucial, as these are particularly distinctive molecular features that impart to polymersomes a broad range of carrier properties [21]. For instance, PEO-polylactide (PEO-PLA, equivalent to PEG-PLA) can form micelles and nanoparticles [22, 23] and PLA is susceptible to hydrolytic biodegradation, which should foster drug release [24]. Charged polymersomes, such as PAA-PS [25] and PAA-PBD [26], present additional opportunities for controlled release in response to external stimuli, for instance, pH.

In our previous work, a self-assembly vesicle-like structure, pH-sensitive poly (2-(methacryloyloxy)ethyl-phosphorylcholine)-co-poly(2-(diisopropylamino) ethyl methacrylate) (PMPC–PDPA) diblock copolymer was applied in several biomedical applications. The PMPC block is highly biocompatible and non-fouling, while interestingly the PDPA block is pH sensitive ($pK_a \approx 6.4$). The PMPC-PDPA diblock copolymer vesicles (polymersomes) are able to encapsulate different cargos by several methods, such as film hydration, pH switch or electroporation; the encapsulated substances can be both water soluble and insoluble, such as dyes [27, 28], plasmid DNA [29, 30], siRNA and antibodies [31]. The encapsulation efficiency varies from cargo to cargo, and the localisation of cargo within the vesicle is determined by its water-solubility; normally hydrophilic substances are encapsulated within the lumen of the vesicle and hydrophobic compounds are embedded within the bilayer membrane of the polymersomes.

PMPC-PDPA polymersomes have been widely used for intra-cellular delivery in our previous work, and it is already proven that such polymersomes can form around 100-200nm scale vesicles and deliver/release a range of substances efficiently once internalised within cells. The PMPC chain on the polymersomes has an affinity that specifically interacts with scavenger receptor class B1 (SRB1), transits cell membranes by a receptor-mediated endocytosis pathway, then leads to a mildly acidic early endosome. As the pK_a of the PDPA block is around 6.4, once internalised by cellular endosomes, this reduction in local pH triggers disassembly of the PMPC-PDPA polymersomes; this phase transition is due to the protonation of the tertiary amine group on the PDPA chains, which switch from being hydrophobic at physiological pH to hydrophilic in mildly acidic solution. Because each polymersome consists of very large single copolymer chains, the dissociation of the polymersomes results in a sharp rise in the number of species present, and produces an osmotic pressure that lyses the endosome membrane, permitting release of encapsulated substances. After this process, the cellular local pH gradually goes back to neutral, leading to de-protonation of the PDPA chains and restoration of the diblock copolymer amphiphilic property, hence interaction/self-assembly with the cellular endosome membrane occurs.

Lomas et al. reported more effective GFP (Green fluoresce protein) expression observed in CHO cells and primary HDF (human dermal fibroblasts) when plasmid DNA was delivered by PMPC-PDPA pH-sensitive polymersomes compared with lipofectamine and calcium phosphate [29]. By contrast, the non-pH-sensitive PEO-PBO polymersomes cannot successfully achieve intracellular internalisation [32]. Massignani et al. systematically studied the mechanism of polymersome disruption and release in the cytosol *via* endosomal escape [28] and reported sufficient quantities of fluorescent (functionalised) probes such as PI (propidium iodide), FITC-antibodies and Cy3-nucleic acid were delivered into the cytosol [33]. Such intracellular targeting applications have been expanded in the last few years, including siRNA and therapeutic agent delivery. Wang et al. introduced a novel cargo-encapsulation method by electroporation; BSA (Bovine Serum Albumin), IgG (Immunoglobulin G), plasmid DNA and several other biomolecules have been shown to be loaded in PMPC-PDPA polymersomes; HEK 293T cells then successfully expressed E2-Crimson plasmid DNA delivered by PMPC-PDPA polymersomes [31]. One of the most commonly used anti-cancer drugs, DOXO (doxorubicin), which intercalates into the DNA double helix in cellular nuclei, has also been encapsulated within the PMPC-PDPA polymersomes and efficiently internalised within melanoma cells [34].

Size, surface chemistry and surface topology of polymersomes are all critical factors that together affect cell internalisation. For instance, at a certain radius, nanoparticle size influences the efficiency of their endocytotic uptake. Aoyama and colleagues found that 25nm-radius particles were more effective than larger particles (50nm and 100nm) and smaller particles (2.5nm and 7.5nm) [35]. In another example [28], PMPC-PDPA polymersomes demonstrated an inverse ratio between endocytosis efficiency and diameter, while 400nm PMPC/PEO (25:75) hybrid polymersomes showed more effective cellular internalisation than 100nm and 200nm PMPC/PEO (25:75) hybrid polymersomes. This suggests that nanoparticle internalisation into cells is not solely due to size, but also to the properties of their surface morphology and topology. Furthermore, copolymers can be modified by introducing a functional peptide; this, in turn, enables control of cell internalisation in a more specific manner. The flexibility to manipulate size, surface chemistry and surface topology of polymersomes (Figure 2.3 [19]) gives great potential to use it as a vector to target specific tissue and cell regions *in vitro* and *in vivo*.

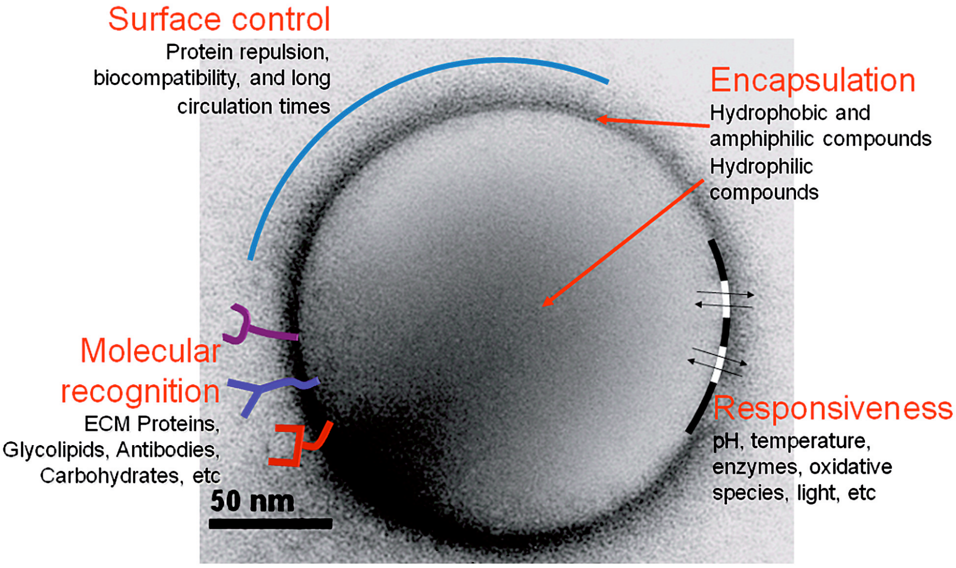

Figure 2.3* | *Different properties that can be included into the molecular design of polymersomes[19].

2.3 Polymersomes for targeting endothelial transcytosis

With recent advances in polymer science and nanotechnology, using functionalised polymersomes to target the CNS via transcytosis mechanisms is becoming a possibility. Several conditions are required for certain polymersomes to penetrate the BBB via endocytosis/transcytosis:

Size: The reticuloendothelial system (RES), also called the macrophage system or mononuclear phagocyte system, is part of the body's defence mechanism; its role includes engulfing and destroying bacteria and viruses, and large foreign substances. The RES is known to recognise particles over 500nm [36] (size can be over 1μm), particle(s) mediated via phagocytosis or pinocytosis [37, 38]. However, a few new studies have shown that phagocytosis could internalise nanoscale particles, such as viruses [39], gold

[40], silver [41] and quantum dots [42]. Size also has a strong influence on cellular uptake mechanisms, bio-distribution and blood circulation time [43]. Considering all these factors, the optimum size for nanocarriers targeting the CNS should be around 80-200nm, in order to escape RES recognition, prolong bio-distribution and blood circulation, and most importantly, have access to the key endothelial transcytosis vesicles via structures such as caveolae [44].

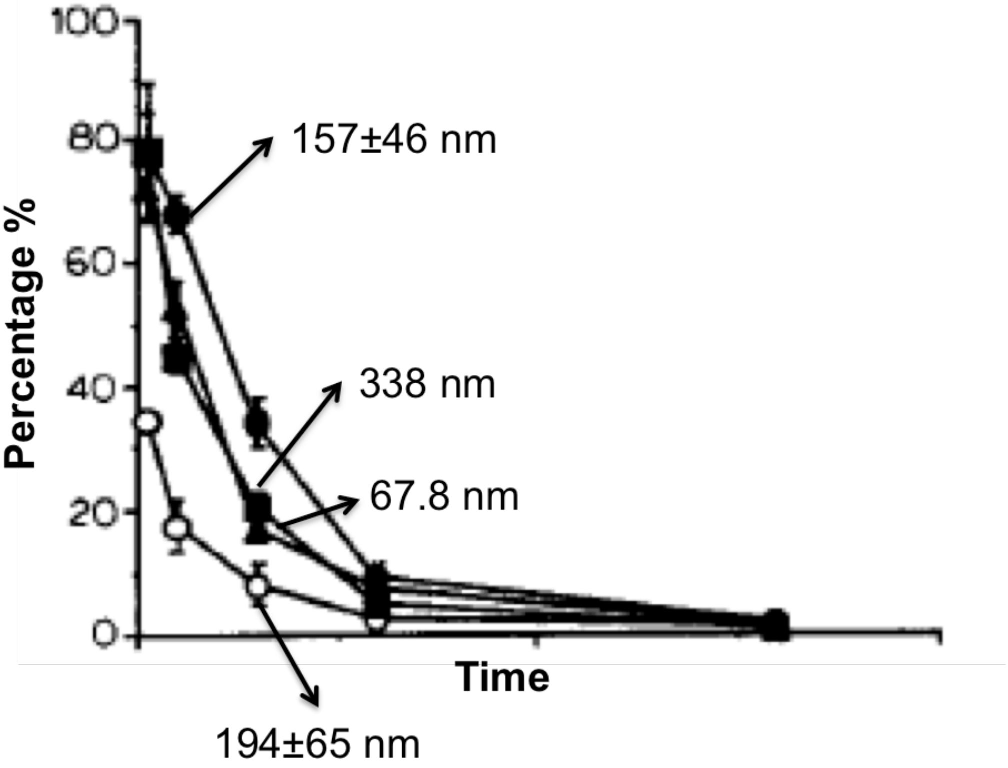

Figure 2.4 Biodistribution of PEG-PE-containing liposomes of different size.(Modified from [*43*]), 157nm size particles shown least blood clearance over time.

The eventual size of polymersomes can be controlled. As there is a relationship between amphiphilic molecular weight and self-assembly size [45], size can firstly be controlled during synthesis; further, during the formation procedure, size can be affected by different methods [46]. Even after formation, size can be manipulated by physical processes, such as ultrasonication and extrusion. The extruder [28] can be applied by using a filter with nanopores, and the polymersome size can be made uniform to 50nm, 100nm, 200nm, 400nm and 800nm by pressing through certain filters.

Stealth: Polymersomes with an optimum size are still far from optimal for preventing recognition by the body's immune system and for enhanced blood circulation time. Organs such as the liver play a pivotal role in detoxification and the spleen acts as a blood filter. These are critical obstacles for therapeutic-specific targeting. Indeed, most reported CNS-targeting drug bio-distribution studies have revealed that much more is accumulated within such organs, consequently bringing unexpected side effects and an overdose liability. Furthermore, mononuclear phagocytes (MPS*) in vivo* also rapidly clear nanocarriers [47]; this clearance mechanism is generally known to start with adhesion between nanocarriers and protein, especially opsonisation (with opsonins) [48]. Carrier-opsonin complexes are then removed by phagocytic cells via the traditional PAMP (Pathogen-Associated Molecular Pattern) and DAMPs (Damage-Associated Molecular Pattern) molecules, followed by subsequent binding of complex to the phagocytic cells and eventually internalisation of the nanocarriers. To minimise these immune-system-associated effects, PEGylated nanoparticles are widely applied *in vivo* due to their 'stealth-like' behaviour and lower toxicity. This is basically due to the polyethylene glycol (PEG) (also known as polyethylene oxide) polymer, a neutral and water-soluble polymer that possesses the unique ability to hinder non-specific protein absorption [49, 50]. This can be achieved by the minimisation of interfacial free energy and consequent generation of steric repulsion forces [51]. This, in turn, deters opsonisation and consequent immune responses, enabling long circulation in the bloodstream that can last for days. The protein repulsion properties of PEG depend on its molecular weight and the density that is grafted to a given surface [49]. Generally speaking, the higher the molecular weight and the higher the grafting density the less protein fouling is observed [50]. Alternatives to PEG to reduce opsonisation include pHPMA (poly(*N*-(2-hydroxypropyl)methacrylamide), polyamino acids, polysaccharides and oligosaccharides, such as dextran and its derivates, polyvinyl pyrrolidone and polyoxalines [52].

Surface-functionalisation: PEGylation stops any type of interaction, including beneficial ones that can enable cell selectivity, and for this reason PEGylation is often combined with functionalisation using ligands and other moieties that enable cell targeting. This approach can be easily implemented in polymersomes using copolymers with reactive ends. These can be used to anchor fluorescence/isotope tags, proteins, antibody fragments, oligopeptides, sugars, vitamins and other ligands.

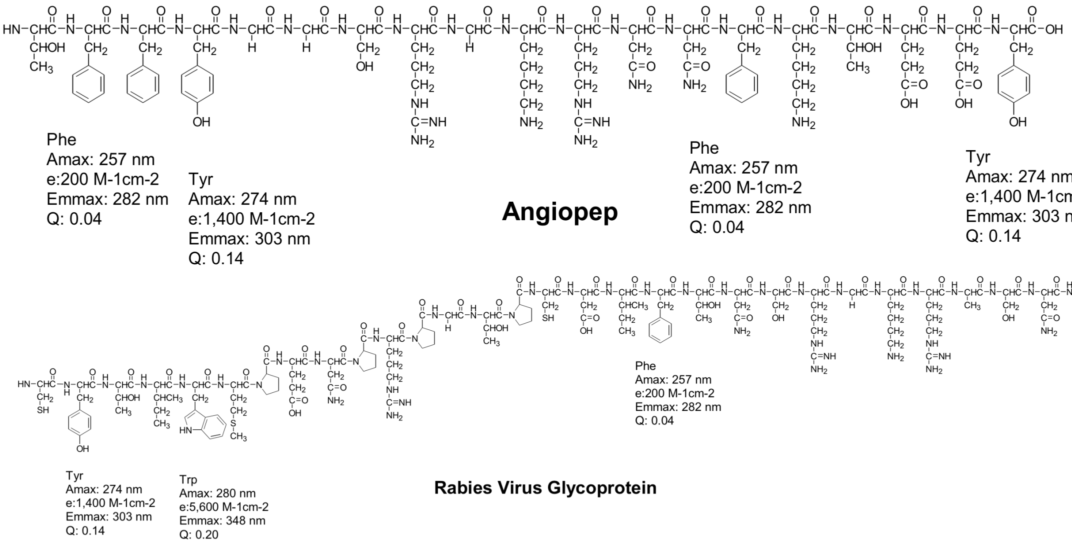

Figure 2.5 *Chemical structure of two transcytosis receptor ligands, Angiopep-2 and rabies virus glycoprotein (RVG).*

Albumin and catalase-modified PEG [53, 54] polymers were first reported in the mid-1970s; since then, use of functionalised PEG has broadened and developed dramatically.

Transcytosis-specific ligands such as Angiopep-2 target the low-density lipoprotein receptor-related protein 1 (LRP-1), which is over-expressed by the blood-brain barrier, and can help nanoparticles to penetrate the BBB and target the CNS [55, 56]. Recent efforts have also shown that RVG can be used to target the brain across the BBB [13], although the receptor(s) involved and penetration mechanism remain unclear. These peptides (Figure 2.5) conjugated to polymersomes make it possible to enter the CNS via receptor-mediated transcytosis.

Besides size, stealth and surface chemistry, control beyond ‘smart’ vectors can also be exerted over shape, surface charge, surface topology and release mechanism, which also influence *in vivo* circulation time and cellular uptake. For instance, introducing a slight negative or positive charge on nanocarriers may help decrease the opsonisation interaction, resulting in longer circulation; by contrast, a surface with a highly loaded positive or negative charge causes significant clearance of such nanocarriers [57]. Polymersomes with different surface domains, whose size and morphology are controlled by the molar ratio of two types of diblock copolymer, also influence cellular uptake over time [28].

In summary, stealth polymersomes of optimum size and with the necessary surface topology, together with specific functional/dual functional surface chemistry, which are able to release their cargo in a controlled manner, are proposed as ideal tools to target transcytosis across the BBB. Good examples in the literature of effective brain targeting across the BBB are limited; this motivated us to develop such a vector based on PDPA pH-sensitive polymersomes.

References

1. Krewson, C. E., Klarman, M. L. and Saltzman, W. M., Distribution of Nerve Growth Factor following direct delivery to brain interstitium. *Brain Research*, 1995. **680**(1-2): 196-206.
2. Newcomb, R. et al., Bioavailability of Ziconotide in brain: influx from blood, stability, and diffusion. *Peptides*, 2000. **21**(4): 491-501.
3. Hall, W. A., Increasing volume of distribution to the brain with interstitial infusion: Dose, rather than convection, might be the most important factor – Comment. *Neurosurgery*, 1996. **38**(4): 752-753.
4. Bobo, R. H. et al., *Convection-enhanced delivery of macromolecules in the brain.* Proceedings of the National Academy of Sciences of the United States of America, 1994. **91**(6): 2076-2080.
5. Yaksh, T. L. et al., Safety assessment of encapsulated morphine delivered epidurally in a sustained-release multivesicular liposome preparation in dogs. *Drug Delivery*, 2000. **7**(1): 27-36.
6. Neuwelt, E. A. et al., Therapeutic dilemma of disseminated CNS germinoma and the potential of increased platinum-based chemotherapy delivery with osmotic Blood-Brain barrier disruption. *Pediatric Neurosurgery*, 1994. **21**(1): 16-22.
7. Doran, S. E. et al., Gene-expression from recombinant viral vectors in the central-nervous-system after Blood-Brain barrier disruption. *Neurosurgery*, 1995. **36**(5): 965-970.
8. Wu, D. F., Boado, R. J. and Pardridge, W. M., Pharmacokinetics and blood-brain barrier transport of [H-3]-biotinylated phosphorothioate oligodeoxynucleotide conjugated to a vector-mediated drug delivery system. *Journal of Pharmacology and Experimental Therapeutics*, 1996. **276**(1): 206-211.
9. Foust, K. D. et al., Intravascular AAV9 preferentially targets neonatal neurons and adult astrocytes. *Nature Biotechnology*, 2009. **27**(1): 59-65.
10. Foust, K. D. et al., Rescue of the spinal muscular atrophy phenotype in a mouse model by early postnatal delivery of SMN. *Nature Biotechnology*, 2010. **28**(3): 271-U126.
11. Ke, W. L. et al., Gene delivery targeted to the brain using an Angiopep-conjugated polyethyleneglycol-modified polyamidoamine dendrimer. *Biomaterials*, 2009. **30**(36): 6976-6985.
12. Shao, K. et al., Angiopep-2 modified PE-PEG based polymeric micelles for amphotericin B delivery targeted to the brain. *Journal of Controlled Release*, 2010. **147**(1): 118-126.
13. Kumar, P. et al., Transvascular delivery of small interfering RNA to the central nervous system. *Nature*, 2007. **448**(7149): 39-43.
14. Georgieva, J. V. et al., Peptide-Mediated Blood-Brain Barrier transport of polymersomes. *Angewandte Chemie – International Edition*, 2012. **51**(33): 8339-8342.

15. Dakwar, G. R. et al., Delivery of proteins to the brain by bolaamphiphilic nano-sized vesicles. *Journal of Controlled Release*, 2012. **160**(2): 315-321.

16. Misra, A. et al., Drug delivery to the central nervous system: a review. *Journal of Pharmacy and Pharmaceutical Sciences*, 2003. **6**(2): 252-273.

17. Discher, D. E. and Eisenberg, A., Polymer vesicles. *Science*, 2002. **297**(5583): 967-973.

18. Battaglia, G. and Ryan, A. J., Bilayers and interdigitation in block copolymer vesicles. *Journal of the American Chemical Society*, 2005. **127**(24): 8757-8764.

19. LoPresti, C. et al., Polymersomes: nature inspired nanometer sized compartments. *Journal of Materials Chemistry*, 2009. **19**(22): 3576-3590.

20. Smart, T. et al., Block copolymer nanostructures. *Nano Today*, 2008. **3**(3-4): 38-46.

21. Discher, D. E. and Ahmed, F., Polymersomes. *Annu. Rev. Biomed. Eng.*, 2006. **8**: 323-341.

22. Gref, R. et al., Biodegradable long-circulating polymeric nanospheres. *Science*, 1994. **263**(5153): 1600-1603.

23. Yasugi, K. et al., Preparation and characterization of polymer micelles from poly (ethylene glycol)-poly (D, L-lactide) block copolymers as potential drug carrier. *Journal of Controlled Release*, 1999. **62**(1): 89-100.

24. Batycky, R. P. et al., A theoretical model of erosion and macromolecular drug release from biodegrading microspheres. *Journal of Pharmaceutical Sciences*, 1997. **86**(12): 1464-1477.

25. Zhang, L., Yu, K. and Eisenberg, A., Ion-induced morphological changes in "crew-cut" aggregates of amphiphilic block copolymers. *Small*, 1996. **1**: 1777-1779.

26. Geng, Y. et al., Visualizing worm micelle dynamics and phase transitions of a charged diblock copolymer in water. *The Journal of Physical Chemistry* B, 2005. **109**(9): 3772-3779.

27. Tian, X. H. et al., Live Cell Luminescence Imaging As a Function of Delivery Mechanism. *Chembiochem*, 2011. **12**(4): 548-551.

28. Massignani, M. et al., Controlling Cellular Uptake by Surface Chemistry, Size, and Surface Topology at the Nanoscale. *Small*, 2009. **5**(21): 2424-2432.

29. Lomas, H. et al., Biomimetic pH sensitive polymersomes for efficient DNA encapsulation and delivery. *Advanced Materials*, 2007. **19**(23): 4238-4240.

30. Little, D. et al., Polymersome mediated gene therapy for spinal muscular atrophy. *Human Gene Therapy*, 2011. **22**(10): A83-A84.

31. Wang, L. G. et al., Encapsulation of biomacromolecules within polymersomes by electroporation. *Angewandte Chemie – International Edition*, 2012. **51**(44): 11122-11125.

32. Lomas, H. et al., Non-cytotoxic polymer vesicles for rapid and efficient intracellular delivery. *Faraday Discussions*, 2008. **139**: 143-159.

33. Massignani, M. et al., Enhanced Fluorescence Imaging of Live Cells by Effective Cytosolic Delivery of Probes. *Plos One*, 2010. **5**(5).

34. Pegoraro, C. et al., Enhanced drug delivery to melanoma cells using PMPC-PDPA polymersomes. *Cancer Letters*, 2013. **334**(2): 328-37.

35. Nakai, T. et al., Remarkably size-regulated cell invasion by artificial viruses. saccharide-dependent self-aggregation of glycoviruses and its consequences in glycoviral gene delivery. *Journal of the American Chemical Society*, 2003. **125**(28): 8465-8475.

36. Doshi, N. and Mitragotri, S., Macrophages recognize size and shape of their targets. *Plos One*, 2010. **5**(3).

37. Harashima, H. and Kiwada, H., Liposomal targeting and drug delivery: Kinetic consideration. *Advanced Drug Delivery Reviews*, 1996. **19**(3): 425-444.

38. Harashima, H. et al., Enhanced hepatic-uptake of liposomes through complement activation depending on the size of liposomes. *Pharmaceutical Research*, 1994. **11**(3): 402-406.

39. Clement, C. et al., A novel role for phagocytosis-like uptake in herpes simplex virus entry. *Journal of Cell Biology*, 2006. **174**(7): 1009-1021.

40. Franca, A. et al., Macrophage scavenger receptor A mediates the uptake of gold colloids by macrophages *in vitro*. *Nanomedicine*, 2011. **6**(7): pp. 1175-1188.

41. Park, J. et al., Size dependent macrophage responses and toxicological effects of Ag nanoparticles. *Chemical Communications*, 2011. **47**(15): 4382-4384.

42. Fischer, H. C. et al., Exploring primary liver macrophages for studying quantum dot interactions with biological systems. *Advanced Materials*, 2010. **22**(23): 2520-2524.

43. Litzinger, D. C. et al., Effect of liposome size on the circulation time and intraorgan distribution of amphipathic poly(Ethylene Glycol)-containing liposomes. *Biochimica Et Biophysica Acta-Biomembranes*, 1994. **1190**(1): 99-107.

44. Ragnarsson, E. G. E. et al., Yersinia pseudotuberculosis induces transcytosis of nanoparticles across human intestinal villus epithelium via invasin-dependent macropinocytosis. *Laboratory Investigation*, 2008. **88**(11): 1215-1226.

45. Wang, W. et al., Controls on polymer molecular weight may be used to control the size of palmitoyl glycol chitosan polymeric vesicles. *Langmuir*, 2001. **17**(3): 631-636.

46. Howse, J. R. et al., Templated formation of giant polymer vesicles with controlled size distributions. *Nature Materials*, 2009. **8**(6): 507-511.

47. Koide, H. et al., Elucidation of accelerated clood clearance phenomenon caused by repeat injection of PEGylated nanocarriers. *Yakugaku Zasshi Journal of the Pharmaceutical Society of Japan*, 2009. **129**(12): 1445-1451.

48. Jenkin, C. R. and Rowley, D., Role of Opsonins in Clearance of Living and Inert Particles by Cells of Reticuloendothelial System. *Journal of Experimental Medicine*, 1961. **114**(3): 363-366.

49. Meng, F. H. et al., Pegylated polystyrene particles as a model system for artificial cells. *Journal of Biomedical Materials Research Part A*, 2004. **70A**(1): pp. 97-106.

50. Photos, P. J. et al., Polymer vesicles in vivo: correlations with PEG molecular weight. *Journal of Controlled Release*, 2003. **90**(3): 323-334.

51. Woodle, M. C., Surface-modified liposomes – assessment and characterization for increased stability and prolonged blood-circulation. *Chemistry and Physics of Lipids*, 1993. **64**(1-3): 249-262.

52. Duncan, R., The dawning era of polymer therapeutics. *Nature Reviews Drug Discovery*, 2003. **2**(5): 347-360.

53. Abuchowski, A. et al., Effect of covalent attachment of polyethylene-glycol on immunogenicity and circulating life of bovine liver catalase. *Journal of Biological Chemistry*, 1977. **252**(11): 3582-3586.

54. Abuchowski, A. et al., Alteration of immunological properties of bovine serum-albumin by covalent attachment of polyethylene-glycol. *Journal of Biological Chemistry*, 1977. **252**(11): 3578-3581.

55. Xin, H. L. et al., Angiopep-conjugated poly(ethylene glycol)-co-poly(epsilon-caprolactone) nanoparticles as dual-targeting drug delivery system for brain glioma. *Biomaterials*, 2011. **32**(18): 4293-4305.

56. Xin, H. L. et al., The brain targeting mechanism of Angiopep-conjugated poly(ethylene glycol)-co-poly(epsilon-caprolactone) nanoparticles. *Biomaterials*, 2012. **33**(5): 1673-1681.

57. Aoki, H. et al., Effects of positive charge density on the liposomal surface on disposition kinetics of liposomes in rats. *International Journal of Pharmaceutics*, 1997. **156**(2): 163-174.

Chapter 3

Aims and Outline

This project is part of the VINCENS (Virus like Nano-particles for targeting the Central Nervous System) project. Its research aim is to develop a novel strategy based on functionalised pH-sensitive polymersomes, to overcome the BBB by targeting receptor-mediated (LRP-1) transcytosis, eventually releasing cargo/therapeutics within CNS cells.

The flexibility of polymersome design at both the molecular and supra-molecular level allows the tuning of several properties such as size, shape, surface chemistry and topology. The general aim for this PhD project was to develop a sequential screening method for identifying the most promising formulation(s) to facilitate CNS delivery. As schematized in Figure 3.1, the initial effort was focused on the characterization and synthesis of 50 polymersome formulations. These were first screened using fast 2D cell culture, with cellular uptake measured for the initial target, the brain endothelial cells forming the BBB, and also immune cells, as control. The most successful candidate was further screened using a 3D *in vitro* BBB model. Finally, the most successful formulation was moved to *in vivo* testing in mice.

2-dimensional (2D) cell screening

- Synthesis of functionalised pH-sensitive polymersomes based on $PMPC_{25}$-$PDPA_{70}$, biotin-$PMPC_{25}$-$PDPA_{70}$, PEO_m-$PDPA_n$ (m=22, 45, 113. n=17, 22, 56.) and $P(EO_{10}GMA)_{20}$-$PDPA_{100}$ chemistry. $PMPC_{25}$-$PDPA_{70}$/ biotin-$PMPC_{25}$-$PDPA_{70}$, PEO-PDPA Angiopep-2 and RVG (rabies virus glycoprotein) were tested to identify potential functional groups for targeting transcytosis, as mentioned in Chapter 2.
- Size and morphology of different formulation polymersomes were characterised by Dynamic Light Scattering (DLS) and Transmission Electron Microscopy (TEM).
- All formulations were tested on a mouse brain endothelial cell line bEND.3, at time points from 1 to 24 hours. According to observed brain endothelial uptake, we then chose $P(EO_{10}GMA)_{20}$-$PDPA_{100}$-based polymersomes to further examine their internalisation by immune system cells, using a mouse lymphocyte cell model.

3-dimensional (3D) BBB model screening

- 3D *in vitro* BBB models were developed based on a 12-well transwell system, by first culturing the bEND.3 cells on the upper surface of the transwell microporous filter insert. More complex 3D models were also studied using co-culture of the bEND.3 cells with astrocyte and pericyte cell models.
- Tight junction formation and protein expression were characterised for both the 2D and 3D models. Transendothelial

electrical resistance (TEER) was recorded for *all vitro* BBB models as a measure of junctional tightness.

- The permeability of RVG- and Angiopep-functionalised $P(EO_{10}GMA)_{20}$-$PDPA_{100}$ polymersomes was tested on the bEND.3 *in vitro* BBB model and on the bEND.3/astrocytes, bEND.3/pericytes co-culture models.

- ***In vivo* assessment**
  - The initial *in vivo* test were based on Angiopep-functionalised $P(EO_{10}GMA)_{20}$-$PDPA_{100}$ polymersomes, using $PMPC_{25}$-$PDPA_{70}$ and non-functionalised $P(EO_{10}GMA)_{20}$-$PDPA_{100}$ polymersomes as controls. Tissue sections of both liver and brain were examined by confocal laser scanning microscopy (CLSM).
  - Brain slices were examined from choroid plexus (CP), cerebellum (CB) and hippocampus (HP) by CLSM.
  - A human IgG was successfully encapsulated within Angiopep-functionalised $P(EO_{10}GMA)_{20}$-$PDPA_{100}$ polymersomes, demonstrating brain delivery by homogenate analysis and immunocytochemistry.

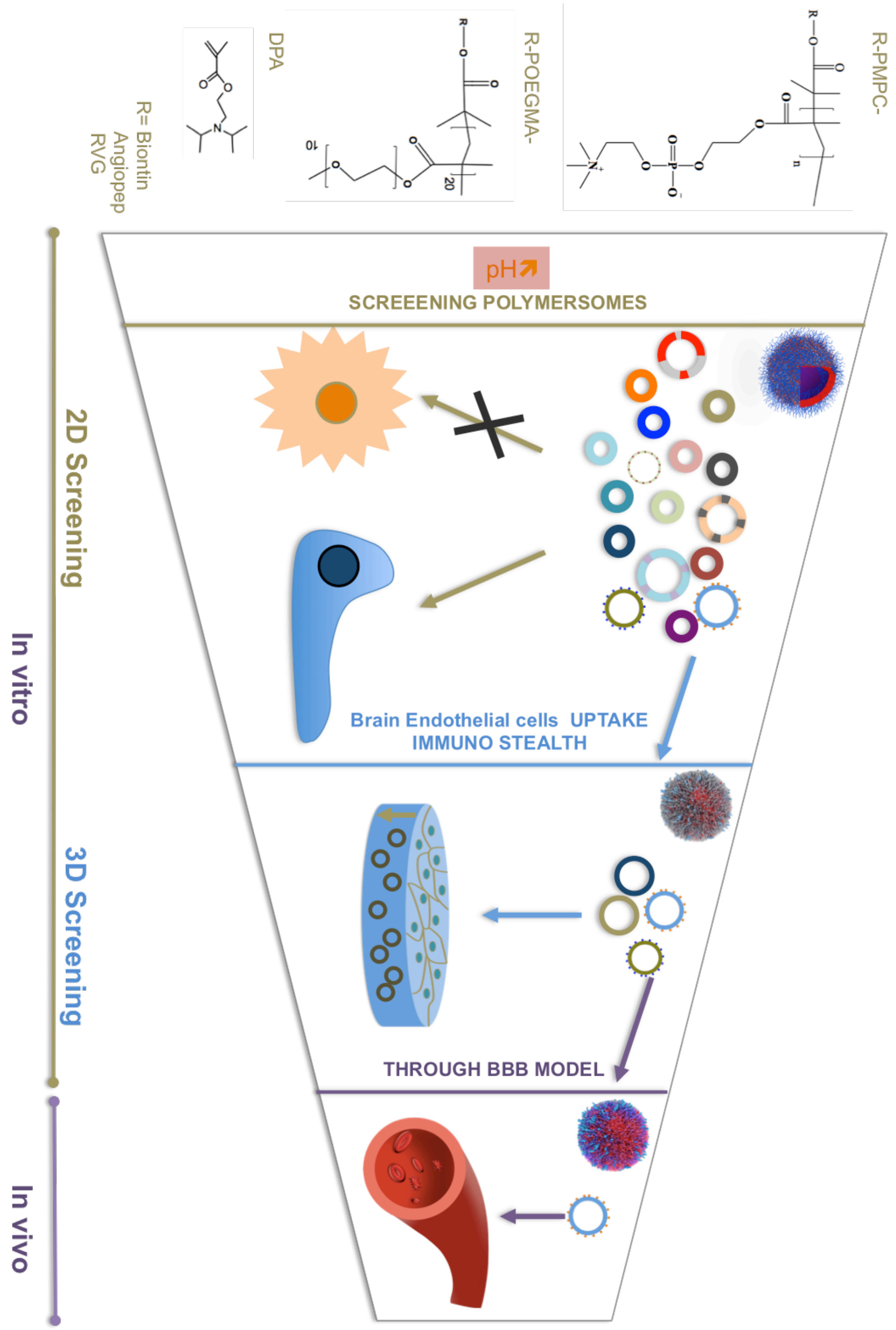

Figure 3.1 Project outline. By screening over 40 formulations polymersomes and examining their internalisation both in 2D and 3D in vitro BBB models, we aimed to find a functionalised polymersome formulation able to target transcytosis across BBB efficiently and release its cargo in brain. Such functionalised polymersomes would offer opportunities for further therapeutic application to treat CNS disorders and disease.

Chapter 4

Experimental Methods

4.1 Preparation of polymers and functionalised polymers

(All polymers used in the thesis were purposely made by Dr. Jeppe Madson at Department of Chemistry, University of Sheffield)

Materials:

The 4-(2-bromoisobutyryl ethyl)morpholine initiator (MEBr) was prepared according to a previously published procedure [1]. The protected maleimide initiator was prepared according to a previously published procedure [2]. The Rhodamine 6G-based initiator was prepared according to a previously published procedure [1]. The disulfide-based initiator ($BiBOE_2S_2$) was prepared according to a previously published procedure [3, 4]. Copper (I) Chloride (CuCl, 99.99 %), 2,2'-bipyridine (bpy, 99 %), Copper (I) bromide (CuBr, 99.999 %), methanol (anhydrous, 99.8 %), Poly (ethylene glycol) methyl ether methacrylate ($OEG_{10}MA$), tri-N-butylphosphine (≥93.5 %), Biotin-maleimide (≥95 %), Biotin (≥99 %) and the HABA/Avidin Reagent were purchased from Sigma Aldrich UK (Dorset, UK) and were used as received. The silica gel 60 (0.063 – 0.200 μm) was purchased from E. Merck (Darmstadt, Germany) and was used as received. HPLC grade chloroform, dichloromethane, ethanol and methanol were obtained from Fisher Scientific (Loughborough, UK) and were used as received. Regenerated cellulose dialysis membranes (1,000 MWCO, 3,500 MWCO and 50,000 MWCO) were from Spectra/Por. Cellulose dialysis membrane (8,000 MWCO) was from BioDesign. 2-(Methacryloyloxy)ethyl phosphorylcholine monomer (MPC, 99.9 % purity) was donated by Biocompatibles UK Ltd. (Farnham, UK) and was used as received. 2-(Diisopropylamino)ethyl methacrylate (DPA) was purchased from Scientific Polymer Products (Ontario, US) and passed through an inhibitor removal column (DHR-4, Scientific Polymer Products) prior to use.

ATRP synthesis of $P(OEG_{10}MA)_{20}$-$PDPA_{100}$ from ME-Br, RH-Br and Mal-Br initiators

In a typical procedure, the functional ATRP initiator (0.105 mmol, 1 eq.) was mixed with $OEG_{10}MA$ (1 g, 2.11 mmol, 20 eq.). When homogeneous, 1 mL water was added, and the solution was purged with nitrogen for 40 minutes. Then, a mixture of CuCl (10.4 mg, 0.105 mmol) and bpy (32.9 mg, 0.210 mmol) was mixed. After 8 minutes, a sample was removed and a nitrogen-purged mixture of DPA (2.2455 g, 0.0105 mol, 100 eq.) mixed with 3 mL isopropanol was added to the viscous mixture via cannula. After 18 h, the mixture was opened to the atmosphere and diluted with methanol, which gave a dispersion that gradually turned green due to oxidised copper catalyst.

Then, 2 volumes of dichloromethane were added, leading to a transparent solution. This was passed through a column of silica using dichloromethane:methanol 2:1 to remove the spent copper catalyst. The resulting solution was dialysed (MWCO 1,000 Da) against ethanol and water. The resulting dispersion was freeze-dried to give a white powder. $P(OEG_{10}MA)_{20}$ homopolymer was removed by dialysis against water using dialysis bags with a molecular weight cut-off of 50,000 Da.

The resulting copolymer composition was determined by ^1H NMR in $CDCl_3$ and the polydispersity was determined by size exclusion chromatography in THF.

Deprotection of $Mal\text{-}P(OEG_{10}MA)_{20}\text{-}PDPA_{100}$

Deprotection of the protected maleimide-polymer was facilitated by placing the solid purified Mal- $P(OEG_{10}MA)_{20}\text{-}PDPA_{100}$ polymer in a vacuum oven at 100 °C for 15 h[5]. This led to a slight decoloration and melting of the polymer. The formed maleimide-group could not be reliably quantified by ^1H NMR. Instead, the reactivity of the end-group was demonstrated by its ability to couple to thiol-functional peptides, as assessed by HPLC with fluorescence detection.

Reaction of $Mal\text{-}P(OEG_{10}MA)_{20}\text{-}PDPA_{100}$ with cysteine-terminated peptides Cys-Angiopep and Cys-RVG

The deprotected $Mal\text{-}P(OEG_{10}MA)_{20}\text{-}PDPA_{100}$ (105.6 mg, ~3.4 μmol maleimide) was dispersed in 4.5 mL nitrogen-purged PBS at pH 7.3. The pH was lowered by addition of concentrated HCl (10 μL) to give a uniform solution. The pH was then increased to 7.8 with 5 M NaOH and the resulting opaque dispersion was ultrasonicated for 10 minutes. 2.3 mL of this solution was transferred to a 2nd flask. Both solutions were then purged with nitrogen for 10 minutes. This should give an approximate maleimide amount in each flask of 1.7 μmol.

Functionalisation

To the original solution was then added Cys-Angiopep (5.5 mg, 2.3 μmol thiol) followed by TCEP (2 mg, 7 μmol). To the 2nd solution was added Cys-RVG (6.0 mg, 1.8 μmol thiol) followed by TCEP (2.3 mg, 8.0 mmol). The pH in each solution was measured to 7. Both solutions were left for 17 h. Then, both solutions were dialysed against water (MWCO 8,000) to remove any excess peptide, followed by freeze-drying. Successful labelling was confirmed using a HPLC with fluorescence and absorption detection: Angiopep contains fluorescent tyrosine residues rendering the polymer-peptide conjugates fluorescent at 303 nm, when excited at 274 nm. In addition to containing tyrosine, RVG also contains one fluorescent tryptophan residue, which emits at 348 nm when excited at 280 nm. On the other hand, the non-labelled polymer does not exhibit any fluorescence at these wavelengths (but can be detected using the absorption detector).

Preparation of $(PDPA_{70}\text{-}PMPC_{25}\text{-}S)_2$

To MPC (6.045 g, 20.47 mmol, 50 eq.) under nitrogen was added a solution of $BiBOE_2S_2$ (185.0 mg, 0.409 mmol, 0.818 mmol Br, 2 eq.) in methanol (4 mL) via cannula. To the $BiBOE_2S_2$-containing flask was added a further 4 mL of methanol, which was transferred via cannula. The resulting solution was purged with nitrogen for 35 minutes. Then a mixture of CuBr (116.9 mg, 0.815 mmol, 2 eq.) and bpy (254.3 mg, 1.628 mmol, 4 eq) was added.

After 1 h, a nitrogen-purged solution of DPA (12.130 g, 56.9 mmol, 140 eq.) in methanol (14 mL) was added via cannula. The reaction mixture was left for 24 h, where ^{1}H NMR indicated essentially no methacrylic protons. The contents of the flask were exposed to the atmosphere and diluted with methanol. When the catalyst had oxidised as indicated by the formation of a green dispersion, dichloromethane (2 volumes) was added. The solution was passed through silica using dichloromethane 3:2 V: V as eluent. The solution was then dialysed (MWCO 1,000) against methanol and dichloromethane and the polymer was isolated by evaporation at 40 °C, reduced pressure.

Reaction of $(PDPA_{70}\text{-}PMPC_{25}\text{-}S)_2$ with biotin-maleimide

$(PDPA_{70}\text{-}PMPC_{25}\text{-}S)_2$ (1.9954 g, ~45 μmol disulfide to give 90 μmol thiol) was dissolved in 50 mL chloroform:methanol 3:1 V:V. The solution was purged with nitrogen for 30 min. Then, tributylphosphine (25 μL, 20 mg, 100 μmol) was added. After 5 minutes, biotin-maleimide (44.8 mg, 99.2 μmol) was added and the solution was left at 20 °C for 23 h. The solution was then dialysed (MWCO 3,500 Da) against methanol and water, followed by freeze-drying. The biotin-content of the final polymer was determined by a commercial HABA-Avidin assay at pH 6 and pH 7.2.

HABA-Avidin displacement assay at pH 6 and pH 7.2

In general the manufacturer's procedure was followed for polymersomes at pH 7.2. In addition, the assay was tested at pH 6 using biotin, and the results at this pH value were used for measurements of dissolved polymers at pH 6.

The HABA/Avidin reagent was reconstituted using PBS (10 mL), where the pH had been adjusted to pH 6 with concentrated HCl.

A stock solution of biotin (20.3 mg, 83.1 μmol) in 100 mL PBS, pH 6 (0.831 mM) was diluted ten-fold to give a biotin concentration of 0.0831 mM. The assay was calibrated by diluting the biotin-solution and reading the absorption to give an absorption coefficient at 500 nm of the HABA/Avidin complex of $24 \cdot 10^{-3}$ $M^{-1}cm^{-1}$, which is lower than the manufacturer's value of $34 \cdot 10^{-3}$ $M^{-1}cm^{-1}$ at pH 7.5.

For all samples, the absorption of the sample diluted with buffer in the absence of reagent was subtracted in order to correct for absorption of sample due to aggregate formation. The Avidin-accessible biotin-content was determined to be 82 % of the theoretical at pH 6 and 64 % at pH 7, consistent with a lower accessibility on formation of nanoparticles

4.2 Preparation of polymersomes by the pH switch method

1. The polymersomes or cargo-loaded polymersomes were prepared using PMPC-PDPA (10% Rho-PMPC-PDPA), PEG-PDPA (10% Rho-PEO-PDPA) and POEGMA-PDPA (10% Rho-POEGMA-PDPA).

2. To make 10mg/ml polymersomes, the amount of polymers was weighed and dissolved using pH 2 PBS. Once the film dissolved the pH was increased to 5.0.

3. Cargo or peptide-functionalised polymers can be added at this point, in order to avoid acidic degradation.

4. The pH was gradually increased to pH 6.8-7.0, eventually stopping at pH 7.4-7.5. Prolonged stirring at pH 6.8-7.0 allowed polymersomes to form.

5. Polymersomes were then ultrasound sonicated for 15-30mins, at 4^{o}C.

6. The purification of polymersomes was finally performed by passing through a GPC column.

NOTE: For long-term storage, polymersomes should be kept at 4^{o} C protected from light. However, it is highly recommended that the peptide-functionalised polymersomes should be freshly made just before use.

4.3 Cell culture and sub-culture

bEND.3 cell line

bEND.3 cells (ATCC® CRL-2299™) were seeded on a rat-tail collagen Type I (SIGMA-ALDRICH®, C3867) pre-coated T-75 flask, maintained in DMEM medium (Dulbecco's Modified Eagle's Medium-high glucose, D5671-SIGMA) supplemented with 2 mM L-glutamine, 100 IU/mL penicillin, 100 mg/ml streptomycin, and 10% fetal calf serum (FCS). Cultures were maintained at 37 °C in an atmosphere of 5% CO_2 and 95% air and sub-cultured routinely using 0.02% (w/v) EDTA trypsin (5ml, 5min 37 °C, 5% CO_2 incubation) once 100%

confluence was achieved.

Astrocytes

Mouse astrocytes (ATCC® CRL-2541™, C8-D1A Astrocyte Type I clone) were seeded in T-75 flask, maintained in DMEM medium (Dulbecco's Modified Eagle's Medium-high glucose, D5671-SIGMA) supplemented with 2 mM L-glutamine, and 10% fetal calf serum (FCS) without 100 IU/ml penicillin, 100 mg/ml streptomycin. Cultures were maintained at 37 °C in an atmosphere of 5% CO_2 and 95% air and sub-cultured routinely using 0.02% (w/v) EDTA trypsin (5ml, 5min 37 °C, 5% CO_2 incubation) once 80%-90% confluence was achieved.

Mesenchymal stem cells (MSC)

Mesenchymal Stem Cells (MSC, Gibco® Mouse, C57BL/6) as surrogate for pericytes were seeded in a rat-tail collagen type I (SIGMA-ALDRICH®, C3867) pre-coated T-75 flask, maintained in DMEM/F12 medium (SKU# 10565-018, with GlutaMAX with 2 mM L-glutamine) supplemented with 5μg/ml Gentamicin and 10% fetal calf serum (FCS). Cultures were maintained at 37 °C in an atmosphere of 5% CO_2 and 95% air and sub-cultured routinely using 0.02% (w/v) EDTA trypsin (5ml, 5min 37 °C, 5% CO_2 incubation) once 70% - 80% confluence was achieved.

4.4 FACS flow cytometry

1. BEND.3cells were seeded in rat-tail collagen Type I (SIGMA-ALDRICH®,

C3867) pre-coated 6-well plate, maintained in DMEM medium (2ml) at 37 °C in an atmosphere of 5% CO_2 and 95% air.

2. Once 100% confluence was achieved, prepared polymersomes 200μl/well (1mg/ml) were added, and incubated for a certain time as the experiment required.

3. After treatment, the cells were washed with PBS X2, and harvested using 0.02% (w/v) EDTA trypsin (1ml/well, 5min 37 °C, 5% CO_2 incubation).

4. The cell suspension was collected into a 1.5 ml Eppendorf tube and centrifuged at 600g (5min, 25°C) to obtain the cell pellet.

5. The liquid supernatant was discarded and the cell pellet re-suspended in prepared 4°C PBS (400 μl/Ep). 150-200μl/well cell suspension was added to a 96-well plate.

6. The cells were analysed by BD® FACSVerse™, for detection of positive Rho-polymersome cells, excitation wavelength=560nm, emission wavelength= 565-600nm.

4.5 Immunofluorescence (IF)

1. Cells grown in multi-well plate, transwell insert and chamber slides were fixed with 4% formaldehyde in PBS, 15min at room temperature.

The following protocol was used for both cultured cells and fixed tissue sections:

2. Block specimen in Blocking Buffer (1XPBS/5% normal serum/0.3% Triton ™ X-100 for 60min. Serum species may vary due to primary antibody (Ab) species.

3. While blocking, prepare primary Ab in Antibody Dilution Buffer (1XPBS/1%

BSA/0.3% Triton ^{TM} X-100). Incubate overnight at 4° C, or 2-4 hours at room temperature.

4. Wash in PBS 3 times, 5min each time.

5. Incubate specimen in fluorochrome-conjugated secondary antibody diluted in Antibody Dilution Buffer for 1–2 hrs at room temperature in the dark.

6. Wash in PBS 3 times, 5min each time.

7. Coverslip slides with mounting medium with DAPI. For long-term storage, keep slides flat at 4° C protected from the light.

4.6 3D *in vitro* BBB model set up

1. bEND.3cells were seeded on rat-tail collagen Type I (SIGMA-ALDRICH®, C3867) pre-coated 12-transwell plate inserts (Corning®3401^{TM} clear, Polycarbonate membrane, clear, no pre-coating), maintained in DMEM medium (400μl/well) at 37 °C in an atmosphere of 5% CO_2 and 95% air. Cells were allowed to attach for 12-24 hours (Figure 4.1 a).

2. The transwell inserts pre-seeded with bEND.3 cells were then placed, inverted, in a Petri dish (Figure 4.1 b).

3. The astrocyte or MSC cell suspension was added to the underside of the transwell-insert membrane (opposite side to bEND.3 cells), at a maximal volume of 200μl (2000-4000cells/cm^2). The Petri dish was then filled with cell culture medium, in order to keep a moist environment (Figure 4.1 b).

4. The transwell inserts in the Petri dish were maintained at 37 °C in an atmosphere of 5% CO_2 and 95% air. Cells were allowed to attach for 12-24 hours.

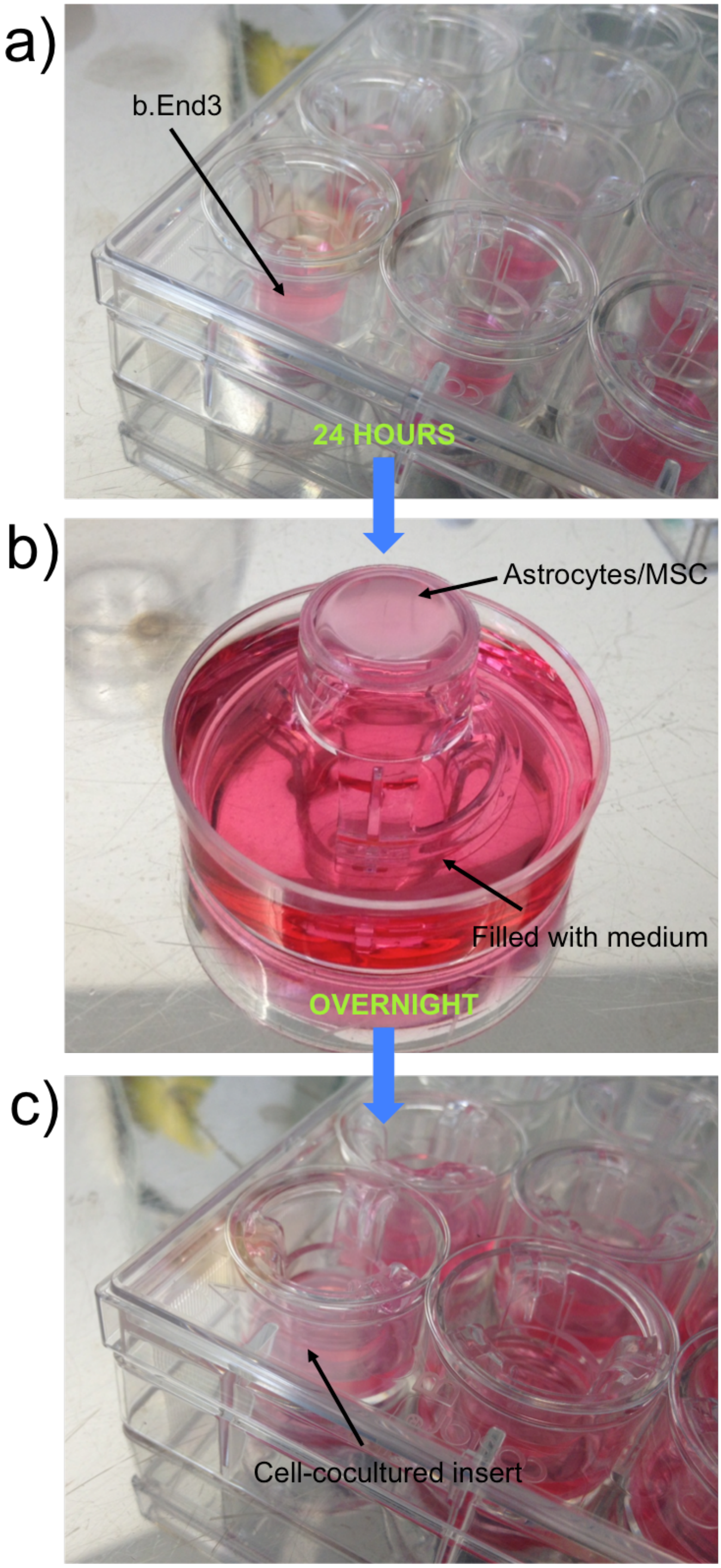
a)
b.End3
24 HOURS
b)
Astrocytes/MSC
Filled with medium
OVERNIGHT
c)
Cell-cocultured insert

Figure 4.1 Setting up the 3D *in vitro* BBB model. a) bEND.3cells were seeded in rat-tail collagen Type I pre-coated transwell inserts in a 12-transwell plate maintained in DMEM medium at 37 °C in an atmosphere of 5% CO_2 and 95% air. b) The inserts pre-seeded with bEND.3 cells were then inverted in a Petri dish, and seeded with MSC cells or astrocytes. c) The inserts were put back in the transwell plate once the MSC clls or astrocytes had attached. The wells were then filled with cell-culture medium: upper compartment 400μl, lower compartment 800-1000μl.

5. The transwell inserts were then returned to the transwell plate, and filled with cell culture medium: upper compartment 400μl, lower compartment 800-1000μl (Figure 4.1 c).
6. The transwells were maintained at 37 °C in an atmosphere of 5% CO_2 and 95% air. Experiments were performed on the 3D *in vitro* BBB models 5-7 days after cells reached confluence.
7. For TEER measurements, the cells were allowed to attach for 24-48 hours, for both monoculture and co-culture models. Resistance measurements were taken once a day with an EVOM voltohmmeter (World Precision Instruments) until cells reached confluence. The background resistance was subtracted. Unit resistance was calculated by multiplying the resistance by the area of the filter membrane (1.12cm^2 for 12 well-plate transwell insert), and averaged for each sample (*n* = 5).

4.7 Preparation of trans-well slides for microscopy: Protocol

1. Once experiments have been performed on the *in vitro* BBB model, discard the cell medium and wash both sides of the filter inserts with PBSX3
2. Fix the cells with methanol for 5-10 minutes at -20°C, using 400μl for upper

compartment, 800-1000µl for lower compartment.

3. Place the transwell filter insert onto a glass slide, right side up. Keep a liquid film (normally PBS) between the filter and the slide.

4. Using a scalpel and holding the transwell insert flat against the glass, make two cuts along the boundary: first cut from 1:00 to 6:00, second cut from 11:00 to 6:00 (numbers as on clockface). The PBS droplet helps keep the filter flat.

5. Slightly tilt the insert towards you; the point of attachment of the filter should be slightly off the glass. Use a small pair of scissors to cut the filter still attached to the plastic insert rim.

6. Flatten out the filter if necessary. Carefully wick off the PBS with a paper-wipe, and add a glass coverslip. Seal the edges with nail polish. The slide is then ready for microscopic imaging

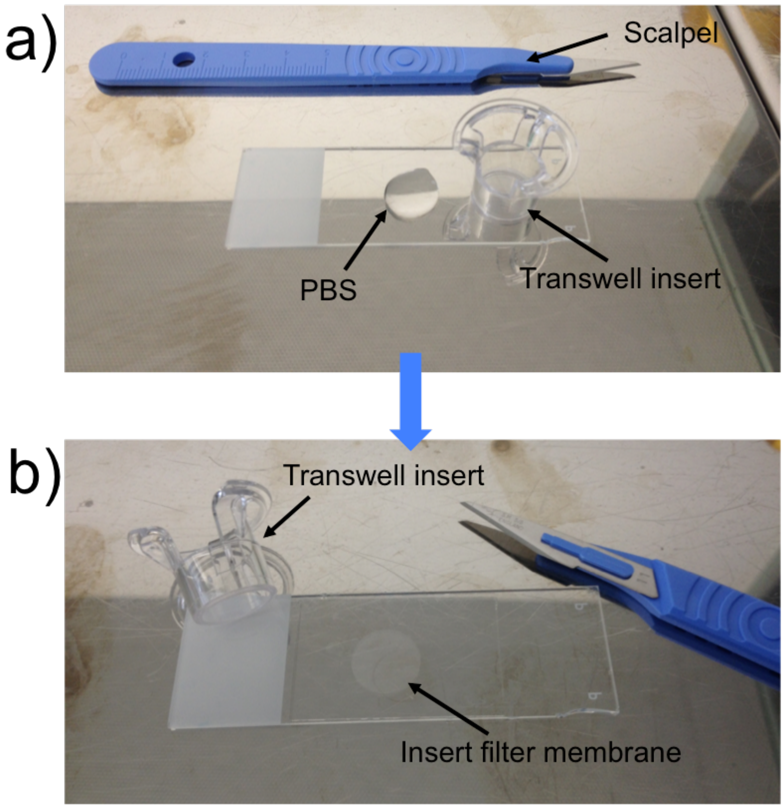

Figure 4.2 Preparation of trans-well slide for microscopy

4.8 Microscopy

4.8.1 Transmission Electron Microscopy (FEI Tecnai G2)

Polymersomes sample preparation:

PTA (Phosphotungstic acid) solution preparation: 37.5 mg of PTA was dissolved in 5mL of boiling distilled water while stirring for 5 min. The pH of the solution was adjusted to 7.0 by adding small drops of 5 M NaOH under continuous stirring. The PTA solution was then filtered through a 0.2 μm filter. Polymersomes/PBS dispersions (5 ml) at 5 mg/ml were deposited onto glow-discharged copper grids. After 1 min, the grids were blotted with filter paper and then immersed in the PTA staining solution. The grids were blotted a second time and dried under vacuum for 1 min. PTA was used as a selective staining agent for the PMPC–PDPA block copolymer. Different dwell times of the grids in the PTA solution were tested in order to find the best conditions for obtaining both negative and positive staining. After 10 s dwell time, the majority of the vesicles were negatively stained, while after 5 s the resulting staining was mainly positive.

Cell sample preparation

1. Specimens were received pelleted in Eppendorf tubes. Fresh 3% glutaradehyde in 0.1M phosphate buffer was added to re-suspend the pellet to ensure optimal fixation, and left overnight at 4°C. The specimens were then washed in 0.1M phosphate buffer at 4°C, twice at 30min intervals.
2. Secondary fixation was carried out in 2% aqueous osmium tetroxide for 2 hours at room temperature, followed by washing in buffer as above.

Continuing at room temperature, this was followed by dehydration through a graded series of ethanol: 75% (15min), 95% (15min), 100% (15min) and 100% (15min). 100% ethanol was prepared by drying over anhydrous copper sulphate for 15min.

3. The specimens were then placed in an intermediate solvent, propylene oxide, for two changes of 15mins duration.

4. Resin infiltration was accomplished by placing the specimens in a 50/50 mixture of propylene oxide/Araldite resin. The specimens were left in this mixture overnight at room temperature.

5. The specimens were left in full strength Araldite resin for 6-8 hrs at room temperature (with change of resin after 3-4 hrs) after which they were embedded in fresh Araldite resin for 48-72 hrs at 60 ^{o} C.

6. Semi-thin sections approximately 0.5 μm thick were cut on a Leica ultramicrotome and stained with 1% Toluidine blue in Borax.

7. Ultra-thin sections, approx. 70-90nm thick, were cut on a Leica ultramicrotome and stained for 25mins with saturated aqueous uranyl acetate followed by staining with Reynold’s lead citrate for 5mins.

8. The sections were examined using a FEI Tecnai Transmission Electron Microscope at an accelerating voltage of 80kVv. Electron micrographs were taken using a Gatan digital camera.

NOTE: Cell suspensions were washed free of media using several changes of buffer.

4.8.2 Confocal laser scanning microscopy (ZEISS LSM 510)

1. All the confocal laser scanning microscopy was performed on a ZEISS LSM 510 microscope, equipped with the following lasers: Ar laser, 30mW; HeNe laser, 1mW and HeNe laser, 5mW.

2. The laser excitation wavelengths used were: 405nm (DAPI), 488nm (TJ, Lectin and FITC-collagen etc.), 548nm (TJ, NeuN and Rho-Polymersomes), 633nm (CD140, SBA IgG).

3. For live-cell and Real-Time (RT) imaging, an incubation chamber was applied, connected to ZEISS temperature control unit 37-2 and CO_2 controller. (1-2 hours before the experiment was allowed for stabilization of the temperature and CO_2 concentration).

Figure 4.3 ZEISS Temperature and CO_2 controller.

4. Several microscope stage frames and inserts for imaging and slide formats are available for different cell-culture requirements, holding multi-well plates

and standard glass slides. These were used as appropriate


Universal Mounting Frame AK
Universal Mounting frame KM
Heating Insert P Lab-Tek

Figure 4.4 ZEISS imaging stage frames.

5. For high-resolution micrographs, water/oil immersion lenses (40X.W, 63X.O) are highly recommended and were used in this study.

NOTES on technique:

- For multi-color image capture and image modelling the imaging mode normally used was “Sequential”, which allows the microscope to take images in each channel separately. This helps avoid multiple channel contamination. The “Spontaneous” image mode (multiple-channel imaging at the same time) was used for imaging live cell organelles at high resolution.
- For multi-color image capture, instead of using LP (long-band pass) filter, BP (short-band pass) filter is highly recommended. This helps avoid multiple channel contamination in a multiple staining experiment.
- To avoid auto-fluorescence and unexpected fluorescence from Out Of Focus regions (or layers), the pinhole should be carefully adjusted. A smaller pinhole can filter more auto-fluorescence and unexpected fluorescence, hence giving much “cleaner” micrographs. To improve the quality of micrographs, slower ‘Scanning Speed’ and more

"Scanning number" are often required.

4.9 Image processing and analysis

In this project image processing and analysis basically using **Image J 64**

ImageJ 1.43u / Java 1.6.0_51 (64-bit)

Figure 4.5 Image J64 working platform (Mac).

4.9.1 Multiple channel micrographs, colour change and re-merge

Image J can easily change channel colours and make composite images. Several methods can be used.

1. Open the original **.lsm** file. If it is a multiple channel micrograph, all colours can be split by following the steps: **Image** >> **Color**>>**Split Channel**.

2. In each individual channel, the original colour can be modified in two ways. One is by following the steps: **Image** >> **Color**>>**Channel tool**>>**More**, then picking the colours to be used. However the choice is limited between Red, Blue, Green, Cyan, Magenta, Yellow and Grays. More colour options are available by following: **Image** >> **Color**>>**Lookup tables**, or **Image** >> **Color**>>**Color picker.**

3. Once the colour for each channel is decided, the merged micrograph can be obtained by following: **Image** >> **Color**>>**Merge Channel**, then choosing the corresponding channel for each colour. But in this case, only four colours (Red, Green, Blue and Gray) are available.

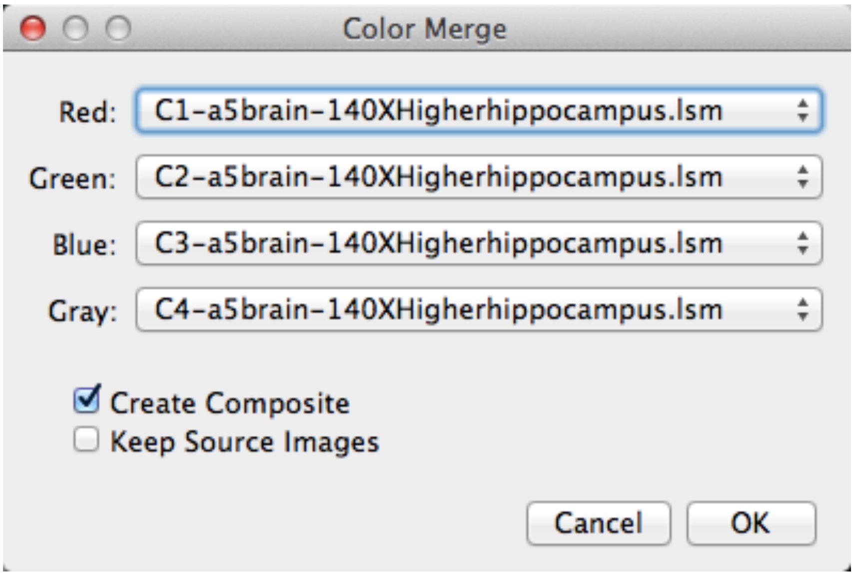

Red: C1-a5brain-140XHigherhippocampus.lsm
Green: C2-a5brain-140XHigherhippocampus.lsm
Blue: C3-a5brain-140XHigherhippocampus.lsm
Gray: C4-a5brain-140XHigherhippocampus.lsm

☑ Create Composite
☐ Keep Source Images

Figure 4.6 Image J64 channel overlay.

4. Alternatively in order to use colours besides these 4, choose specific colours then follow **Process >> Image calculator.**

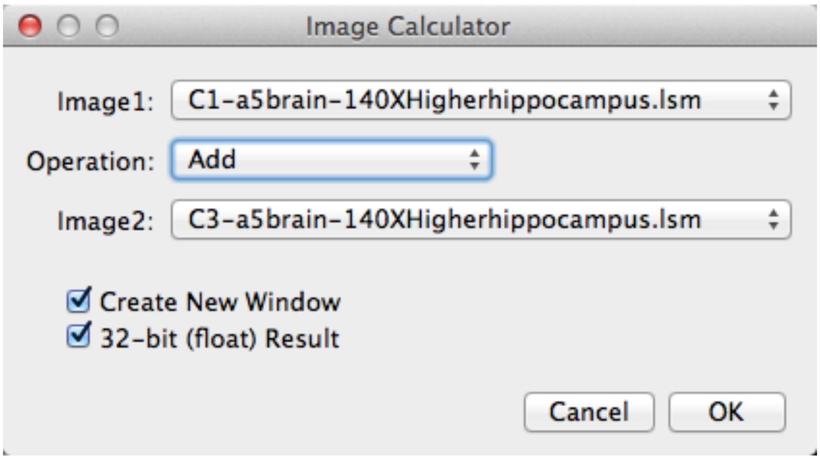

Image1: C1-a5brain-140XHigherhippocampus.lsm
Operation: Add
Image2: C3-a5brain-140XHigherhippocampus.lsm

☑ Create New Window
☑ 32-bit (float) Result

Figure 4.7 Image J64 channel overlay via image calculator.

4.9.2 Z-stack image reconstruction (3D plugin is required).

Image J is a powerful software that can use existing Z-stack images to generate 3D Animation and 3D Volume views.

1. Open a Z-stack image, adjust the colour and contrast before further processing, and choose the region of interest (ROI) if needed (using Selection tool and Duplicate).

2. Before processing a 3D application, follow the steps: **Image** >> **Color**>>**Make Composite** and **Image** >> **Color**>>**Stack to RGB**.
3. Use the newly-generated RGB image, and follow **Plugins** >> **3D**.
4. The Image J 3D viewer gives a 360 degree view of the sample in three dimensions. 360^o animation or free hand animation can be recorded by following **View** >> **Record 360 animation** or **View** >> **Record Free Hand**
5. The Volume Viewer gives the whole landscape in the sample (see Chapter 6 and Chapter 7 for applications in this project).

4.9.3 Quantitative analysis of micrograph fluorescence intensity (ROI Manager plugin required).

Quantification of the fluorescence intensity requires more sample micrographs, in order to provide more data points to minimize the error. Hence, normally 3 micrographs for each experiment are required, and 10 data points from each micrograph are obtained.

1. Open micrograph, merge channels if needed.
2. Follow **Analyze** >> **Tools** >> **ROI manager.**
3. Choose the “region of interest” in the sample micrograph, using the appropriate “Choosing” tool.
4. Add each data point to the “ROI Manage” list.

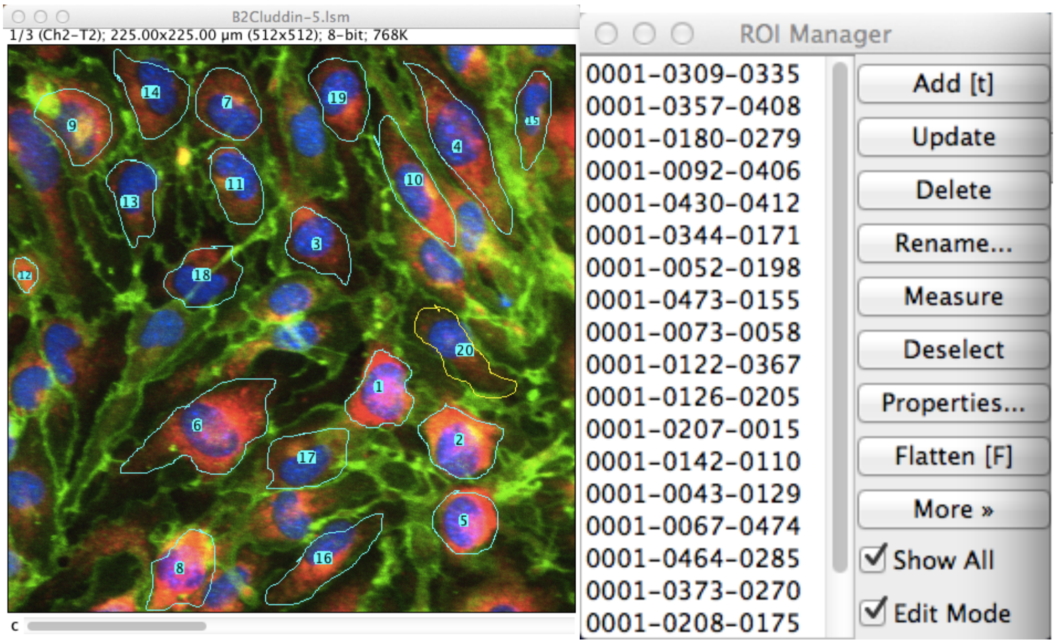

Figure 4.8 Image J64 fluorescence intensity analysis by ROI manager.

5. After all data points are collected, click “**Measure**”. Then quantified data should pop up in a new window, with “**Min Intensity**”, “**Max Intensity**” and “**Average Intensity”** for each data point. Export “**Average Intensity”** into Excel or Prism for further analysis.

References:

1. Weaver, J.V.M., et al., *Stimulus-responsive water-soluble polymers based on 2-hydroxyethyl methacrylate.* Macromolecules, 2004. **37**(7): 2395-2403.
2. Mantovani, G., et al., *Design and synthesis of N-maleimido-functionalized hydrophilic polymers via copper-mediated living radical polymerization: A suitable alternative to PEGylation chemistry.* Journal of the American Chemical Society, 2005. **127**(9): 2966-2973.
3. Madsen, J., et al., *Biocompatible wound dressings based on chemically degradable triblock copolymer hydrogels.* Biomacromolecules, 2008. **9**(8): 2265-2275.
4. Tsarevsky, N.V. and K. Matyjaszewski, *Reversible redox cleavage/coupling of polystyrene with disulfide or thiol groups prepared by atom transfer radical polymerization.* Macromolecules, 2002. **35**(24): 9009-9014.
5. Pounder, R.J., et al., *Metal free thiol-maleimide 'Click' reaction as a mild functionalisation strategy for degradable polymers.* Chemical Communications, 2008(41): 5158-5160.

Chapter 5

Polymersome 2D Screening

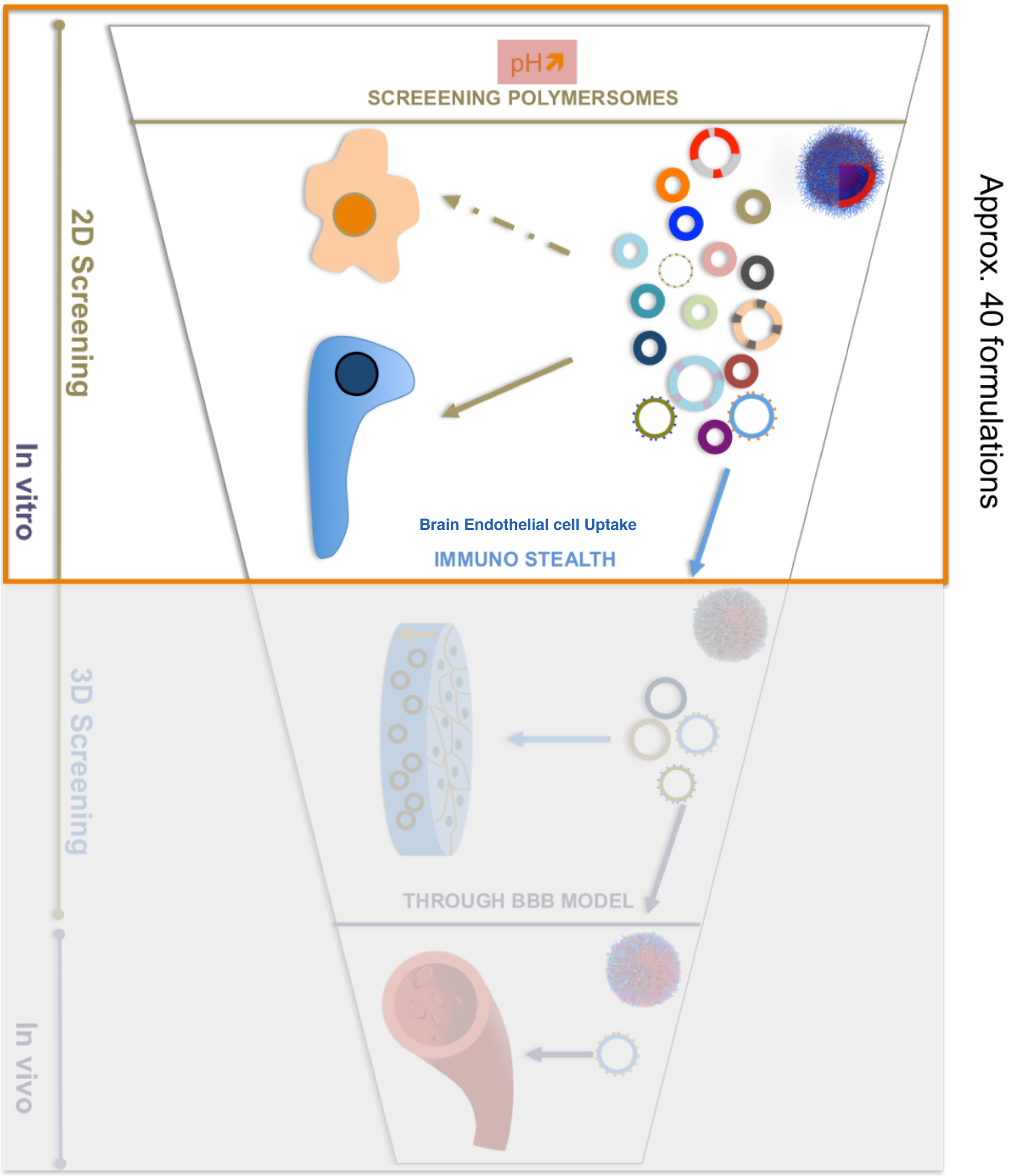

Schematic representation of screening polymersomes in 2D

5.1 Introduction

Polymersomes formed by amphiphilic diblock copolymers have been widely used in several applications, as detailed in Chapter 2. In our lab, we have demonstrated that pH-sensitive poly((2- methacryloyloxy) ethyl phosphorylcholine))-co-poly(2-(diisopropylamino)ethyl methacrylate) (PMPC-PDPA) (Figure 5.1b) polymersomes are an ideal tool for intra-cellular delivery. These can be applied for the delivery of both hydrophilic and hydrophobic molecules, such as dyes, several small-molecule drugs, nucleic acid and proteins [1-5]. PMPC-PDPA displays low toxicity and fast internalisation in several cell types [3]. Recent work in our group has shown that PMPC interacts strongly with a specific class of receptors known as scavenger receptors B. Other people in the group have shown that PMPC internalisation is controlled by the binding of PMPC chains with scavenger receptors B1 (SRB1) and its internalisation is regulated by scavenger receptors B CD36 and tetraspannin CD81 (Avila-Olias et al. in preparation). While there are reports showing that SRB1 is over expressed in brain endothelial cells and associated with transcytosis [6], SRBs are also over expressed by most immune cells. This would quickly rid the bloodstream of the PMPC polymersomes. For this reason, we also used PEG-based systems, which, by contrast, do not interact with immune cells and enable long circulation times (discussed in Chapter 2). As a consequence, in this project a series of PEO_m-$PDPA_n$ (poly(ethylene glycol)-co-poly(2

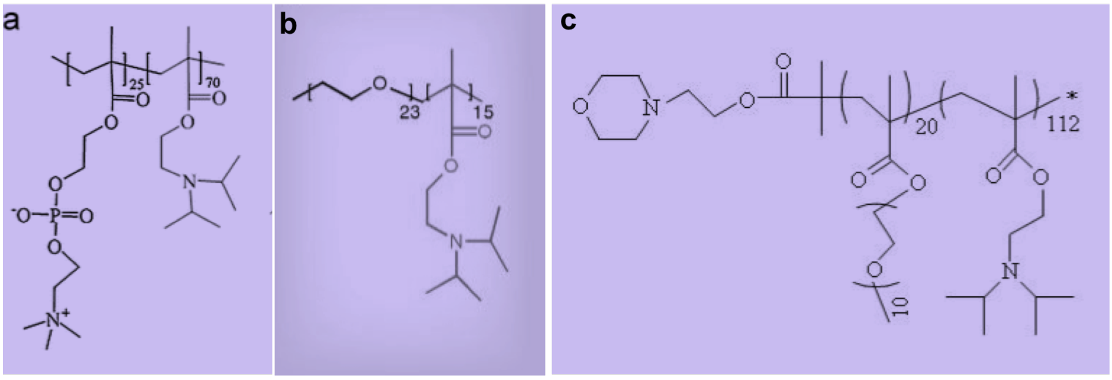

Figure 5.1 Chemical structures of PDPA-based diblock copolymers. *a) $PMPC_{25}$-$PDPA_{70}$, previously revealed strong internalisation by several cell types. b) PEO_{23}-$PDPA_{15}$, the 'stealth' polymer prolongs circulation time. c) $P(EO_{10}GMA)_{20}$-$PDPA_{112}$, the analogue of PEO-PDPA.*

-(diisopropylamino)ethyl methacrylate)) diblock copolymers (Figure 5.1c) and their analogue $P(EO_{10}GMA)_{20}$-$PDPA_{112}$ diblock copolymers (Figure 5.1d) were also used to form polymersomes. These were screened against brain endothelial and immune system cells. Transcytosis receptor ligands, RVG [7] and Angiopep-2 [8], were conjugated with PMPC block and POEGMA block either via direct conjugation or using biotin-streptavidin complex. Polymersome topology also plays an essential role in regulating cellular uptake [3], hence binary polymersomes PMPC-PDPA/PEO- use different molecular weights PEO_m-$PDPA_n$ (m=22, 45, 113. n=17, 22, 56.). All of these formulations are fully characterised; cellular uptake properties both on brain endothelial cells and immune system cells were also examined and discussed in this chapter. The aim of screening polymersomes was not only to find an optimal formulation that targets endocytosis/transcytosis across the blood-brain barrier, but also to establish structure/function analysis between cellular internalisation and polymersome parameters such as size, surface chemistry and topology.

5.2 PMPC-PDPA vs. PEO-PDPA

5.2.1 PMPC-PDPA polymersomes

PMPC$_{25}$-PDPA$_{70}$ diblock copolymers and rhodamine-PMPC$_{25}$-PDPA$_{70}$ (Rh-PMPC-PDPA) were synthesised by atom-transfer radical-polymerisation (ATRP, refer to the work of Dr. Jeppe Madsen, Chapter 4, section 4.1). As reported previously [9], PMPC-PDPA polymersomes were generally formed by pH switch method (see Chapter 4, section 4.2). A typical size distribution by intensity and morphology of PMPC- PDPA polymersomes before and after GPC purification is shown in Figure 5.2. Transmission electron microscopy

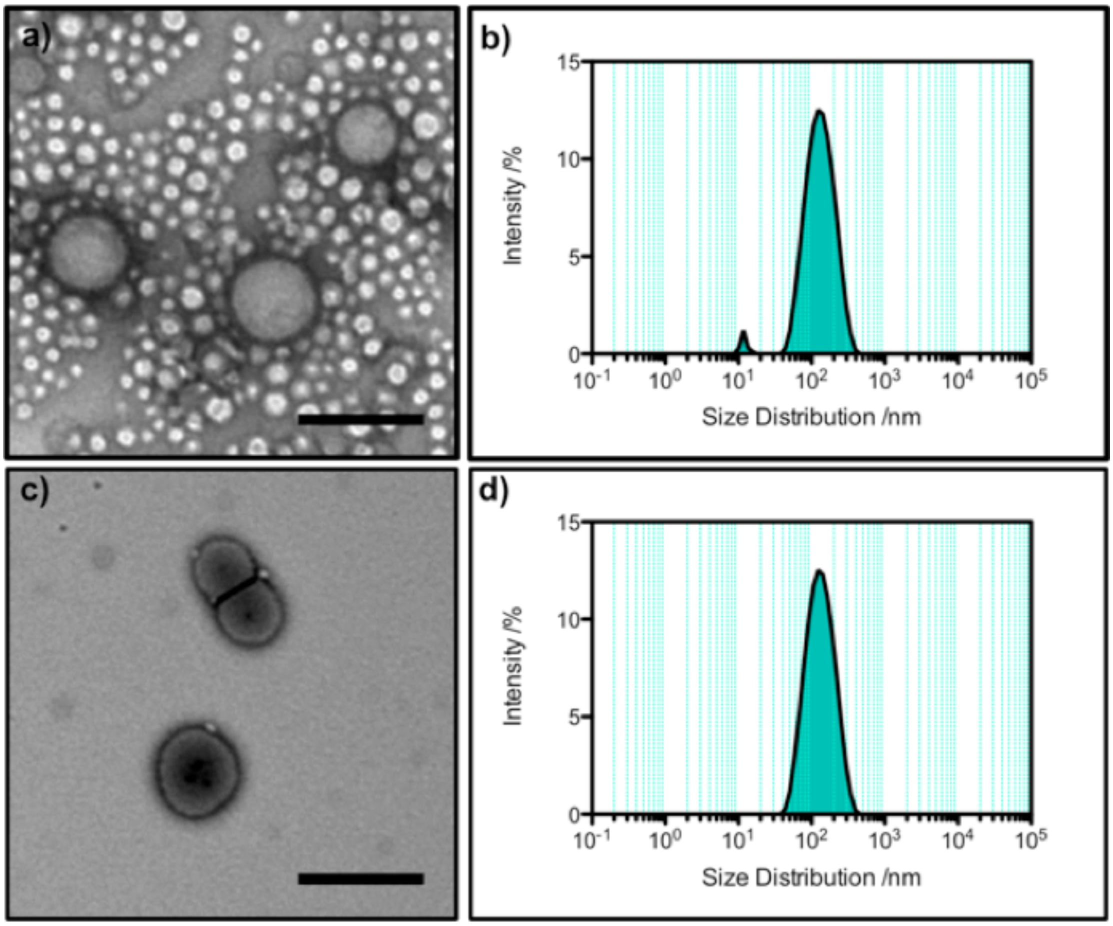

ZP=0.990±0.13

Figure 5.2 Morphology and size distribution by intensity of PMPC-PDPA. *a) and b) TEM micrograph of PMPC$_{25}$-PDPA$_{70}$ and its size distribution before GPC purification. The scale bar represents 200nm.*

(TEM) shows the typical morphology of polymersomes, while dynamic light scattering (DLS) quantifies their size distribution. The pH switch method, as well as other solvent switch methods [10], has the advantage of operating in solution and hence to control purity and self-assembly bottom-up. However, when it comes to forming vesicles, bottom-up self-assembly goes through the formation of spherical and cylindrical micelles [11-13]. This means that polymersomes formed by pH switch will always co-exist with other side-product structures such as micelles or high genus structures. This is shown in the TEM micrograph in Figure 5.2a where both vesicles (100-200nm in diameter) and micelles (diameter 10-20nm) are visible. As size and morphology strongly affect cellular interaction [14], we always purify polymersomes using GPC. The resulting dispersion is shown in Figure 5.2c where almost only polymersomes are visible.

As mentioned before, PMPC-PDPA polymersomes can be internalised by numerous cell types including primary animal cells, primary human cells and several cancer cells with no toxicity or cellular stress associated with their endocytosis [3].

Brain endothelial 3 (bEnd.3) is a cell line isolated and immortalised from mouse brain endothelium. It is a very common model for both BBB biology and to assess BBB transport. bEnd.3 retains most of the features of the original endothelial barrier, including tight junctions and transport by endocytosis/transcytosis. Here, $PMPC_{25}$-$PDPA_{70}$ polymersomes (1 mg/ml, 10% Rho-labelled) showed successful and efficient uptake by the confluent bEnd.3 cells' monolayer within 6 hours (Figure 5.3b), and revealed relatively low toxicity over 24 hours; only the high concentration dose (5 mg/ml) slightly reduced cell viability (Figure 5.3a). Both fluorescence micrographs (Figure 5.3b) and fluorescence analysis (Figure 5.3c, ROI, region of interest subtract cellular nuclear) demonstrate that bEnd.3 uptake of PMPC-PDPA occurs very quickly and equilibrates (i.e. endocytosis is as fast as exocytosis) in 180 minutes.

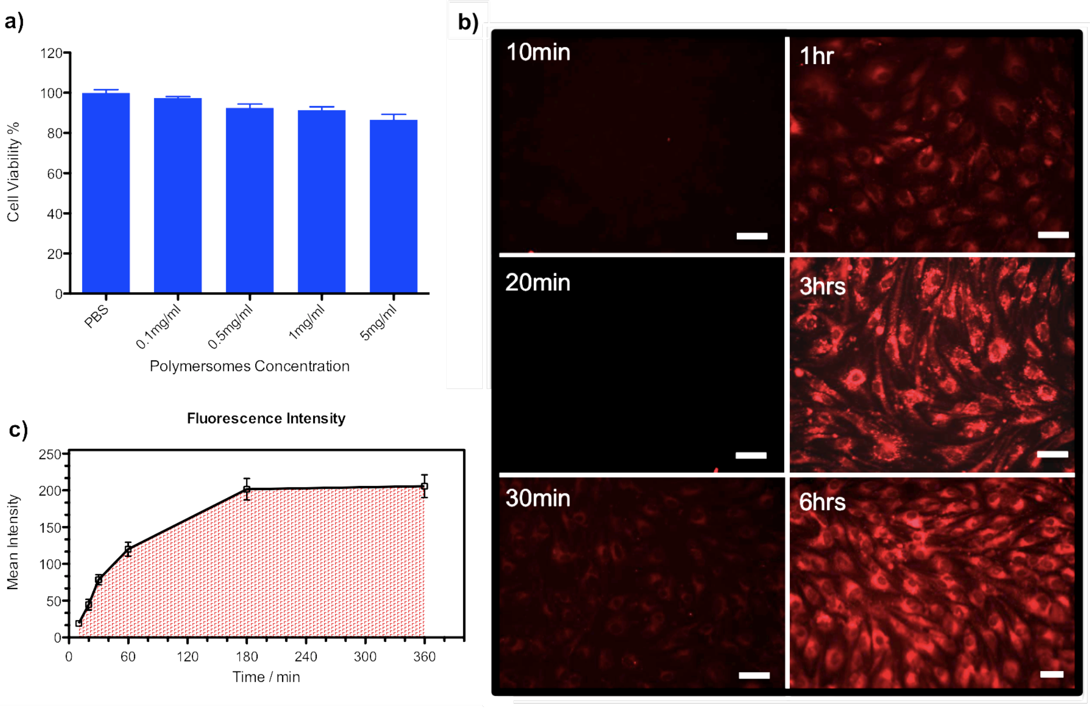

Figure 5.3 MTT assay of PMPC-PDPA polymersomes on bEnd.3 and kinetics of their cellular uptake. a) MTT assay of PMPC-PDPA polymersomes on bEnd.3 cells for 24 hours; the polymersome concentration is 0.1 mg/ml, 0.5 mg/ml, 1 mg/ml and 5 mg/ml respectively, while PBS is the control. b) Fluorescence micrograph of bEnd.3 uptake of PMPC-PDPA polymersomes (1 mg/ml); images were taken at 10 mins, 20 mins, 30 mins, 1 hour, 3 hours and 6 hours respectively; cells were imaged in PBS without fixation. c) Fluorescence intensity analysis of PMPC-PDPA cellular uptake kinetic (note: Mean $_{Min}$ = 0, Mean $_{Max}$ = 255). The scale bar represents 20 µm.

5.2.2 PEO-PDPA polymersomes

PEO-PDPA diblock copolymer and rhodamine-PEO-PDPA (Rh-PEO-PDPA) were synthesised as reported previously [15]; PEO polymersomes have already been shown to be poorly internalised by several cell types [3].

Here three types of PEO-PDPA copolymer with different molecular weights were used to form polymersomes PEO_{22}-$PDPA_{17}$, PEO_{45}-$PDPA_{22}$ and PEO_{113}-$PDPA_{56}$. Polymersome (10 mg/ml, 10% Rh-PEO-PDPA) preparation and purifying processes are similar to those of PMPC-PDPA polymersomes. Polymersome formation and size distribution are shown in Figure 5.4.

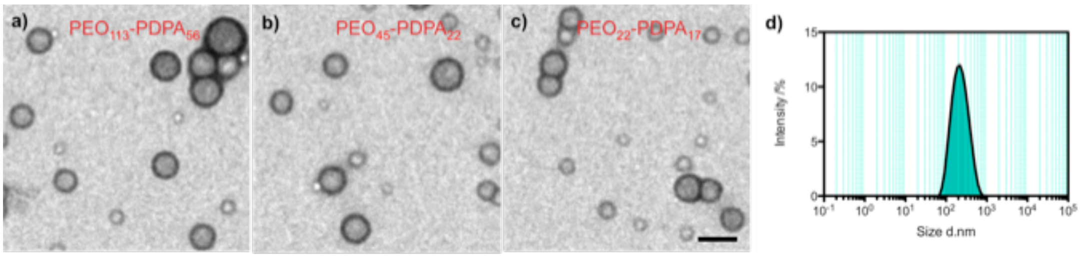

ZP = -0.69±0.41

Figure 5.4 Morphology and size distribution by intensity of PEO-PDPA.
a), b) and c) show TEM micrographs of PEO_{113}-$PDPA_{56}$, PEO_{45}-$PDPA_{22}$ and PEO_{22}-$PDPA_{17}$ respectively. d) A typical size distribution of PEO-PDPA polymersomes measured by dynamic light scattering. The scale bar represents 200 nm.

We confirm here that PEO polymersomes do not interact strongly with bEnd.3 cells, as 24-hour incubation studies with PEO-PDPA polymersomes showed relatively much lower cell interaction compared with PMPC-PDPA (Figure 5.5a).

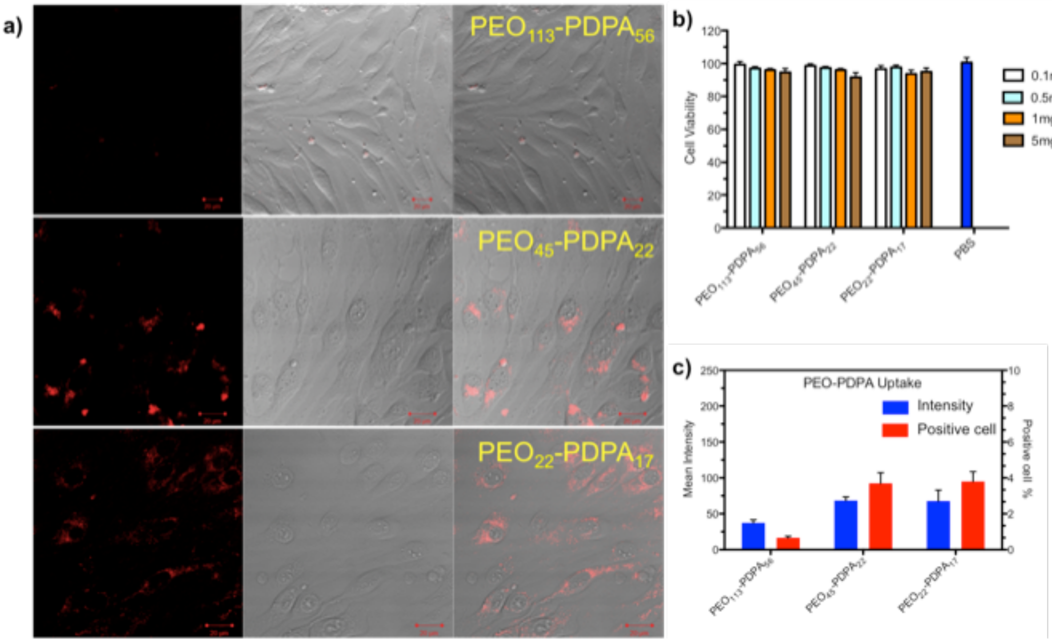

Figure 5.5 MTT assay of PEO-PDPA on bEnd.3 and its cellular uptake.
a) CLSM (confocal laser scanning microscopy) micrograph showing the cellular uptake of PEO_{113}-$PDPA_{56}$, PEO_{45}-$PDPA_{22}$ and PEO_{22}-$PDPA_{17}$ by bEnd.3 cells over 24 hours (red = polymersomes, white = DIC transmission light; cells were imaged without fixation). b) MTT assay of PEO_{113}-$PDPA_{56}$, PEO_{45}-$PDPA_{22}$ and PEO_{22}-$PDPA_{17}$ polymersomes on bEnd.3 cells for 24 hours; the polymersome concentration is 0.1 mg/ml, 0.5 mg/ml, 1 mg/ml and 5 mg/ml respectively, with PBS as a control. c) Fluorescence intensity analysis and FACS flow cytometry show differences between PEO_{113}-$PDPA_{56}$, PEO_{45}-$PDPA_{22}$ and PEO_{22}-$PDPA_{17}$ cellular uptake (note: Mean $_{Min}$ = 0, Mean $_{Max}$ = 255).

Not surprisingly, the two short formulations PEO_{45}-$PDPA_{22}$ and PEO_{22}-$PDPA_{17}$ showed higher cellular uptake over 24 hours, compared with the longer PEO_{113}-$PDPA_{56}$ (Figures 5.5a and c). As these polymersomes share the same chemistry, the cellular uptake property is highly determined by their different molecular weights. The longer the PEO chains, the less interaction they have with soluble proteins [16]. This has implications for polymersome pharmacokinetics as previously proved by the Discher group [17]; here the PEGylated polymersomes were shown to expand half-life time ($\tau_{1/2}$) *in vivo* by increasing the PEGylated chain molecular weight.

Although PMPC-PDPA and PEO-PDPA have different cellular uptake properties, the mixture of these two polymers to form binary polymersomes may possess the advantages of both functional-PMPC-specificity for internalisation by certain cells, and the PEO brush to prevent recognition by immune system cells.

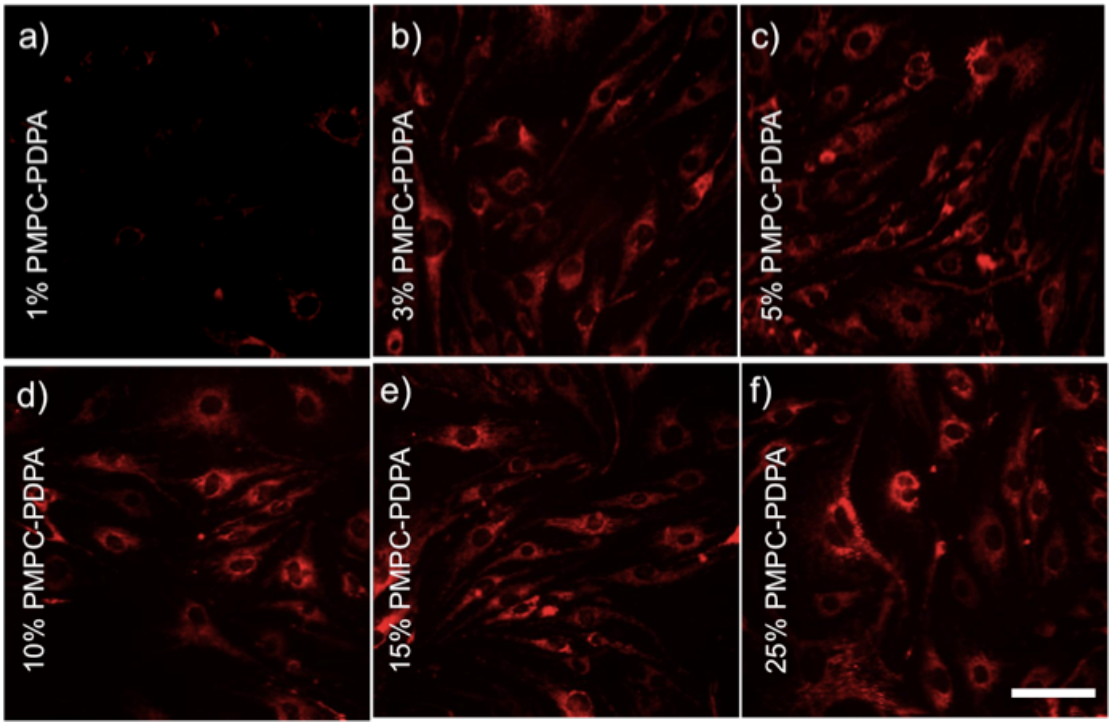

Figure 5.6 Confocal micrograph of bEnd.3 cellular uptake of different ratio $PMPC_{25}$-$PDPA_{70}$/PEO_{113}-$PDPA_{56}$ polymersomes in 6-hour incubation. a) 1% $PMPC_{25}$-$PDPA_{70}$, 99% PEO_{113}-$PDPA_{56}$. b) 3% $PMPC_{25}$-$PDPA_{70}$, 97% PEO_{113}-$PDPA_{56}$. c) 5% $PMPC_{25}$-$PDPA_{70}$, 95% PEO_{113}-$PDPA_{56}$. d) 10% $PMPC_{25}$-$PDPA_{70}$, 90% PEO_{113}-$PDPA_{56}$. e) 15% $PMPC_{25}$-$PDPA_{70}$, 85% PEO_{113}-$PDPA_{56}$. f) 25% $PMPC_{25}$-$PDPA_{70}$, 75% PEO_{113}-$PDPA_{56}$. Note: all formulations have 10% Rh-PEO_{113}-$PDPA_{56,}$ The scale bar represents 20 μm.

Cellular uptake (bEnd.3) of a series of binary PMPC/PEO polymersomes was further tested (Figure 5.6). The data showed that PMPC induces cellular uptake at a concentration as low as 3% w/w. For higher concentrations, cellular uptake becomes controlled by the polymersome topology as the PMPC and PEO blocks start to form clusters on the vesicle surface [3, 18].

5.3 Functionalised-polymersomes

5.3.1 Functionalised biotinylated-PMPC-PDPA

Biotin (Bt) also known as vitamin H or B7 is a water-soluble vitamin (Figure 5.6b). Biotin forms one of the strongest non-covalent bonds with protein streptavidin (StAv). This complex is often used for biological assays as well as to conjugate biomolecules to other biomolecules or synthetic materials [19]. We used this strategy here to decorate polymersomes with several ligands using an *ad hoc* synthesised biotinylated PMPC-PDPA.

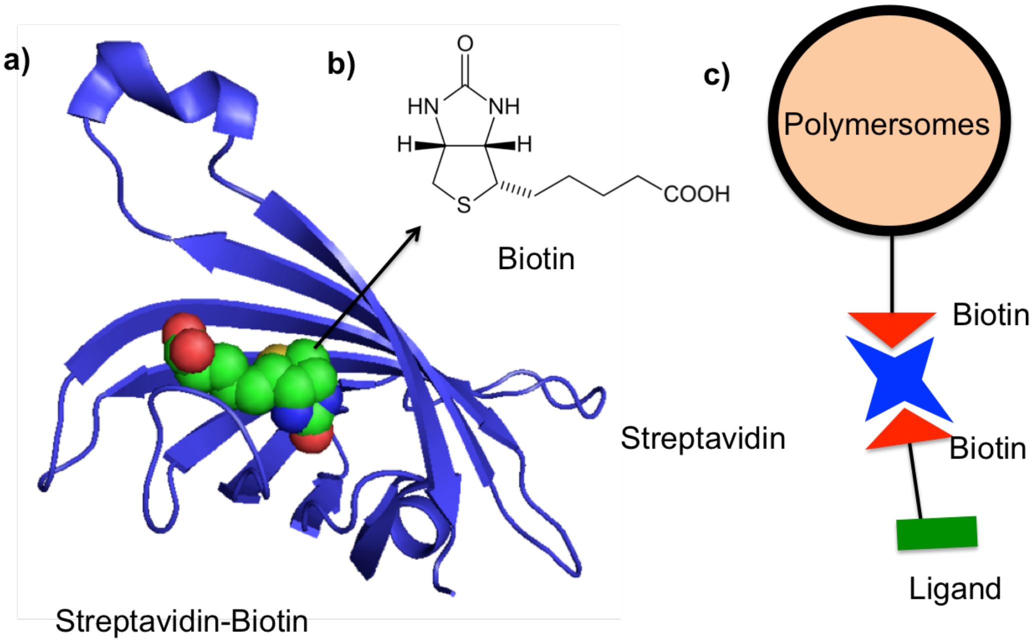

Figure 5.7 Schematic representation of polymersome-biotin-streptavidin-biotin-ligand system. a) Monomeric streptavidin with bound biotin. b) The chemical structure of biotin. c) Polymersomes functionalised by biotin-streptavidin system.

Biotinylated $PMPC_{25}$-$PDPA_{70}$ (Bt-PMPC-PDPA) was synthesised and mixed with PEO_{113}-$PDPA_{56}$ (10% Rh-PEO_{113}-$PDPA_{56}$) to form biotin (rhodamine)-labelled polymersomes (10 mg/ml). The Bt-polymersomes were firstly functionalised by adding 100 µg/ml StAv; after an approximately 2-hour coating the polymersomes were then purified by GPC column, followed by secondary functionalisation by incubating with biotinylated-RVG (Rabies Virus Glycoprotein) and/or botinylated-Angiopep-2. By comparing to the 'stealth' polymersomes (PEO_{113}-$PDPA_{56}$), the aim was to

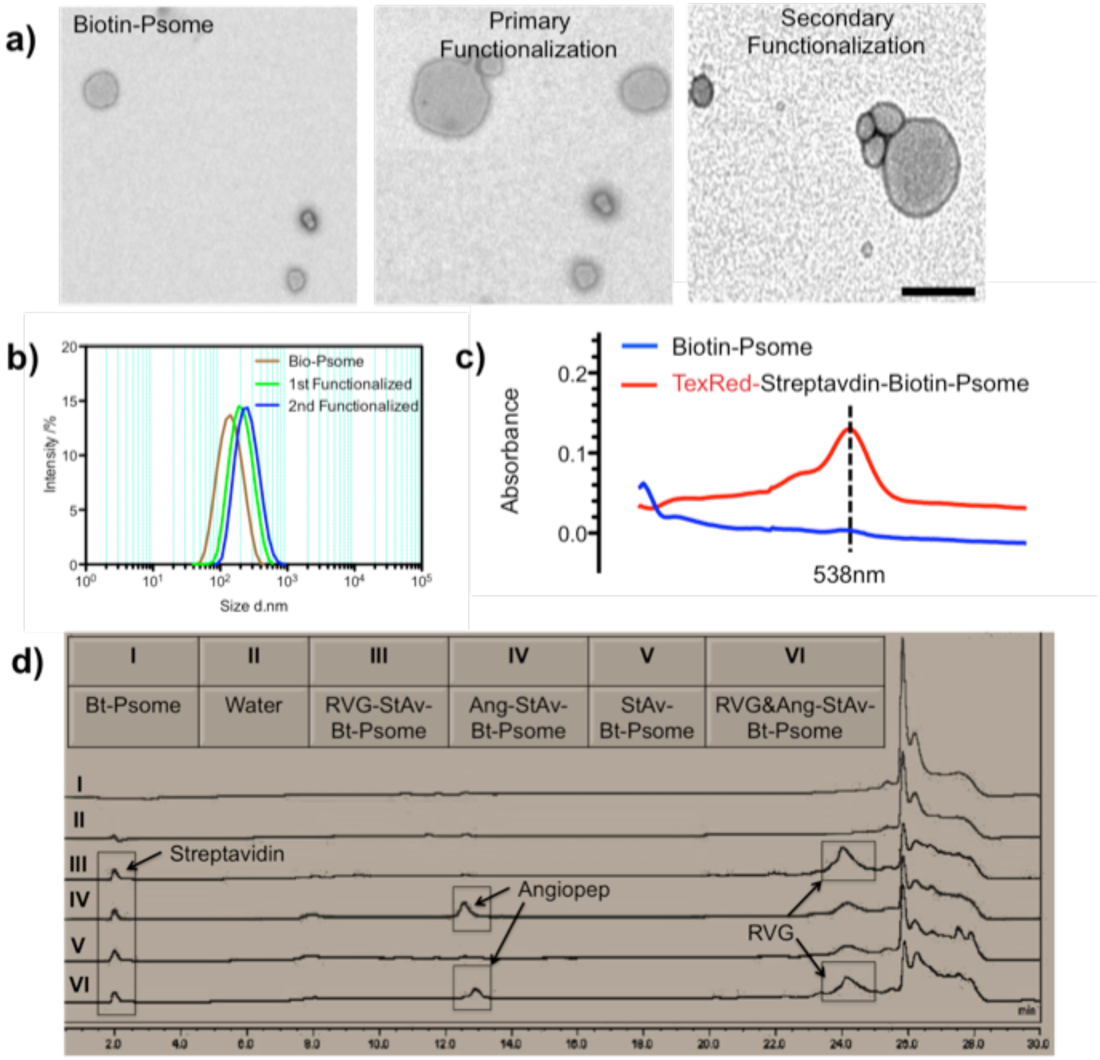

ZP_{Bt} = -1.119±0.27, $ZP_{Bt\text{-}Av}$ = -2.24±0.56

Figure 5.8 Characterisation of Bt-polymersomes and peptide functionalised-Bt-polymersomes. a) From left to right, TEM micrographs of Bt-polymersomes, StAv-Bt-polymersomes and biotinylated-peptide-StAv-Bt-polymersomes. b) Size distribution of Bt-polymersomes, StAv-Bt-polymersomes and biotinylated-peptide-StAv-Bt-polymersomes. c) UV spectrum of Bt-polymersomes and Tex-Red-conjugated StAv-Bt-polymersomes. d) HPLC graph of water (II), Bt-polymersomes (I), StAv-Bt-polymersomes (V), biotinylated-RVG-StAv-Bt-polymersomes (III), biotinylated-Angiopep-StAv-Bt-polymersomes (IV) and biotinylated-Angiopep and RVG-StAv-Bt-polymersomes (IV). The scale bar represents 200 nm.

find out if the surface functionalisation of BBB transcytosis ligand-based Bt-StAv-Bt-polymersomes could improve cellular uptake by brain endothelial cells (bEnd.3). (Some of these data were generated by Miss Burcin Ustbas, MSc Bionanotechnology under my supervision.)

The polymersome morphology was firstly confirmed by TEM, including Bt-polymersomes, StAv-Bt-polymersomes (primary functionalisation) and peptide-Bt-StAv-Bt-polymersomes (secondary functionalisation) (Figure 5.7a, from left to right). It is interesting to note in primary and secondary functionalisation that a few polymersome aggregates were observed; this is possibly due to the polymersome/polymersome interaction between two or more biotin-functionalised polymersomes. DLS measurements also revealed there was a slight increase in size after each functionalisation (Figure 5.7b); the peak in polymersome size shifted from approximately 100 nm-150 nm to approximately 150 nm-200 nm, however, such a size change may not significantly alter cellular uptake. In order to confirm that the added streptavidin was conjugated with Bt-polymersomes, the TexRed®-Streptavidin (TexRed®: λ_{Ex}=538-560) was applied and incubated with Bt-polymersomes and the UV spectrum of TexRed®-StAv-polymersomes (pH=2) was measured. Compared with Bt-polymersomes (pH=2), there was a clear peak of 538 nm in the TexRed®-StAv-Bt-polymersomes spectrum (Figure 5.7c); this proved the strong binding between streptavidin and biotinylated polymersomes. Further secondary functionalisation of biotinylated-RVG/biotinylated-Angiopep with StAv-Bt-polymersomes was fully confirmed by using HPLC (high-performance liquid chromatography), a chromatographic technique used to separate a mixture of compounds in order to identify and quantify the individual components of the mixture. As shown in Figure 5.7d, StAv-Bt-polymersomes (III, IV, V, VI) revealed a clear peak at approximately 2 minutes of elution time compared to the pristine formulation (formulation I) and water. StAv binding with the Bt-polymersomes was successful; the Angiopep peak (IV and VI) shows between 12 and 14 minutes and the RVG peak (III and VI) shows at 24 minutes.

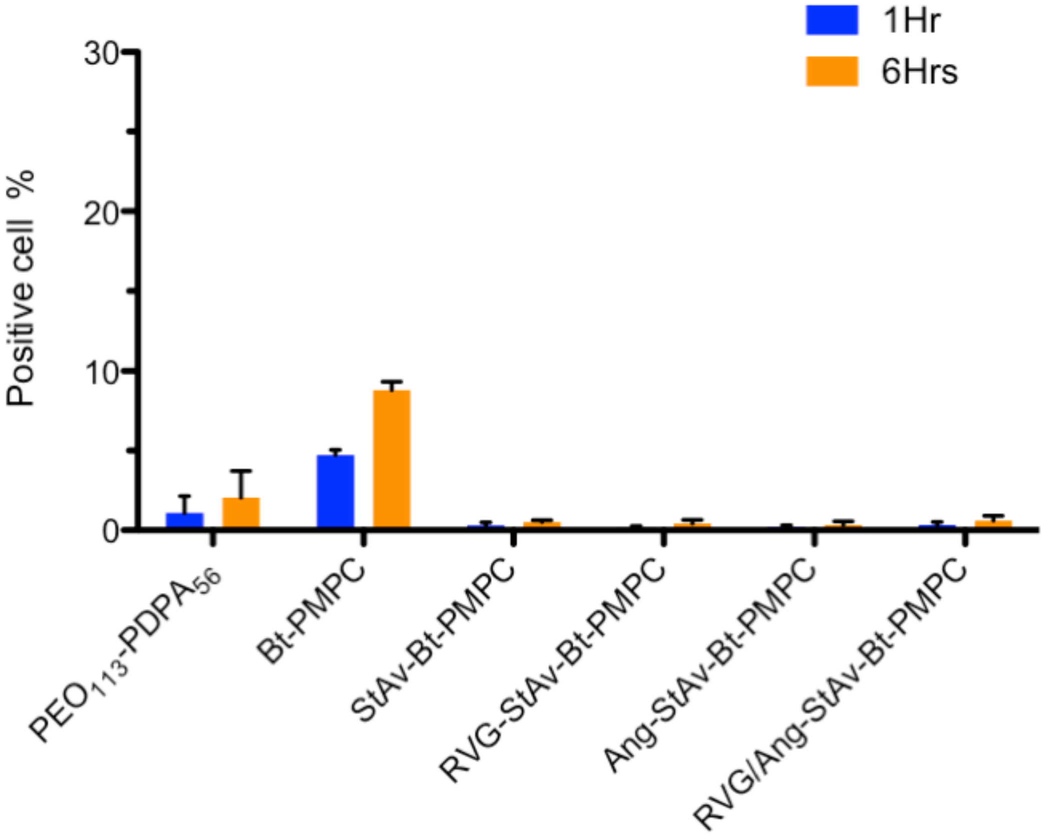

Figure 5.9 bEnd.3 cellular uptake of RVG and Angiopep-functionalised StAv-Bt-polymersomes. Note: all formulations contain 10% Rh-PEO_{113}-$PDPA_{56}$, 87% PEO_{113}-$PDPA_{56}$ and 3% Bt-PMPC-PDPA. RVG/Ang ratio = 2:1 in RVG/Ang-StAv-Bt-PMPC-PDPA polymersomes. ($n=3$, $p<0.005$)

To assess whether the functionalisation led to active cellular uptake, StAv-Bt-polymersomes and RVG/Angiopep-functionalised StAv-Bt-polymersomes were incubated with mouse brain endothelial cells (bEnd.3) for 1 hour and 6 hours. The data show that PEO-PDPA and Bt-PMPC-PDPA polymersomes were negative and positive controls respectively (Figure 5.9). It is not surprising that PEO_{113}-$PDPA_{56}$ revealed little positive cell interaction, as demonstrated in the previous section; Bt-PMPC-PDPA (3%) polymersomes significantly increase the positive cell percentage, indicating that the existing PMPC domain on the surface of polymersomes may play an important role in uptake by the endocytosis mechanism. However, in the functional group including the primary coated StAv-Bt-polymersomes and secondary peptide-coated StAv-Bt-polymersomes, the cellular internalisation almost vanished between 1 hour and 6 hours, indicating minimal cellular uptake of StAv-functionalised polymersomes. These data suggest that conjugated streptavidin acts as an 'inhibitor' of PMPC, and peptide-functionalised polymersome cellular uptake possibly interferes with its binding to their respective receptors. A single streptavidin tetrameric quaternary structure is approximately 4 nm [20], considering that 3% biotin-PMPC-PDPA might form a 3-6 nm nanoscopic domain in a 100-200 nm diameter polymersome [18]; it is very likely that the protein screens the interaction of PMPC with its receptors. Similarly, the large size of the protein can inhibit the binding of the relatively small peptide (either Angiopep-2 or RVG), consequently hindering polymersome uptake.

5.3.2 Functionalised PMPC-PDPA

Although Bt-PMPC-PDPA (3%) polymersomes showed positive cellular uptake in brain endothelial cells, streptavidin-functionalised Bt-polymersomes, StAv-Bt-polymersomes and further peptide (RVG and/or Angiopep)-functionalised Bt-StAv-Bt-polymersomes hardly show any cellular uptake. We discussed how such a consequence was possibly due to the overlapping of the streptavidin over the PMPC nano-domain and joint polymersome formation. Efforts were made to avoid bt/StAv complex using more chemical protocols. RVG and Angiopep-2 were directly conjugated with $PMPC_{25}$-$PDPA_{70}$ into RVG-$PMPC_{25}$-$PDPA_{70}$ and Angiopep-$PMPC_{25}$-$PDPA_{70}$ (the conjugate efficiency was approximately 40%), mixed with PEO_{113}-$PDPA_{56}$ (10% Rh-PEO_{113}-$PDPA_{56}$) to form peptide (rhodamine)-labelled polymersomes (10 mg/ml) by pH switch method. The polymersome preparation and purification processes were similar to those discussed above; the only difference was that the peptide-$PMPC_{25}$-$PDPA_{70}$ was added when the pH rose to 5.0-5.5 in order to avoid peptide degradation in strong acidic solution.

We first characterised the size distribution and morphology of these functionalised polymersomes, including Angiopep-polymersomes (3% Angiopep-PMPC-PDPA, 97% PEO-PDPA), RVG-polymersomes (3% RVG-PMPC-PDPA, 97% PEO-PDPA) and dual functionalised Angiopep/RVG-polymersomes (1% Angiopep-PMPC-PDPA, 2% RVG-PMPC-PDPA, 97% PEO-PDPA). As expected, dynamic light scattering showed that the size peak by intensity lay at 172.6 nm, 143.6 nm and 157 nm respectively, which is similar to the control pristine PMPC-PDPA (164 nm) and PEO-PDPA (169 nm) in the same experiment (Figure 5.9a).

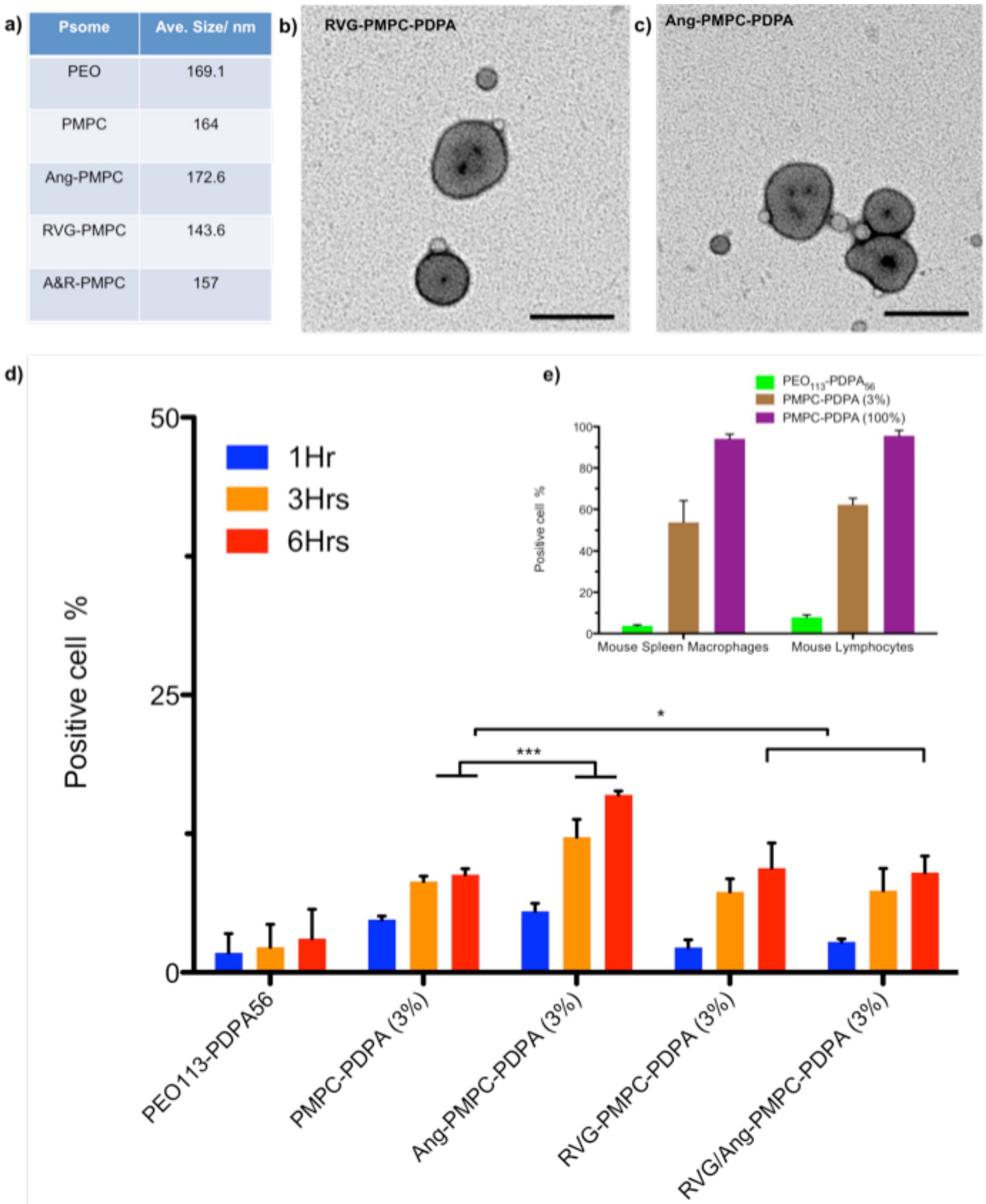

Psome	Ave. Size/ nm
PEO	169.1
PMPC	164
Ang-PMPC	172.6
RVG-PMPC	143.6
A&R-PMPC	157

ZP_{RVG} = -2.011±0.37, ZP_{Ang} = -1.978±0.25

Figure 5.10 Characterisation of peptide-PMPC-PDPA polymersomes and their cellular uptake. a) Table of average polymersome size from DLS measurements. Note: all formulations contain 10% Rh-PEO_{113}-$PDPA_{56}$, 87% PEO_{113}-$PDPA_{56}$ and 3% peptide-PMPC-PDPA. RVG/Ang ratio = 2:1 in RVG/Ang-PMPC-PDPA polymersomes. b) TEM micrograph of RVG-PMPC-PDPA polymersomes. c) TEM micrograph of Angiopep-PMPC-PDPA polymersomes. d) bEnd.3 cellular uptake of peptide-functionalised PMPC-PDPA polymersomes, with pure PEO-PDPA as the negative control. e) 3% PMPC-PDPA polymersomes (97% PEO-PDPA) cellular uptake by mouse immune system cells: macrophages and lymphocytes. Pure PEO-PDPA is the negative control and pure PMPC-PDPA is the positive control. The scale bar represents 200 nm. (Error bar SEM, n=6, $p<0.005$)

Their architectures were further confirmed by TEM; as indicated in Figures 5.10b and 5.10c, both RVG and Angiopep-functionalised polymersomes formed a vesicular structure. Brain endothelial cells (bEnd.3) were then used to test whether such a direct conjugation to PMPC-PDPA polymersomes could improve cellular uptake. As shown in Figure 5.10d, bEnd.3 cells were incubated with functionalised polymersomes for between 1 hour and 6 hours, while 100% PEO-PPDA and 3% PMPC-PDPA were used as negative and positive controls; the results were obtained by FACS flow cytometry. As observed before, PEO-PDPA polymersomes showed minimal cellular internalisation during the 6 hours. 3% PMPC-PDPA-labelled polymersomes increased the positive cell population due to the existence of the PMPC nano-domain. It is interesting to compare the 3% PMPC-PDPA group with the functionalised PMPC-PDPA group, particularly Ang-PMPC-PDPA polymersomes which showed a significant cellular internalisation increase from 3 to 6 hours, confirmed by a one-way ANOVA (one-way analysis variance, $p<0.005$). Statistical analysis suggested that the transcytosis ligand Angiopep-2 on the surface of the polymersomes improved cellular uptake by triggering specific endocytosis mechanisms. The RVG-PMPC-PDPA polymersomes and the dual functional RVG/Ang-PMPC-PDPA (ratio: 2:1) polymersomes showed a similarly increasing trend. However, such an increase was not significant until the 6-hour point. It is worth pointing out that although the RVG-functionalised carrier previously showed its ability to penetrate across the blood-brain barrier and target the brain [7, 21], interacting with AChR [21], no specific brain endothelial receptor was reported.

As our next aim is to apply polymersomes as a potential delivery system *in vivo*, interaction between polymersomes and immune system cells had to be evaluated. We employed as sentinel cells two different types of immune cell: spleen macrophages and lymphocytes. While the former act as cleaner for the bloodstream, removing all pathogens and any other particulate materials that trigger pathogen- and danger-associated molecular patterns (PAMP and DAMP) including nanoparticles, lymphocytes are a good model to evaluate any eventual blood-borne nonspecific interaction.

Hence, here, mouse spleen macrophages and mouse lymphocytes were used to examine their interaction with polymersomes, including PEO_{113}-$PDPA_{56}$ and $PMPC_{25}$-$PDPA_{70}$, 3%PMPC-PDPA (97% PEO-PDPA); formulation was also tested, due to all peptide-functionalised polymersomes possessing the same components. As shown in Figure 5.10e, the ‘stealth’ PEO-PDPA polymersomes exhibited minimal cellular internalisation in either macrophages or lymphocytes, indicating that the PEO coating was hardly recognised by the immune system cells. The immune recognition changed significantly when cells were incubated with 100% PMPC-PDPA polymersomes. Almost all of the cells (both macrophages and lymphocytes) indicated a positive reaction; the cell population internalising the polymersomes reached nearly 90% by 6 hours (Figure 5.10e). Both cell types over expressed PMPC-targeting SRB receptors. However, while the PMPC-PDPA ratio dropped to 3%, the immune recognition (positive cell percentage) did not decrease significantly, suggesting that the immune response was likely to be due to the existence of a PMPC chain of polymersomes, but this may not be a linear response due to the ratio of PMPC in the binary polymersomes. As all the peptide-functionalised polymersomes (peptide-PMPC-PDPA/PEO-PDPA) contain PMPC-PDPA, although cellular uptake by brain endothelial cells improved, their immune response (uptake) by the macrophages and lymphocytes could also be observed.

5.3.3 Functionalised POEGMA-PDPA

PEGylated nanoparticle delivery systems have been extensively used for delivering active peptides, proteins or genetic agents in the past decade [22-24]. The PEGylated delivery system has been constructed via different synthetic approaches in recent years; CRP (controlled radical polymerisation) techniques such as ATRP (atom transfer radical polymerisation), RAFT (reversible addition-fragmentation transfer polymerisation) and NMP (nitroxide-mediated polymerisation) have been more widely used as a straightforward alternative for preparing more accurate building blocks [25-27]. In particular, ATRP was considered a very versatile method for PEG-based amphiphilic block preparation, but the possibility of using PEGylation in such a method is still very limited [28]. A common method used in ATRP for incorporating PEG in macromolecular constructions is a macro-initiator approach, however, this method requires work at the interface between anionic polymerisation and CRP, hence it is not straightforward [29]; a commercially available α-methoxy-ω-hydroxy-PEG polymer can be used here [30, 31], but the disadvantage in this case is that the PEG molecular weight is highly limited by commercial sources. The other method is to directly polymerise poly oligo (ethylene glycol) methacrylate (POEGMA), a PEG macro-monomer; such an approach has been proved to be a more convenient alternative for incorporating PEG in macromolecular structures built by CRP [32, 33].

POEGMA-based amphiphilic copolymers have the capability to form polymersomes as well as PEO amphiphilic copolymers; as it is the PEO's analogue, POEGMA polymersomes may retain similar 'stealth' characteristics to PEO polymersomes. When comparing POEGMA with PEO, it is easier to synthesise and surface functionalise; moreover, so far there are very few studies based on POEGMA polymersomes for either intra-cellular or *in vivo* delivery.

Here, $P(EO_{10}GMA)_{20}$-$PDPA_{112}$ (POEGMA-PDPA) and rhodamine-labelled $P(EO_{10}GMA)_{20}$-$PDPA_{112}$) (Rh-POEGMA-PDPA) were synthesised and modified with Angiopep and RVG peptides. The peptide conjugation efficiency is approximately 40%, which is confirmed by HPLC, in order to form peptide-functionalised POEGMA-PDPA polymersomes (10% Rh-POEGMA-PDPA mixed). A series of polymersomes was made with different peptide (both Angiopep-2 and RVG) concentrations, with peptide mol/mol ratios of 0.4%, 1.2%, 2.0%, 2.8%, 3.6% and 5.4%. All the formulations (10 mg/ml) were prepared by pH switch method, and purification processes were similar, as discussed above. The peptide POEGMA-PDPA was added when the pH increased to 5.0-5.5, in order to avoid degradation of the peptides in strong acidic solution.

The physical properties of all formulations were fully characterised by both DLS and TEM (Figure 5.11). Size distribution by numbers measured by DLS indicated that POEGMA-PDPA diblock copolymers are able to form into particles of approximately 100 nm in diameter (Figure 5.11a1). Both

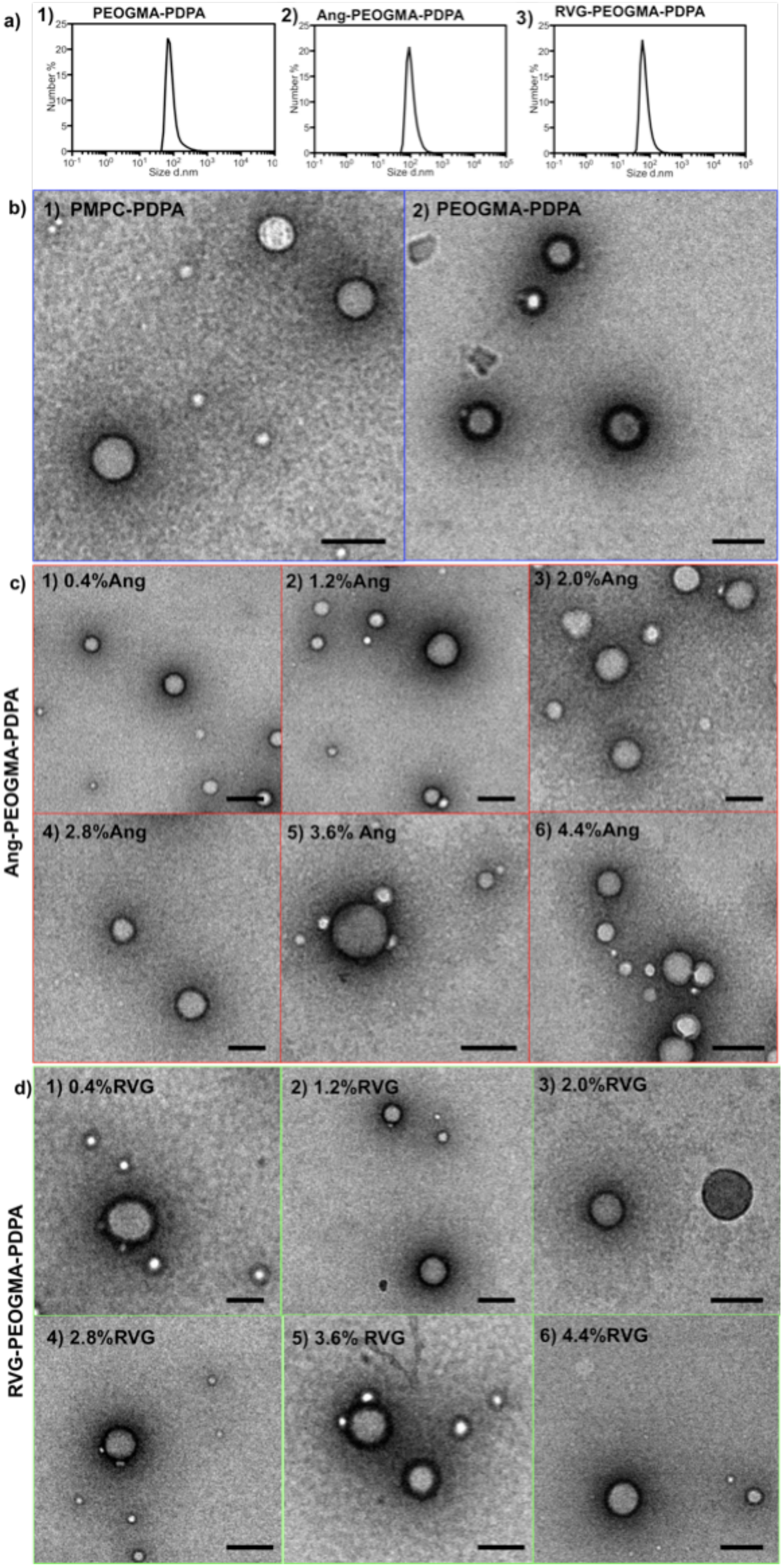
a)
1) PEOGMA-PDPA
2) Ang-PEOGMA-PDPA
3) RVG-PEOGMA-PDPA
Number %
Size d.nm
b)
1) PMPC-PDPA
2) PEOGMA-PDPA
c)
Ang-PEOGMA-PDPA
1) 0.4%Ang
2) 1.2%Ang
3) 2.0%Ang
4) 2.8%Ang
5) 3.6% Ang
6) 4.4%Ang
d)
RVG-PEOGMA-PDPA
1) 0.4%RVG
2) 1.2%RVG
3) 2.0%RVG
4) 2.8%RVG
5) 3.6% RVG
6) 4.4%RVG

ZP_{POEGMA} = -0.795±0.42, ZP_{RVG} = -2.013±0.69, ZP_{Ang} = -1.125±0.73

Figure 5.11 Characterisation of peptide-POEGMA-PDPA polymersomes a) Typical size distribution of POEGMA-PDPA polymersomes (a1), selected Ang-POEGMA-PDPA polymersome size distribution (a2) and RVG-POEGMA-PDPA polymersome size distribution (a3) measured by dynamic light scattering. Note: distribution is sorted by number. b) TEM characterisation of PMPC-PDPA (b1) and POEGMA-PDPA (b2) polymersomes in same experiment. c) TEM characterisation of Angiopep-functionalised POEGMA-PDPA polymersomes; Angiopep ratio is arranged at 0.4%(c1), 1.2%(c2), 2.0%(c3), 2.8%(c4), 3.6%(c5) and 5.4%(c6) respectively. d) TEM characterisation of RVG-functionalised POEGMA-PDPA polymersomes; RVG ratio is arranged at 0.4%(d1), 1.2%(d2), 2.0%(d3), 2.8%(d4), 3.6%(d5) and 5.4%(d6) respectively. The scale bar represents 200 nm.

Angiopep-2 and RVG surface-functionalised POEGMA-PDPA (Figures 5.11a2 and a3) could also form into around 100nm-diameter particles; compared with non-functionalised POEGMA-PDPA (Figure 5.11a1), there is no significant size increase or decrease, suggesting the size distribution remains stable after conjugation with both peptides. It is interesting to point out that the higher molecular weight of the PDPA block $P(EO_{10}GMA)_{20}$-$PDPA_{112}$ leads to thicker polymersome membranes of about 8 nm (Figure 5.11b), compared to $PMPC_{25}$-$PDPA_{70}$ polymersome membrane thickness which is about 5 nm (Figure 5.11a).

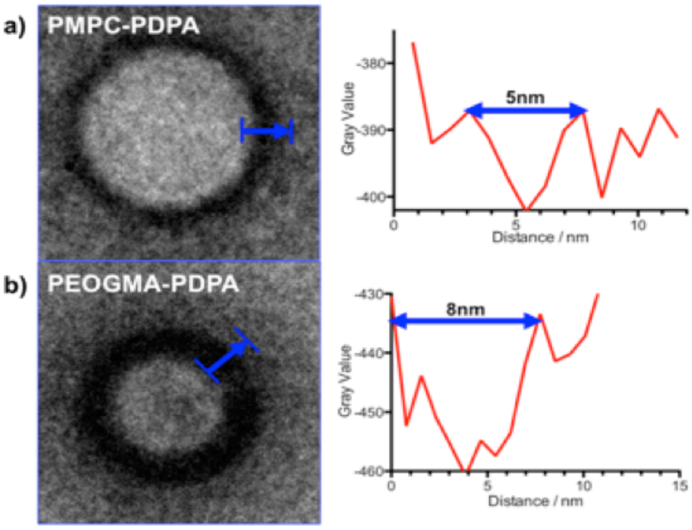

Figure 5.12 Measurements of membrane thickness of PMPC-PDPA and

POEGMA-PDPA polymersomes. a) A single PMPC-PDPA polymersome and distance measurement show its membrane thickness is around 5 nm. b) A single PMPC-PDPA polymersome and distance measurement show its membrane thickness is around 8 nm. (Image J64 performed analysis.)

As indicated in Figures 5.10c and 5.10d, both Angiopep-2 and RVG-functionalised POEGMA-PDPA diblock copolymers are capable of forming uniform polymersomes. While the ratio of peptides (both Angiopep and RVG) increased (Figures 5.10c1, c2, c3, c4, c5 and c6; Figures 5.10d1, d2, d3, d4, d5 and d6), there was no obvious change in morphology, suggesting successful formation of functionalised POEGMA-PDPA polymersomes with different peptide concentrations.

Low cellular toxicity of POEGMA-PDPA polymersomes was observed after a 24-hour incubation with brain endothelium bEnd.3 (Figure 5.13a). All of the formulations were subsequently evaluated for cellular uptake. These results were obtained by FACS flow cytometry; the experiments were triplicated and statistical analysis was performed by one-way ANOVA ($p<0.05$).

As shown in Figure 5.13c, non-functionalised POEGMA-PDPA and biotin-PMPC-PDPA were used as negative and positive controls respectively. Both peptide-functionalised polymersomes showed a typical bell-shaped uptake profile with respect to the peptide concentration, with optimal uptake peaking at around 1.2% in both cases. It is worth noting that this concentration of cellular uptake is either comparable to, or better than, that of PMPC-PDPA polymersomes.

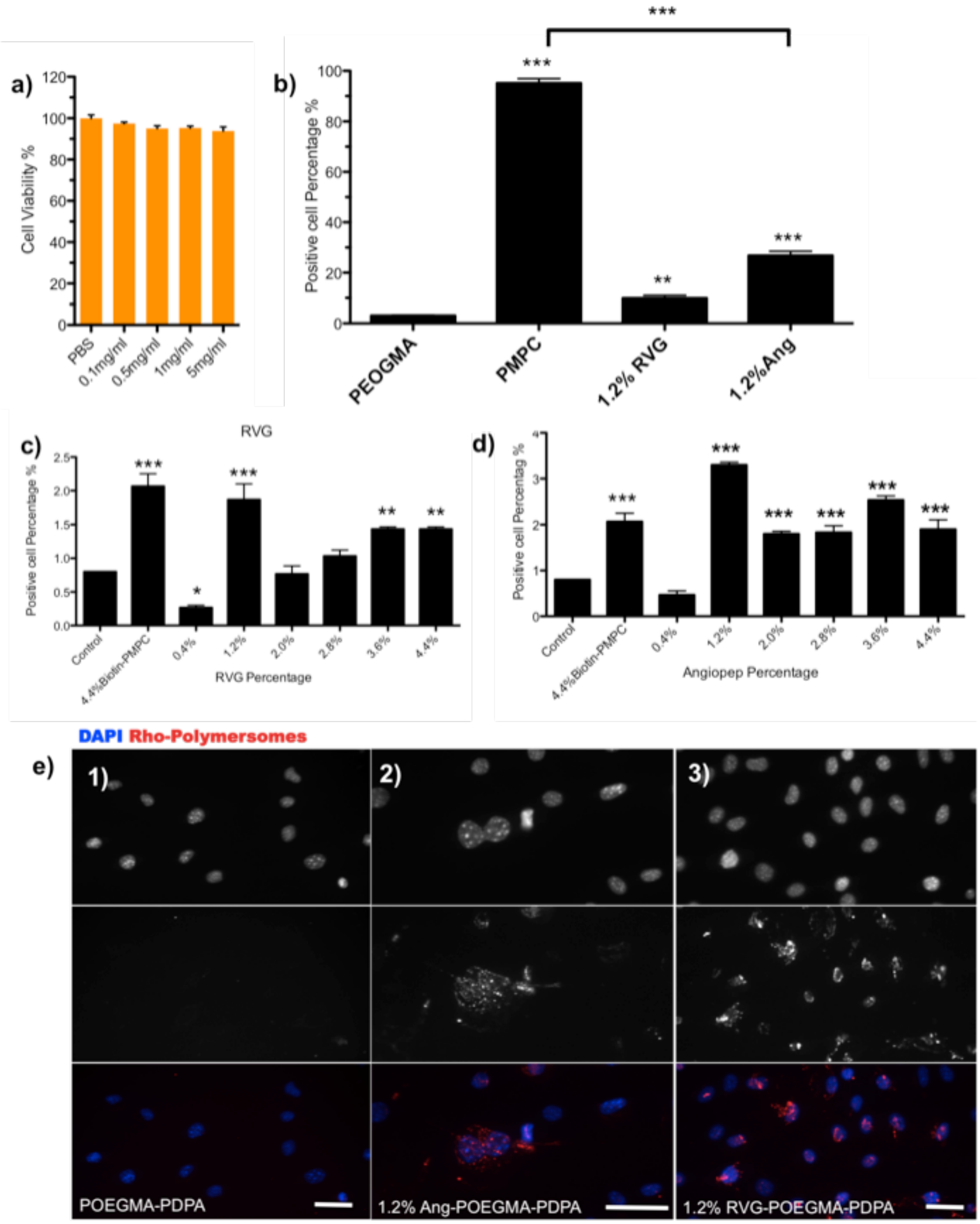

Figure 5.13 Cellular interaction of functionalised POEGMA-PDPA polymersomes on brain endothelium. a) MTT assay of POEGMA-PDPA polymersomes on bEnd.3 cells. b) 24-hour incubation of bEnd.3 cells with 1.2 % Ang-POEGMA-PDPA and 1.2% RVG-POEGMA-PDPA polymersomes. c) 3-hour incubation of bEnd.3 cells with Ang-POEGMA-PDPA polymersomes. (Angiopep ratio from 0.4%, 1.2%, 2.0%, 2.8%, 3.6% to 5.4% respectively.) d) 3-hour incubation of bEnd.3 cells with RVG-POEGMA-PDPA polymersomes. (RVG ratio from 0.4%, 1.2%, 2.0%, 2.8%, 3.6% to 5.4% respectively.) e) Confocal micrograph of 3-hour incubation of bEnd. cells with POEGMA-PDPA polymersomes and functionalised POEGMA-PDPA polymersomes. e1, POEGMA-PDPA; e2, 1.2% ang-POEGMA-PDPA; e3, 1.2% RVG-POEGMA-PDPA. The scale bar represents 20 μm. (Error bar is SEM, n=3, $p<0.05$).

As the Angiopep-2 ratio rose to 5.4% (2.0%, 2.8%, 3.6%), there was a slight decrease, however, compared with 1.2% Ang-POEGMA-PDPA polymersomes, such a decrease is not statistically significant. 24-hour incubation experiments (Figure 5.13b) further demonstrated that the two POEGMA-PDPA formulations functionalised with 1.2% RVG and 1.2% Angiopep-2 clearly increased cellular uptake over non-functionalised POEGMA-PDPA polymersomes; in addition, Figure 5.13b shows that the 1.2% Angiopep-2 formulation gave more efficient cellular uptake than the 1.2% RVG formulation over the 24-hour period. Confocal laser microscopy images (Figure 5.13e) also demonstrated uptake of POEGMA polymersomes by brain endothelial cells over 3 hours, while no obvious fluorescence could be detected in the cells cultured with pristine POEGMA-PDPA polymersomes; 1.2% Angiopep and 1.2% RVG-functionalised. POEGMA-PDPA polymersomes clearly interacted with the cells and were mostly located within the cellular cytosol.

These cellular uptake results strongly suggest that within an *in vitro* 2D (two-dimensional plate cell culture) culture environment, functionalised POEGMA-PDPA polymersomes possess the capability to significantly increase brain endothelial cell uptake.

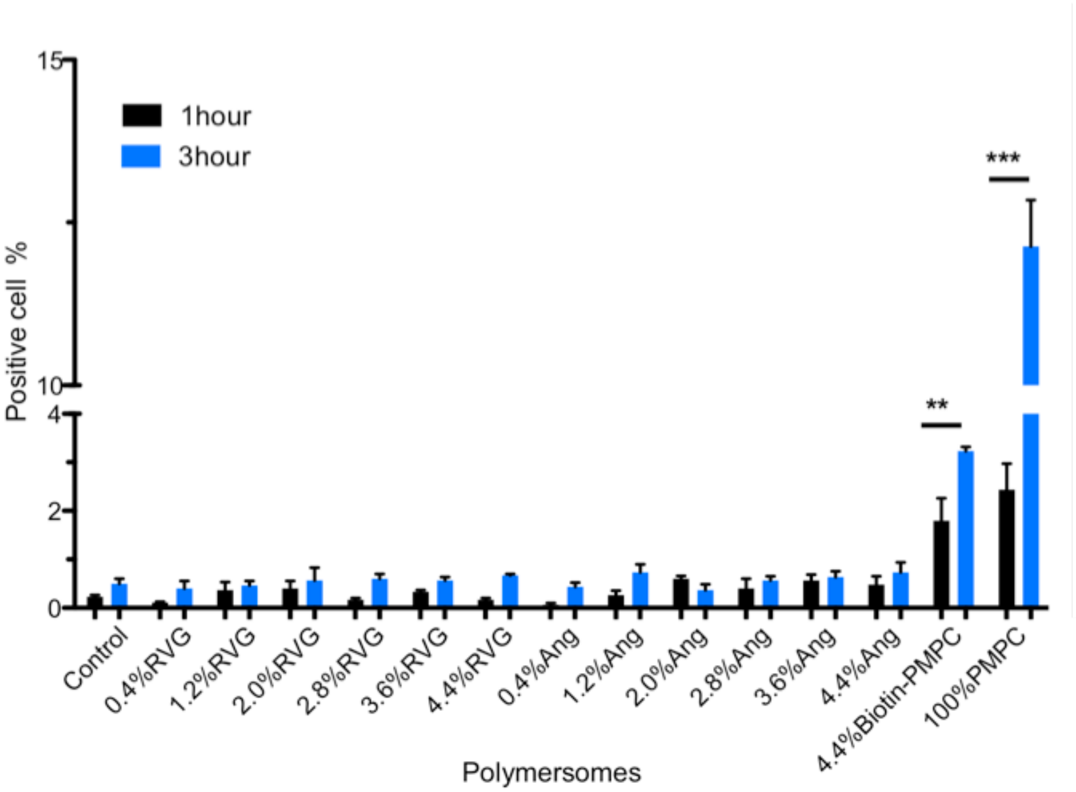

Figure 5.14 Cellular interaction of functionalised POEGMA-PDPA polymersomes with mouse lymphocytes. 1-hour and 3-hour incubation of all functionalised polymersomes with the immune system cells: mouse lymphocytes. (n=3, $p<0.005$)

We then tested cellular internalisation of functionalised POEGMA-PDPA polymersomes by the immune system cells, as described above. Previous experiments in the last section indicated that PMPC-PDPA-based functionalised polymersomes interact strongly with immune system cells, (Figure 5.10e). As shown in Figure 5.14, the PEO analogue POEGMA-based polymersomes POEGMA-PDPA exhibited very little cellular internalisation by mouse lymphocytes, suggesting that POEGMA-PDPA polymersomes have similar ‘stealth’ characteristics to PEO-PDPA polymersomes. All peptide-functionalised (Angiopep: 0.4%, 1.2%, 2.0%, 2.8%, 3.6% to 5.4%, RVG: 0.4%, 1.2%, 2.0%, 2.8%, 3.6% to 5.4%) POEGMA-PDPA polymersomes were also tested on mouse lymphocytes for between 1 hour and 3 hours. Again, as shown in Figure 5.14, neither Angiopep- nor RVG-functionalised polymersomes showed significant cellular uptake; all the immune recognition towards functionalised formulations remained at an extremely low level (positive cell percentage < 1%), not statistically significant compared to the 1-hour and 3-hour groups. It is interesting to note that between such peptide ratio ranges (0.4%-5.4%), the immune response did not follow the peptide increase trend; instead it exhibited a relatively stable response. By contrast, in the biotin-PMPC-PDPA (5.4% Bt-PMPC-PDPA, 95.6 % POEGMA-PDPA) and pure PMPC-PDPA experiment, the immune system cells showed clear recognition, as uptake increased sharply in both the 1-hour and 3-hour experiments.

Finally, POEGMA-PDPA diblock copolymer and peptide-functionalised (Angiopep and RVG) POEGMA-PDPA diblock copolymers were able to form uniform polymersomes (100-150nm). Both Angiopep-2 and RVG-functionalised POEGMA-PDPA significantly improved brain endothelial cell uptake in both short and long incubation periods: in the bEnd.3 cellular uptake screening experiment, the two functionalised polymersomes, 1.2% Ang-POEGMA-PDPA and 1.2% RVG-POEGMA-PDPA, were found to be the most efficient formulations. More importantly, while these functionalised polymersomes showed enhanced brain endothelial uptake, they did not interact with the immune cells. These characteristics of functionalised POEGMA-PDPA polymersomes give the possibility of further investigations using the *in vitro* BBB model and *in vivo* tests.

The ability of functionalised POEGMA-PDPA polymersomes to encapsulate cargo was further examined. Here, 6nm gold nanoparticles (GNP, rabbit polyclonal secondary antibody to goat IgG-H&L, ab39610) were used. The gold nanoparticles (100µg/ml) were encapsulated within both PMPC-PDPA polymersomes (GNP-PMPC-PDPA, 10 mg/ml) and Angiopep-functionalised POEGMA-PDPA polymersomes (GNP-Ang-POEGMA-PDPA, 10 mg/ml) by pH switch method. As shown in Figure 5.15a, the 6 nm GNP exhibit a clear

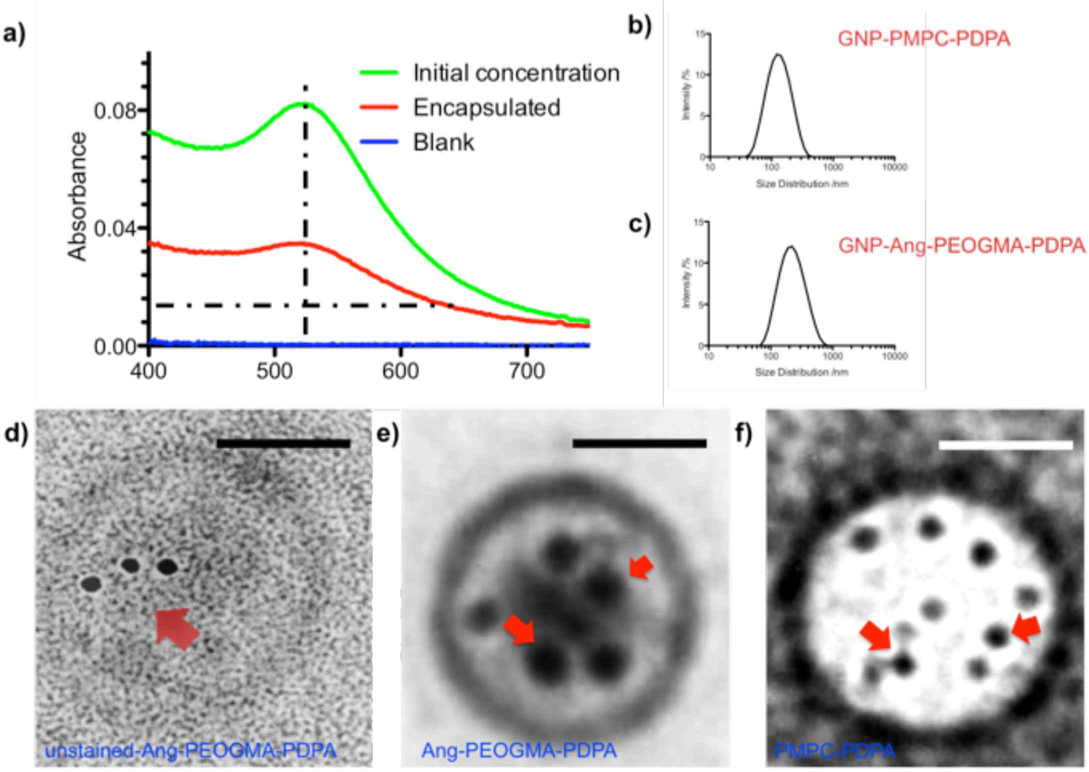

Figure 5.15 Characterisation of IgG-Gold encapsulated polymersomes. a) The UV spectrum of IgG-gold before and after encapsulation by polymersomes, with non-encapsulated polymersomes used as a control (measured pH=2). b) Size distribution by intensity of gold nanoparticle (GNP)-encapsulated PMPC-PDPA polymersomes. c) Size distribution by intensity of gold nanoparticle (GNP)-encapsulated POEGMA-PDPA polymersomes. d) TEM micrograph of gold nanoparticle (GNP)-encapsulated Ang-POEGMA-PDPA polymersomes without TPA staining. e) TEM micrograph of gold nanoparticle (GNP)-encapsulated Ang-POEGMA-PDPA polymersomes with TPA staining. f) TEM micrograph of gold nanoparticle (GNP)-encapsulated PMPC-PDPA polymersomes with TPA staining. The scale bar represents 100 nm.

absorbance peak at around 530 nm at the initial concentration (100 µg/ml, pH=2); after polymersome formation, free GNPs were purified by passing through a GPC column. GNP-encapsulated polymersomes (pH=2) clearly showed an absorbance peak located at the same position (around 530nm), which indicated successful GNP encapsulation (encapsulation efficiency approximately 20%) within the polymersomes. Both GNP-PMPC-PDPA and GNP-Ang-POEGMA-PDPA showed that the major size distribution was around 100-200 nm (Figures 5.15b and 5.15c), suggesting the size of polymersomes remained stable while encapsulating such cargo. Polymersome morphology and encapsulated GNPs were further confirmed by transmission electron microscopy. To avoid confusion between GNP and TPA staining, unstained GNP-Ang-POEGMA-PDPA was firstly examined (as shown in Figure 5.15d); a few GNPs were clearly observed, suggesting they are encapsulated within a single polymeric vesicle. A TPA-stained polymersome sample gave much greater detail of GNP-encapsulated polymersomes; as indicated by the red arrow in Figures 5.15e and 5.15f, both Angiopep-functionalised POEGMA-PDPA and PMPC-PDPA were capable of encapsulating multiple GNPs within a single polymersome.

Following the successful encapsulation of GNPs within both PMPC-PDPA and Ang-POEGMA-PDPA polymersomes, we then further tested the cellular uptake of these GNP polymersomes on brain endothelial cells, in order to understand how the cargo was sorted when polymersomes were internalised by the cells in 2D. GNP-PMPC-PDPA and GNP-Ang-POEGMA-PDPA polymersomes were added to bEnd.3 cells in a T75 flask at a concentration of 1 mg/ml; the cells were collected after 3 hours and 24 hours.

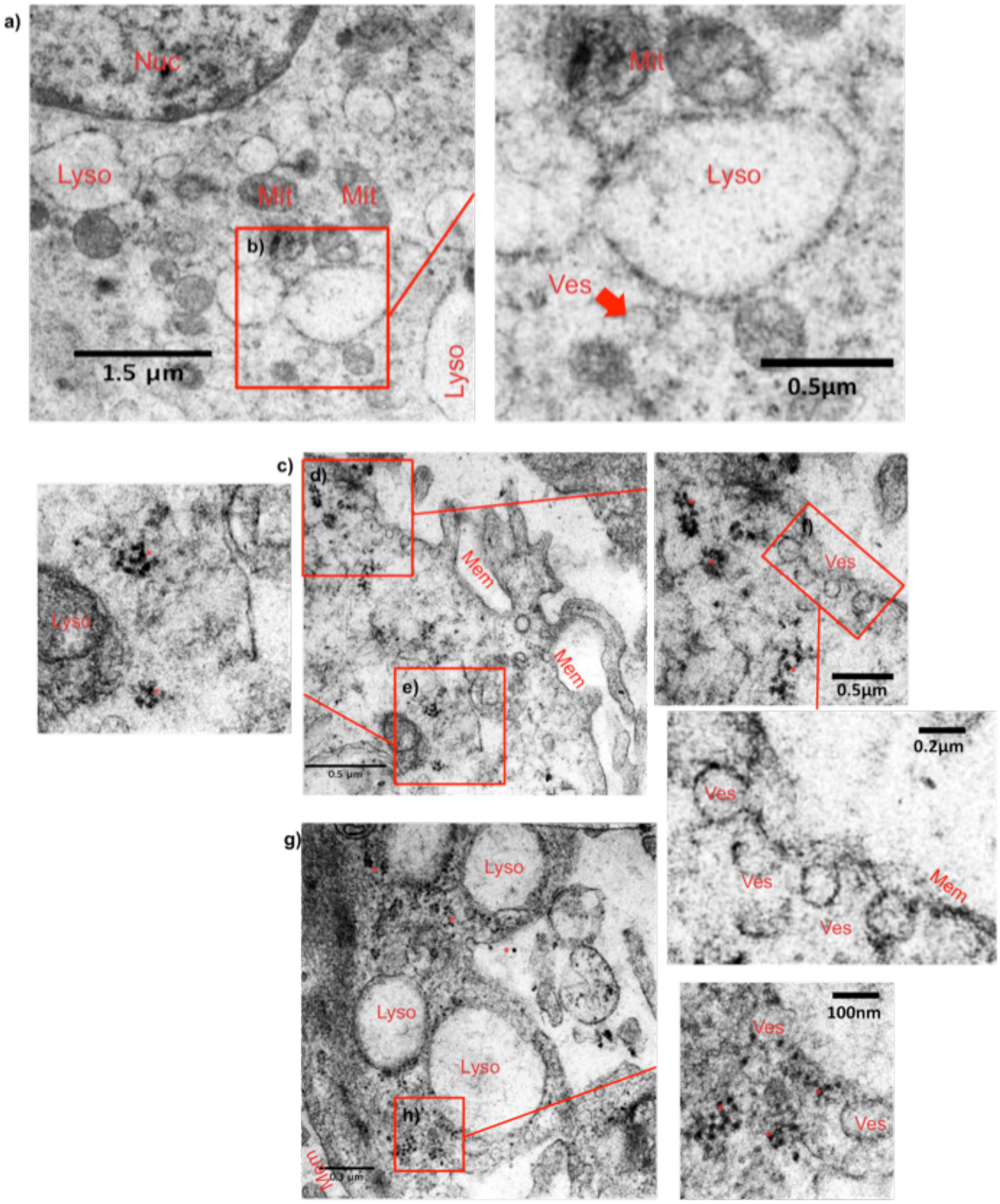

Figure 5.16 TEM ultra-thin section examination of bEnd.3 cells incubated with GNP-PMPC-PDPA polymersomes for 3 hours and 24 hours. a) Non-treated bEnd.3 cells. b) Higher magnification of the indicated region of bEnd.3 cells from a). c) bEnd.3 cells treated with GNP-PMPC-PDPA for 3 hours. d) & e) Higher magnification of the indicated regions from c) demonstrated vesicular membrane structure and location of GNP. f) Higher magnification of the indicated regions from d) show greater detail of membrane vesicular structure. g) bEnd.3 cells treated with GNP-PMPC-PDPA for 24 hours. h) Higher magnification of the indicated regions from g) show released GNP from endosome Nuc: nuclear, Lyso: lysosome, Mit: mitochondria, Mem: plasma membrane, Ves: vesicles. Note: '*' indicates the location of GNP.

Details of preparation of TEM cell ultra-thin sections are found in the experimental section (refer to Chapter 4). In Figure 5.16a a non-treated bEnd.3 cell is shown; a higher-magnification TEM micrograph revealed more sub-cellular details, including mitochondria, lysosomes and other trafficking vesicles (Figure 5.16b). After being treated with GNP-PMPC-PDPA for 3 hours, GNPs were clearly located within the cellular cytosol (Figures 5.16c and 5.16e). It is interesting to focus on the edge of the cell membrane area; a higher magnification image from Figure 5.16c (Figure 5.16d) showed vesicular structures at the surface of the membranes (Figure 5.16f), also showed dozens of GNPs, suggesting that the GNP-PMPC-PDPA might be taken up by bEnd.3 in a very active endocytosis mechanism within a membrane vesicular structure. Such a hypothesis has already been supported by previous temperature control and inhibitor studies in our group [3]. After uptake by an endocytotic pathway, polymersomes then migrate to the early endosome; as the local pH value drops from neutral to a mildly acidic, PDPA chains of the polymersomes turn from hydrophobic to hydrophilic. As a consequence, GNPs encapsulated within the PMPC-PDPA will be released as the polymersomes disassemble; and this, in turn, triggers an increase in osmotic pressure and consequent endosome lysis. GNPs are so delivered from endosomes into the cellular cytosol. The appearance of cytosolic GNPs in this study (Figures 5.16g and 5.16h) is consistent with this sequence. These results, together with previous flow cytometry and microscopy studies, suggest that in a 2D-culture environment PMPC-PDPA polymersomes are able to strongly internalise within brain endothelial cells (bEnd.3) via a very active endocytosis pathway, and more importantly their cargo (GNPs) can be efficiently delivered and localised within the cellular cytosol.

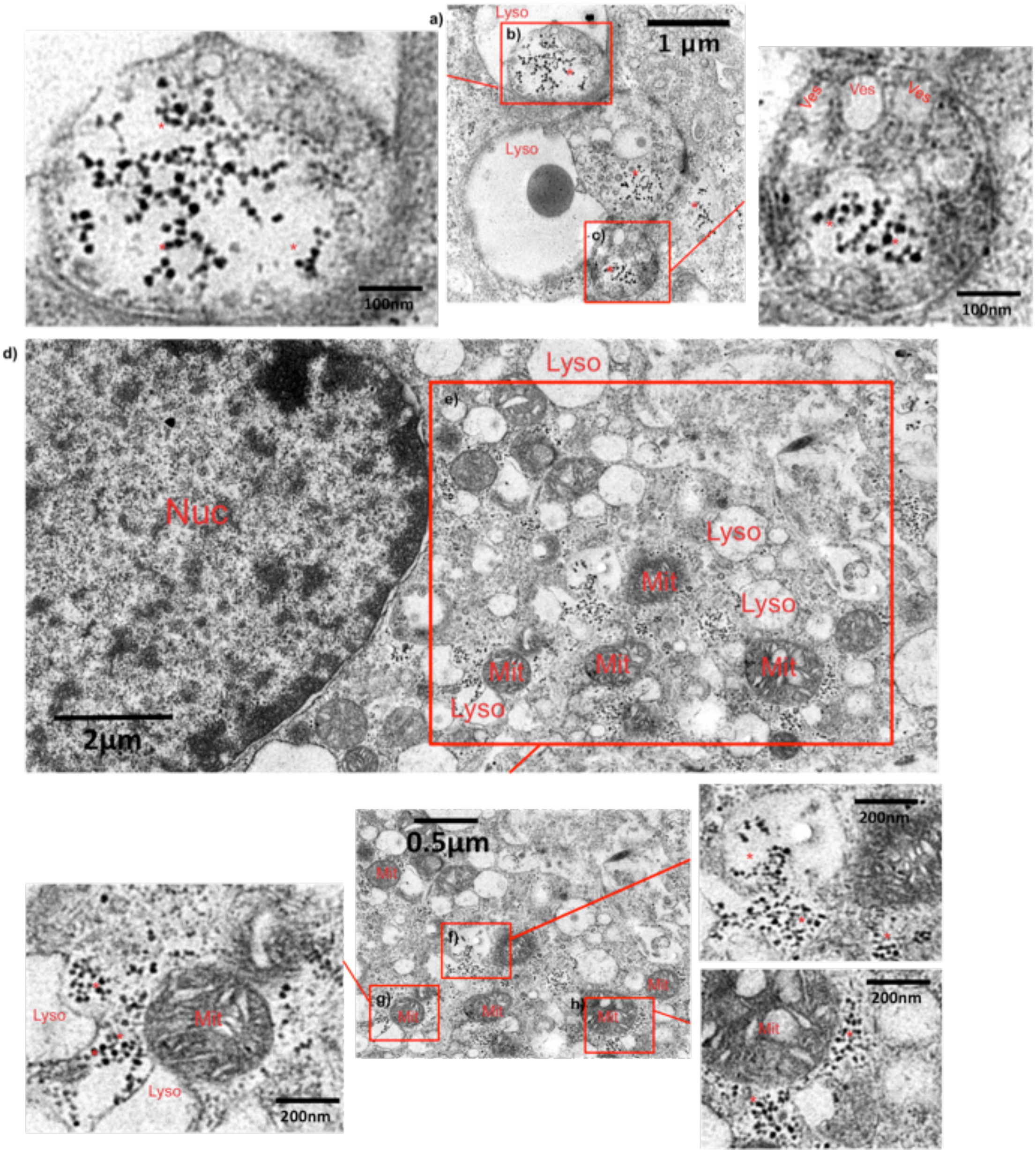

Figure 5.17 TEM ultra-thin section examination of bEnd.3 cells incubated with GNP-Ang-POEGMA-PDPA polymersomes for 3 hours and 24 hours. a) bEnd.3 cells treated with GNP-Ang-POEGMA-PDPA for 3 hours. b) & c) Higher magnification of the indicated regions from f) show GNP accumulated within a membrane bounded structure. d) bEnd.3 cells treated with GNP-Ang-POEGMA-PDPA for 24 hours. e) Higher magnification of the indicated regions from d). f), g) & h) Higher magnification of the indicated regions from e) show greater detail of GNP location up to 24 hours. Nuc: nuclear, Lyso: lysosome, Mit: mitochondria, Ves: vesicles. Note: ‘*’ indicates the location of GNPs.

An experiment involving incubation of bEnd.3 cells with GNP-loaded Ang-POEGMA-PDPA polymersomes (1.2% angiopep) was also performed for between 3 hours and 24 hours (Figure 5.17). Some very interesting phenomena were observed at an early point in the experiment. As shown in Figure 5.17a, GNPs are clearly taken up into the cellular cytosol and accumulate in the multi-vesicular body. The number of GNPs observed is approximately 30 to 100; considering that a single polymersome vesicle may encapsulate 5-10 GNPs, this indicates the delivery of at least 5 to 10 polymersomes in a single multi-vesicular body. Two higher-magnification micrographs (Figures 5.17b and 5.17c) magnified from Figure 5.17a give much more detail of such a GNP aggregation in the multi-vascular body. All the GNPs seem to be wrapped up within luminal vesicles; the size of such a multi-vesicular body is approximately 0.8-1.2 micrometres and a single vesicular structure around 50-100 nm in diameter can also be seen in the multi-vesicular body (Figure 5.17b). As suggested by a flow cytometry cellular uptake study and fluorescence micrograph, Angiopep-2-functionalised POEGMA-PDPA polymersomes (1.2% angiopep ratio) can clearly improve brain endothelial cellular uptake over non-functionalised POEGMA-PDPA polymersomes. The comparison between PMPC and Angiopep-POEGMA polymersomes using TEM shows some differences in cellular trafficking, indicating different entry mechanisms.

Compared to receptor-mediated endocytosis, the actual mechanism of transcytosis and most importantly how the cargo is sorted and whether there is any endosome/lysosome involvement still remain unknown. Our data on Angiopep-2 polymersomes show that delivered GNPs accumulate within the multi-vesicular body at an early time point (Figures 5.17a, 5.17b and 5.17c). This may suggest the existence of the transcytosis ‘sorting compartment’.

Transcytosis across the blood-brain barrier takes place extensively in polarised endothelial cells of brain micro-vessels, generally from the apical to the basal side; this process is accomplished in a three-dimensional (3D) environment. However, transcytosis cannot be fully completed in a two-dimensional (2D) cell culture situation, as much less clear apical to basal polarity exists in the tissue culture flask. As a consequence, GNPs encapsulated within the Ang-POEGMA-PDPA are delivered into the brain endothelial cells via receptor-mediated endocytosis, eventually ending up within the cellular cytosol (Figures 5.17d and 5.17e) after a 24-hour incubation. It is interesting to note that in the higher-magnification images (Figures 5.17f, 5.17g and 5.17h) from the indicated regions in Figure 5.17e, the majority of GNPs were located near the cellular mitochondria, consistent with the fact that endocytosis/transcytosis of a substance at the blood-brain barrier is an energy-expensive and ATP-dependent transport process. Indeed, previous studies showed that the density of cellular mitochondria in brain endothelial cells is approximately five times higher than in peripheral endothelium [34]; this has been attributed to the requirement of energy/ATP for solute transporters and vesicular transport. The TEM ultra-thin cell section studies give some information at a sub-cellular level of the way peptide-functionalised POEGMA-PDPA polymersomes are internalized and trafficked by brain endothelial cells

5.4 Conclusions

To date, the following polymersomes formed by PDPA-based diblock copolymers have been fully characterised and screened against mouse brain endothelial cells/mouse immune system cells: $PMPC_{25}$-$PDPA_{70}$, PEO_{22}-$PDPA_{17}$, PEO_{45}-$PDPA_{22}$, PEO_{113}-$PDPA_{56}$, $PMPC_{25}$-$PDPA_{70}$/PEO_{113}-$PDPA_{56}$ binary polymersomes (molar ratio: 1/99, 3/97, 5/95, 10/90, 15/85, 25/75), Bt-$PMPC_{25}$-$PDPA_{70}$, StAv-Bt-$PMPC_{25}$-$PDPA_{70}$, RVG-StAv-Bt-$PMPC_{25}$-$PDPA_{70}$, Ang-StAv-Bt-$PMPC_{25}$-$PDPA_{70}$, RVG-$PMPC_{25}$-$PDPA_{70}$, Angiopep-$PMPC_{25}$-$PDPA_{70}$, $P(EO_{10}GMA)_{20}$-$PDPA_{112,}$ RVG-$P(EO_{10}GMA)_{20}$-$PDPA_{112}$(RVG molar ratio: 0.4%, 1.2%, 2.0%, 2.8%, 3.6% and 5.4%) and Angiopep-$P(EO_{10}GMA)_{20}$-$PDPA_{112}$(RVG molar ratio: 0.4%, 1.2%, 2.0%, 2.8%, 3.6% and 5.4%), primary cargo (IgG-GNP). Cellular delivery has also been investigated based on GNP-$PMPC_{25}$-$PDPA_{70}$ and GNP-Angiopep-$P(EO_{10}GMA)_{20}$-$PDPA_{112}$. The dynamic light-scattering measurement indicated the size distribution of all formulations ranges from 80-250 nm, with the majority of the population at 150-200 nm; transmission electron microscopy tests suggested that by a simple purification process through a GPC (gel permeation chromatography) column, vesicular-structure polymersomes can eventually be obtained. Moreover, different membrane thicknesses ($PMPC_{25}$-$PDPA_{70}$ and $P(EO_{10}GMA)_{20}$-$PDPA_{112}$) can also be controlled by their diblock molecular weight. More accurately controlling the final polymersome size into a specific range (50-80 nm, 80-100 nm, 100-120 nm and 150-200 nm) and their cellular uptake properties have been fully studied in our group (Robertson et al. in preparation).

It is essential to mention the electrical stability of the polymersome system. The electrical stability of polymersomes, generally characterised by Zeta

Potential (ZP) and measured by dynamic light scattering, is one of the most important features to determine circulation time *in vivo*. The value of ZP can be related to stability in blood, as discussed in Chapter 2; a higher-charged carrier can strongly interact with blood cellular components, such as platelets, RBC (red blood cells) and PBMC (peripheral blood mononuclear cells). In the polymersome system, Zeta Potential is used to quantify the membrane surface charge of the polymersome bilayer; as shown in Table 5.1, all the polymersome formulations' ZP values have been characterised at room temperature. PMPC-PDPA, biotin-PMPC-PDPA and PEO-PDPA at 0.990mv -1.119mv and -0.691mv ZP values respectively – indicate the neutral property of PMPC and PEO formulations. On conjugating streptavidin, RVG and Angiopep with PMPC-PDPA, the ZP slightly increased, but this will not change the circulation time significantly *in vivo*. Similarly, POEGMA-PDPA when functionalised (RVG and Angiopep) also showed minimal surface charge, giving the possibility of further exploration of their applications *in vivo*.

In addition, after a cellular toxicology study, uptake of all polymersome formulations by brain endothelial cells (bEnd.3) was examined. A kinetic cellular uptake study showed that $PMPC_{25}$-$PDPA_{70}$ polymersomes strongly interacted with bEnd.3 cells in the first 3 hours by a very active endocytosis pathway (Figure 5.3); this was also suggested by a parallel GNP-PMPC-PDPA study (Figure 5.16). PEO-based PEO_{22}-$PDPA_{17}$, PEO_{45}-$PDPA_{22}$ and PEO_{113}-$PDPA_{56}$ showed much less cellular uptake over 24 hours. In particular, the long chain formulation PEO_{113}-$PDPA_{56}$ revealed the best 'stealth' characteristics over PEO_{22}-$PDPA_{17}$ and PEO_{45}-$PDPA_{22}$ (Figure 5.5); this is mainly due to PEO_{113}-$PDPA_{56}$ polymersomes having a much higher PEO molecular weight. Binary $PMPC_{25}$-$PDPA_{70}$ /PEO_{113}-$PDPA_{56}$ polymersomes showed similar cellular uptake to pure $PMPC_{25}$-$PDPA_{70}$ polymersomes, although the kinetics may be different for the $PMPC_{25}$-$PDPA_{70}$ /PEO_{113}-$PDPA_{56}$, suggesting that with such binary formulations, the PMPC surface domain response modulates cellular internalisation, and there is no significant difference between PMPC ratio of 5% and 25%.

The PMPC-PDPA polymersome-based biotin-streptavidin system showed that cellular uptake was considerably hindered, with almost no positive cells observed (Figure 5.9); these results are likely due to the large molecular size of streptavidin and its steric hindrance of both the functional PMPC and RVG/Angiopep-2 domains. Advanced formulations that use RVG and Angiopep directly conjugated with PMPC-PDPA demonstrated improved cellular uptake over the same time period compared to non-functionalised formulations (Figure 5.10). This improvement suggests endocytosis/ transcytosis receptor ligand (either RVG or Angiopep)-functionalised polymersomes could enhance brain endothelial recognition, hence increasing cellular uptake. However, such functionalised polymersomes based on PMPC-PDPA polymersomes showed greater clearance by immune system cells; the immune clearance is basically due to the existence of the PMPC domain and enhances immune cell recognition, compared with pure PEO-PDPA polymersomes which hardly showed any cellular response in the same experimental conditions (Figure 5.10).

As a consequence, POEGMA, a PEO analogue, was applied due to its easier manufacture and functionalisation characteristics. RVG and Angiopep-2 were directly conjugated to POEGMA to form RVG-POEGMA-PDPA and Ang-

POEGMA-PDPA polymersomes. These functionalised POEGMA-PDPA polymersomes showed significantly increased cellular uptake, particularly at a peptide concentration of 1.2% mol/mol (Figure 5.13). More importantly, POEGMA-PDPA polymersomes and their functionalised formulations demonstrated minimal immune response (Figure 5.14), suggesting these formulations may be subject to less clearance within blood circulation compared with any other polymersome. GNPs delivered by functionalised (1.2% Angiopep) POEGMA-PDPA polymersomes showed different sub-cellular localisation compared to GNPs delivered by PMPC-PDPA (Figures 5.16 and 5.17), and suggest that early stages of transcytosis (in this case by LRP-1 mediated transcytosis) may follow a different route to early endocytosis. Further studies in our lab on the 3D cultures using antibodies against Rab5 (early endosome), Rab7 (late endosome), Rab11 (recycling endosome), and LAMP1 (lysosome) may help clarify the possible route. As a result, further *in vitro* and *in vivo* studies will be based on the functionalised POEGMA-PDPA polymersomes.

Screening studies have provided a view of several physical and biological features of polymersomes based on different chemistries, including size distribution, architecture, topology, cellular localisation, cellular uptake kinetics and immune response. They show that it is possible to control cellular internalisation and cargo destinations by manipulating surface chemistry and specific ligands. *In vitro* models and *in vivo* studies will rely on such screening results to further investigate and understand the potential ability of functionalised polymersomes to enter the CNS through the blood-brain barrier by targeting transcytosis.

References:

1. Little, D. et al., Polymersome mediated gene therapy for spinal muscular atrophy. *Human Gene Therapy*, 2011. **22**(10): A83-A84.
2. Lomas, H. et al., Biomimetic pH sensitive polymersomes for efficient DNA encapsulation and delivery. *Advanced Materials*, 2007. **19**(23): 4238.
3. Massignani, M. et al., Controlling cellular uptake by surface chemistry, size, and surface topology at the nanoscale. *Small*, 2009. **5**(21): 2424-2432.
4. Tian, X. H. et al., Live cell luminescence imaging as a function of delivery mechanism. *Chembiochem*, 2011. **12**(4): 548-551.
5. Wang, L. G. et al., Encapsulation of biomacromolecules within polymersomes by electroporation. *Angewandte Chemie – International Edition*, 2012. **51**(44): 11122-11125.
6. Schwarz, A. K. et al., Hepatoma cell density promotes claudin-1 and scavenger receptor BI expression and hepatitis C virus internalisation. *Journal of Virology*, 2009. **83**(23): 12407-12414.
7. Kumar, P. et al., Transvascular delivery of small interfering RNA to the central nervous system. *Nature*, 2007. **448**(7149): 39-43.
8. Shao, K. et al., Angiopep-2 modified PE-PEG based polymeric micelles for amphotericin B delivery targeted to the brain. *Journal of Controlled Release*, 2010. **147**(1): 118-126.
9. Du, J. Z. et al., pH-sensitive vesicles based on a biocompatible zwitterionic diblock copolymer. *Journal of the American Chemical Society*, 2005. **127**(51): 17982-17983.
10. LoPresti, C. et al., Polymersomes: nature inspired nanometer sized compartments. *Journal of Materials Chemistry*, 2009. **19**(22): 3576-3590.
11. Blanazs, A. et al., Mechanistic insights for block copolymer morphologies: how do worms form vesicles? *Journal of the American Chemical Society*, 2011. **133**(41): 16581-16587.
12. Fernyhough, C., Ryan, A. J. and Battaglia, G., pH controlled assembly of a polybutadiene-poly(methacrylic acid) copolymer in water: packing considerations and kinetic limitations. *Soft Matter*, 2009. **5**(8): 1674-1682.
13. Pearson, R. T. et al., Effect of pH and Temperature on PMPC-PDPA Copolymer Self-Assembly. *Macromolecules*, 2013. **46**(4): 1400-1407.

14. Canton, I. and Battaglia, G., Endocytosis at the nanoscale. *Chemical Society Reviews*, 2012. **41**(7): 2718-2739.

15. Matyjaszewski, K. and Xia, J., Atom transfer radical polymerisation. *Chemical Reviews*, 2001. **101**(9): 2921-2990.

16. Vonarbourg, A. et al., Parameters influencing the stealthiness of colloidal drug delivery systems. *Biomaterials*, 2006. **27**(24): 4356-4373.

17. Photos, P. J. et al., Polymer vesicles in vivo: correlations with PEG molecular weight. *Journal of Controlled Release*, 2003. **90**(3): 323-334.

18. LoPresti, C. et al., Controlling Polymersome Surface Topology at the Nanoscale by Membrane Confined Polymer/Polymer Phase Separation. *Acs Nano*, 2011. **5**(3): 1775-1784.

19. Livnah, O. et al., *3-Dimensional Structures of Avidin and the Avidin-Biotin Complex.* Proceedings of the National Academy of Sciences of the United States of America, 1993. **90**(11): 5076-5080.

20. Li, H. Y. et al., DNA-templated self-assembly of protein and nanoparticle linear arrays. *Journal of the American Chemical Society*, 2004. **126**(2): 418-419.

21. Lafon, M., Rabies virus receptors. *Journal of Neurovirology*, 2005. **11**(1): 82-87.

22. Greenwald, R. B. et al., Effective drug delivery by PEGylated drug conjugates. *Advanced Drug Delivery Reviews*, 2003. **55**(2): 217-250.

23. Jiang, X. et al., PEG-b-PPA/DNA micelles improve transgene expression in rat liver through intrabiliary infusion. *Journal of Controlled Release*, 2007. **122**(3): 297-304.

24. Kakizawa, Y. and Kataoka, K., Block copolymer micelles for delivery of gene and related compounds. *Advanced Drug Delivery Reviews*, 2002. **54**(2): 203-222.

25. Godwin, A. et al., Narrow molecular weight distribution precursors for polymer-drug conjugates. *Angewandte Chemie – International Edition*, 2001. **40**(3): 594-597.

26. Tang, Y. Q. et al., Solubilisation and controlled release of a hydrophobic drug using novel micelle-forming ABC triblock copolymers. *Biomacromolecules*, 2003. **4**(6): 1636-1645.

27. Tao, L. et al., Alpha-aldehyde terminally functional methacrylic polymers from living radical polymerisation: Application in protein conjugation "pegylation". *Journal of the American Chemical Society*, 2004. **126**(41): 13220-13221.

28. Lutz, J. F. and Hoth, A., Preparation of ideal PEG analogues with a tunable thermosensitivity by controlled radical copolymerisation of 2-(2-methoxyethoxy)ethyl

methacrylate and oligo(ethylene glycol) methacrylate. *Macromolecules*, 2006. **39**(2): 893-896.

29. Dufresne, M. H., Gauthier, M. A. and Leroux, J. C., Thiol-functionalized polymeric micelles: From molecular recognition to improved mucoadhesion. *Bioconjugate Chemistry*, 2005. **16**(4):1027-1033.

30. Perrier, S. and Haddleton, D. M., Initiating efficiency of poly(ethylene glycol)-based initiators for transition metal mediated living radical polymerisation. *European Polymer Journal*, 2004. **40**(10): 2277-2286.

31. Lee, S. B., Russell, A. J. and Matyjaszewski, K., ATRP synthesis of amphiphilic random, gradient, and block copolymers of 2-(dimethylamino)ethyl methacrylate and n-butyl methacrylate in aqueous media. *Biomacromolecules*, 2003. **4**(5): 1386-1393.

32. Wang, X. S. et al., Facile synthesis of well-defined water-soluble polymers via atom transfer radical polymerisation in aqueous media at ambient temperature. *Chemical Communications*, 1999(18): 1817-1818.

33. Wang, X. S. and Armes, S. P. Facile atom transfer radical polymerisation of methoxy-capped oligo(ethylene glycol) methacrylate in aqueous media at ambient temperature. *Macromolecules*, 2000. **33**(18): 6640-6647.

34. Oldendorf, W. H., Cornford M. E., Brown, W. J., The large apparent work capability of the blood-brain barrier: a study of the mitochondrial content of capillary endothelial cells in brain and other tissues of the rat. *Ann. Neurol.*, 1977. **1**: 409-417.

Chapter 6

Polymersomes 3D Screening

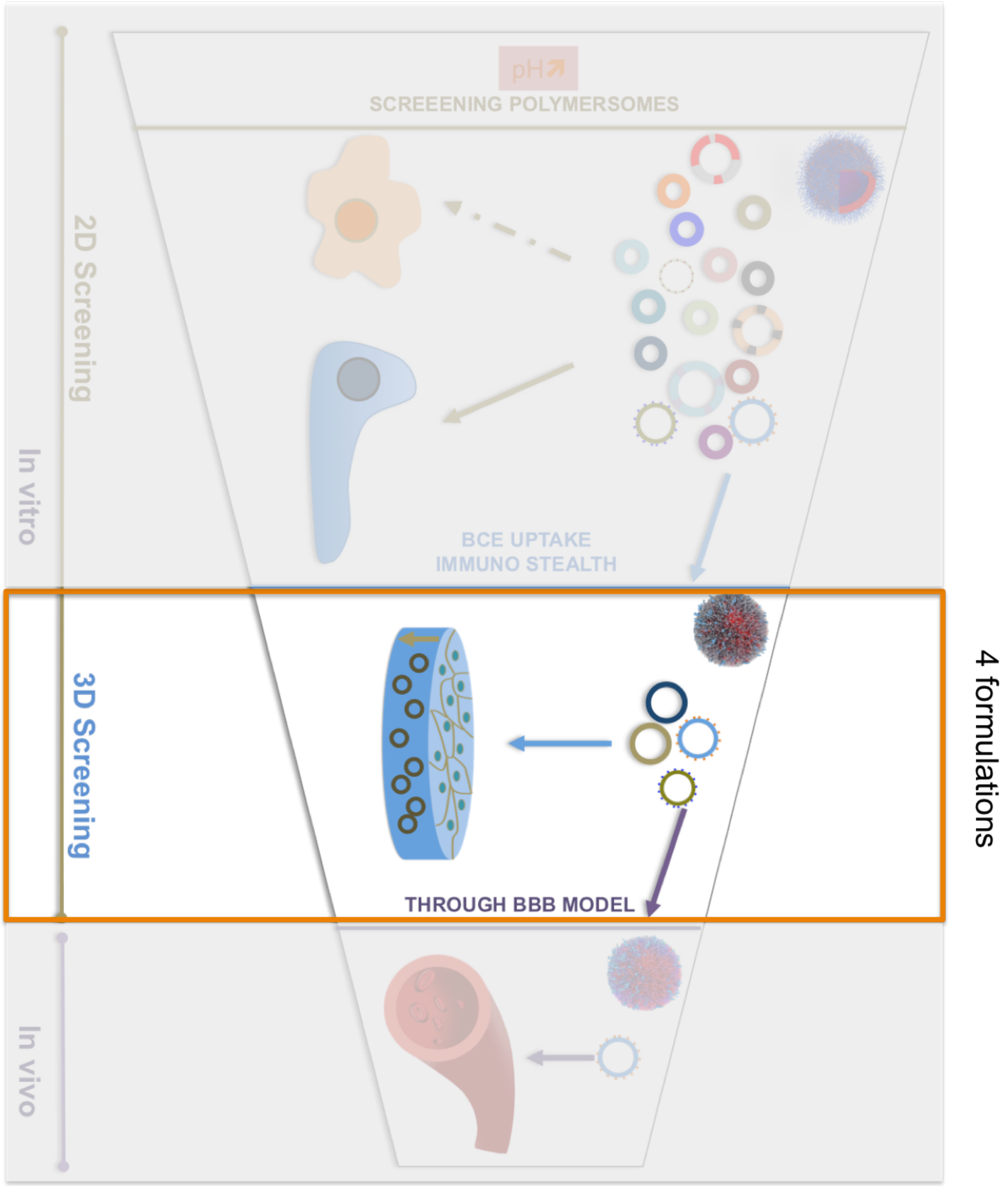

Schematic representation of screening polymersomes on 3D

6.1 Set up of a blood-brain barrier model

6.1.1 What constitutes a “good” BBB model?

The brain of a living animal is a complicated organ and could give more valuable and accurate information on how the blood-brain barrier actually works than any model system. However, for several reasons in the past decades scientists tried to establish a cultured BBB *in vitro* model to understand its properties. Firstly, the number of experimental animals should be limited to a reasonable level for ethical reasons. Secondly, by simplifying a BBB setting, requirements are easier to reach and conditions are much more convenient to standardise. Finally, from previous extensive studies, *in vitro* BBB models based on isolated brain capillary endothelial cells (BCEC) have been shown to retain basic BBB properties and provide worthwhile results to help understand the basic BBB properties.

A good (though less than ideal) *in vitro* model of the blood-brain barrier should perform most functions as in living animals. Firstly, adjacent endothelial cells should be polarised and express (or partly express) tight junction proteins. This leads to good barrier properties typically measured by trans-endothelial electrical resistance (TEER). Secondly, endothelial cell monolayers should express (or partly express) efflux transporters, uptake transporters such as amino acid transporters and Glut1 glucose transporter, and should also be capable of transporting macromolecules via adsorptive-mediated transcytosis and receptor-mediated transcytosis. Furthermore, a good BBB cell model should be able to associate with co-cultured cells, such as astrocytes, pericytes and neurons, with each of them being able to reproduce some of the unique features of the *in vivo* brain capillary endothelium. In addition, several recent studies suggested that flow across the apical surface of the vascular endothelium in a BBB *in vitro* model can significantly increase the TEER value [1], as well as leading to an increased expression of caveolae, G proteins and ion channels [2].

To establish a good BBB cell model, the most important factor is to choose the right substrate. Compared to traditional 2D cell cultures, the BBB model needs to possess a more 3D aspect typically achieved by using a porous substrate that enables the passage of nutrients, signalling molecules and other components necessary to achieve effective endothelial cell polarisation [3, 4]. Micro-porous filters made with various materials and coatings are commercially available (Table 6.1) [5], with pore sizes ranging from 0.1 μm to 12 μm. The choice of pore size is relevant to cell migration: larger pores (normally over 1μm) allow cells or fine processes to migrate or grow through the filter and grow on the other side of the porous surface [6, 7]. However, in the case of brain endothelial cells, especially when transcytosis and other active transport mechanisms need to be studied, pore sizes less than 1μm are more suitable to ensure effective permeability control. Larger pore sizes could lead to unexpected transport of substance from the pore instead of from the surface of cells, generating complexity in cargo permeability analysis.

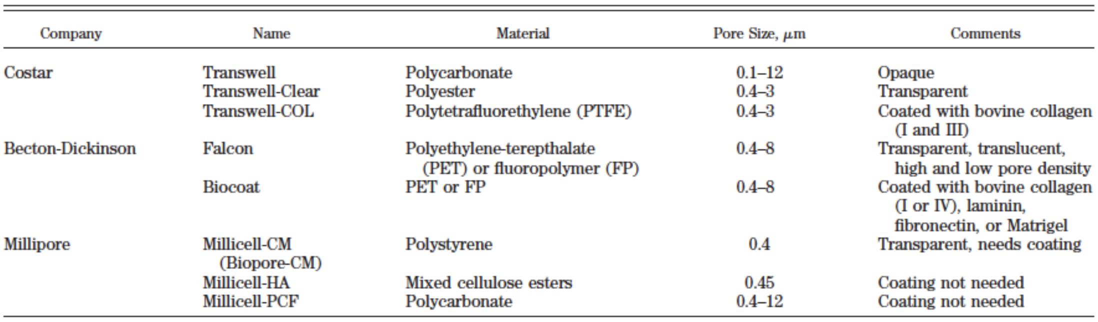

Company	Name	Material	Pore Size, μm	Comments
Costar	Transwell	Polycarbonate	0.1–12	Opaque
	Transwell-Clear	Polyester	0.4–3	Transparent
	Transwell-COL	Polytetrafluorethylene (PTFE)	0.4–3	Coated with bovine collagen (I and III)
Becton-Dickinson	Falcon	Polyethylene-terepthalate (PET) or fluoropolymer (FP)	0.4–8	Transparent, translucent, high and low pore density
	Biocoat	PET or FP	0.4–8	Coated with bovine collagen (I or IV), laminin, fibronectin, or Matrigel
Millipore	Millicell-CM (Biopore-CM)	Polystyrene	0.4	Transparent, needs coating
	Millicell-HA	Mixed cellulose esters	0.45	Coating not needed
	Millicell-PCF	Polycarbonate	0.4–12	Coating not needed

Table 6.1 Commercially available filters. Microporous filters based on different chemistries and coatings. The pore size ranges from 0.1μm to 12μm, suitable for a variety of experimental conditions. The pore density of the 0.4μm polycarbonate membrane is 1×10^8 pores /cm^2.

To quantify the integrity of the endothelial monolayer or co-cultured dual-layer/multi-layer, "classic" trans-epithelial (or endothelial) electrical resistance (TEER) measurements are commonly used. The value of TEER gives an indication of tight junction integrity in a BBB cell *in vitro* model. As mentioned in Chapter 1, regardless of whether under flow or whether a co-culture system is used , the difference between *in vivo* and *in vitro* TEER is significant (from a few hundred to a few thousand Ohms*cm^2), indicating that even the most optimal models are still relatively leaky compared to the *in vivo* blood-brain barrier. It is worth pointing out that such a "classic" TEER measurement is far from ideal, as the measurement is affected by the external temperature, medium used, contact angle and electrode life-time. Normally, it is important to complement TEER measurements with light microscopic inspection, measuring the expression of tight junction proteins, and assessing paracellular permeation of a small inert solute such as sucrose or mannitol.

6.1.2 Set up of the blood-brain barrier model

Based on 2D screening studies, the aim of establishing a BBB cell model in this project is to further understand the transcytosis behaviour of peptide-functionalised polymersomes in a 3D environment, in order to identify the most effective formulation.

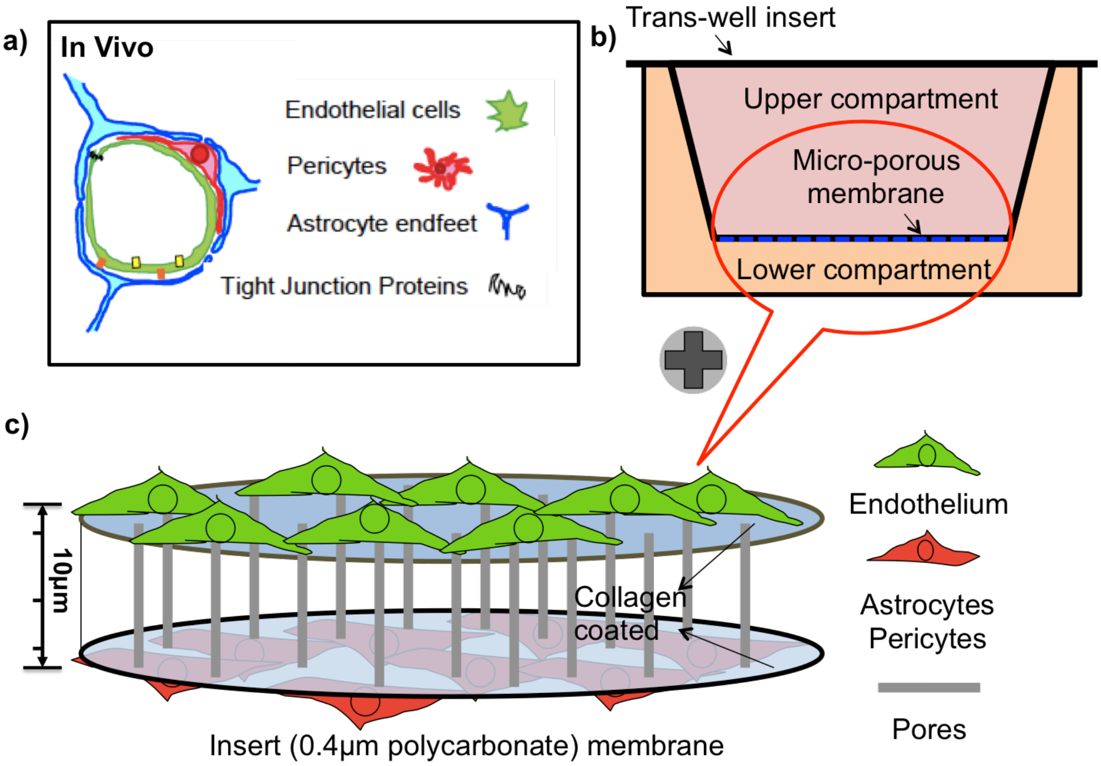

Figure 6.1 Schematic representation of 3D BBB cell model setup. a) Cell associations at the blood-brain barrier [8]. b) Schematic representation of a transwell setup consisting of a transwell filter insert separating the well into an upper and lower compartment. c) Schematic representation of cells grown on the two sides of the transwell insert membrane coated with rat-tail collagen.

To avoid un-wanted cell migration, a 0.4 µm filter Transwell insert (initial Cat. Number: Corning®3401, Polycarbonate membrane, clear, no pre-coating, 12-well transwell plate) [Note: this thesis work was done with Costar polycarbonate Clear (transparent) filters Cat No. 3401. This has since been discontinued, with current No. 3401 being polycarbonate translucent. A possible replacement for the original 3401 is Cat No. 3460, PE filters, transparent.] was chosen; such a filter allows brain endothelial cells to form a monolayer and to polarise. As polymersomes and functionalised polymersomes are around 100-250 nm, a transwell with 0.4 µm pore size (Figure 6.2a) is ideal to study whether and how the polymersomes penetrate the endothelial monolayer via transcytosis from the upper compartment to lower compartment (Figure 6.1b). In the *in vivo* BBB, the capillary endothelium is closely associated with astrocytes and pericytes (Figure 6.1a) that, in turn, control many functions of the BBB endothelium making it different from endothelia in other parts of the body. We therefore added both pericytes and astrocytes to our model to mimic more closely the BBB *in vivo* (Figure 6.1c).

To achieve a confluent brain endothelium monolayer, 10,000 cells/well were seeded at day one in the transwell insert and the medium was changed every three days. After a minimum of seven days' incubation, the bEnd.3 cells formed a confluent and dense monolayer (Figure 6.2b).

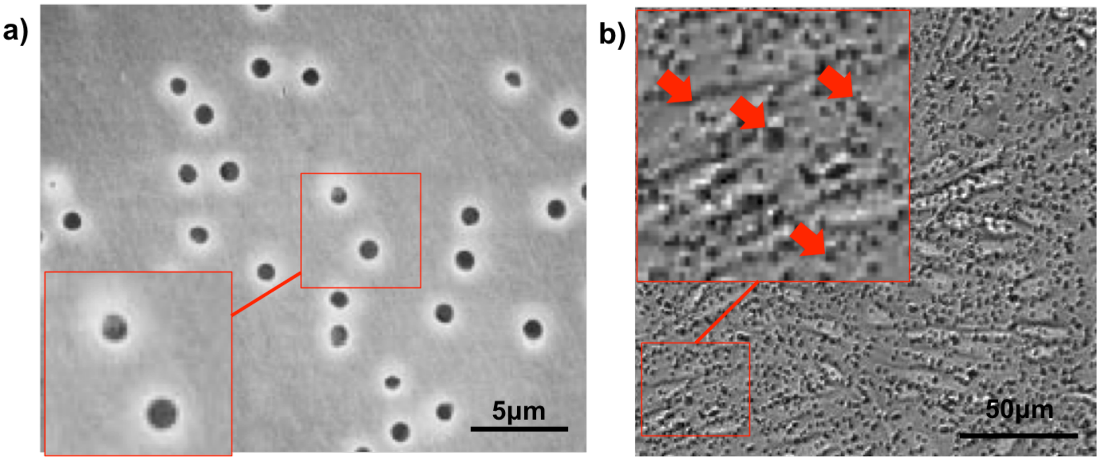

Figure 6.2 Transwell insert microporous membrane and bEND.3 cells. a) SEM (Scanning electron microscopy) micrograph of a 0.4 μm transwell insert membrane without coating or cells. b) Transmission light (DIC) micrograph of bEND.3 cells after 7 days culture on 0.4 μm transwell insert membrane. The pores (black dots) are indicated by arrows.

This endothelial cell monolayer was able to remain in such condition for up to two weeks if the medium was changed regularly. With longer time periods the cells start to form multiple layers. Therefore, the best time to carry out experimental studies was deemed to be between seven and ten days in culture.

6.1.2.1 Quantification of tight junction expression

In order to confirm the integrity of the endothelial monolayer in the 3D culture environment, the expression of three of the major tight junction proteins, claudin-5, occludin and ZO-1 was examined using immunofluorescence (IF) and FACS. We compared the expression levels of these tight junction proteins to the levels in endothelial cells grown in a 2D culture environment (solid plastic culture plate, 6-well plate). Cells both in 2D and 3D were tested after seven days incubation when the cells reached 100% confluence. As shown in Figures 6.3 and 6.4, no major difference was observed in the intensity of expression of the three junctional proteins between 2D and 3D using immunofluorescence, with the three markers clearly visible in both cases.

However, in 2D, claudin 5 (Figure 6.3a) and ZO-1 (Figure 6.3c) were mainly localised within the peri-nuclear area, while in 3D culture conditions, these two tight junction proteins were mainly localised at the cell boundaries (Figure 6.3d and Figure 6.3f). In particular, ZO-1 displayed a belt-like, continuous appearance with numerous branching points in 3D conditions; while in 2D, these structures were only observed with fragmentary patterns. The expression pattern of occludin was similar in the two models, and this tight junction protein was found both in the cytosol and at cellular boundaries (Figure 6.3b and Figure 6.3e). Although no significant differences in individual cell morphology were observed in these two models, in 2D culture conditions, several cell-cell interspaces could be found; while in the 3D culture model, the endothelial monolayer showed a relatively “tighter” morphology. This may suggest that in the 3D brain capillary, endothelial cells communicate with neighbouring cells to form the necessary tight junctions and a consequently tighter monolayer.

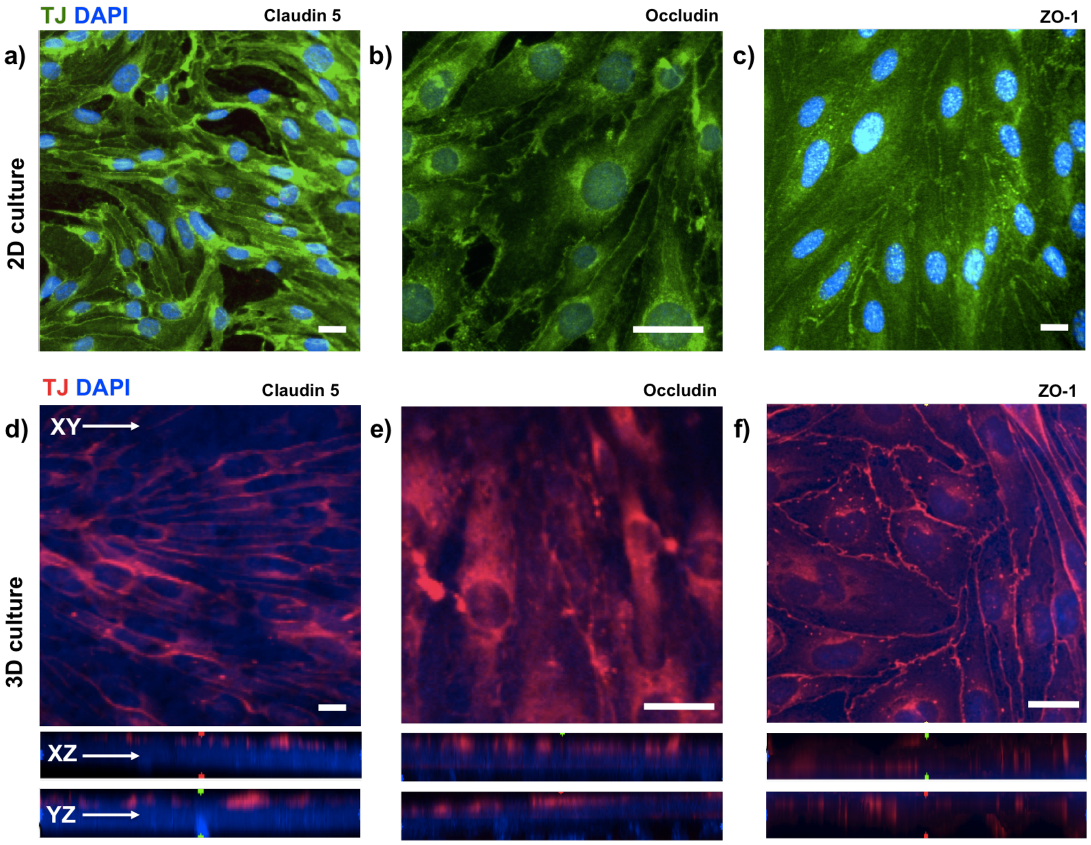

Figure 6.3 Immunofluorescence confocal laser microscopy of tight junction protein expression in bEND.3 cells in 2D and 3D. a) Micrograph of claudin 5 expression in 2D culture. b) Occludin expression, 2D culture. c) ZO-1 expression, 2D culture. d) Z-stack confocal micrograph of claudin 5 expression, 3D culture. e) Z-stack occludin expression, 3D culture. f) Z-stack ZO-1 expression, 3D culture. The scale bars represent 20μm.

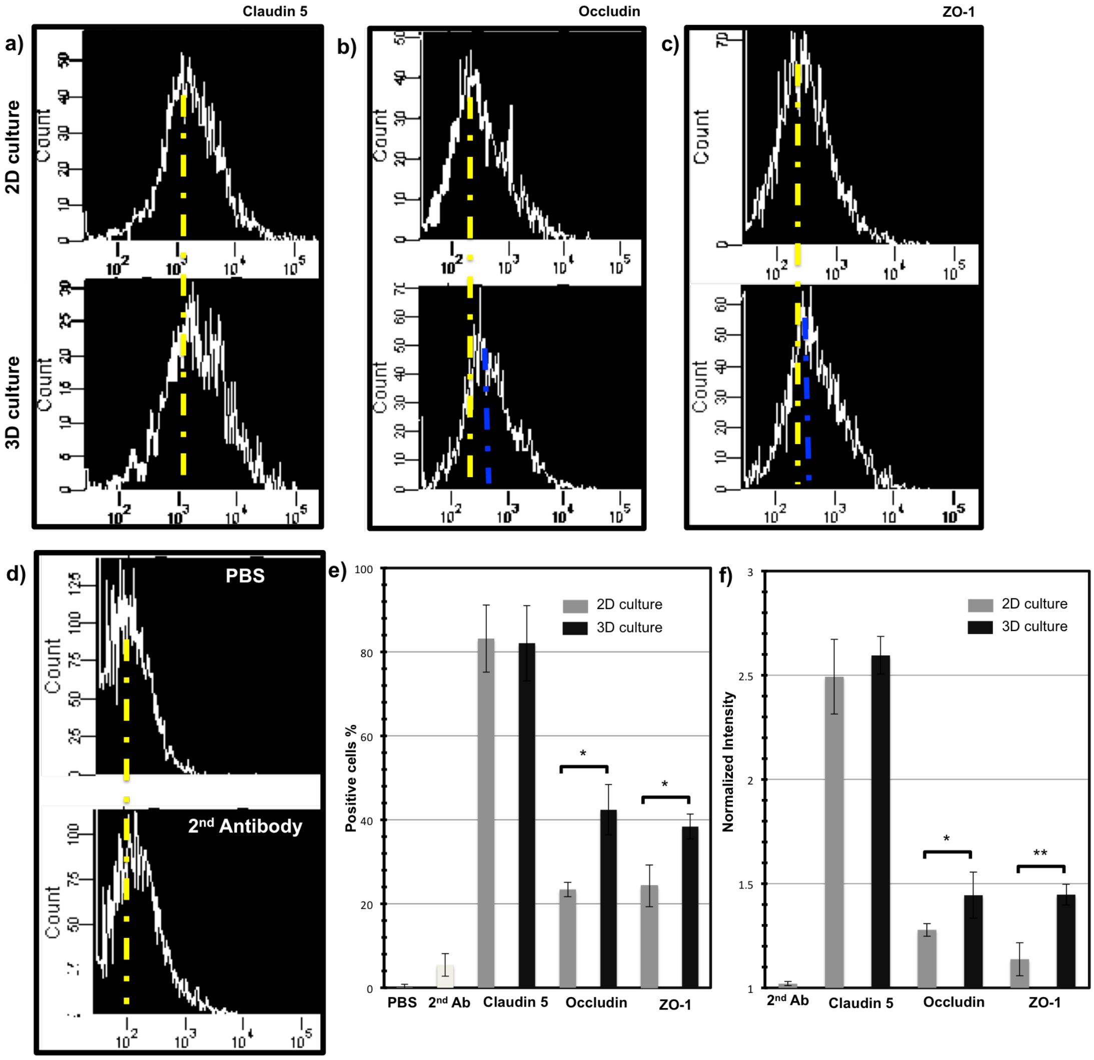

Figure 6.4 FACS flow cytometry measurement of bEND.3 cells tight junction expression in 2D and 3D. a-c) Histograms of protein expression, 2D and 3D culture: a) claudin 5, b) occludin, c) ZO-1. d) Histograms of PBS-treated and 2nd-antibody treated cells. e) and f) Quantitative comparison of 3 types of tight junction protein expression by e) positive cell percentage, f) normalised intensity. (n=3, $p<0.05$)

In support, we used FACS to quantify more accurately the expression of claudin-5, occludin and ZO-1 in both 2D and 3D cell culture conditions (Figure 6.4). Cells treated with PBS and with secondary antibody (λ_{Ex}=560nm) were used as control groups (Figure 6.4d).

Quantification and comparison of the expression of the three types of tight junction protein, expressed as positive cell percentage and normalised intensity per cell, were shown in Figure 6.4e and Figure 6.4f respectively. The results suggested that the claudin 5 expression level remains similar in 2D and 3D. By contrast, occludin and ZO-1 expression levels increased when cells were cultured in a transwell insert in 3D. ZO (*zonula occludens*) proteins (ZO-2 and ZO-3) connecting via ZO-1 to occludin and claudins [9], are considered key features of the blood-brain barrier that significantly reduce the permeability of polar solutes through the para-cellular diffusional pathway [10, 11]. Therefore, the difference between ZO-1 expression in 2D and 3D culture conditions suggested that brain endothelial cells form a tighter cell monolayer in the transwell insert system.

The co-culture system may also affect tight junction protein expression patterns, although data from the literature are still inconclusive. Pericytes were shown to induce a four-fold increase in trans-endothelial cell electrical resistance (TEER) in a murine brain endothelial cell model and to drive the formation of a more sealed endothelial cell monolayer [12]. An astrocyte-endothelial cell co-culture transwell model was shown to have a similar tight junction protein (claudin 5, occludin and ZO-1) expression level [13, 14]. A similar effect was observed using astrocyte-conditioned medium (ACM) [15], suggesting the presence of specific, yet unidentified, signalling molecule(s) released by astrocytes that regulate BBB tight junctions.

Astrocytes may achieve tight junction induction by direct contact with brain endothelial cells. Early electron microscopy research indicated that the distance separating the astrocyte foot process and the abluminal surface of the endothelial cell *in vivo* is only approximately 20 nm [16], a space filled with the micro-vascular basement membrane. In a transwell co-culture model, the micro-porous membrane determines the distance between astrocytes and endothelial cells, which is approximately 10 µm. This is much greater than the actual distance *in vivo*.

6.1.2.2 Use of MSC as pericytes in the BBB *in vitro* model

The French scientist, Charles-Marie Benjamin Rouget described pericytes in 1874 [17], and pericytes were first referred to as Rouget cells. Later, due to their anatomical location around the endothelium, the Rouget cells were renamed pericytes. Since these early studies, pericytes have been described as contractile cells with slender projections that wrap around the capillaries throughout the body. More recently, it has been suggested that pericytes have a stem cell like behaviour with multi-potential properties. This, in addition to the well-characterised function of supporting capillaries, associated with endothelial cells during angiogenesis [18], suggests that they may also possess the capability to differentiate into endothelial cells [19], macrophages [20, 21] and fibroblasts [18, 22] when required.

As a key component of the neurovascular unit, pericytes play an important role in blood-brain barrier formation and regulation. They are largely responsible for down-regulation of the 'default' endothelial phenotype in early brain microvessel development, including tight junction tightening and down-regulation of adhesion molecules and vesicular trafficking [12, 23], before up regulation of specific BBB features by astrocytes [12] . Pericytes also express the same SMA (smooth muscle actin) marker as smooth muscle cells, the cells that adhere to the endovascular cells for blood flow regulation in the microvasculature [24]. Deficiency of pericytes results in either alteration of brain capillary diameter or blood flow rate [25].

There is no commercial (or other) source of pericytes and we investigated the possibility of using mouse mesenchymal system cells (MSC cells) instead. Recent work from the Peault group [26] showed a strong similarity between MSCs and perivascular cells (pericytes). Their studies clearly showed that cells with MSC markers also express pericyte markers (CD146 +, CD34 -, CD45 -, CD56 -). These results allow researchers to speculate that MSCs and pericytes are phenotypically very much alike [27]. Brain pericytes were found to contribute to the up-regulation of BBB functions through TGF-β (transforming growth factor) *in vitro* [28, 29]. TGF signalling is one of the important pathways of communication between the endothelium and pericytes [30]; furthermore, factors in the extracellular matrix, such as collagen, may also change pericyte morphology, marker expression and differentiation significantly *in vitro* [31, 32].

Here we used mouse MSCs as pericytes, and first studied the effect of TGF-β and collagen type I from the extracellular matrix on pericyte marker expression. Further related studies including the influence of flow, functionalised polymersome uptake and *in vivo* functions are ongoing in our laboratory. As shown in Figure 6.5, mouse MSCs were cultured for up to five days on a 6-well plastic plate. To evaluate the effect of TGF-β, 200 ng/ml TGF-β was added to the medium and the medium replaced every two days. Rat-tail collagen type I was used as the extracellular matrix mimic, and pre-coated ($2\mu g/cm^2$) on the 6-well cell culture plate for 24 hours. Approximately 70% cell confluence was reached after five days in culture. Live cells were then imaged by transmission light microscopy using a differential interference contrast (DIC) filter. As shown in Figure 6.5, there was no significant change in cell morphology between non-treated cells and non-treated TGF-β treated cells (Figures 6.5a and 6.5b); cell projections can be observed. In the collagen type I treated group, the cells seem to form a flatter monolayer, fewer cells detached from the culture plate, and the majority of cells showed an elongated and slender morphology. We further examined the MSCs pericyte marker expression in these different conditions (non-treated, + TGF-β and +collagen pre-coating). Four pericyte markers were chosen; NG2 (NG2 proteoglycan), α-SMA (smooth muscle actin), PDGFR-β/CD140 (platelet-derived growth factor receptor-beta) and CD146 (S-endo 1-associated antigen, also referred to as MelCAM). The last is a receptor belonging to the immunoglobulin superfamily that is constitutively expressed in all human endothelial cells [33]. CD146 is also considered a marker of multi-potency for MSCs [34].

It was observed that the entire marker expression pattern increased significantly when cells were grown on a collagen (Type I) pre-coated culture plate. This condition is much closer to the *in vivo* scenario where pericytes share a basement membrane with endothelial cells on a collagen I rich extracellular matrix. The pericyte features of MSCs (collagen Type I coated) were further confirmed by immunofluorescence (Figure 6.6), although both non-treated and TGF-β treated cells (images not shown) showed positive expression of NG2, α-SMA, PDGFR-β/CD140 and CD146; the intensity was relatively lower than that observed in collagen Type I treated cells.

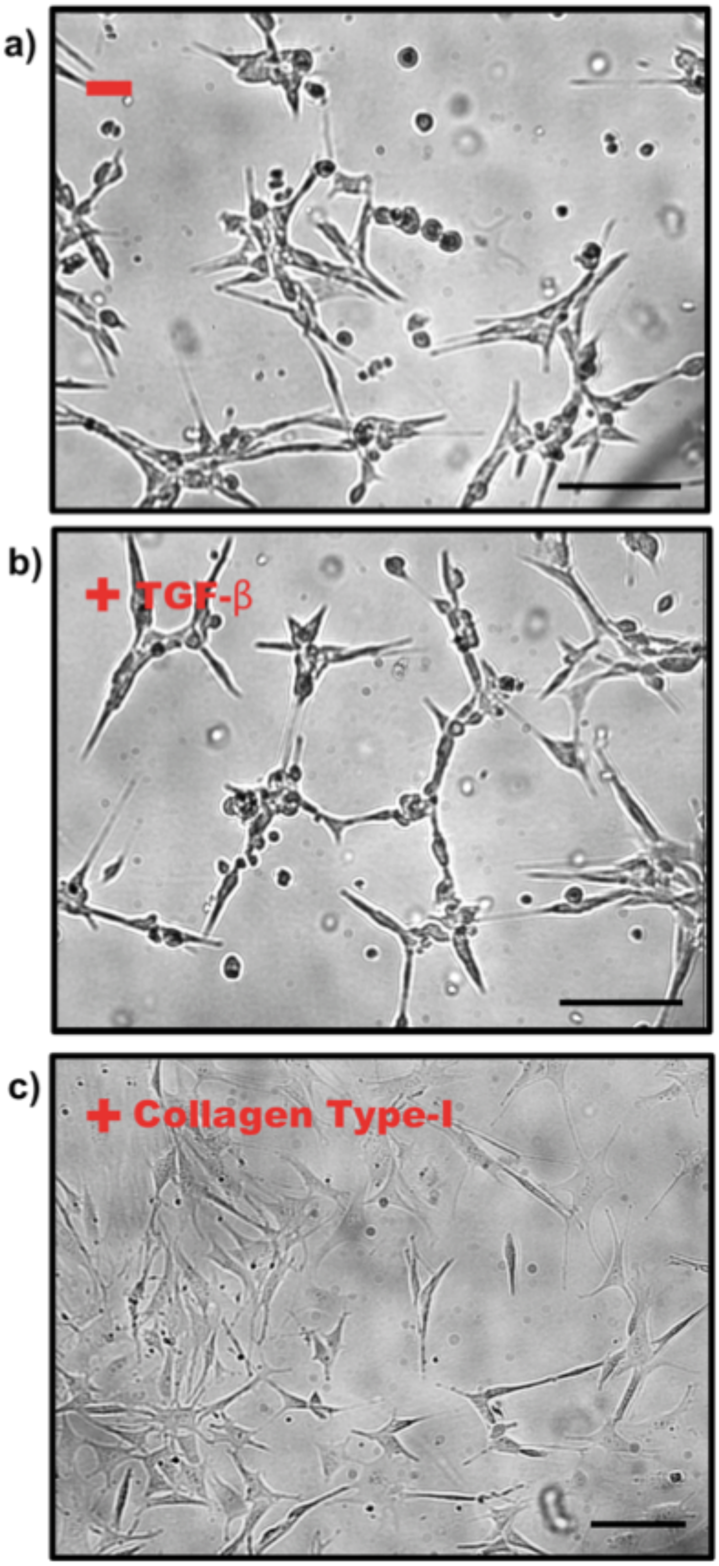

Figure 6.5 Mouse MSC cultured in TGF-β and collagen conditions. Transmission light micrographs of MSC cultures in 6-well plate in a) non-treated, b) +TFG-β and c) Type I collagen pre-coated conditions.

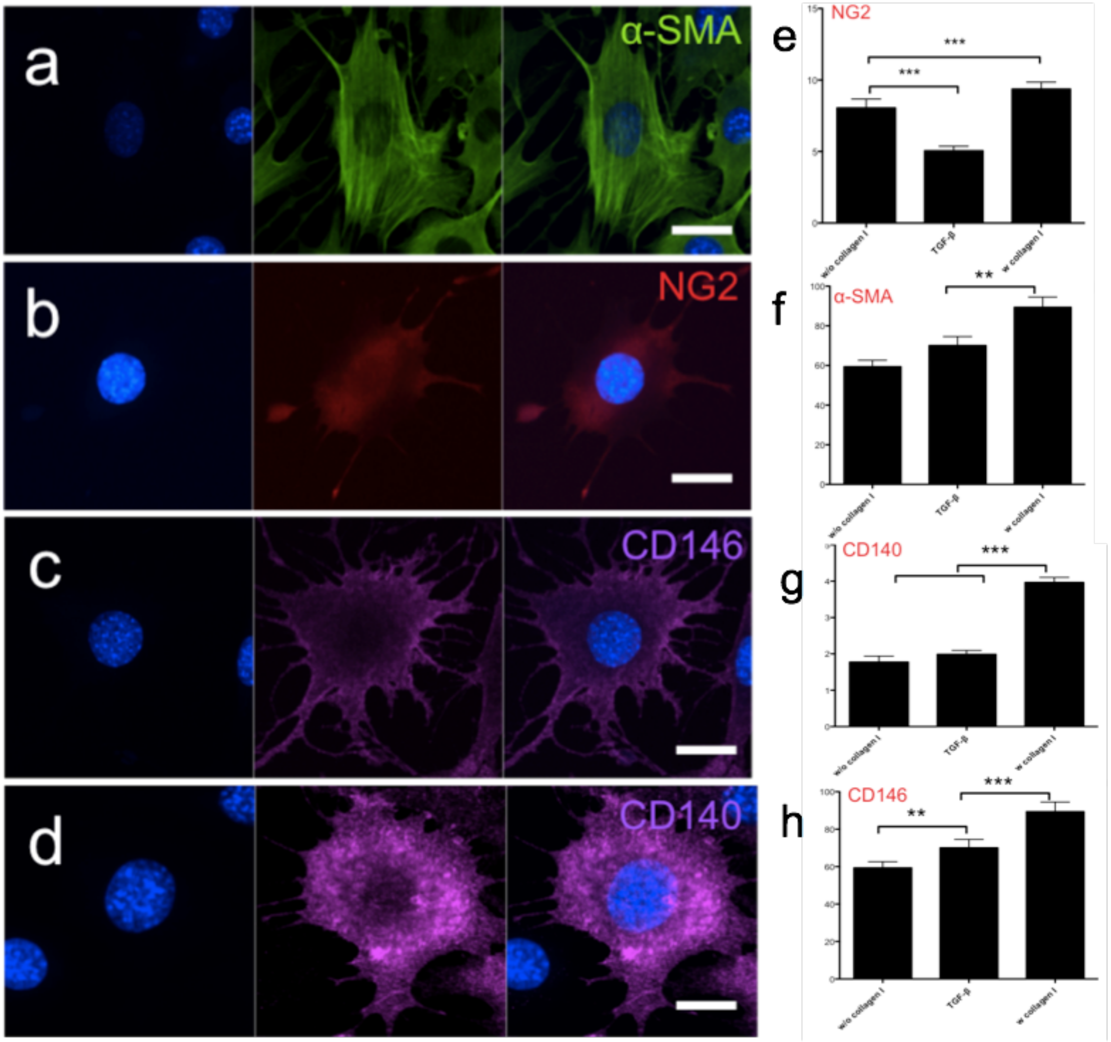

Figure 6.6 Immunofluorecence confocal laser microscopy of pericyte marker expression in MSCs. a) α-SMA (2nd Ab λ_{Ex}=488nm). b) NG2 (2nd Ab λ_{Ex}=538nm). c) PDGFR-β/CD146 (2nd Ab λ_{Ex}=488nm). d) PDGFR-β/CD/140 (2nd Ab λ_{Ex}=633nm). The scale bars represent 10μm. e-h) Fluorescence intensity of MSC marker expression: e) NG2, f) α-SMA, g) PDGFR-β/CD140, h) CD146. (Error bar SEM, Data points=30, $p<0.05$).

As shown in Figure 6.6, α-SMA marker clearly showed actin-fibre structure (Figure 6.6a), while NG2 PDGFR-β/CD140 and CD146 markers indicated distribution within the cytosol. The fluorescence intensity profile shown in Figures 6.6e, 6.6f, 6.6g and 6.6h confirms their similar phenotype to pericytes. For α-SMA and PDGFR-β/CD140 expression, there was no significant difference between non-treated cells and TGF-β treated cells (Figures 6.6f and 6.6g), and TGF-β treated cells showed lower expression of NG2 Figure 6.6e) and increased CD146 (Figure 6.6h) expression over non-treated cells.

6.1.2.3 Trans-endothelial electrical resistance

Since the 1980s, trans-epithelial or endothelial electrical resistance (TEER) measurements have become universally established as the most reliable, convenient and non-destructive method to evaluate and monitor the growth of epithelial and endothelial tissues *in vitro*.

In the BBB *in vitro* model here, TEER was measured using two chopstick electrodes connected to an EVOM Voltometer (STX2, World Precision instrument©. Sarasota, Florida. U.S.A.). As the transwell plate cover must be removed while measuring, continuous monitoring is not possible and recording can be made only at certain time points. As described previously, bEnd.3 cells were seeded on the transwell insert and reached 100% confluence to form a cell monolayer after seven days' incubation. TEER was first measured at day one, then recorded every 24 hours, up to one week.

bEnd.3 cells cultured alone showed TEER 135 Ω.cm^2 on day one

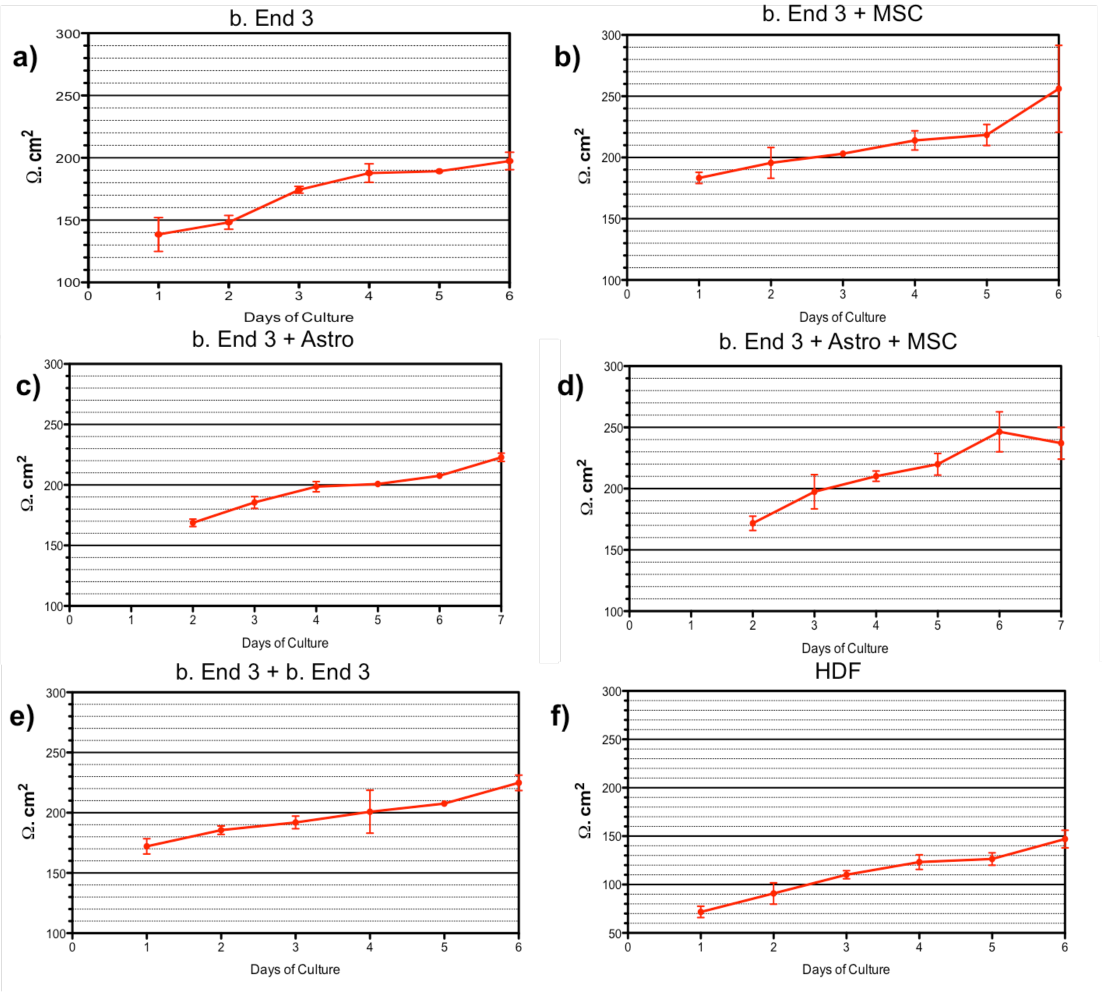

	bEnd.3	bEnd.3 +MSC	bEnd.3 +Astro	bEnd.3+MSC +Astro	bEnd.3+ bEnd.3	HDF
Day1	85	127	114	116	117	17
Day7	143	202	168	182	170	94

TEER average value, corrected for background (filter, coating, media), unit: **Ω. cm^2 .**

Figure 6.7 Transendothelial electrical resistance (TEER) of the *in vitro* BBB models over 7 days. a) bEND.3 cells alone. b) bEND.3 cells co-cultured with MSCs. c) bEND.3 cells co-cultured with astrocytes. d) bEND.3 cells co-cultured with astrocytes and MSCs. e) bEND.3 co-cultured with bEND.3 on the opposite side of transwell insert. f) TEER of HDF (human dermal fibroblast) cell monolayer as control group. (n=6) The table indicate the average TEER value from all co-culture model.

increasing to 195 Ω.cm^2 after seven days' incubation (Figure 6.7a), suggestingthat the more confluent the cells, the tighter the monolayer became. ‘Contact’ ‘Co-culture with mouse MSCs as pericytes (Figure 6.7b) on the opposite side of the transwell filter insert (collagen Type I coated) significantly raised TEER from approx. 180Ω. cm^2 (day 1) to 260Ω. cm^2 (day 7), showing that pericytes can induce tighter monolayers. bEnd.3 cells, co-cultured with mouse astrocytes on underside of filter, also showed a TEER increase (Figure 6.7c), to approx. 225Ω. cm^2, although this was lower than in the MSC co-culture model. In the co-culture model with both MSCs and astrocytes (Figure 6.7d) underneath, the TEER was approx. 240Ω. cm^2 at day seven (lower than bEnd/MSCs model but higher than bEnd/astrocytes). These results suggest a correlation between TEER and presence of pericytes (MSCs). We also performed an experiment where bEnd.3 cells were cultured on both sides of the insert to test whether the simple double-layer can change TEER. As shown in Figure 6.7e, the TEER of such a dual-layer endothelium reaches approx. 230Ω. cm^2 at day seven, not significantly greater than for the single bEnd.3 monolayer alone. This suggests that the barrier improvements observed with both pericytes and astrocytes are not due to a physical barrier but an actual effect on the bEnd.3 cell function. This was further confirmed using a non-barrier cell, fibroblast HDF (Human Dermal Fibroblast) monolayer, which produced a TEER of approx. 150Ω. cm^2, much lower than that of the endothelial cell monolayer that formed tight junctions. Co-culturing with astrocytes on the underside of the transwell filter slightly increased the TEER, but the increase was not significant, possibly due to the endothelial cells and astrocytes being separated by the 10μm-thick filter, a much greater distance than in vivo. Pericytes (MSCs) clearly reduced the permeability of the model barrier, resulting in a higher TEER, suggesting that pericytes play a more important role in regulating the BBB properties in our culture conditions. Note that even a blank transwell filled with PBS can produce an approx. 50 Ω.cm^2 TEER background; cell culture medium and collagen coating can also produce a small TEER. TEER values from day 1 and day 7 corrected for this background TEER are given in the table in Figure 6.7.

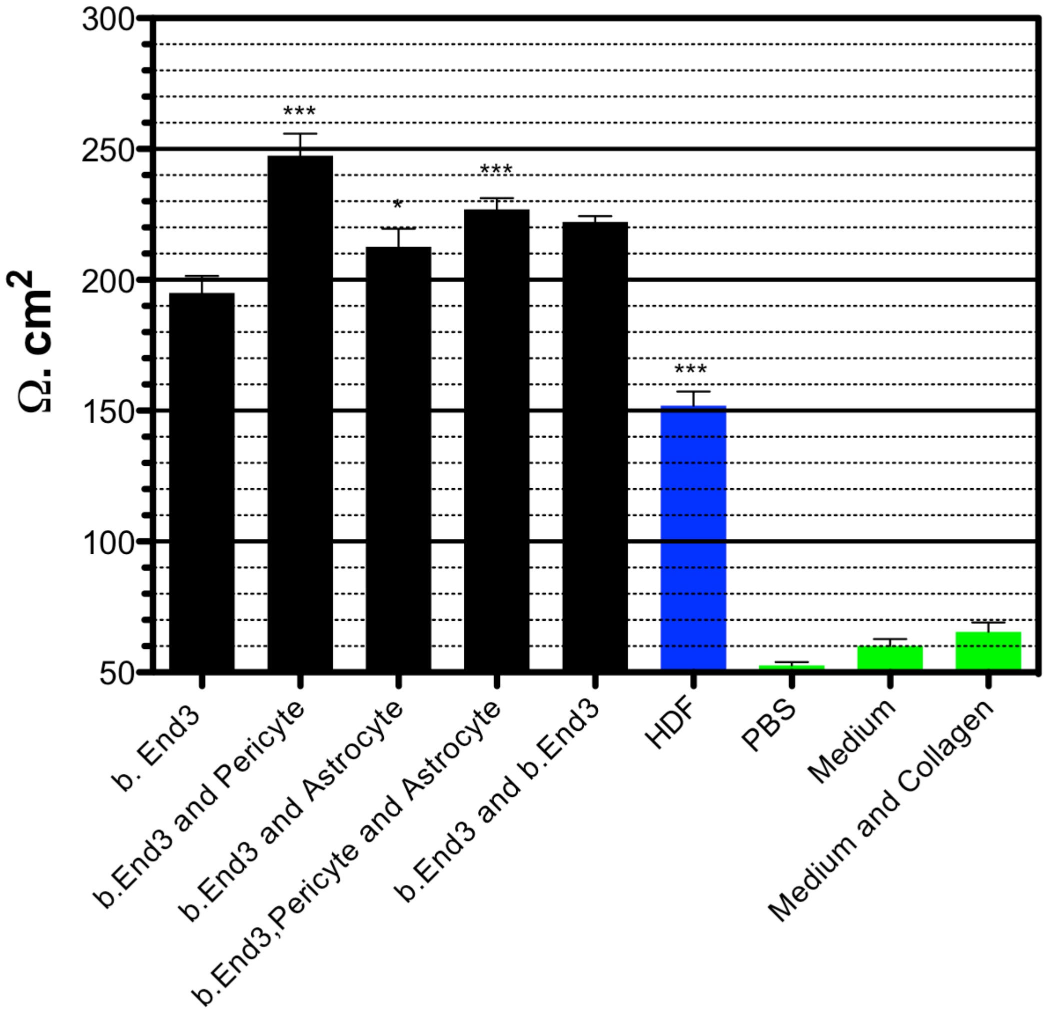

Figure 6.8 Transendothelial electrical resistance (TEER) of the BBB *in vitro* model on day 7. TEER comparison of different BBB culture and co-culture conditions, with fibroblast HDF cells as control cell monolayer, and PBS, medium, and collagen as blank controls. (Error bar SEM, n=6, $p<0.05$)

6.2 Screening polymersomes on the model

In Chapter 5 we discussed the polymersome 2D screening on bEnd.3 and immune cells. Approx. 40 different formulations of polymersomes were tested. Those polymersomes that showed positive internalisation by brain endothelial cells were tested with immune cells. The final 2D screening results suggested that attaching ligand Anigopep-2 or RVG (with the ligand ratio 1.2% and 1.2% respectively) to functionalise $P(EO_{10}GMA)_{20}$-$PDPA_{112}$ polymersomes improved brain endothelial uptake significantly over that of non-functionalised polymersomes. More importantly, these formulations have a “stealth” character with minimal recognition by immune system cells. Hence, Ang (1.2%)-POEGMA-PDPA and RVG (1.2%)-POEGMA-PDPA were chosen for further tests on the established BBB *in vitro* cell model, in order to determine if these functionalised polymersomes can potentially be used as CNS delivery vectors.

Ang (1.2%)-POEGMA-PDPA and RVG (1.2%)-POEGMA-PDPA polymersomes were formed as described before. Non-functionalised POEGMA-PDPA and PMPC-PDPA polymersomes were also prepared as controls. With the purpose of visualising polymersomes under fluorescence/confocal laser microscopy, 10% Rh-POEGMA-PDPA was blended into each POEGMA based formulation. These formulations were first tested on an endothelial (bEnd.3) cell/astrocyte co-culture *in vitro* model. Both sides of the transwell insert were coated with Type I collagen, while the astrocyte side was coated with FITC (λ_{Ex}=488nm) conjugated Type I collagen.

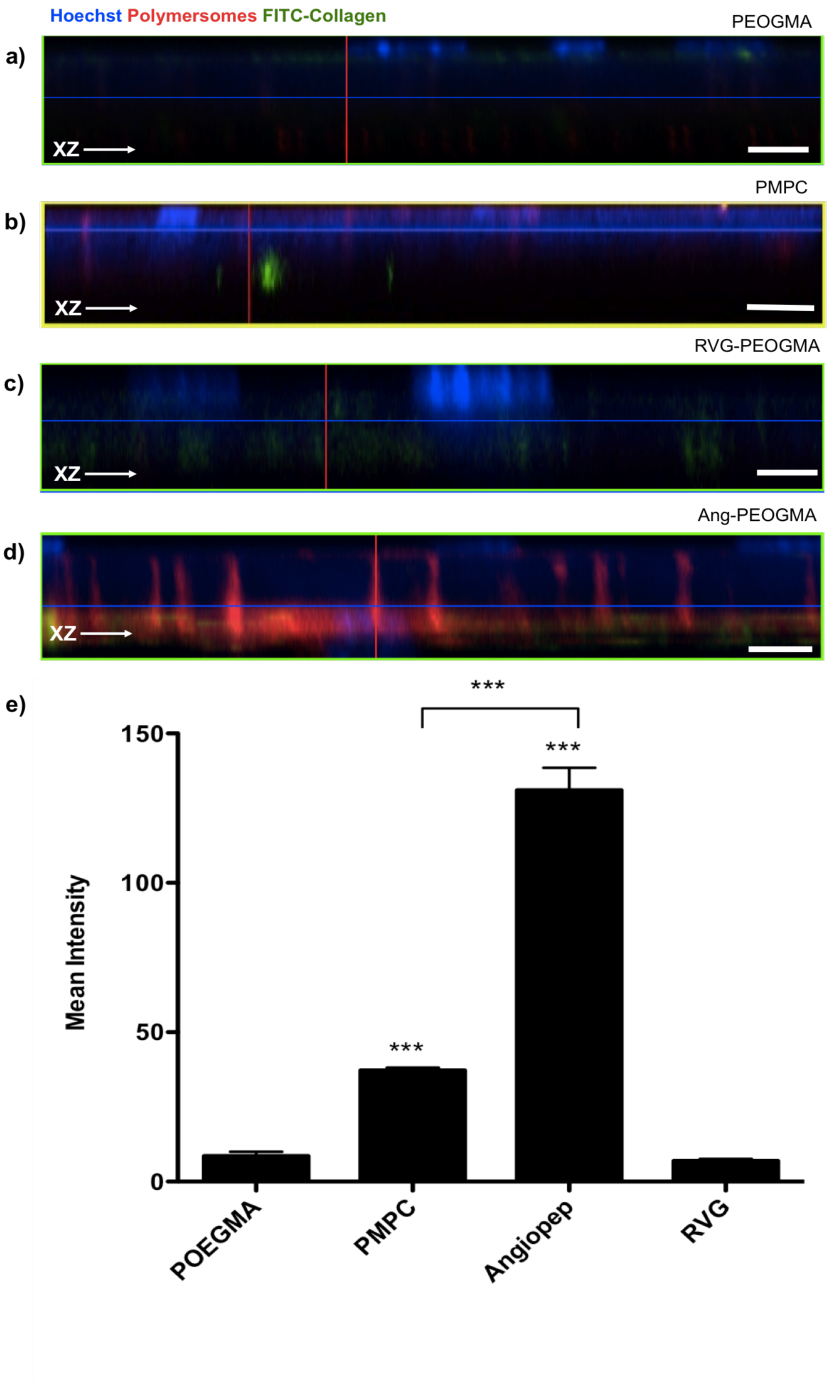

Figure 6.9 Z-stack confocal micrographs of transwell insert membranes treated with polymersomes. Insert membranes treated with polymersomes: a) POEGMA-PDPA, b) PMPC-PDPA, c) RVG-POEGMA-PDPA, d) Ang-POEGMA-PDPA. e) Transwell insert microporous membrane fluorescence intensity analysis after the different polymersome treatments. The scale bars represent 20μm. (Data points=30, $p<0.05$, Hoechst: λ_{Ex}=405nm FITC-collagen: λ_{Ex}=488nm, Rh-polymersomes: λ_{Ex}=560nm)

After the bEnd.3 cells reached confluence at approx. 7-8 days, polymersomes (1 mg/ml) were added to the upper compartment of the transwell and incubated at 37°C, 5% CO_2 environment for three hours. Then the transwell insert membranes were cut down after fixation and imaged by confocal laser scanning microscopy on a glass slide (the preparation of the transwell membrane for imaging is described in Chapter 4). In Figure 6.9, these are shown as a z-projection (with the z axis going along the pores in the insert) showing whether any polymersomes are either retained in or on the endothelial layer (top side) or are shuttled across the pores and reach the astrocyte monolayer on the underside of the filter.

As an analogue of PEO-PDPA, POEGMA-PDPA polymersomes also display the "stealth" property when interacting with brain endothelial cells. The Z-stack image (Figure 6.9a) showed non-cellular uptake during the incubation time, so hardly any positive polymersome signal was found within the whole section. PMPC-PDPA polymersomes, however, are strongly internalised by many types of cells including bEnd.3 and unsurprisingly the top layer of the bEnd.3 cells showed a positive uptake of PMPC-PDPA polymersomes (Figure 6.9b). As shown in Figure 6.9b, transport of polymersomes across the micro-porous membrane was rarely observed, suggesting that the final destination of PMPC-PDPA polymersomes was within the endothelial cell cytosol.

RVG (1.2%)-POEGMA-PDPA polymersomes showed positive brain endothelial cell uptake greater than that of non-functionalised POEGMA-PDPA polymersomes(Figure 5.13, Chapter 5) in the 2D model. However, in the 3D cell culture environment, RVG-POEGMA-PDPA showed minimal cellular internalisation, to the same level as non-functionalised POEGMA-

PDPA polymersomes (Figure 6.9c). To date, it is still not clear what kind of receptor RVG targets on the capillary endothelial cell, although a RVG-modified carrier was shown able to penetrate the BBB to reach the brain *in vivo* [35, 36]. In the present case, RVG-POEGMA-PDPA polymersomes showed very different uptake in 2D and 3D culture environments.

Interestingly, in the Ang (1.2%)-POEGMA-PDPA treated group, although the bEnd.3 monolayer showed less uptake than for PMPC-PDPA polymersomes, a strong fluorescence signal was observed within the micro-porous membrane (Figure 6.9d), suggesting that the majority of polymersomes were shuttled across the endothelial monolayer during the three-hour incubation. After travelling through the micro-porous filter, the Ang-POEGMA-PDPA polymersomes were also found within the FITC-conjugated collagen and partly taken up by the astrocytes underneath. The fluorescence signal from the micro-porous membrane was quantified over three different experiments (Figure 6.9e) revealing that the Ang-POEGMA-PDPA polymersomes were shuttled across the bEnd.3 cell layer more effectively than any other formulation. PMPC-PDPA polymersomes showed some penetration while pristine POEGMA-PDPA and RVG-POEGMA-PDPA polymersomes showed no uptake by bEnd.3, and no fluorescence was observed within the micro-porous filter.

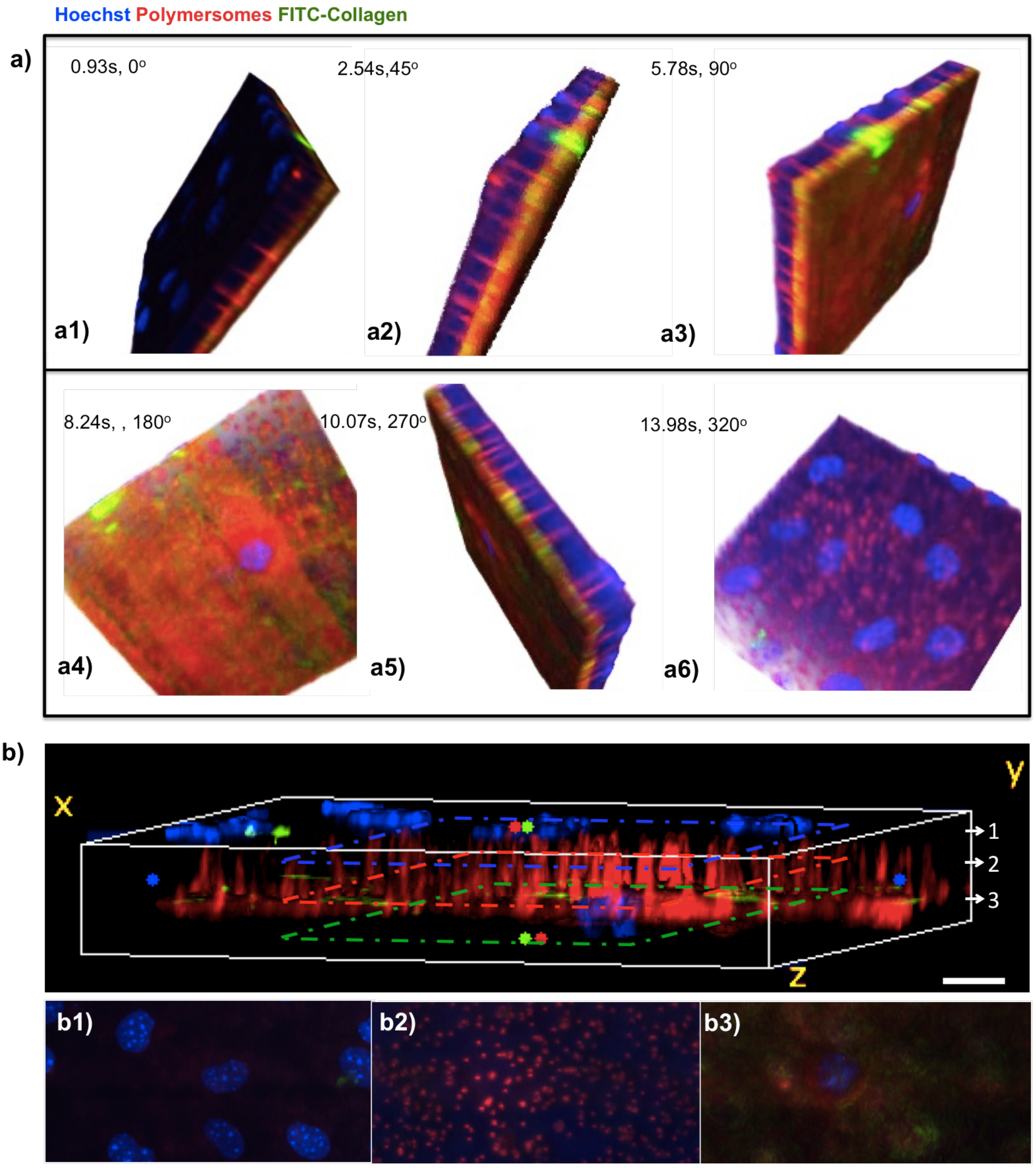

Figure 6.10 3D animation and 3D volume viewer of transwell membrane treated with Ang-POEGMA-PDPA polymersomes a) 6 frames captured from 3D animation of transwell membrane treated with Ang-POEGMA-PDPA polymersomes (a1, 0.93s. a2, 2.54s. a3, 6.78s. a4, 8.24s. a5, 10.07s. a6, 13.98s). b) 3D volume viewer of transwell membrane treated with Ang-POEGMA-PDPA polymersomes, and three section images from top (b1), middle (b2) and bottom (b3) of the transwell membrane respectively.

These results suggest that among these four formulations (PMPC-PDPA, POEGMA-PDPA, RVG-POEGMA-PDPA and Ang-POEGMA-PDPA), the Angiopep-functionalised POEGMA-PDPA polymersome is the only formulation that possesses the ability to rapidly penetrate the brain endothelial cell monolayer, presumably via the RMT (receptor-mediated transcytosis) pathway.

In order to demonstrate in more detail the transcytosis process of Ang-POEGMA-PDPA polymersomes, the stacked images were then reconstructed into 3D rendering (Figure 6.10. Image J64. 18 slices, thickness = 0.75μm/slice). These were displayed at different angle rotations (Figure 6.10 a1) at 0^o. The side face image (Figure 6.10 a2) clearly showed the multi-layer “sandwich-like” composition of this *in vitro* system, including the endothelial monolayer, micro-porous filter membrane and FITC-collagen layer as the substrate for cultured astrocytes. The side face image also showed the micro-porous filter fully filled with Ang-POEGMA-PDPA polymersomes. The 90^o - 180^o rotation (Figures 6.10 a3, a4) revealed the opposite side of the transwell insert membrane, coated with FITC-collagen and seeded with astrocytes. Most importantly, the projections in Figure 6.10 a6 showed that the pores filled with polymersomes were randomly distributed underneath the cell monolayer (including right below the cell nuclei) suggesting that polymersomes did not go through the para-cellular space.

This is further demonstrated in the reconstructed 3D volume viewer (Figure 6.10b), where the details of the different depths of the 3D models were shown and polymersomes were only found within the pores and within the supporting astrocytes.

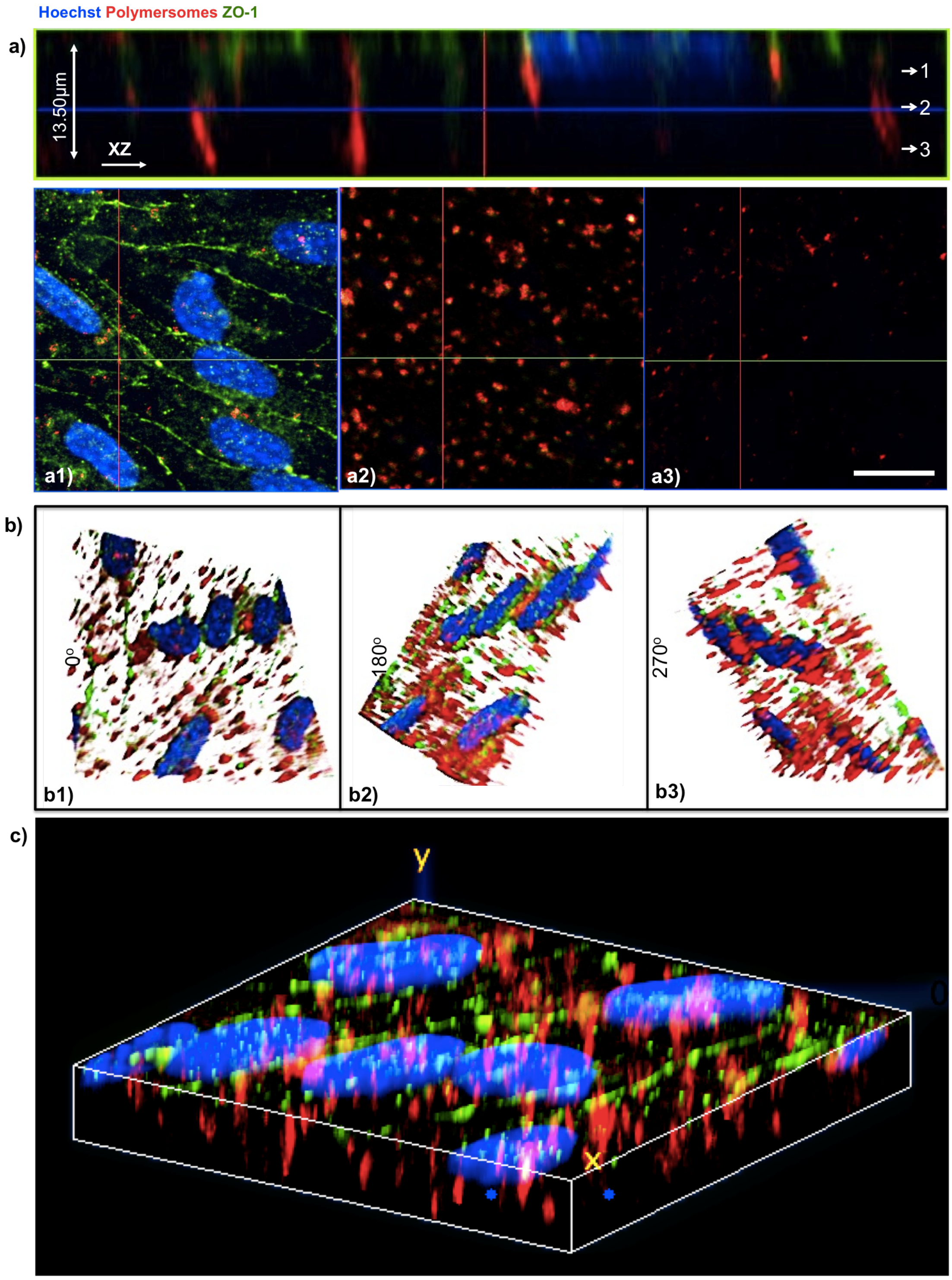

Figure 6.11 bEND.3 monolayer in transwell insert treated with Ang-POEGMA-PDPA polymersomes a) Z-stack confocal micrograph (a1, top layer, a2, middle layer and a3, bottom layer). b) 3 frames captured from 3D animation (b1, 0^{o}. b2, 180^{o} and b3, 270^{o}). c) 3D volume viewer of transwell membrane treated with Ang-POEGMA-PDPA polymersomes. The scale bars represent 20µm. (Hoechst: λ_{Ex}=405nm ZO-1: λ_{Ex}=488nm, Rh-polymersomes: λ_{Ex}=560nm)

The same treatment was performed by adding Ang-POEGMA-PDPA polymersomes (1 mg/ml) into the upper compartment of the *in vitro* model. Here the brain endothelial tight junction protein ZO-1 was also stained via immunofluorescence chemistry. Not surprisingly, after three hours' incubation, Angiopep-functionalised POEGMA demonstrated clear penetration through the endothelial monolayer. No polymersome fluorescence signal was associated with the tight junction marker ZO-1 (Figures 4.11 a1, a2 and a3). The micro-porous filter filled by polymersomes can be observed both underneath the cellular cytosol and cell border (Figure 4.11 b), suggesting that receptor-mediated transcytosis has taken place all over the cell plasma membrane. The whole landscape of the treated micro-porous filter was again reconstructed within a 3D volume viewer (Figure 6.11c).

Previous trans-endothelial electrical resistance studies indicated that pericytes (MSCs) in the co-culture *in vitro* model could significantly reduce the monolayer permeability. To optimize the BBB *in vitro* properties, pericytes (MSCs) were introduced into this *in vitro* model, and the transcytosis mechanism of Ang-POEGMA-PDPA was tested. The endothelial cell monolayer was formed and confirmed by marking the tight junction protein ZO-1. A pericyte (MSCs) monolayer was achieved, and confirmed by testing for the positive expression of PDGFR-β/CD140. Ang-POEGMA-PDPA polymersomes (1 mg/ml) were added into the upper compartment of the transwell insert. After three hours' incubation, the micro-porous filter of the transwell again indicated successful transcytosis achieved by Angiopep-

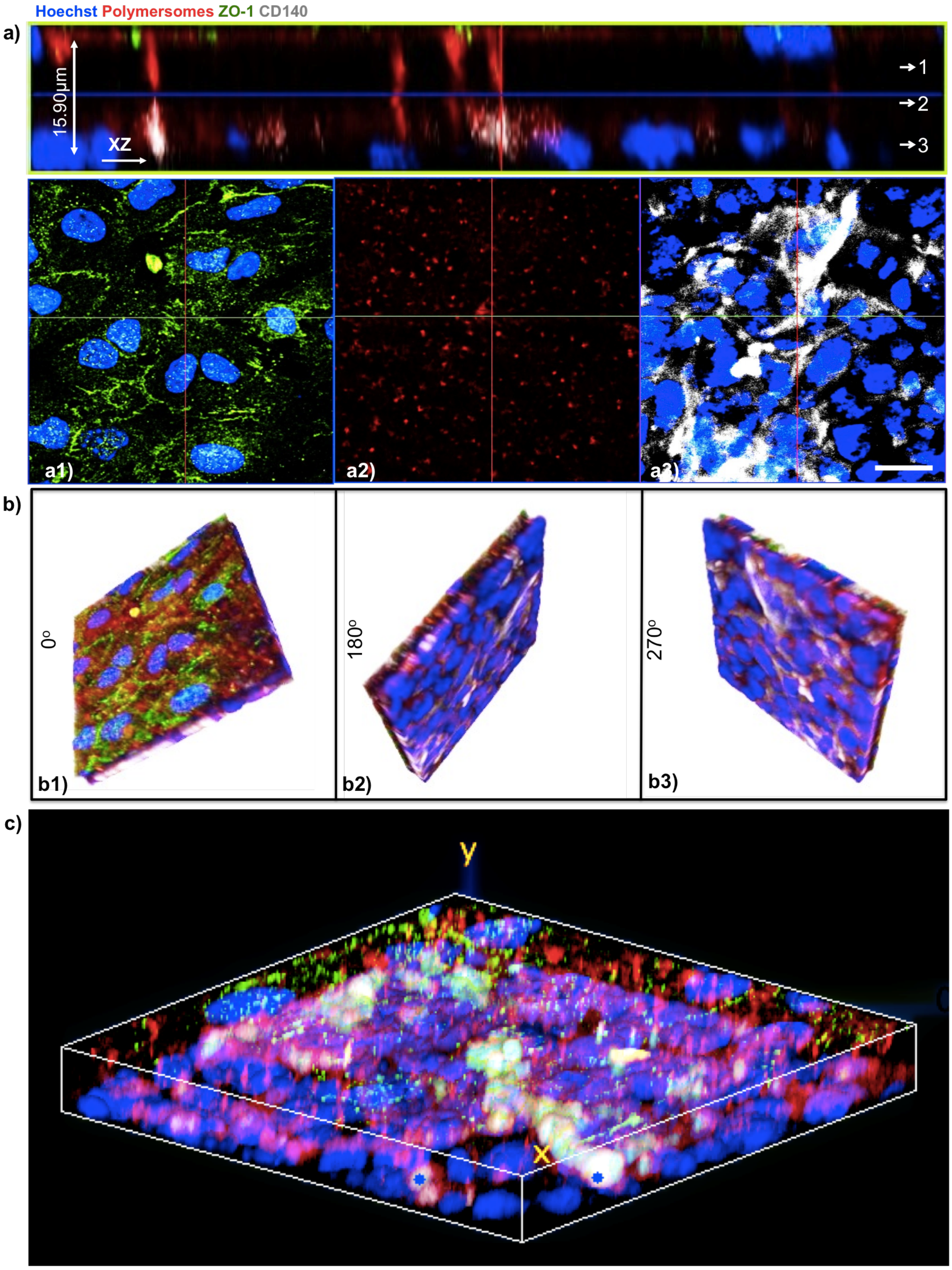

Figure 6.12 bEND.3 co-cultured with pericytes (MSCs) on transwell insert treated with Ang-POEGMA-PDPA polymersomes a) Z-stack confocal micrograph (a1, top layer, a2, middle layer and a3, bottom layer). b) 3 frames captured from 3D animation (b1, 0°. b2, 180° and b3, 270°). c) 3D volume viewer. The scale bars represent 20μm. (Hoechst: λ_{Ex}=405nm ZO-1: λ_{Ex}=488nm, Rh-polymersomes: λ_{Ex}=560nm, CD140: λ_{Ex}=633nm)

functionalised POEGMA-PDPA polymersomes (Figure 6.12a). Images from the top (Figure 6.12 a1), middle (Figure 6.12 a2) and bottom (Figure 6.12 a3) layers of the filter membrane respectively showed a bEnd.3 monolayer, a micro-porous membrane filled by polymersomes and a pericyte (MSCs) monolayer. The “sandwich-like” composition and transcytosis process can be viewed in the 3D projection and rendering (Figures 6.12 b1, b2 and b3). It is interesting to note that in this model, polymersomes penetrated the endothelial monolayer and were then captured by the pericyte monolayer. The micro-porous membrane fluorescence intensity (Figure 6.12 a2) was relatively lower than in the bEnd.3 cell model cultured alone (Figure 6.11 a2), suggesting that the pericyte monolayer underneath increased the barrier properties and produced more resistance for polymersomes crossing the transwell membrane.

Micro-porous membrane fluorescence intensities from the bEnd.3 cell only model and the bEnd.3/pericyte co-culture cell model were both investigated (Figure 6.13). The relative intensity indicated the quantity of functionalised polymersomes within the filter. The middle layer fluorescence intensity (Figure 6.13b) revealed that the pericyte co-culture model regulated the amount of polymersomes that passed through the endothelial monolayer. As a layer of pericytes were present underneath the filter, the trancytosed polymersomes contacted or were taken up by pericytes, so the bottom layer showed a relatively higher intensity than the one without cells. This result demonstrated that pericytes regulated the substances transported in the *in vitro* BBB model;

similar pericyte functions have been shown in previous *in vivo* studies [12, 23].

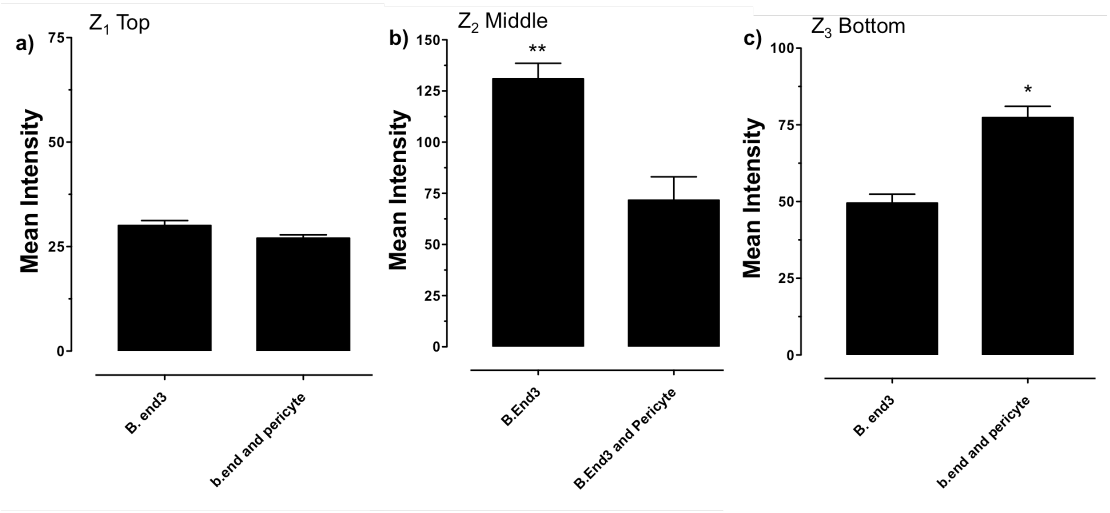

Figure 6.13 Microporous membrane fluorescence intensity comparisons of bEND.3 and bEND.3/Pericytes co-culture models treated with Ang-POEGMA-PDPA polymersomes. a-c) Mean intensity of the filter membrane: a) top layer, b) middle layer, c) bottom layer. (Error bar SEM, Data points=30, $p<0.05$)

To further confirm that Ang-POEGMA-PDPA polymersomes are shuttled across we performed a reversed orientation experiment, where the brain endothelial cells were cultured in the transwell lower compartment on the underside of the filter membrane, and pericytes (MSCs) were seeded in the transwell upper compartment (Figure 6.14a).

To test transcytosis in this reverse model, the same concentration of Ang-POEGMA-PDPA polymersomes (1 mg/ml) was then added to the lower compartment of the transwell. PMPC-PDPA polymersomes were also tested in such a reverse model as a control experiment. This allowed the brain endothelial cells full contact with the polymersome solution, but avoided the possibility of polymersomes precipitating on the transwell filter.

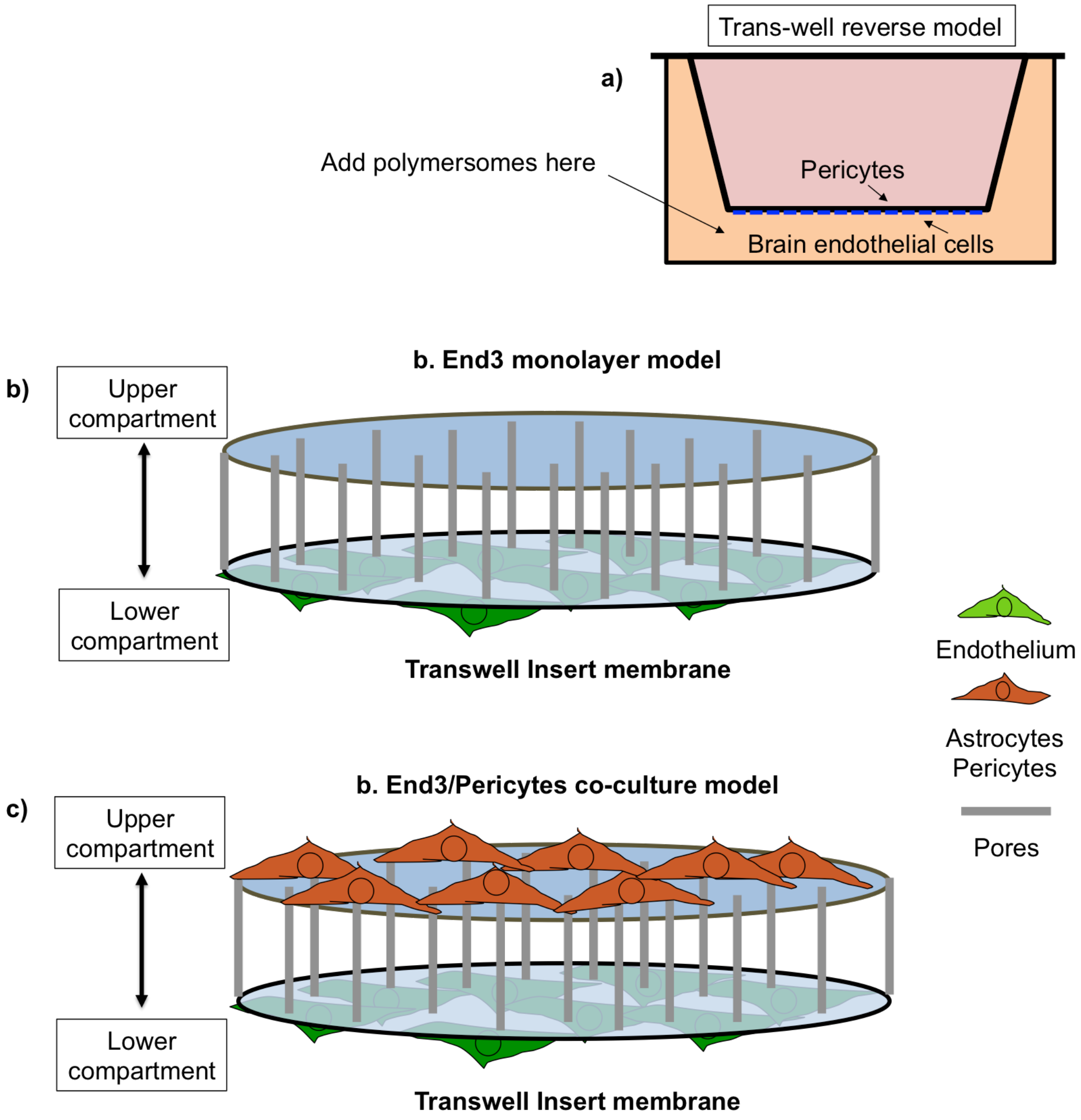

Figure 6.14 Schematic representation of the 'reverse' *in vitro* BBB model. a) Schematic representation of the 'reverse' model with pericytes and brain endothelial cells seeded in the upper and lower compartment respectively. b and c): Transwell filter membrane of the reverse model seeded with b) bEND.3 cells only, c) pericytes above and bEND.3 underneath.

As shown in Figure 6.15a, in the reverse model treated with PMPC-PDPA polymersomes, the brain endothelial cells underneath the filter membrane showed positive cellular internalisation (Figure 6.15 a3). But the majority of the polymersomes were detected within the cells; no polymersomes were observed within the filter micro-pores (Figure 6.15 a2), again suggesting the endocytosis uptake mechanism of PMPC-PDPA formulations. Interestingly, as demonstrated in Figure 6.15b, the reverse model treated with Angiopep-2 functionalised POEGMA-PDPA polymersomes again showed effective transcytosis (Figure 6.15b), similar to that observed in the normal polarity *in vitro* model. There was no obvious cellular uptake within the brain endothelial monolayer (Figure 6.15 b3). However, the micro-porous filter was clearly fluorescent (Figure 6.15 b2), suggesting Ang-POEGMA-PDPA polymersomes penetrated through the bEnd.3 monolayer by transcytosis, then filled up the micro-porous filter. The reverse *in vitro* model was then modified by introducing pericytes in the transwell upper compartment (Figure 6.15 c). The pericyte monolayer on the filter membrane was stained with α-SMA (Figure 6.15 c1). Although the fluorescence intensity within the micro-pores slightly decreased (Figure 6.15 c2) due to the presence of pericytes, clearly the transcytosis process still occurred on this reverse *in vitro* model. The transcytosis of polymersomes in the reverse *in vitro* model showed an opposite dimensional direction compared with the normal polarity model, from the transwell lower compartment to the transwell upper compartment. This result proved the Angiopep functionalised POEGMA-PDPA polymersomes are capable of binding to RMT receptors on the apical surface of brain endothelial cells, and are shuttled via transcytosis to the

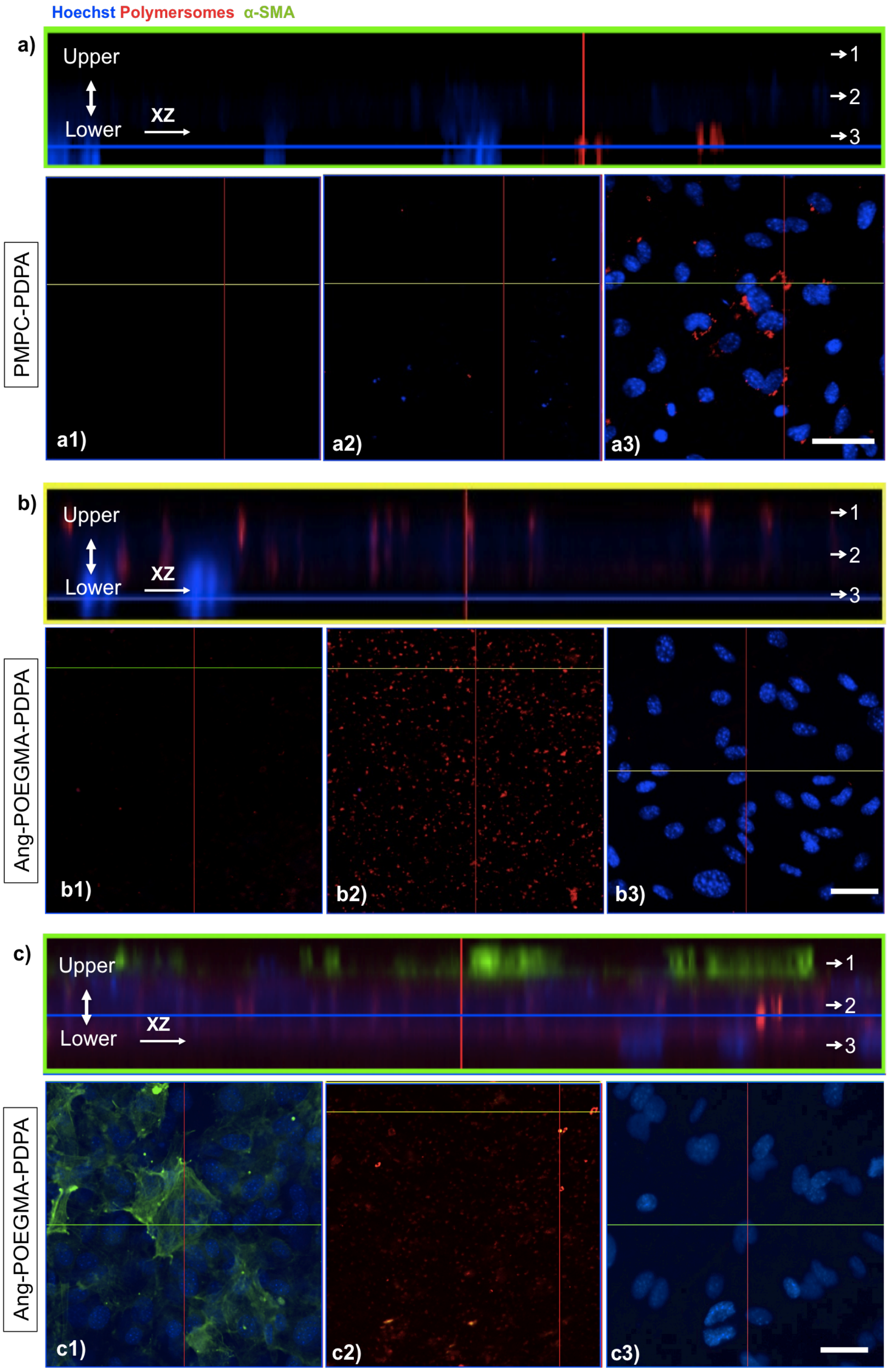

Figure 6.15 Z-stack 3D confocal micrographs of reverse *in vitro* BBB models treated with polymersomes: a) bEND.3 monolayer, PMPC-PDPA. b) bEND.3 monolayer, Ang-POEGMA-PDPA, c) bEND.3/pericytes (MSC) co-culture, Ang-POEGMA-PDPA. The scale bars represent 20µm.

basolateral side. Therefore, the direction of transcytosis occurring in the *in vitro* model was determined by the apical surface orientation; this can be either from the upper to lower compartment or from the lower to upper compartment.

6.3 Conclusions

In this chapter, the set up of the BBB *in vitro* model (and reverse *in vitro* model) was described in detail. The expression of tight junction proteins and TEER studies demonstrated that such an *in vitro* model retains some of the basic BBB characteristics. Based on this *in vitro* model, four polymersome formulations (PMPC-PDPA, POEGMA-PDPA, 1.2%RVG-POEGMA-PDPA and 1.2%Ang-POEGMA-PDPA) were tested. According to the screening results in the *in vitro* model, POEGMA-PDPA and RVG-POEGMA-PDPA polymersomes were found incapable of penetrating through the brain endothelial monolayer. PMPC-PDPA polymersomes showed cellular internalisation within the brain endothelial cells with the majority of polymersomes ending within the cellular cytosol, but rarely showing good penetration.

Angiopep-functionalised POEGMA-PDPA polymersomes demonstrated an effective transcytosis process in the *in vitro* BBB model. The Ang-POEGMA-PDPA formulation was found to penetrate the brain endothelial monolayer, and travelled through the micro-porous membrane from the upper (apical side) to the lower compartment (basolateral side). A more complicated *in vitro* model of endothelial cells co-cultured with pericytes (MSCs) was established.

The Ang-POEGMA-PDPA polymersomes also showed obvious penetration in this *in vitro* model. In addition, the amount of transcytosis of polymersomes was slightly reduced in the presence of pericytes (MSCs), suggesting that pericytes play a barrier function for polymersome transport in such an *in vitro* model.

Finally, Ang-POEGMA-PDPA polymersomes were tested on a “reverse” BBB *in vitro* model. Polymersome transcytosis on this reverse model was clearly observed, again proving that receptor-mediated transcytosis occurred from the apical side of the endothelial monolayer, penetrating the monolayer effectively in an AP (apical) to BL (basolateral) direction.

As seen with the 2-Dimensional screening results, Ang-POEGMA-PDPA polymersomes showed more significant cellular uptake over non-functionalised formulations, and also showed extremely low immune response. In addition, an effective receptor-mediated transcytosis process emerged in the established BBB *in vitro* model treated with Ang-POEGMA-PDPA. All the information suggested such formulations may possess the capability of penetrating the blood-brain barrier *in vivo*, and potentially can be used as vectors to target the central nervous system.

References:

1. Cucullo, L., et al., *A dynamic in vitro BBB model for the study of immune cell trafficking into the central nervous system.* Journal of Cerebral Blood Flow and Metabolism, 2011. **31**(2): 767-777.
2. Ando, J. and K. Yamamoto, *Vascular Mechanobiology - endothelial cell responses to fluid shear stress -.* Circulation Journal, 2009. **73**(11): 1983-1992.
3. Shannon, J.M. and D.R. Pitelka, *The influence of cell-shape on the induction of functional-differentiation in mouse mammary cells-in vitro.* In Vitro-Journal of the Tissue Culture Association, 1981. **17**(11): 1016-1028.
4. Vanmeer, G. and K. Simons, *The function of tight junctions in maintaining differences in lipid-composition between the apical and the basolateral cell-surface domains of MDCK cells.* Embo Journal, 1986. **5**(7): 1455-1464.
6. EJ Hughson, R.H., *Assessment of cell polarity*. Epithelial Cell Culture: A Practical Approach, ed. S. AJ1996, Oxford, UK: Oxford Univ. Press.
7. Giannelli, G., et al., *Induction of cell migration by matrix metalloprotease-2 cleavage of laminin-6.* Science, 1997. **277**(5323): 225-228.
8. Daneman, R., et al., *Pericytes are required for blood-brain barrier integrity during embryogenesis.* Nature, 2010. **468**(7323): 562.
9. Abbott, N.J., *Dynamics of CNS barriers: evolution, differentiation, and modulation.* Cellular and molecular neurobiology, 2006. **25**(1): 5-23.
10. Begley, D.J. and M.W. Brightman, *Structural and functional aspects of the blood-brain barrier.* Progress in drug research, 2003. **61**: 39-78.
11. Wolburg, H., et al., *Brain endothelial cells and the glio-vascular complex.* Cell and Tissue Research, 2009. **335**(1): 75-96.
12. Daneman, R., et al., *Pericytes are required for blood-brain barrier integrity during embryogenesis.* Nature, 2010. **468**(7323): 562-566.
13. Hamm, S., et al., *Astrocyte mediated modulation of blood-brain barrier permeability does not correlate with a loss of tight junction proteins from the cellular contacts.* Cell and Tissue Research, 2004. **315**(2): 157-166.
14. Malina, K.C.K., I. Cooper, and V.I. Teichberg, *Closing the gap between the in-vivo and in-vitro blood-brain barrier tightness.* Brain Research, 2009. **1284**: 12-21.
15. Tio, S., M. Deenen, and E. Marani, *Astrocyte-mediated induction of alkaline phosphatase activity in human umbilical cord vein endothelium: an in vitro model.* European journal of morphology, 1990. **28**(2-4): 289.

16. Paulson, O.B. and E.A. Newman, *Does the release of potassium from astrocyte endfeet regulate cerebral blood flow?* Science (New York, NY), 1987. **237**(4817): 896.

17. Rouget, C., *Note sur le developpement de la tunique contractile des vaisseaux.* Compt Rend Acad Sci, 1874. **59**: 559-62.

18. Gerhardt, H. and C. Betsholtz, *Endothelial-pericyte interactions in angiogenesis.* Cell and Tissue Research, 2003. **314**(1): 15-23.

19. Louissaint, A., et al., *Coordinated interaction of Neurogenesis and angiogenesis in the adult songbird brain.* Neuron, 2002. **34**(6): 945-960.

20. Balabanov, R., T. Beaumont, and P. Dore-Duffy, *Role of central nervous system microvascular pericytes in activation of antigen-primed splenic T-lymphocytes.* Journal of Neuroscience Research, 1999. **55**(5): 578-587.

21. Balabanov, R., et al., *CNS microvascular pericytes express macrophage-like function, cell surface integrin alpha M, and macrophage marker ED-2.* Microvascular Research, 1996. **52**(2): 127-142.

22. Doherty, M.J. and A.E. Canfield, *Gene expression during vascular pericyte differentiation.* Critical Reviews in Eukaryotic Gene Expression, 1999. **9**(1): 1-17.

23. Armulik, A., et al., *Pericytes regulate the blood-brain barrier.* Nature, 2010. **468**(7323): 557.

24. Korn, J., B. Christ, and R. Kurz, *Neuroectodermal origin of brain pericytes and vascular smooth muscle cells.* Journal of Comparative Neurology, 2002. **442**(1): 78-88.

25. Peppiatt, C.M., et al., *Bidirectional control of CNS capillary diameter by pericytes.* Nature, 2006. **443**(7112): 700-704.

26. Crisan, M., et al., *A perivascular origin for mesenchymal stem cells in multiple human organs.* Cell Stem Cell, 2008. **3**(3): 301-313.

27. Caplan, A.I., *All MSCs are pericytes?* Cell Stem Cell, 2008. **3**(3): 229-230.

28. Dohgu, S., et al., *Brain pericytes contribute to the induction and up-regulation of blood-brain barrier functions through transforming growth factor-beta production.* Brain Research, 2006. **1038**(2): 208-216.

29. Antonelliorlidge, A., et al., *An activated form of transforming growth factor-beta is produced by cocultures of endothelial-cells and pericytes.* Proceedings of the National Academy of Sciences of the United States of America, 1989. **86**(12): 4544-4548.

30. Carvalho, R.L.C., et al., *Defective paracrine signalling by TGF beta in yolk sac vasculature of endoglin mutant mice: a paradigm for hereditary haemorrhagic telangiectasia.* Development, 2004. **131**(24): 6237-6247.

31. Canfield, A.E., et al., *Modulation of extracellular-matrix biosynthesis by bovine retinal pericytes in vitro - effects of the substratum and cell-density.* Journal of Cell Science, 1990. **96**: 159-169.

32. Schor, A.M., et al., *Differentiation of pericytes in culture is accompanied by changes in the extracellular-matrix.* In Vitro Cellular & Developmental Biology, 1991. **27**(8): 651-659.

33. Bardin, N., et al., *S‚ÄêEndo 1, a pan‚Äêendothelial monoclonal antibody recognizing a novel human endothelial antigen.* Tissue antigens, 1996. **48**(5): 531-539.

34 Cerletti, M., et al., *Melanoma cell adhesion molecule is a novel marker for human fetal myogenic cells and affects myoblast fusion.* Journal of cell science, 2006. **119**(15): 3117-3127.

35. Kumar, P., et al., *Transvascular delivery of small interfering RNA to the central nervous system.* Nature, 2007. **448**(7149): 39-43.

36. Tao, Y.H., J.F. Han, and H.Y. Dou, *Brain-targeting gene delivery using a rabies virus glycoprotein peptide modulated hollow liposome: bio-behavioral study.* Journal of Materials Chemistry, 2012. **22**(23): 11808-11816.

Chapter 7

Polymersomes *In vivo* Assessment

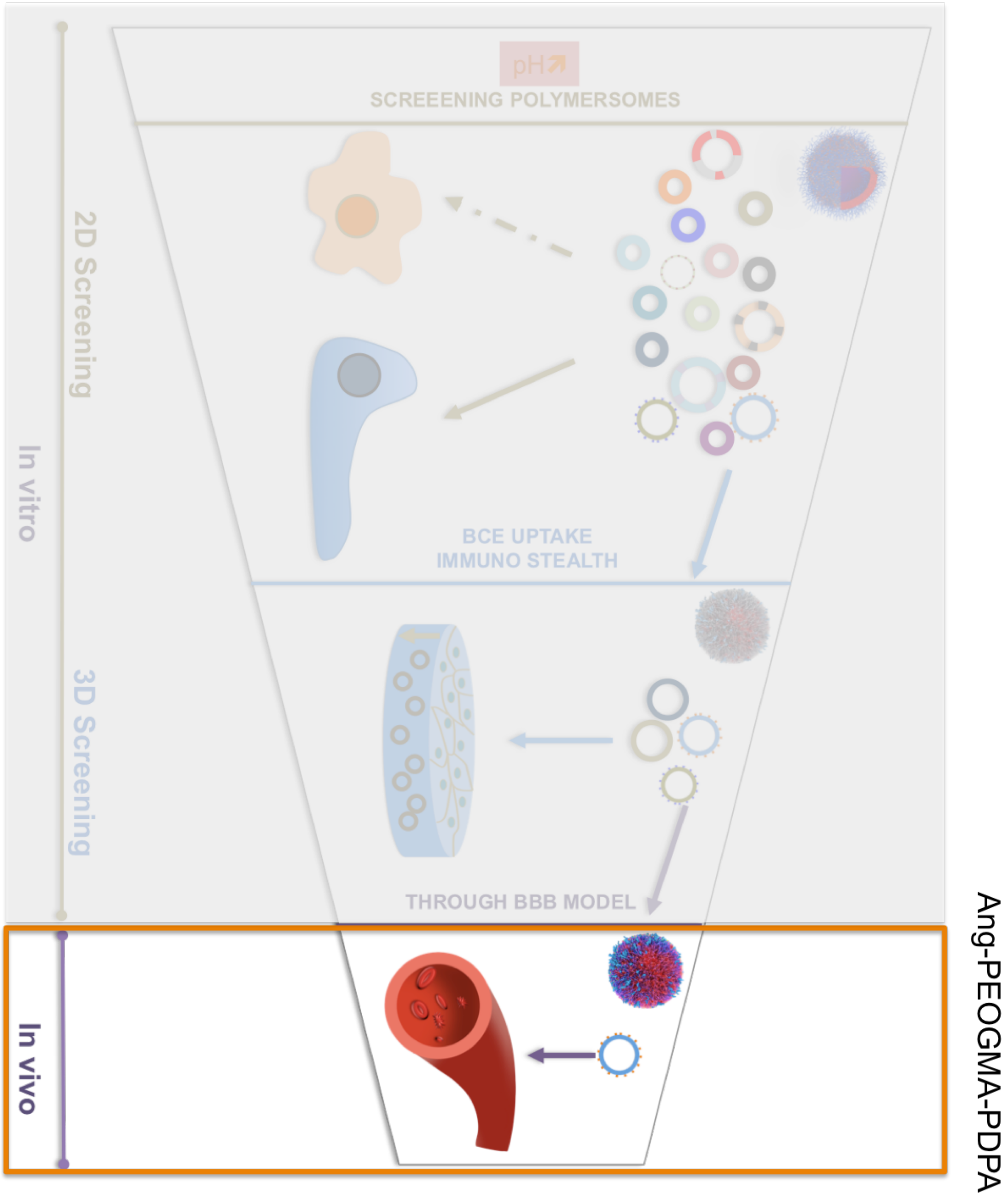

Schematic representation of polymersomes *in vivo administration*

7.1 Preliminary study of polymersome *in vivo* CNS distribution

Angiopeps (Angiopep1, Angiopep2) are known to bind to the LRP-1 (low-density lipoprotein related protein-1), which is associated with receptor-mediated transcytosis. Angiopep2 has recently been used as a BBB targeting ligand for several CNS delivery systems. Previous studies have demonstrated that Angiopep-functionalised PEGylated nanoparticles [1, 2], polymeric micelles [3] and dendrimers [4] show good penetration into the CNS after intravenous (IV) administration.

In this project, after screening approximately 40 formulations of polymersomes in 2D and 3D *in vitro* BBB models (Chapter 5 and Chapter 6), Angiopep (1.2%)-functionalised POEGMA-PDPA polymersomes were found to target the receptor-mediated transcytosis pathway.

Compared to other Angiopep-modified delivery vectors, Ang-POEGMA-PDPA polymersomes with a pH-sensitive delivery system possesses several advantages. Firstly, the vesicular nature of polymersomesmallows encapsulation of hydrophobic and/or (almost uniquely) hydrophilic molecules. Secondly, the supra-molecular nature of polymersomes enables fine control of the amount of ligand both in terms of type and concentration (work in progress) toward the design of multifunctional systems. Thirdly, PDPA-based polymersomes are pH sensitive and, as discussed in Chapter 2, this enables effective cytosolic delivery.

To demonstrate the potential capability of Angiopep-functionalised polymersomes to penetrate the BBB *in vivo*, Ang (1.2%)-POEGMA-PDPA

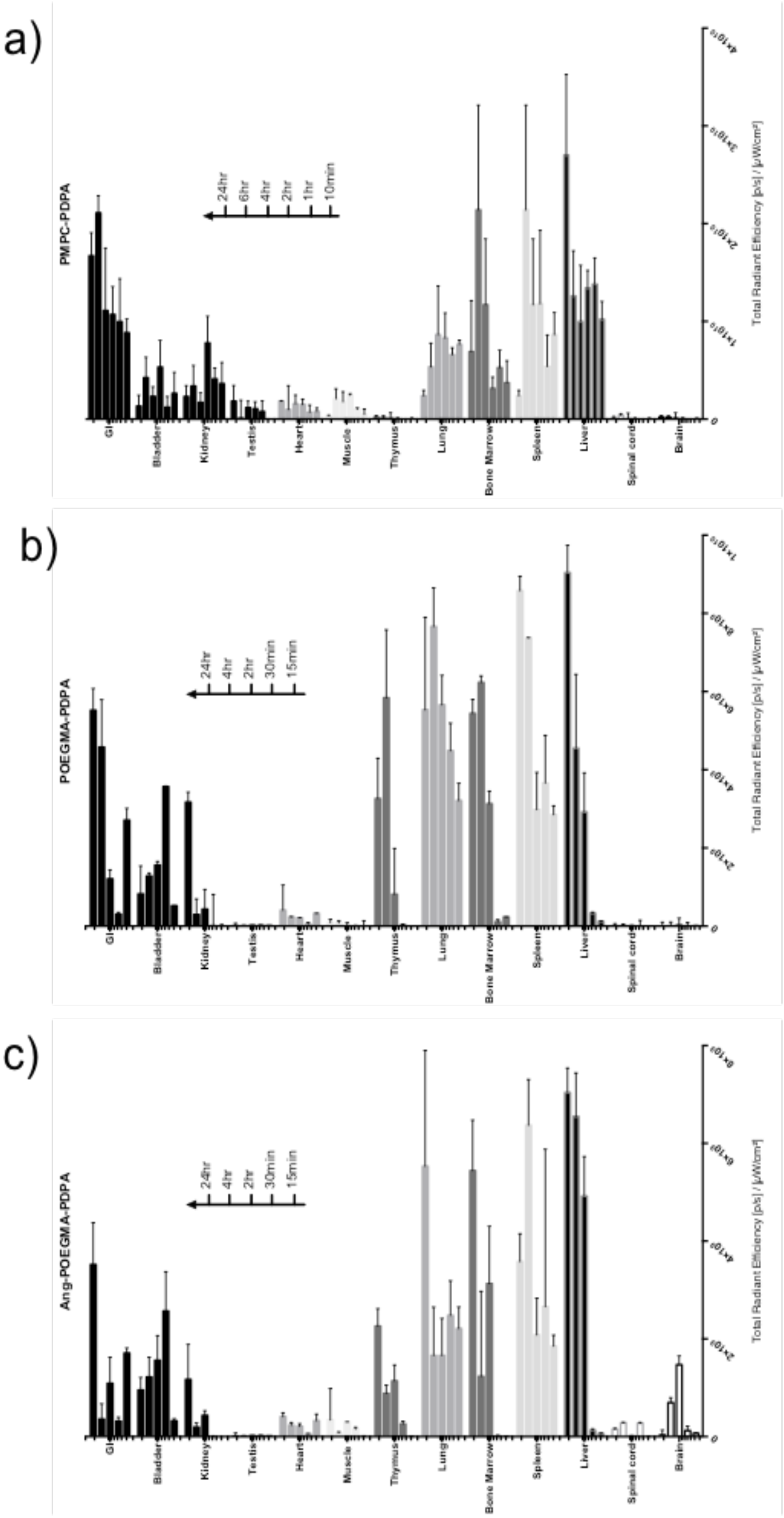

Figure 7.1 *Ex vivo* quantitative fluorescence imaging using IVIS Spectrum. *Ex vivo* quantitative fluorescence imaging showing time-course of signal

from polymersomes in different tissues after IV injection in mice: a) PMPC-PDPA, b) Pristine POEGMA-PDPA, c) Angiopep-2-POEGMA-PDPA. (Error bar SD, N=5)

(10% Rh-POEGMA-PDPA) polymersomes, PMPC-PDPA (10% Rh-PMPC-PDPA)and pristine POEGMA-PDPA (10% Rh-POEGMA-PDPA) were administered in mice by tail-vein injection. PMPC-PDPA, pristine PEOGMA-PDPA and Angiopep-2-POEGMA-PDPA polymersome distribution in animals was analysed by *ex vivo* quantitative fluorescence imaging using IVIS Spectrum (data supplied by Dr Nooshin Danespour). The half-life of PMPC and POGEMA polymersome plasma circulation time was measured by collecting blood at several time points and this was estimated to be c.a. 10 minutes for PMPC-PDPA and about two hours for POEGMA systems (both pristine and peptide modified). In Figure 7.1 the distribution of the three different polymersomes were shown as total radiant efficiency measured from the excised organ; this value is the absolute count of photons and can be assumed to change linearly with the polymersome concentration. More work is underway to calibrate this relation and to translate these data into actual polymersome mass. However, at this stage, these are a good indication of the polymersome distribution. Figure 7.1a shows PMPC-PDPA polymersomes rapidly internalised within the liver, spleen and bone marrow, being detectable at very early time points (15 minutes and 30 minutes). This is expected, considering the strong affinity of PMPC for the scavenger receptor B and the high expression of these receptors in immune cells and liver cells. However, some PMPC-PDPA polymersomes were also found in the CNS (both brain and spinal cord). The pristine POEGMA-PDPA polymersomes (Figure 7.1b) showed much less material within the liver, spleen and bone marrow at early time points (15 minutes and 30 minutes) in accordance with their longer half-life. Angiopep-2-functionalised POEGMA-PDPA polymersomes (Figure 7.1c) showed a similar uptake level in the liver and the spleen compared to pristine POEGMA-PDPA polymersomes, suggesting that the peptide functionalisation did not alter the POEGMA immune response. The dose percentage for brain uptake (at two hours and 24 hours) from each polymersome formulation was normalised, as shown in Figure 7.2.

Interestingly, Angiopep-2-POEGMA-PDPA polymersome brain uptake showed a sharp increase from 30 minutes to approximately two hours, then gradually dropped to a low level at 24 hours. This can be better visualised in Figure 7.3. Here it is shown that functionalised polymersomes have a different uptake trend in the brain and the liver. Ang-POEGMA-PDPA polymersome

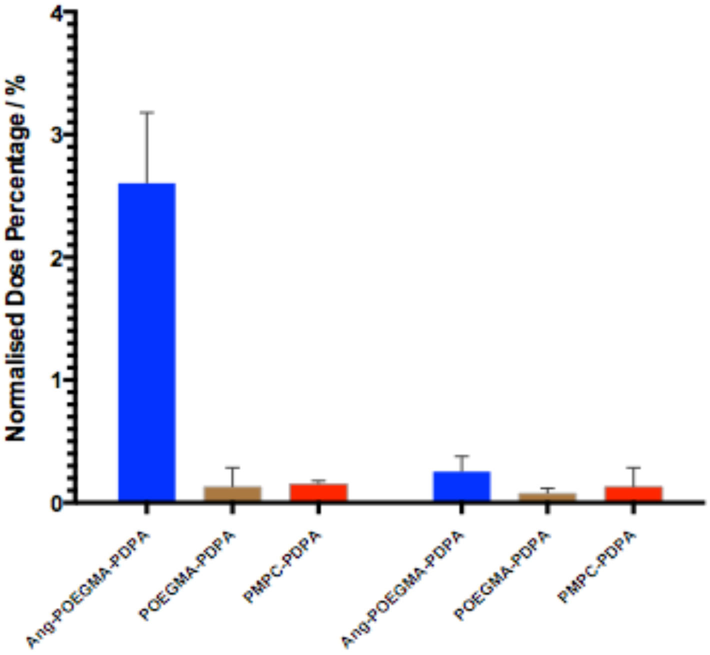

Figure 7.2 Normalised percentage dose in mouse brain at 2 hours (left) and 24 hours (right) post IV injection for PMPC-PDPA, POEGMA-PDPA and Ang-POEGMA-PDPA polymersomes**.** (Error bar SD, N=5)

distribution in the brain and the liver are very similar at an early time point. However, for longer times, while the brain uptake peaks at around two hours, at 24 hours the polymersome signal drops significantly. This likely indicates brain clearance over this time course.

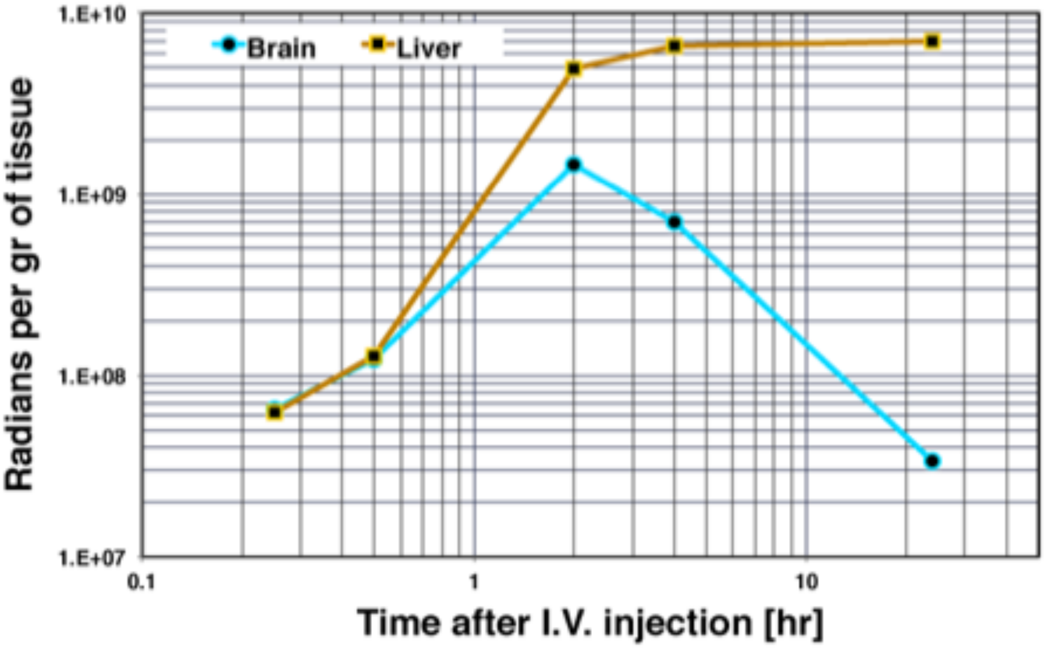

Figure 7.3 Angiopep-2-POEGMA-PDPA polymersomes in mouse brain and liver over time. *Ex vivo* quantitative fluorescence imaging using IVIS Spectrum, showing Ang-POEGMA-PDPA polymersome uptake in brain and liver over time following IV injection.

In this chapter I focus on understanding polymersome distribution within the CNS tissues. To visualise the spatial distribution we sectioned organs and analysed the polymersome distribution by immunofluorescence. In order to minimise live tissue auto-fluorescence, brain sections from non-treated mice were taken and examined under confocal microscopy. The microscopy parameters, including laser power, laser transmission intensity, pinhole aperture, detector-gain and emission filter, were carefully adjusted (more details are given in the Experimental section), and the auto-fluorescence was minimised, as shown in the cerebellum section (CB, Figure 7.4a) and choroid plexus (CP, Figure 7.4b) section. The microscopy parameters were first adjusted with a control section then kept the same for all other samples.

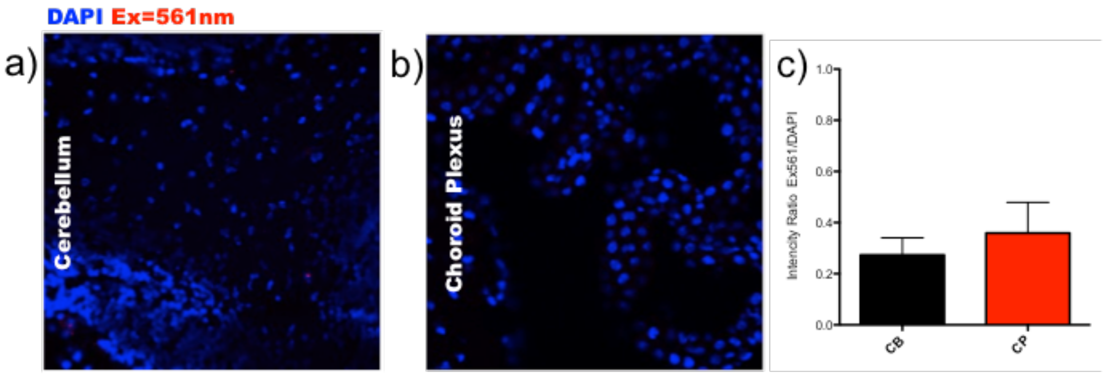

Figure 7.4 Confocal micrographs of brain sections (control) from mouse not treated with polymersomes. Control sections a) cerebellum (CB), b) choroid plexus (CP). (Ch1, λ_{Ex}=405nm, Ch2, λ_{Ex}=560nm). c) Fluorescence intensity analysis for control CB and CP. (Error bar SEM, data points = 30).

As shown in Figure 7.5, the fresh liver sections were primarily stained by DAPI, and the polymersome signal was excited in 560nm PMPC-PDPA and showed significant uptake by liver tissues (Figure 7.5a), in accordance with its affinity for SRB receptors. Tissue sections for both POEGMA-PDPA polymersomes (Figure 7.5a) and Angiopep-2-functionalised POEGMA-PDPA polymersomes (Figure 7.5a) showed that fewer polymersomes were retained within the liver, confirming the pharmacokinetics analysis.

As shown in Figure 7.5, 24 hours post-injection liver and brain tissues were analysed by confocal imaging. In Figures 7.5a-c representative

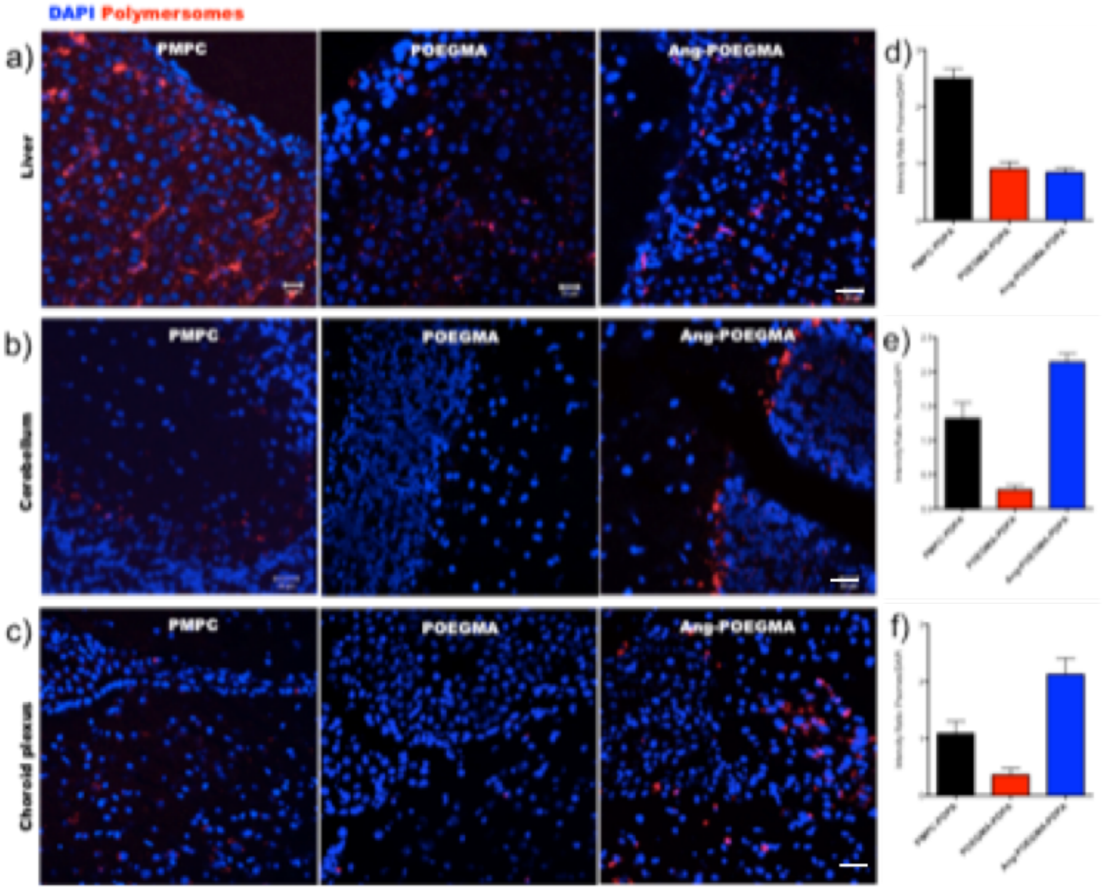

Figure 7.5 Histological analysis of liver and brain, 24 hours post IV injection. a) Liver, b) Cerebellum, c) Choroid plexuses. The scale bars represent 20µm. d). e) and f) Fluorescence intensity analysis and comparison of PMPC-PDPA, PEOGMA-PDPA and Ang-POEGMA-PDPA polymersomes in liver, cerebellum and choroid plexus respectively. (Error bar SEM, ROI data points=30, $Y_{value}=In_{Psomes}/In_{DAPI}$)

micrographs were shown, while Figures 7.5d-f show respective quantitative analyses performed across three different animals (for each, three slices were analysed) to show the polymersomes. All cells were stained by DNA dye DAPI and the rhodamine signal was normalised against the DAPI signal. PMPC-PDPA polymersomes showed much less internalisation within the cerebellum (Figures 7.5b and e); very likely the majority of the material was removed by immune cells and RES organs before reaching the CNS. As discussed previously, this was due to the affinity of PMPC for SRB receptors. However, SRBs, and SRB-1 in particular, was expressed in brain endothelial cells and associated with transcytosis [5, 6]. This could explain why some minimal signal was visible within the brain sections. As anticipated, pristine PEOGMA-PDPA polymersomes showed hardly any signal in brain (Figures 7.5b and e). By contrast, Ang-POEGMA-PDPA polymersomes showed considerable uptake in the brain sections (Figure 7.5b and e), suggesting Angiopep-2-functionalised POEGMA polymersomes entered CNS more effectively than PMPC-PDPA and pristine POEGMA-PDPA polymersomes. As described in the 3D BBB *in vitro* model, Angiopep-2-functionalised POEGMA-PDPA polymersomes penetrated brain endothelial cells via receptor-mediated transcytosis. Similar to the cerebellum, the polymersome signal can also be found in the choroid plexus (CP) sections. Non-functionalised PEOGMA-PDPA showed little uptake in the CP (Figures 7.5c and f). PMPC-PDPA showed relatively higher intensity in the CP (Figures 7.5c and f). Angiopep-2-functionalised POEGMA-PDPA polymersomes revealed much more uptake than shown in Figures 7.4c and f. As discussed in Chapter 1, CP is a vascularised tissue formed by epithelial cells with tight junctions, and a fenestrated endothelium. The major function of the CP is to produce the CSF. Recent studies [7] have demonstrated that some CSF combines with interstitial fluid (ISF) flowing through the perivascular space within the NVU (BBB and astrocyte end feet) and may help clear metabolic waste from the parenchyma. However, this is unlikely to be a route back to the CP since the CP is the source not the drainage site for CSF. More likely is that polymersomes enter CP by crossing the leaky capillary endothelium there, then are either trapped in CP stroma, or taken up by the CP epithelium.

However, these possibilities need further investigation, e.g. following *in situ* brain perfusion with CP sampling and higher resolution microscopy.

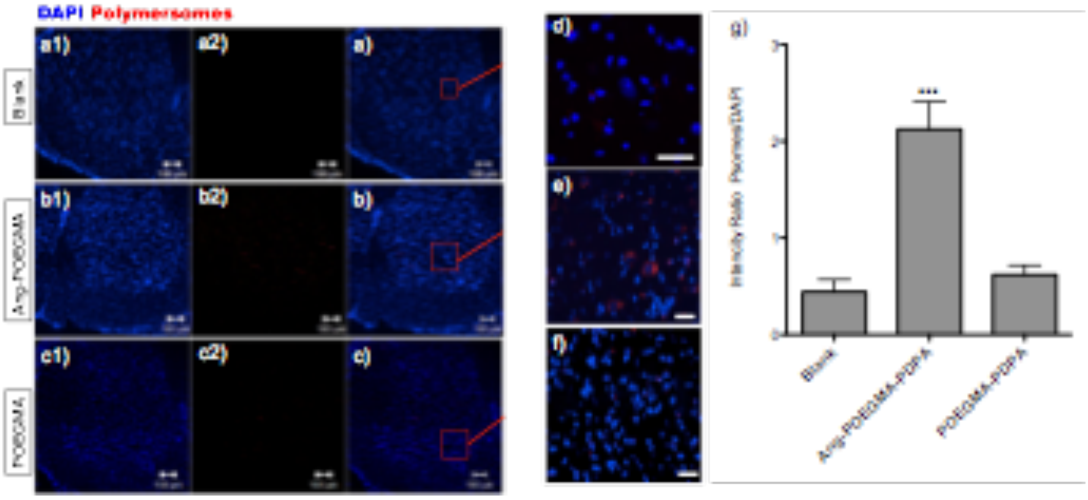

Figure 7.6 Confocal micrographs of spinal cord sections from mice treated with polymersomes (24 hours, IV). Polymersome treatments: a) PMPC-PDPA, b) POEGMA-PDPA, c) Ang-POEGMA-PDPA . a1), b1) and c1) DAPI (λ_{Ex}=405nm). a2), b2) and c2), polymersomes (λ_{Ex}=560nm). The scale bars represent 100μm. d), e) and f) Higher magnification images of selected regions from a), b) and c). The scale bars represent 20μm. g) Fluorescence intensity analysis and comparison of blank, PEOGMA-PDPA and Ang-POEGMA-PDPA polymersomes in spinal cord. (Error bar SEM, ROI data points=30, $Y_{value}=In_{Psomes}/In_{DAPI}$).

Spinal cord sections were also examined (Figure 7.6). Higher magnification micrographs from specific regions in spinal cord grey matter were shown in Figures 7.6d-f. It is clear that the Ang-POEGMA-PDPA-treated spinal cord showed a higher signal than for non-functionalised POEGMA-PDPA polymersomes. More studies on polymersome uptake by spinal cord will be done in the future.

7.2 Assessing transcytosis *in vivo*

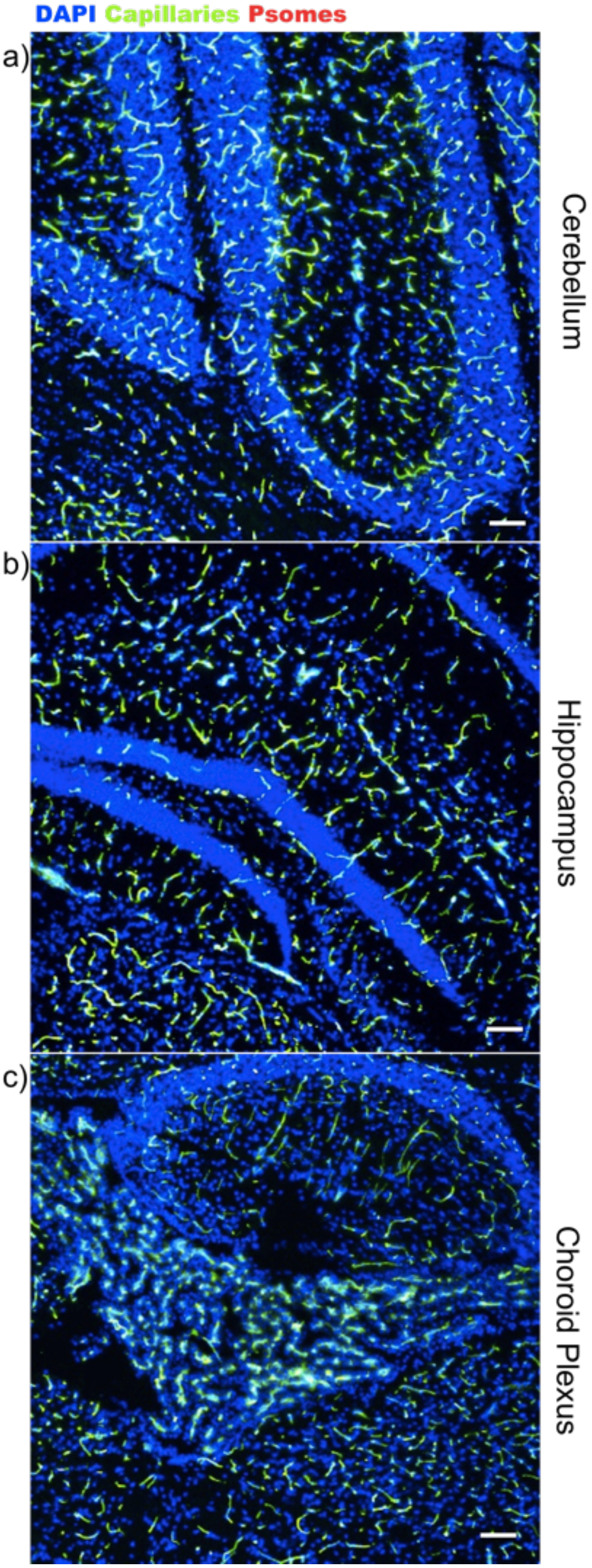

Figure 7.7 Lectin-stained capillaries in brain sections from mice at 24 hours post IV injection with POEGMA-PDPA polymersomes. Sections from a) Cerebellum, b) Hippocampus, c) Choroid plexus. Capillaries (lectin, λ_{Ex}=488nm). The scale bars represent 50μm.

As outlined in Chapter 2, the endothelial cells of brain capillaries forming the BBB are thin cells with many specialized transport systems allowing rapid but controlled exchange of critical substances between the blood and the brain, and exclusion of many potentially damaging agents. In order to seek more detail on Angiopep-2-functionalised POEGMA-PDPA polymersomes that transcytose the BBB *in vivo*, all the brain blood capillaries were stained using lectin marker [9,10] to provided a useful landmark. As indicated in the pharmacokinetic studies, the uptake of Ang-POEGMA-PDPA in the CNS reached the highest level at an early time point, hence micrographs from two hours post-injection were captured. In Figure 7.6 CNS sections were shown for non-functionalised POEGMA-PDPA polymersomes (10mg/ml, 50µl) after 24 hours.

As shown in Figure 7.7, all images revealed details of the brain cellular structure; in addition, the endothelial cells stained by lectin showed the complexity of the brain capillary network throughout the brain tissue. As the non-functionalised POEGMA-PDPA polymersomes remained ‘stealthy’ over 24 hours, there was no obvious uptake in any examined section.

Following this negative control test, PMPC-PDPA and Ang-POEGMA-PDPA polymersomes were then injected into the tail vein at a dose of 50 µl 10mg/ml. Two groups of animals were sacrificed two hours and 24 hours respectively post-injection. Micrographs from two-hour and 24-hour CP and hippocampus (HP) sections treated with PMPC-PDPA and Ang-POEGMA-PDPA polymersomes are shown in Figure 7.8.

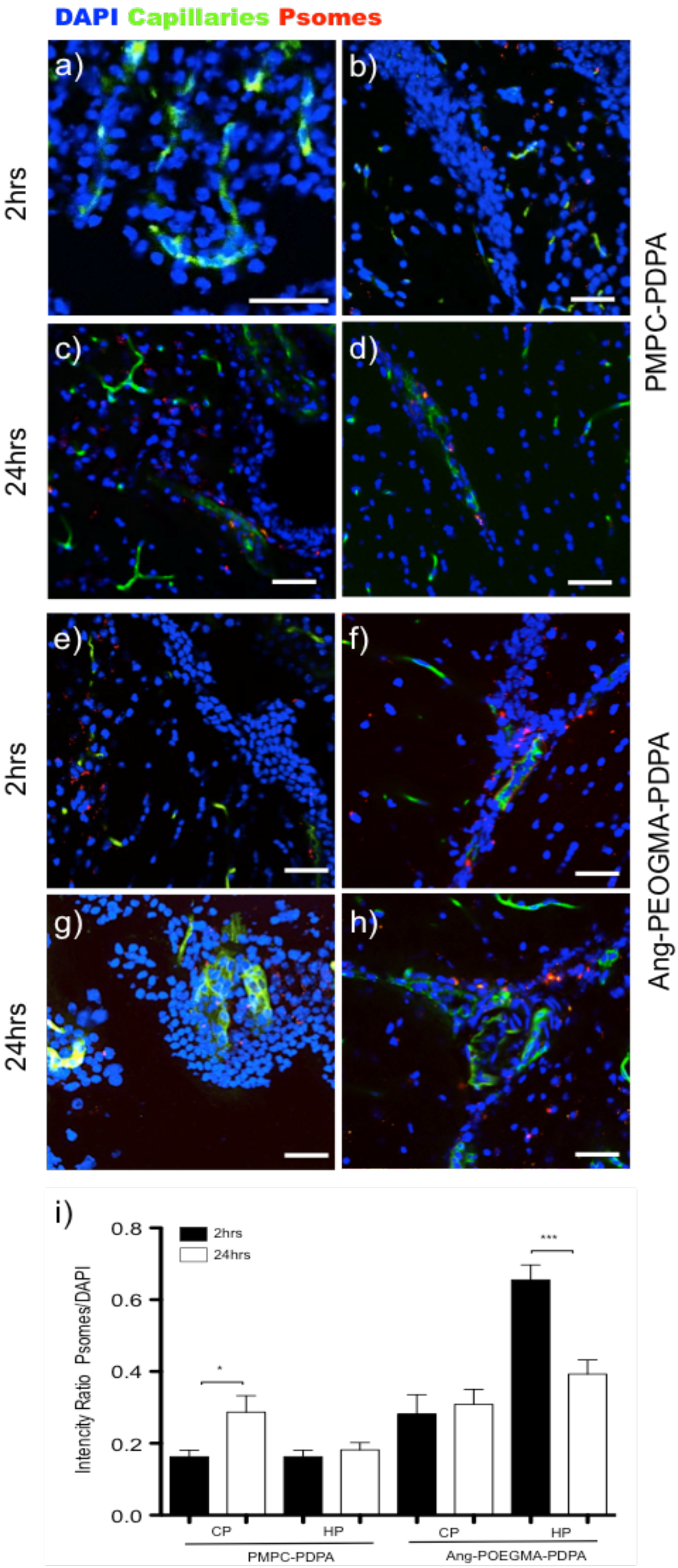

Figure 7.8 Choroid plexus (CP) and hippocampus (HP) sections from mice treated with PMPC-PDPA or Ang-POEGMA-PDPA polymersomes at

2 hours and 24 hours post-injection (IV). a) CP, PMPC-PDPA, 2 hours. b) HP, PMPC-PDPA, 2 hours. c) CP, PMPC-PDPA, 24 hours. d) HP, PMPC-PDPA, 24 hours. e) CP, Ang-POEGMA-PDPA, 2 hours. f) HP, Ang-POEGMA-PDPA. 2 hours. g) CP, Ang-POEGMA-PDPA, 24 hours. h) HP, Ang-POEGMA-PDPA, 24 hours. The scale bars represent 50μm. i) Florescence intensity analysis of PMPC-PDPA and Ang-POEGMA-PDPA polymersome uptake in CP and HP, at 2 hours and 24 hours. (ROI data points=30, $Y_{value}=In_{Psomes}/In_{DAPI}$).

The signal of PMPC-PDPA polymersomes (CP Figure 7.8a, HP figure 7.8b) was retained at a very low level after two hours of treatment. Polymersome uptake increased from two hours to 24 hours in both CP (Figure 7.8c) and HP (Figure 7.8d), and showed a close association with the capillary endothelium (Figure 7.8d). There was a strong internalisation of PMPC-PDPA polymersomes by capillary endothelial cells, consistent with SRB-1 receptors being over-expressed on brain capillary endothelium (as discussed before). The PMPC-PDPA polymersome signal that can be observed in CP may be derived from blood in leaky CP capillaries as discussed above.

The *in vivo* PMPC-PDPA polymersome uptake data matched the results from the 2D screening and 3D *in vitro* models. In 2D, PMPC-PDPA polymersomes showed effective uptake by brain endothelial bEnd.3 cells, while in the 3D blood-brain barrier *in vitro* model, PMPC-PDPA polymersomes also showed strong internalisation by a bEnd.3 monolayer. However, hardly any PMPC-PDPA polymersomes were able to cross the monolayer and pass the microporous filter, suggesting they may follow the endocytosis pathway and end up in the cell monolayer.

As studied previously *in vitro* both at the 2D cellular and 3D level, Angiopep-functionalised POEGMA-PDPA polymersomes have different cellular uptake properties compared with PMPC-PDPA polymersomes (Chapter 5). Ang-POEGMA-PDPA (1.2% angiopep) showed effective transcytosis in the *in vitro*

BBB model (Chapter 6), and demonstrated presence in CNS in our initial polymersome CNS distribution studies. Can such functionalised polymersomes cross the blood-brain barrier *in vivo*? To answer this, lectin pre-injected brain sections treated with Ang-POEGMA-PDPA polymersomes (two hours and 24 hours) were examined under confocal laser scanning microscope without fixation.

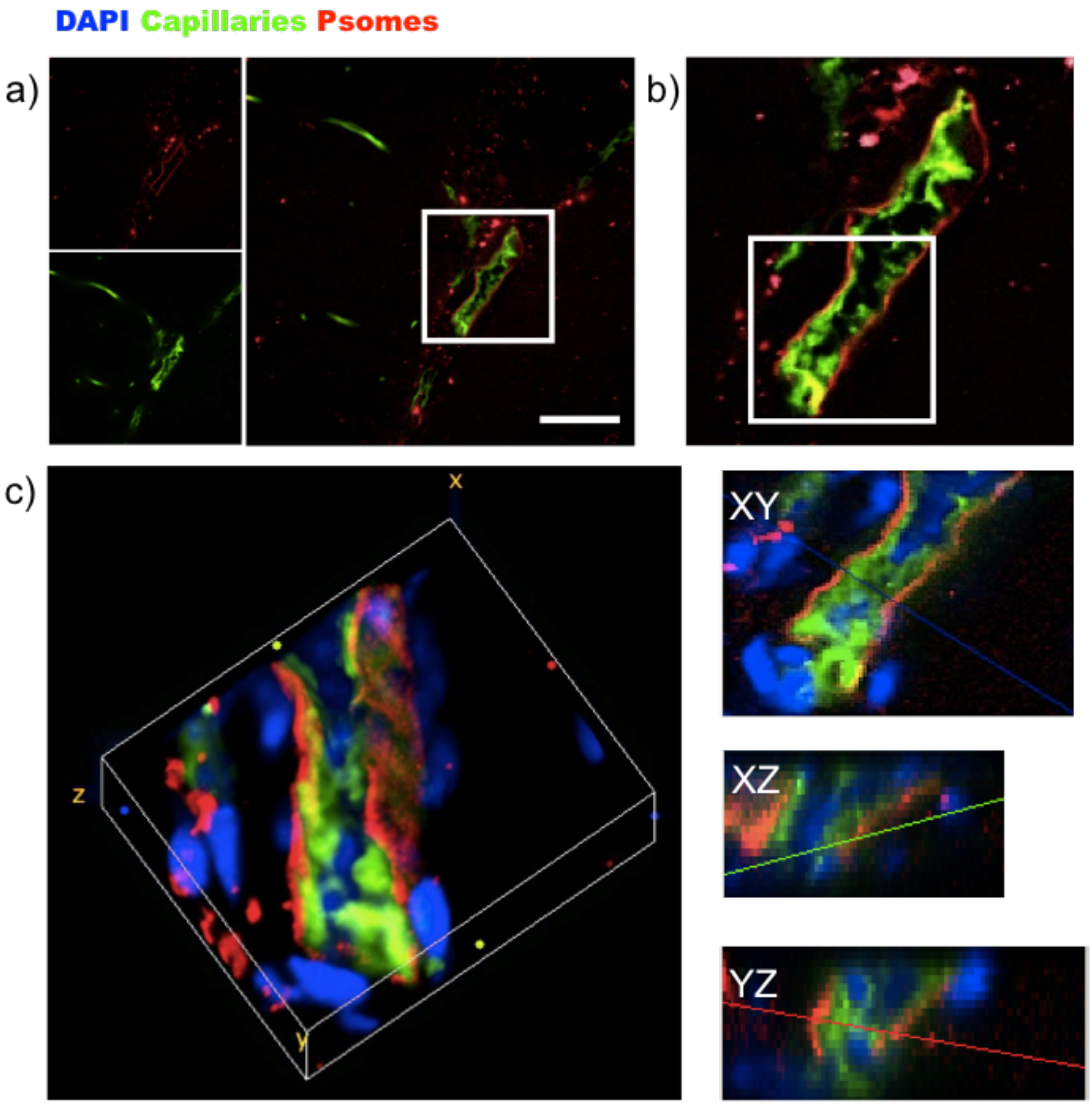

Figure 7.9 Confocal micrographs of hippocampus section from mouse 2 hours after IV injection of Ang-POEGMA-PDPA polymersomes. a) Hippocampus section. b) Higher magnification micrograph from selected region in a). c) Higher magnification micrograph from selected region in b). d) 3D reconstruction in volume viewer from selected region in c). DAPI (λ_{Ex}=405nm), Capillaries (λ_{Ex}=488nm), polymersomes (λ_{Ex}=560nm). The scale bar represent 50μm.

Unlike the PMPC-PDPA polymersome distribution in the brain, the Ang-POEGMA-PDPA polymersome signal was observed at an early time point (two hours). As shown in examined CP and HP sections (Figures 7.8e and f), florescence from Ang-POEGMA-PDPA was clearly present at two hours. The Ang-POEGMA-PDPA signal was also detected in the CP and HP sections 24 hours post-injection (Figure 7.8g and Figure 7.8h, same microscopy setting); the majority of the material appears more distributed within deeper brain tissue. As discussed above, the presence of Ang-POEGMA-PDPA in the CP may derive from the CP vasculature across the leaky fenestrated capillaries. As Ang-POEGMA-PDPA polymersomes enter the CNS much more effectively than PMPC-PDPA polymersomes, they were present at the earlier time point. As indicated previously, PMPC-PDPA polymersomes were only observed in brain tissue at 24 hours; strong internalisation within the brain capillaries was shown, but hardly any penetration could be found in the ventricular system. Angiopep-2-functionalised polymersomes, however, can be found at both two hours and 24 hours in CP sections. This could indicate either strong local binding or uptake into CP epithelium; drainage from the perivascular spaces involving CSF/ISF circulation into subarachnoid CSF spaces and back into the CP from the ventricles is unlikely given the normal circulation and drainage route for CSF, but could be investigated.

We further analysed all the micrographs taken at two hours and 24 hours, both from CP and HP sections. As shown in Figure 7.8i, PMPC-PDPA polymersomes showed less internalisation in the brain compared to Ang-POEGMA-PDPA polymersomes; fluorescence intensity of CP sections only showed a significant increase 24 hours post-injection. Fluorescence intensity from Ang-POEGMA-PDPA polymersomes reached a much higher level. Interestingly, the two-hour post-injection HP sections showed significantly higher intensity than the 24-hour sections, compatible with rapid entry then some clearance over this timecourse.

Ang-POEGMA-PDPA polymersomes crossing the BBB were further studied by 3D imaging of the brain sections at two hours and 24 hours. In Figure 7.9a, 2D imaging of the hippocampus section is shown with the polymersomes in red and the capillaries in green. These were subsequently analysed using confocal 3D reconstruction, as shown in Figure 7.9c. (Note: lower magnification views of these sections were shown in the ANNEX). Brain capillaries formed by multiple endothelial cells and associated with functionalised polymersomes (red signal) emerged, uniformly distributed at the borders of the blood vessels (Figure 7.9b, 63X magnification). In addition, it was shown that functionalised polymersomes were distributed in the brain parenchyma beyond the endothelium of the capillaries. This suggests that the Ang-POEGMA-PDPA polymersomes exploit receptor-mediated transcytosis and cross the blood-brain barrier *in vivo*. In order to view more details of polymersome transcytosis *in vivo*, a higher magnification Z-stack image was captured from the indicated region shown in Figure 7.9b (63X magnification, thickness = 20 μm); all sections were reconstructed in a 3D volume viewer (Figure 7.9c). The capillary fragment can be visualised in 3D using rendering software. This showed clearly that Angiopep-2-functionalised POEGMA-PDPA polymersomes cross the blood vessel wall.

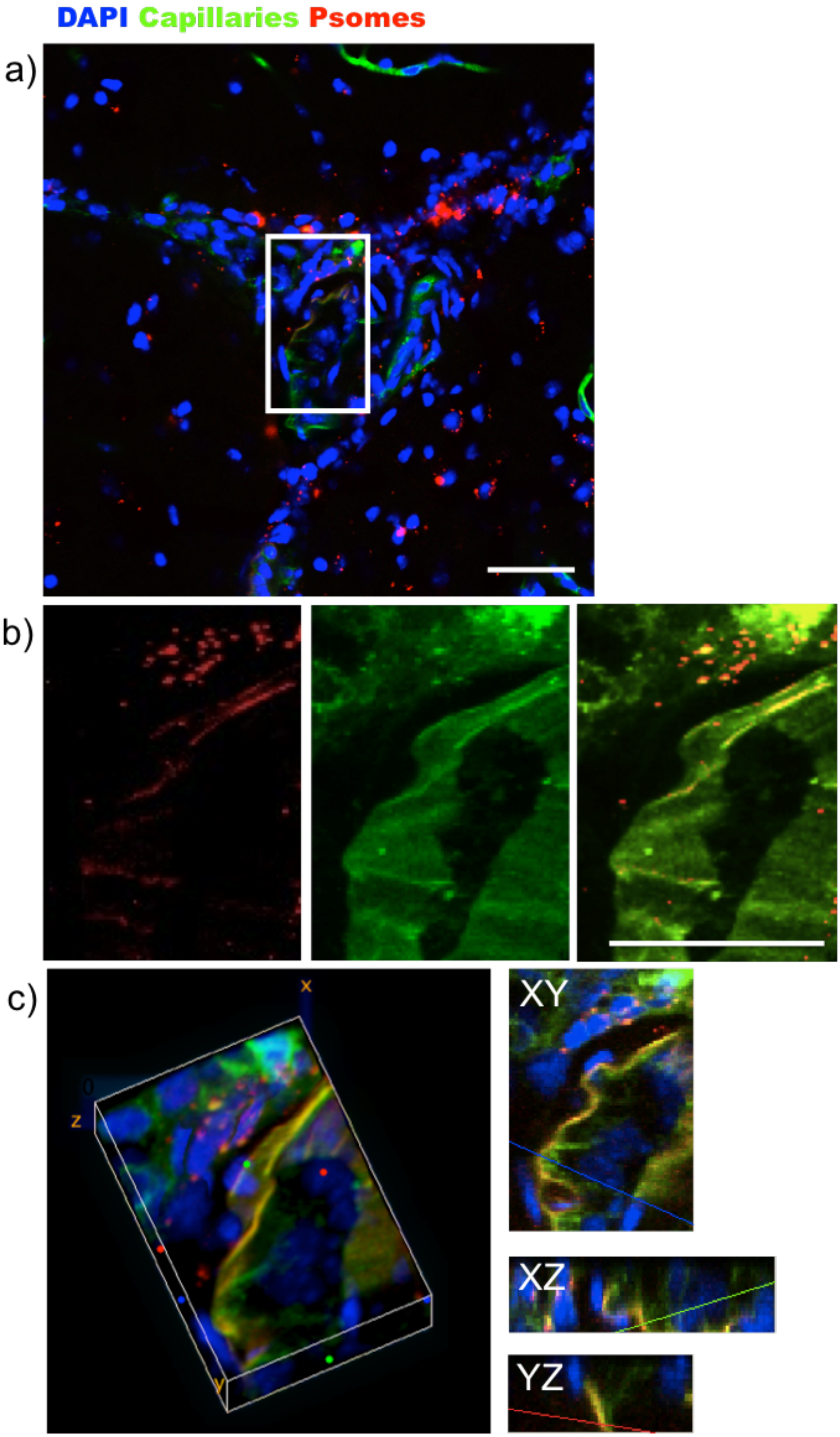
DAPI Capillaries Psomes
a)
b)
c)
x
0
z
y
XY
XZ
YZ

Figure 7.10 Confocal micrographs of hippocampus section from mice 24 hours after IV injection of Ang-POEGMA-PDPA polymersomes. a) Hippocampus section 24 hours post-injection. b) Higher magnification micrograph from selected region in a). c) 3D reconstruction in volume viewer from selected region in b). DAPI (λ_{Ex}=405nm), Capillaries (λ_{Ex}=488nm), polymersomes (λ_{Ex}=560nm). The scale bars represent 50μm.

Making a comparison between the two-hour treated sections and the 24-hour treated sections was also interesting. As indicated in Figure 7.10, signals from Ang-POEGMA-PDPA polymersomes can be found in the 24-hour treated sections; many cells throughout these brain sections showed internalised polymersomes (Figure 7.10a). However, unlike the two-hour experiment, the higher magnification image (Figure 7.10b, 40X magnification, region selected from Figure 7.10a) showed no ‘red border’ from the functionalised polymersome signal, suggesting that receptor-mediated transcytosis induced by Ang-POEGMA-PDPA polymersomes is a rapid process and may be accomplished by an earlier time point. Therefore, while many polymersomes were observed at the borders of the brain capillaries at the early time point, suggesting ongoing transcytosis, by 24 hours most of the functionalised polymersomes had already crossed through the capillary endothelium and penetrated into the parenchyma.

Further investigation of the fluorescence intensity signal from the functionalised polymersomes through the capillaries, showed a significant difference in polymersome penetration between the short and longer time points (Figure 7.11). A ROI (region of interest) was marked by a red line (Figure 7.11a and Figure 7.11c), and the fluorescence intensity of the functionalised polymersomes and lectin across the line was analysed. At the earlier two-hour time point (Figure 7.11b), polymersomes show co-localisation at the borders of capillaries, as indicated by the red (polymersomes) intensity. However, by 24 hours, the red polymersome border has disappeared (Figure 7.11d), hence the red (polymersome) intensity within the capillary endothelial cells decreased significantly compared with the two hours graph.

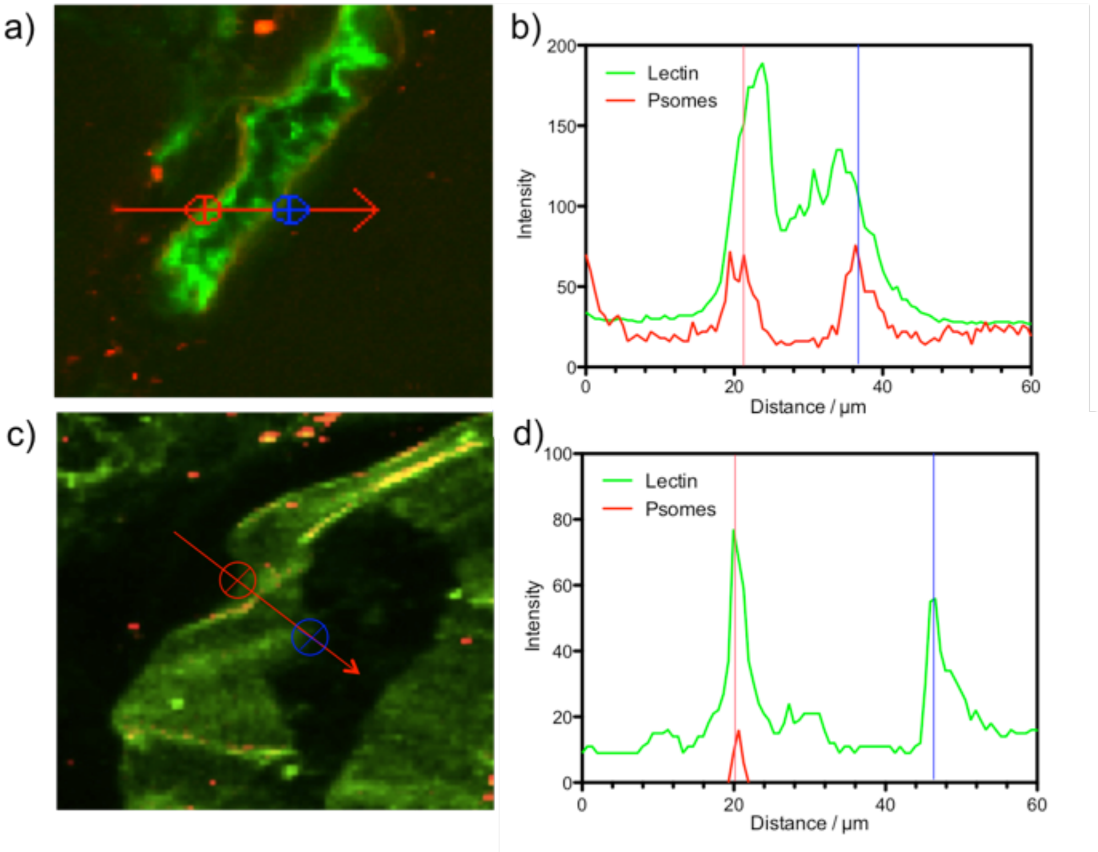

Figure 7.11 Fluorescence intensity analysis of polymersomes and lectin across hippocampus brain capillary. a) Confocal micrograph, 2 hours post-injection (IV) with Ang-POEGMA-PDPA polymersomes, showing ROI (region of interest, red line). b) 2 hours ROI Fluorescence intensity analysis for polymersomes and lectin across the brain capillary in a). c) Confocal micrograph, 24 hours post-injection with Ang-POEGMA-PDPA polymersomes showing ROI. d) 24 hours ROI Fluorescence intensity analysis for polymersomes and lectin across the brain capillary.in c).

7.3 IgG delivery into CNS by functionalised polymersomes

So far, evidence for penetration of Angiopep-2-functionalised polymersomes Ang-POEGMA-PDPA (1.2%) into the brain via receptor-mediated transcytosis has been presented. Not only can abundant functionalised polymersomes be found fully distributed into brain tissues in examined long-term treated sections, but also the ongoing receptor-mediated transcytosis has been captured by CLS microscopy at an early time point.

However, several questions remain unanswered. Firstly, although the polymersomes appear to have penetrated the brain tissue, the cellular events mediating the proposed RMT have not been examined. It is crucial to clarify whether any endosomal or lysosomal process is involved when polymersomes cross brain endothelial cells, as PDPA polymersomes are pH sensitive and disassemble in an acidic environment [10]. Hence we cannot distinguish whether the signal in the brain parenchyma is from polymersomes or from disassembled polymer chains. Second, the BBB is part of a complex neurovascular unit involving endothelium, astrocytes, pericytes and neurons [11]. Can such functionalised polymersomes target astrocytes or neurons after BBB penetration?

To clarify and answer the above questions, we tested the use of Angiopep-2-functionalised POEGMA-PDPA polymersomes as a tool for CNS delivery *in vivo*. Therefore, an antibody (Abcam) was encapsulated within Ang-POEGMA-PDPA polymersomes (10mg/ml, initial IgG concentration: 200μl/ml) via electroporation as reported previously [12]. The IgG-loaded Ang-POEGMA-PDPA polymersomes were then purified as described before, their vesicular morphology was confirmed by TEM and the loading efficiency was calculated by HSA UV spectrum, which is approximately 7% (data not shown).

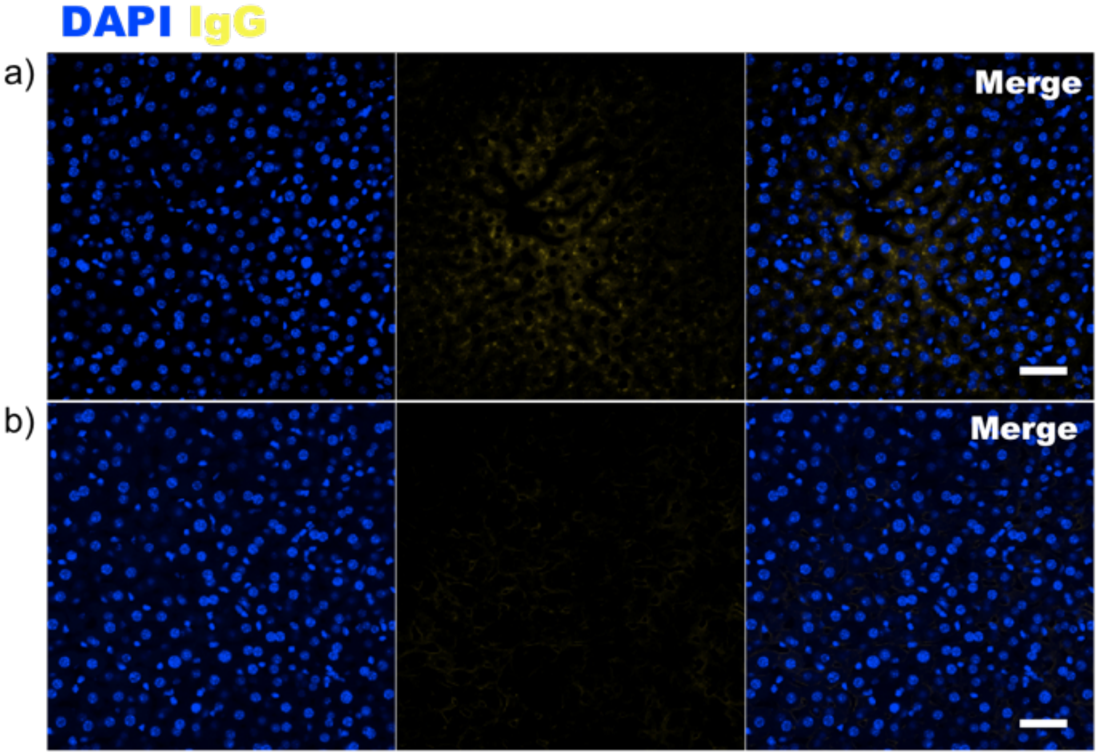

Figure 7.12 Confocal micrographs of liver sections from mice treated with free IgG or IgG-loaded functionalised polymersomes. Sections from mice 2 hours post-injection (IV) with a) free IgG, b) IgG-loaded Ang-POEGMA-PDPA polymersomes. DAPI (λ_{Ex}=405nm, λ_{Em}= BP420-450nm). IgG (λ_{Ex}=560nm, λ_{Em}= BP575-615nm). The scale bars represent 50μm.

To examine whether such functionalised polymersomes were able to transport cargo across the blood-brain barrier via transcytosis, 50μl IgG-loaded Ang-POEGMA-PDPA polymersomes were injected into a mouse-tail vein. A control animal was also injected with the same amount of free IgG (50μl X 10^{-3} X 200μl/ml X 0.07). As indicated previously, brain sections after short time points (two-hour treatment) showed ongoing transcytosis, and functionalised polymersomes clearly demonstrated BBB penetration. Hence, the IgG-loaded Ang-POEGMA-PDPA polymersome-treated animals and control animals were both sacrificed after two hours post-injection.

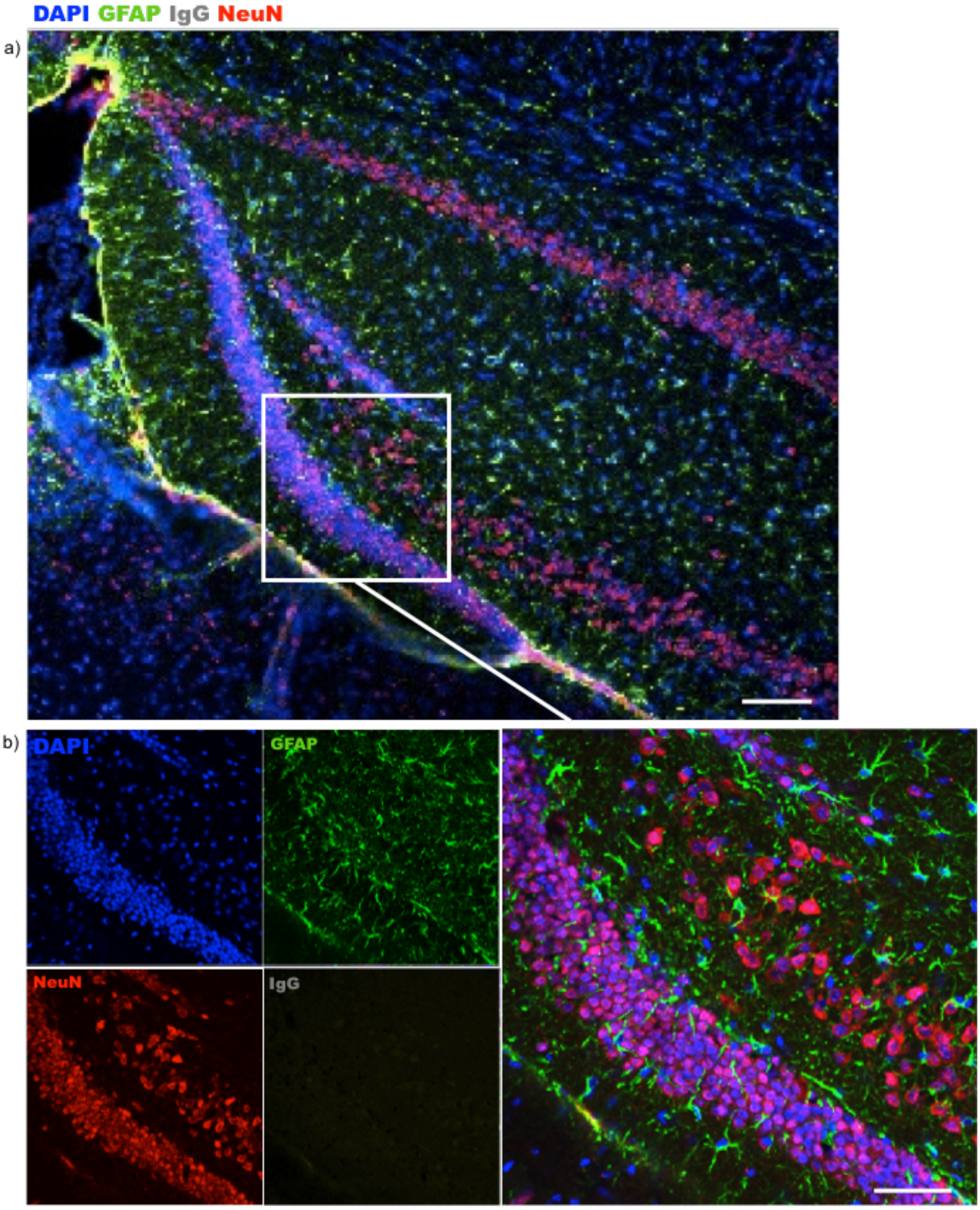

Figure 7.13 Confocal micrographs of control mouse brain sections 2 hours after IV injection with free IgG. a) Control brain section with astrocyte and neuronal cell double labelling, 10X magnification. b) Higher magnification image from indicated region in a) with serial windows demonstrating nuclear (DAPI), astrocyte (GFAP), neuronal (NeuN) and IgG labelling. DAPI (λ_{Ex}=405nm, λ_{Em}= BP420-450nm), GFAP (λ_{Ex}=480nm, λ_{Em}= BP500-520nm), NeuN (λ_{Ex}=633nm, λ_{Em}= BP650-700nm) IgG (λ_{Ex}=560nm, λ_{Em}= BP575-615nm). The scale bars represent 50µm.

Liver sections from both experimental and control animals were examined first. IF (immunofluorescence chemistry) was performed on the sections in order to visualise delivered cargo IgG (Figure 7.12). As presented in Figure 7.12a, the free IgG clearly shows distribution and internalisation within liver tissues. However, the liver sections showed minimal uptake of IgG loaded Ang-POEGMA-PDPA polymersomes (Figure 7.12b), suggesting that at two hours, functionalised POEGMA-PDPA polymersomes remain ‘stealthy’ towards liver response.

The control brain sections treated with free IgG were then examined. In order to study this in more detail, astrocytes and neurons were stained using GFAP and NeuN antibodies respectively. As presented in Figure 7.13a, brain sections (10X magnification) show a hippocampus region and part of the third ventricle. All cellular nuclei were stained by DAPI, and astrocytes (GFAP, green) and neurons (NeuN, red) are shown. As the choroid plexus mainly consists of epithelial cells and endothelium, with associated stroma (connective tissue), no GFAP and NeuN signal was present within the ventricular region. A higher magnification (40X) image of the hippocampus region in Figure 7.13a shows greater detail (Figure 7.13b). The several layers of neurons characteristic of mammalian hippocampus are clearly shown by NeuN labelling. In addition, GFAP-labelled astrocytes distributed within the hippocampus sections showed their typical ‘star-shaped’ morphology, closely associated with neuronal synapses. However, injected free IgG was not observed in the control brain tissues; only some weak signals coming from the second antibody can be seen beyond the folded section border. These control results suggest that the free IgG may be internalised by liver tissues, but there is lack of penetration into brain tissues due to the existence of the blood-brain barrier.

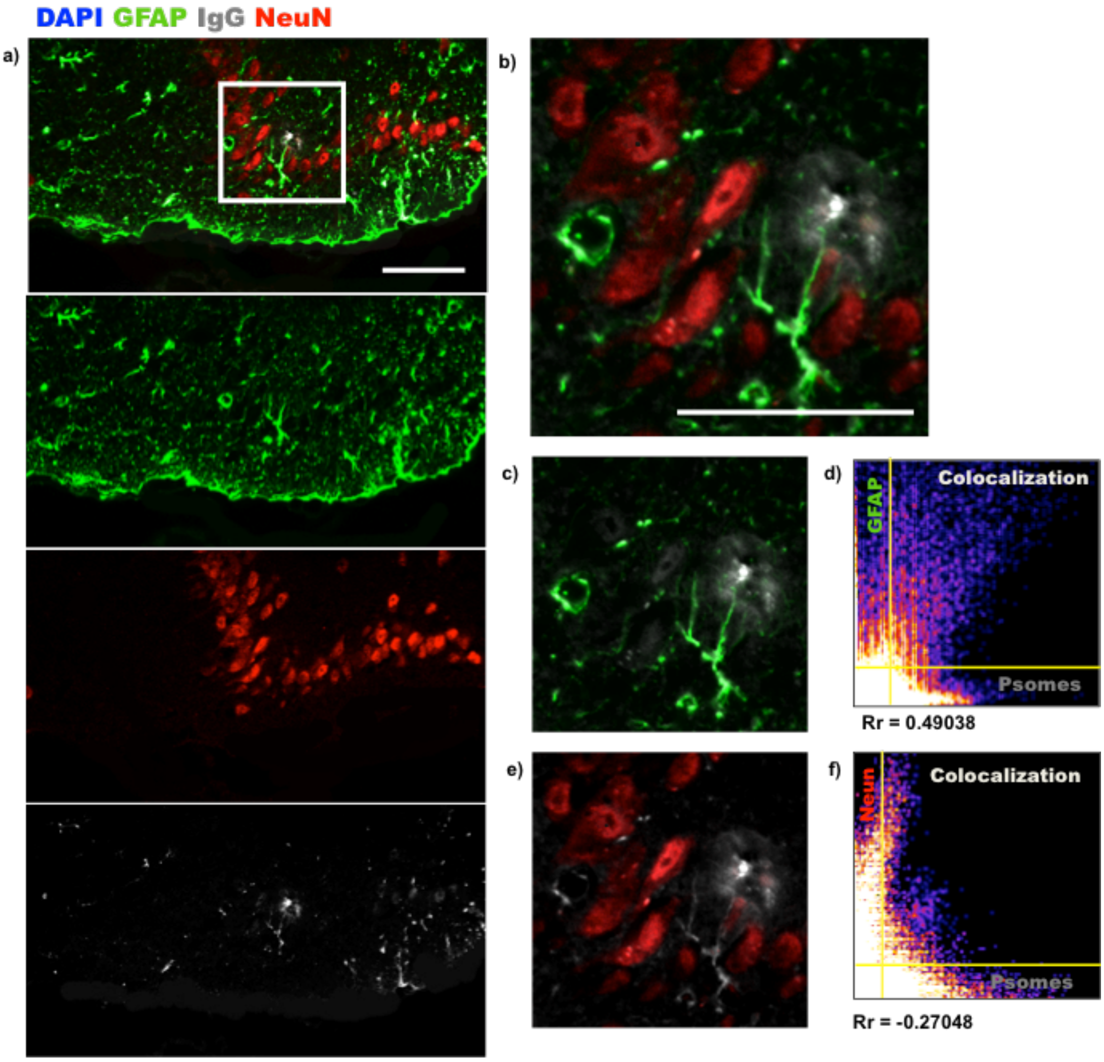

Figure 7.14 Confocal micrographs of mouse brain section 2 hours after IV injection with IgG-loaded functionalised polymersomes. a) Brain section with astrocyte and neuronal cell double labelling, 40X magnification, and serial windows demonstrating astrocyte, neuronal and IgG labelling. b) Higher magnification image (100X) from indicated region in a). c) Merged micrograph IgG and astrocytes. d) Scatter plot of colocalisation profile of IgG and astrocytes. e) Merged micrograph IgG and neurons. f) Scatter plot of colocalisation profile of IgG and neurons. GFAP (λ_{Ex}=480nm, λ_{Em}= BP500-520nm), NeuN (λ_{Ex}=633nm, λ_{Em}= BP650-700nm), IgG (λ_{Ex}=560nm, λ_{Em}= BP575-615nm). The scale bars represent 50μm.

In order to establish whether the functionalised polymersomes can deliver BBB-impermeable Cargo-IgG into the CNS, brain sections treated with IgG loaded Ang-POEGMA-PDPA polymersomes were then examined. As before, astrocytes and neurons were labelled by GFAP and NeuN antibodies, and visualised by immunofluorescence. The lower resolution (10X magnification) images showed fine brain sections including the hippocampus and associated ventricular system, with successful astrocyte and neuron double labelling (see ANNEX). However, unlike the free IgG-treated brain sections, the HSA Ab signal from loaded Ang-POEGMA-PDPA polymersomes can also be observed in the brain tissue.

Higher resolution (40X magnification, Figure 7.14a and 63X magnification, Figure 7.14b) images show this in more detail. There was a minimal signal in the ventricular region (see ANNEX). However, some identified signal from HSA Ab came from an area above the ventricular region, consisting of a dense population of neurons associated with a few astrocytes. Higher magnification (63X) confirmed the location of cargo IgG (Figure 7.14b). We further processed the colocalisation profile between the IgG signal delivered by Ang-POEGMA-PDPA polymersomes, with both astrocytes (Figure 7.14c) and neurons (Figure 7.14e). Some IgG signals were associated either with astrocytes or neurons; however, some IgG signals indicated internalisation within glial cells to a certain degree (Rr=0.49038. Rr refers to the Pearson correlation coefficient, where: Rr=1 = perfect colocalisation; Rr=0 = random localisation; Rr=-1 = perfect exclusion) and indicated a much higher level of colocalisation than IgG with neurons (Rr:-0.27048). Although so far there is no quantitative data analysis on the amount of delivered cargo, these microscopy data strongly suggest that Ang-POEGMA-PDPA polymersomes possess the capability of targeting transcytosis, crossing the blood-brain barrier and delivering macromolecules into the CNS.

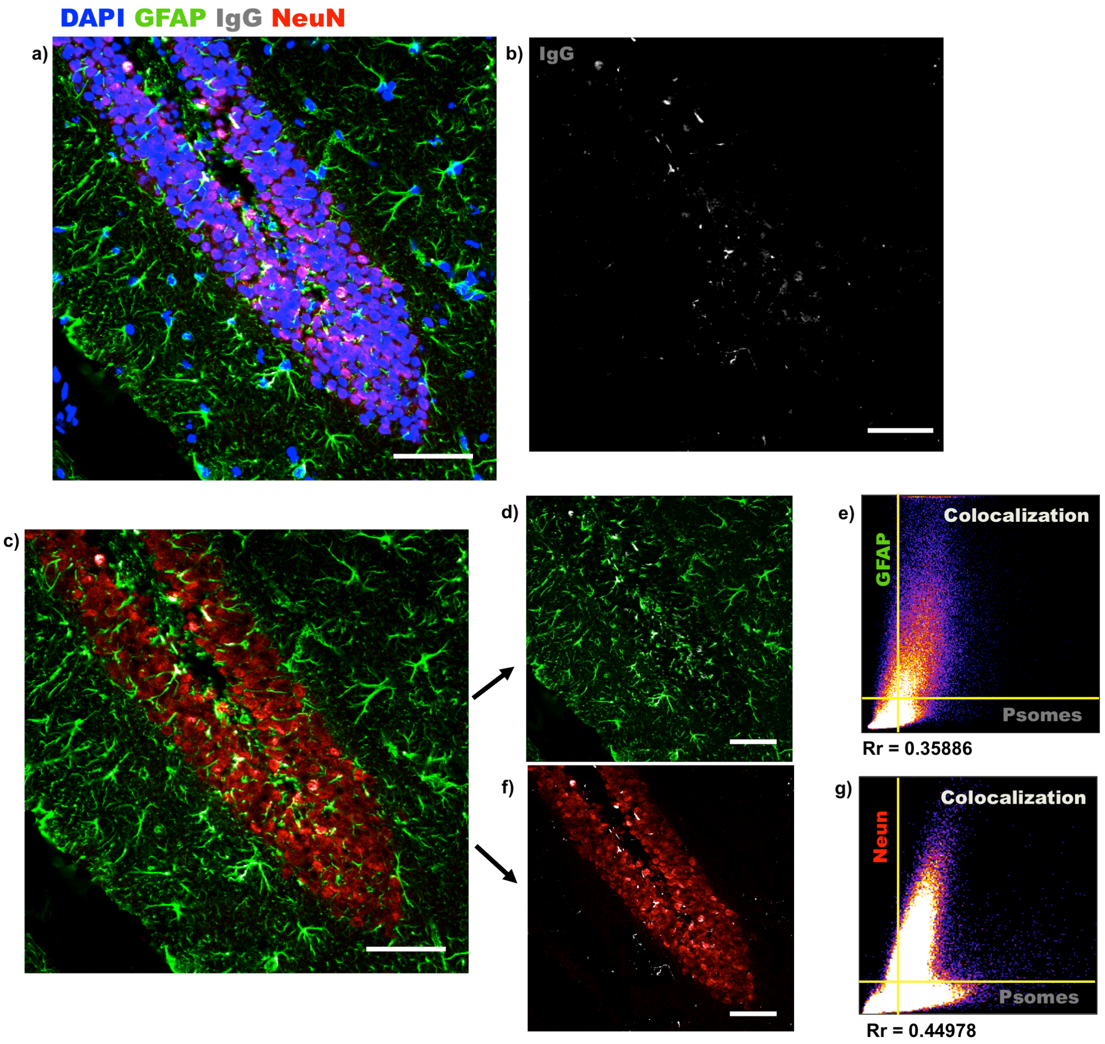

Figure 7.15 Confocal micrographs of mouse hippocampal section 2 hours after IV injection with IgG-loaded functionalised polymersomes. a) Astrocyte and neuronal cell double labelling, 40X magnification. b) IgG channel from a). c) Merged micrograph IgG, neurons and astrocytes. d) Merged micrograph IgG and astrocytes. e) Scatter plot of colocalisation profile of IgG and Astrocytes. f) Merged micrograph IgG and neurons. g) Scatter plot of colocalisation profile of IgG and neurons. GFAP (λ_{Ex}=480nm, λ_{Em}= BP500-520nm), NeuN (λ_{Ex}=633nm, λ_{Em}= BP650-700nm), IgG (λ_{Ex}=560nm, λ_{Em}= BP575-615nm). The scale bars represent 50µm.

Higher-resolution (40X magnification) images from the hippocampus region (Figure 7.15) and choroid plexus (Figure 7.16) were also captured. The hippocampus section illustrated a dense neuronal cell layer closely associated with astrocytic glial cells (Figure 7.15a). Delivered HSA Ab was clearly observed in this section (Figure 7.15b) showing internalisation by astrocytes and less association with neurons. As the scatter plot profile again demonstrates, the level of colocalisation between IgG and astrocytes (Rr: 0.3586) was much higher than between IgG and neurons (Rr: 0.04978). The colocalisation studies suggest that astrocyte end feet might be particularly effective at interacting with IgG-loaded functionalised polymersomes. This is possibly due to the distance between astrocytes and brain capillaries, which is much shorter than between neurons and capillaries. By contrast, hardly any HSA Ab signal could be found in the choroid plexus section (Figure 7.16). This suggests that the central nervous system might sort the polymersomes (or polymer blocks) and the loaded cargo (IgG) into different pathways, hence their final destination is different.

In conclusion, Angiopep-2 (1.2%)-functionalised POEGMA-PDPA polymersomes were chosen for *in vivo* administration according to 3D BBB *in vitro* screening results. The initial *in vivo* distribution data indicated that Ang-POEGMA-PDPA polymersomes were present in brain sections. A further short-term (two-hour) blood capillary labelling experiment demonstrated that these functionalised polymersomes are able to penetrate the blood-brain barrier via an effective receptor-mediated transcytosis pathway. In addition, functionalised polymersomes that triggered ongoing RM transcytosis were successfully captured using CLS microscopy. Further work was performed using Ang-POEGMA-PDPA polymersomes encapsulating model cargo IgG, and successfully delivered into a mouse CNS system.

Work presented in this thesis can provide a useful platform for further examination of CNS delivery of polymersomes and their cargos.

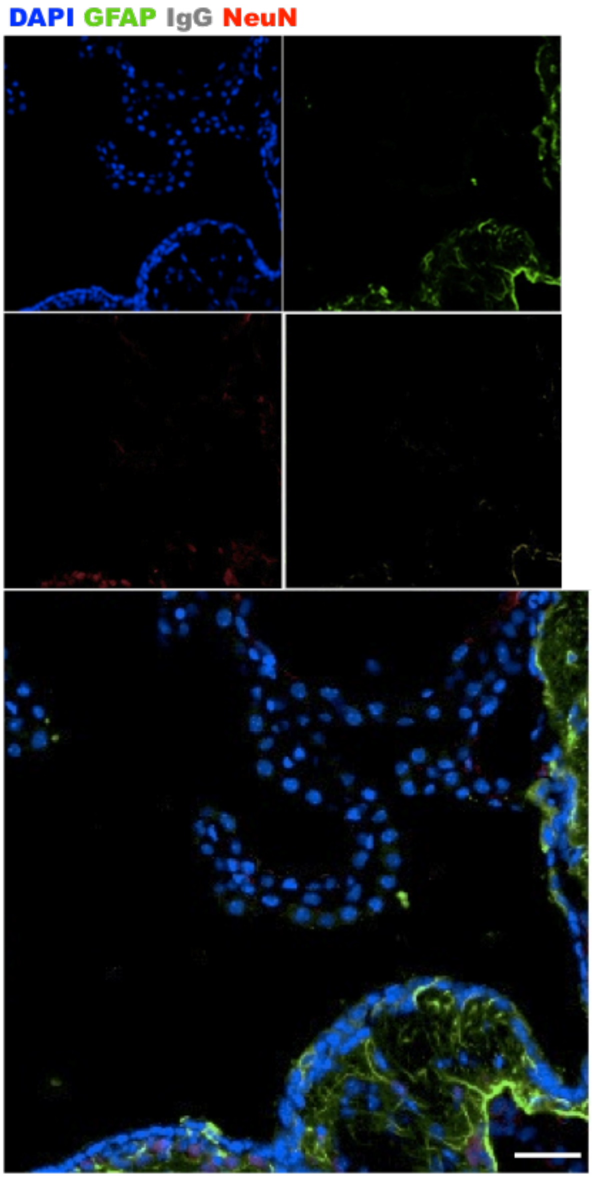

Figure 7.16 Confocal micrographs of mouse choroid plexus section 2 hours after IV injection with IgG-loaded functionalised polymersomes. Serial windows demonstrating nuclear, astrocyte, neuronal and IgG labelling, 40X magnification; merged image larger scale in lowest window. Brain adjacent to choroid plexus is shown at right and lower margins, with prominent astrocyte staining. DAPI (λ_{Ex}=405nm, λ_{Em}= BP420-450nm), GFAP (λ_{Ex}=480nm, λ_{Em}= BP500-520nm), NeuN (λ_{Ex}=633nm, λ_{Em}= BP650-700nm), IgG (λ_{Ex}=560nm, λ_{Em}= BP575-615nm). The scale bar represents 50μm.

References:

1. Huang, S.X., et al., *Dual targeting effect of Angiopep-2-modified, DNA-loaded nanoparticles for glioma.* Biomaterials, 2011. **32**(28): 6832-6838.
2. Xin, H.L., et al., *The brain targeting mechanism of Angiopep-conjugated poly(ethylene glycol)-co-poly(epsilon-caprolactone) nanoparticles.* Biomaterials, 2012. **33**(5): 1673-1681.
3. Shao, K., et al., *Angiopep-2 modified PE-PEG based polymeric micelles for amphotericin B delivery targeted to the brain.* Journal of Controlled Release, 2010. **147**(1): 118-126.
4. Ke, W.L., et al., *Gene delivery targeted to the brain using an Angiopep-conjugated polyethyleneglycol-modified polyamidoamine dendrimer.* Biomaterials, 2009. **30**(36): 6976-6985.
5. Goti, D., et al., *Scavenger receptor class B, type I is expressed in porcine brain capillary endothelial cells and contributes to selective uptake of HDL-associated vitamin E.* Journal of Neurochemistry, 2001. **76**(2): 498-508.
6. Srivastava, R.A.K., *Scavenger receptor class B type I expression in murine brain and regulation by estrogen and dietary cholesterol.* Journal of the Neurological Sciences, 2003. **210**(1-2): 11-18.
7. Iliff, J.J., et al., *Brain-wide pathway for waste clearance captured by contrast-enhanced MRI.* Journal of Clinical Investigation, 2013. **123**(3): 1299-1309.
8. Little, D., et al., *Endothelial-cell markers in vascular neoplasms - an immunohistochemical study comparing factor-viii-related antigen, blood-group specific antigens, 6-Keto-Pgf1-Alpha, and ulex-europaeus-1 lectin.* Journal of Pathology, 1986. **149**(2): 89-95.
9. Ordonez, N.G. and J.G. Batsakis, *Comparison of ulex-europaeus-I lectin and factor-viii-related antigen in vascular-lesions.* Archives of Pathology & Laboratory Medicine, 1984. **108**(2): 129-132.
10. Lomas, H., et al., *Biomimetic pH sensitive polymersomes for efficient DNA encapsulation and delivery.* Advanced Materials, 2007. **19**(23): 4238.
11. Hawkins, B.T. and T.P. Davis, *The blood-brain barrier/neurovascular unit in health and disease.* Pharmacological Reviews, 2005. **57**(2): 173-185.
12. Wang, L.G., et al., *Encapsulation of biomacromolecules within polymersomes by electroporation.* Angewandte Chemie-International Edition, 2012. **51**(44): 11122-11125.

ANNEX

Supporting Information

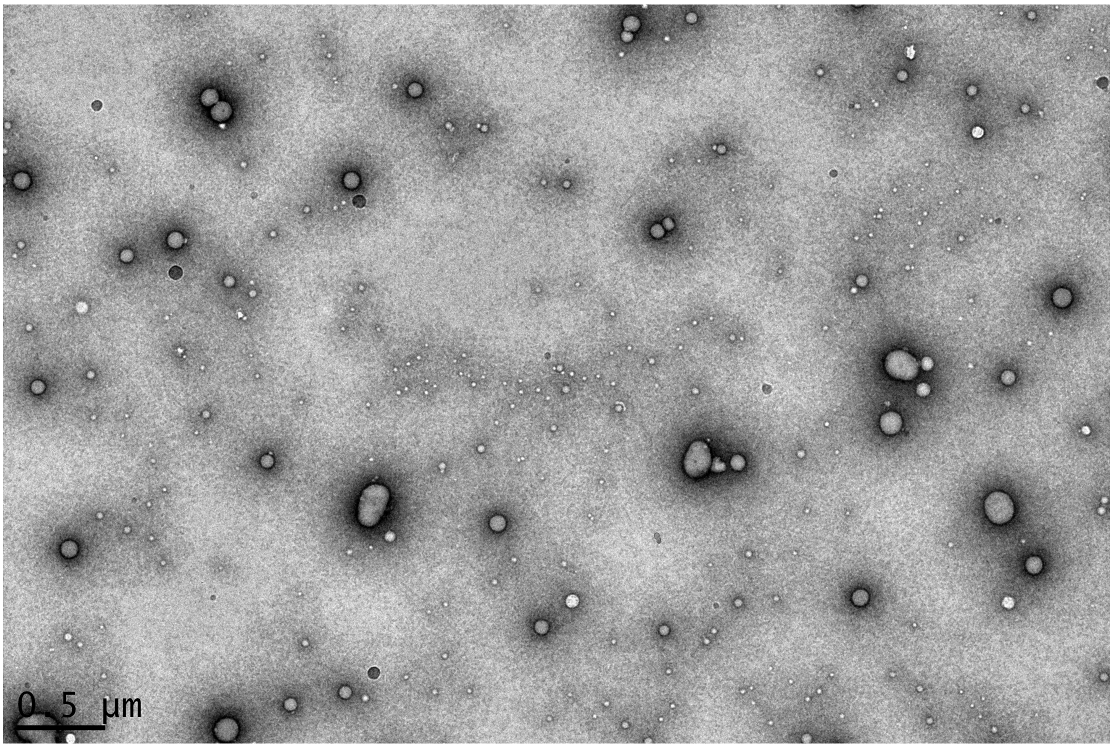

Figure S.1 | Low-resolution TEM micrograph of pristine POEGMA-PDPA polymersomes.

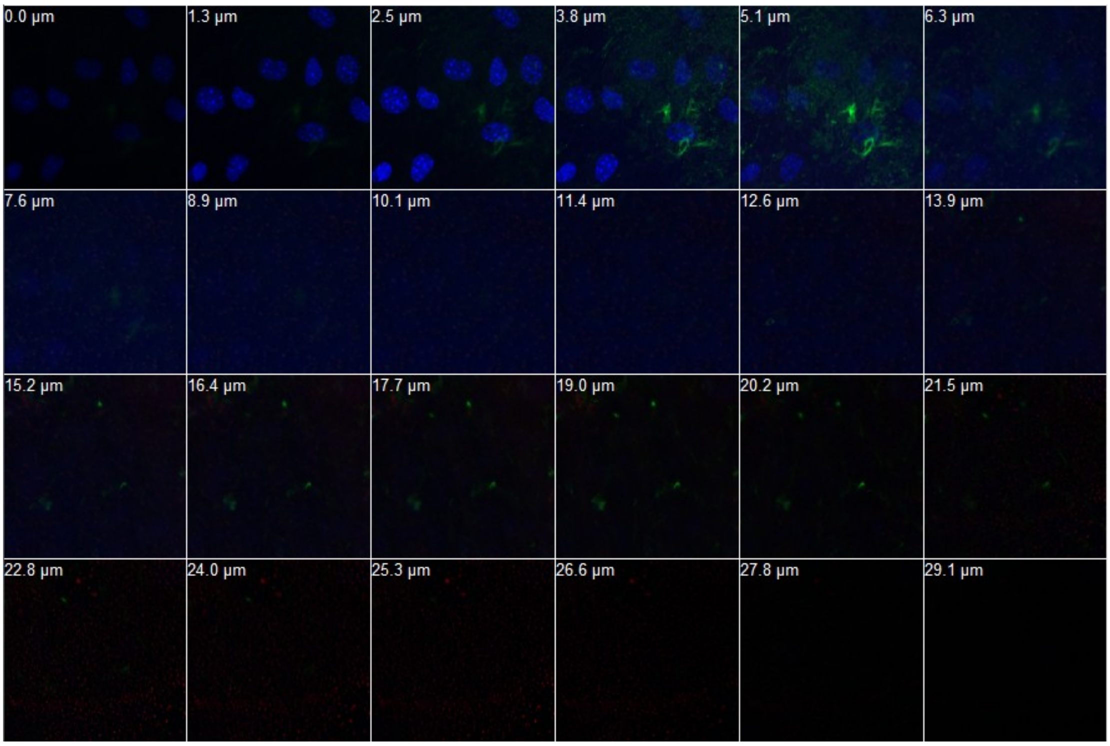

Figure S.2 | Z-stack gallery image from Figure 6.9a (Pristine POEGMA-PDPA).

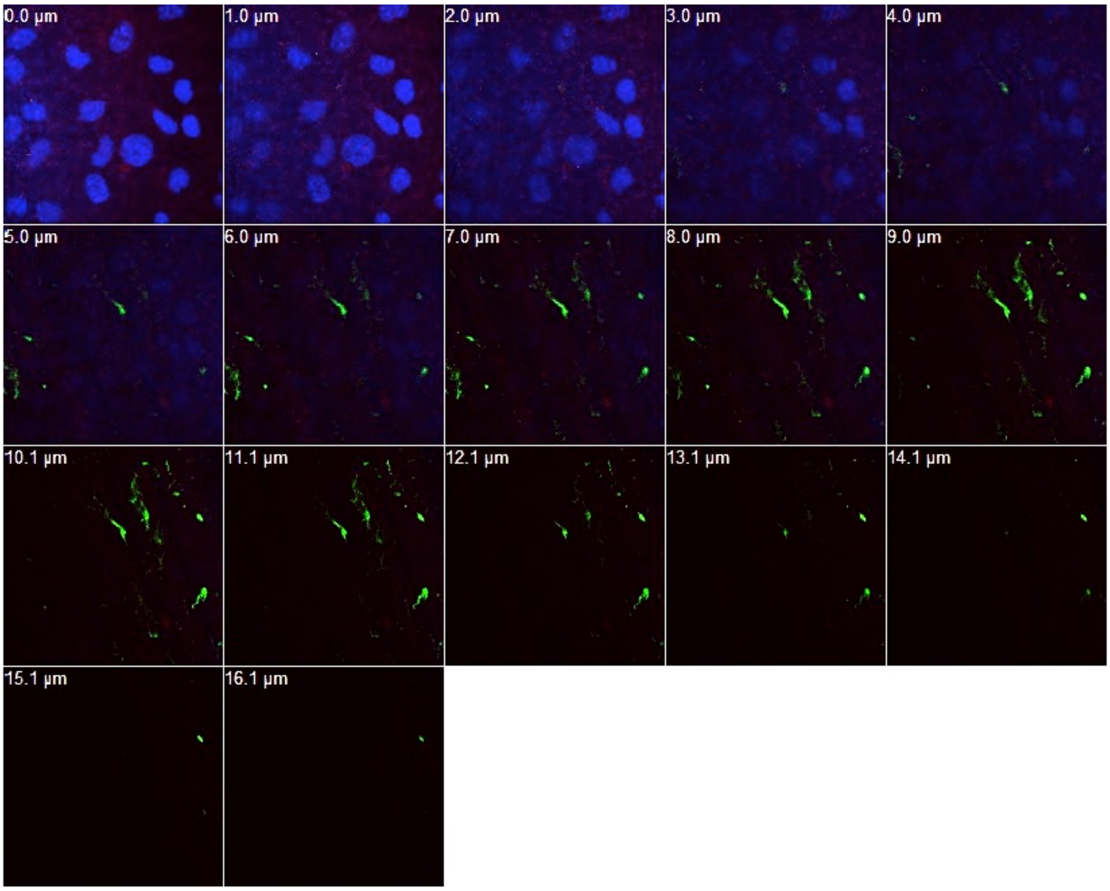

Figure S.3 | Z-stack gallery image from Figure 6.9b (PMPC-PDPA).

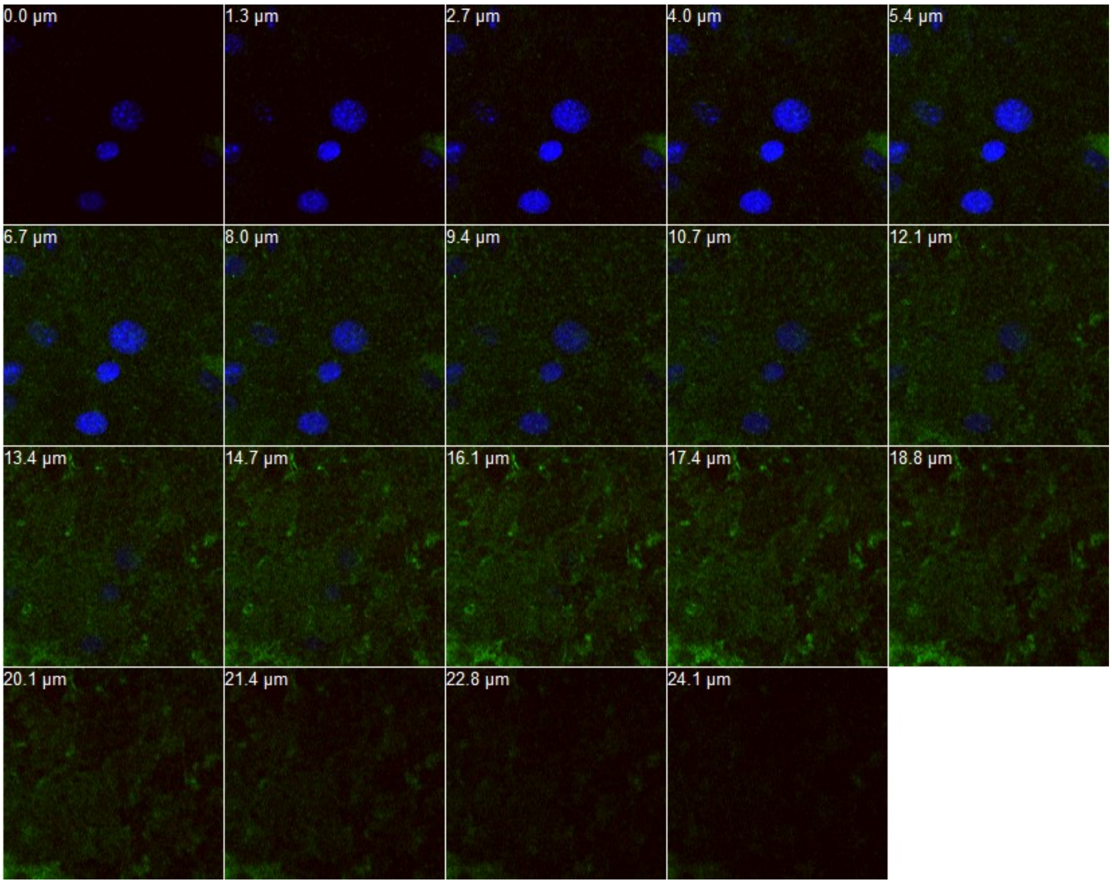

Figure S.4 | Z-stack gallery image from Figure 6.9c (RVG-POEGMA-PDPA).

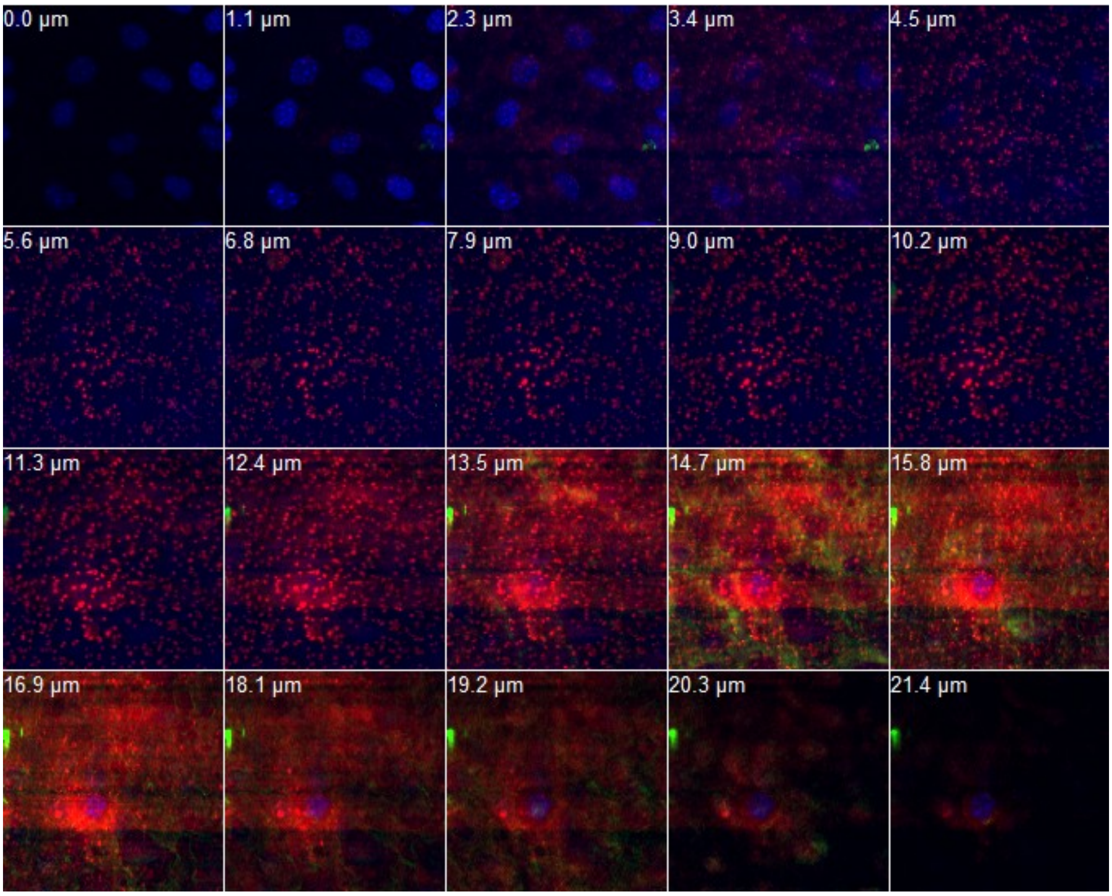

Figure S.5 | Z-stack gallery image from Figure 6.9d (Ang-POEGMA-PDPA).

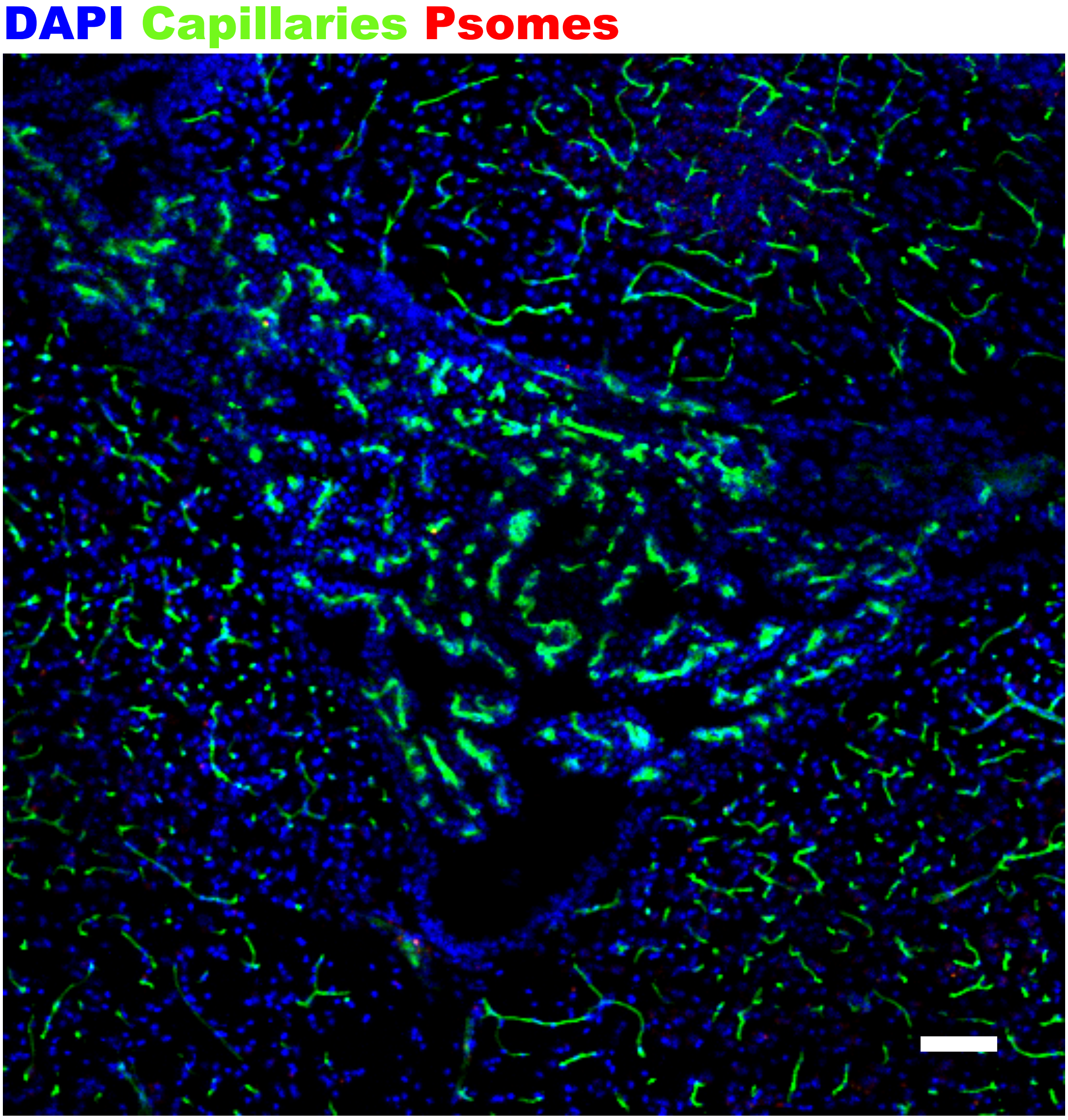

Figure S.6 | 10X magnification micrograph for Figure 7.7c , 24 hours post PMPC-PDPA polymersome IV injection.

Figure S.7 | 10X magnification micrograph for Figure 7.7d, 24 hours post PMPC-PDPA polymersome IV injection.

Figure S.8 | 10X magnification micrograph for Figure 7.7f (indicated region), 2 hours post IV injection of Ang-POEGMA-PDPA polymersomes.

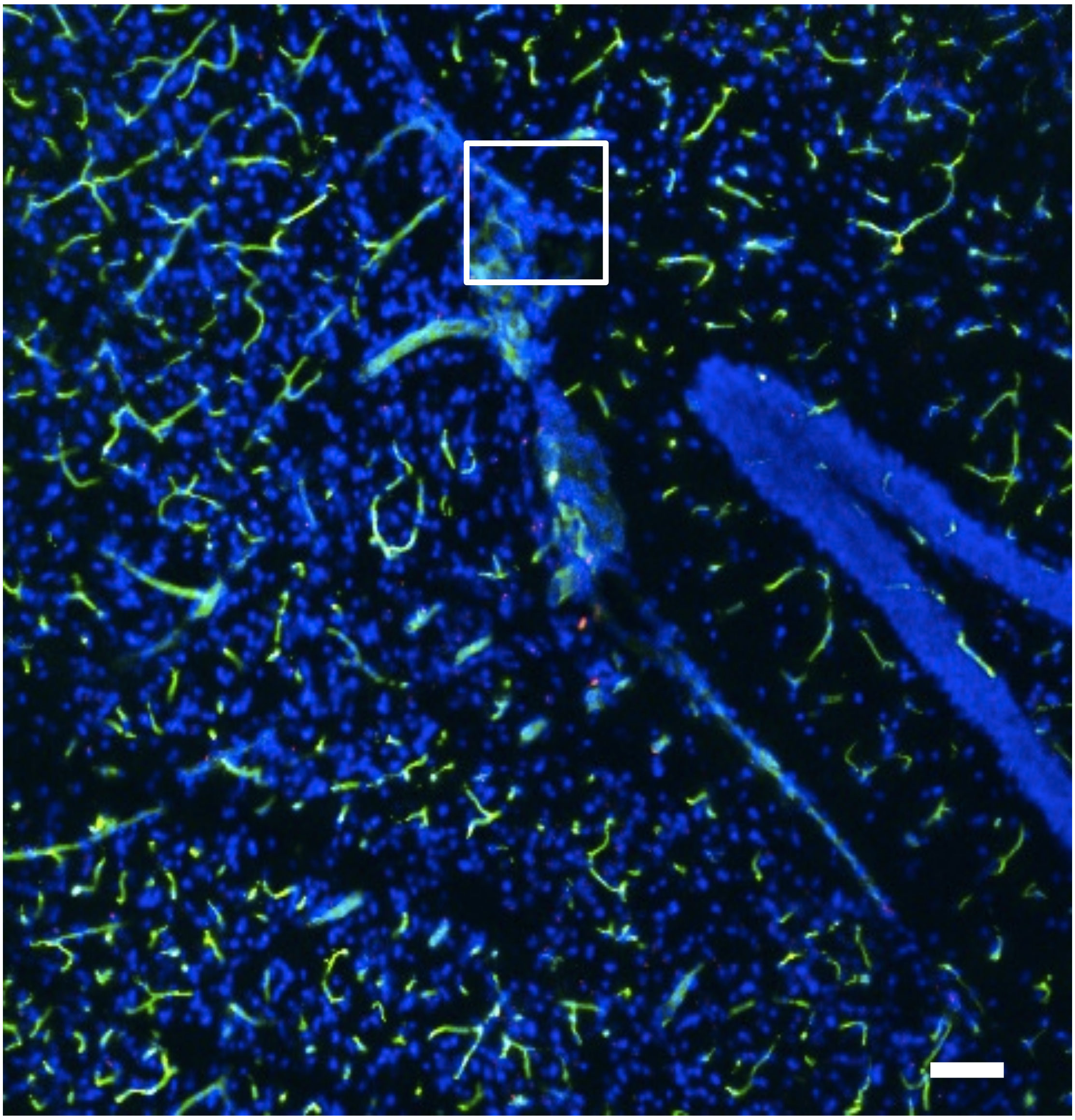

Figure S.9 | 10X magnification micrograph for Figure 7.7h (indicated region), 24hours post IV injection of Ang-POEGMA-PDPA polymersomes.

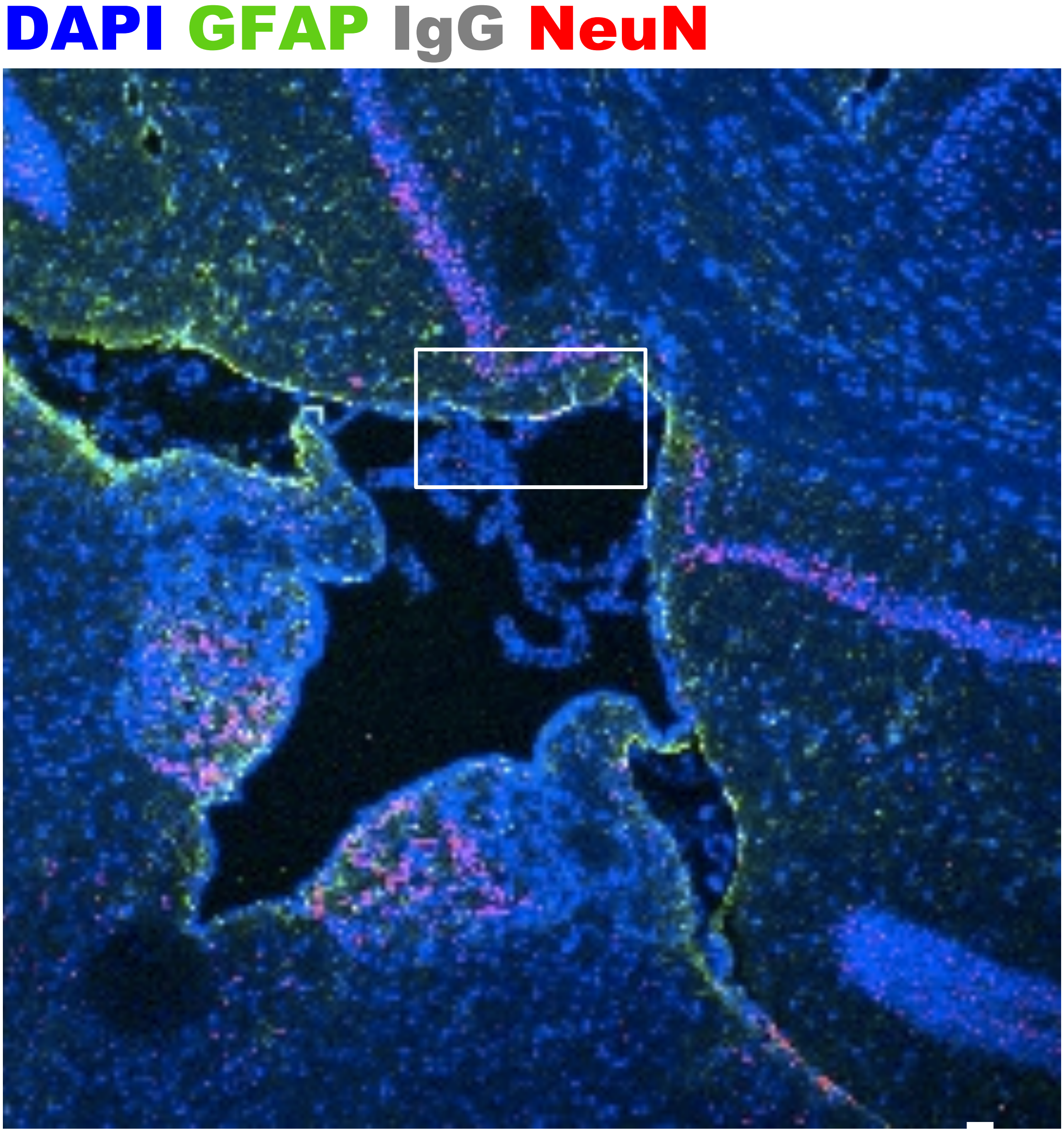

Figure S.10 | 10X magnification micrograph for Figure 7.13 (indicated region), 2hours post IV injection of IgG loaded Ang-POEGMA-PDPA polymersomes.

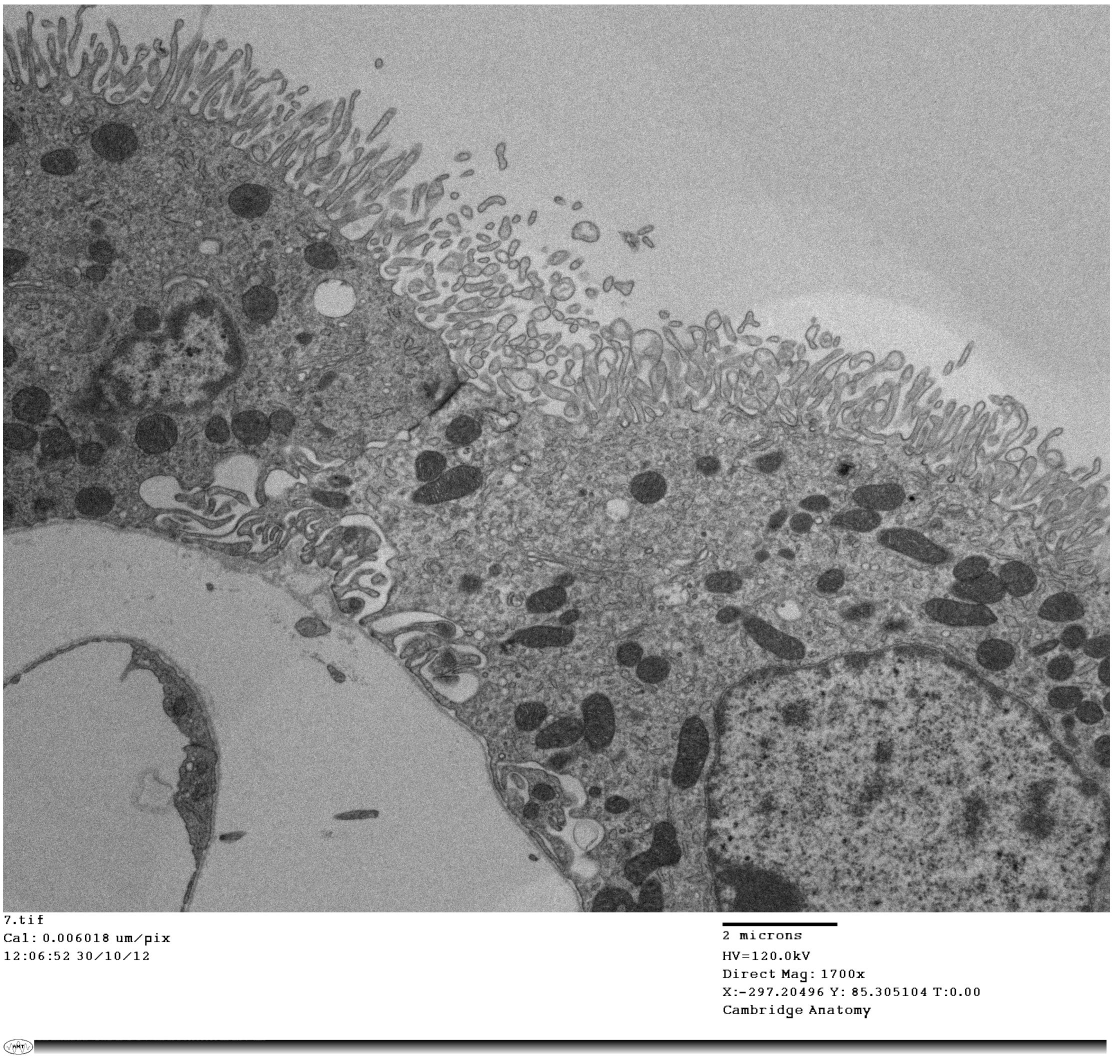

Figure S.11 | TEM micrograph of epithelial cells of mouse brain choroid plexus.